SLAC-R-938

Measurement of the $\bar{B}^0 \to D^{*+}\ell^-\bar{\nu}$ Branching Fraction with a Partial Reconstruction Technique

A Dissertation

Presented for the

Doctor of Philosophy

Degree

The University of Mississippi

Peter Sonnek

August 2009

Work supported in part by US Department of Energy contract DE-AC02-76SF00515.
SLAC National Accelerator Laboratory, Menlo Park, CA 94025

Acknowledgments

I would like to express my gratitude to all the people who have guided me throughout the duration of this work and for the support I have received from so many people which has enabled me to pursue this degree. I would like to thank my adviser Dr. Lucien Cremaldi for his guidance and words of encouragement through the years of the graduate program. Along with Dr. Lucien Cremaldi I would also like to extend my gratitude to Dr. Breese Quinn, Dr. Don Summers, Dr. Robert Kroeger, Dr. Gerard Buskes and Dr. Romulus Godang for serving on the dissertation committee, for their hard work and for the constructive feedback which they have provided for this dissertation. I am very thankful to the *BABAR* Collaboration for their friendly and helpful communication and for providing such a large data set, without which this work would not have been possible. I would like to also thank Dr. David Sanders for his thorough attention to my work and his correction suggestions. Lastly I would like to thank my parents for their support throughout the years. The encouragement which they have provided is what enabled me to pursue my goals and ultimately produce this work.

Abstract

Presented is a precise measurement of the $\bar{B}^0 \to D^{*+}\ell^-\bar{\nu}_\ell$ branching fraction using $81.47 fb^{-1}$ of data collected with the *BABAR* detector at the PEP-II e^+e^- storage ring at the Stanford Linear Accelerator Center. The measurement was performed by partially reconstructing the D^{*+} meson from $\bar{B}^0 \to D^{*+}\ell^-\bar{\nu}_\ell$ decays using only the soft pion of the $D^{*+} \to D^0\pi^+$ decay to reconstruct its four vector. The branching fraction was measured to be $\mathcal{B}(\bar{B}^0 \to D^{*+}\ell^-\bar{\nu}_\ell) = (4.91 \pm 0.01_{stat} \pm 0.15_{syst})\%$.

Contents

1 Physics of B Decays and Theoretical Concepts **1**
- 1.1 CP Violation . . . 1
- 1.2 The CKM Matrix . . . 4
- 1.3 The $\bar{B}^0 \to D^{*+}\ell^-\bar{\nu}_\ell$ Decay . . . 6
- 1.4 Heavy Quark Symmetry . . . 9
- 1.5 Heavy Quark Effective Theory (HQET) . . . 9
- 1.6 The Isgur-Wise function . . . 11
- 1.7 Form Factors . . . 12
  - 1.7.1 Differential Decay Rates . . . 14
  - 1.7.2 HQET Form Factors . . . 16
  - 1.7.3 Generic Form Factor Expansion . . . 22

2 The *BABAR* Experiment at SLAC **24**
- 2.1 SLAC . . . 24
- 2.2 The $\Upsilon(4S)$ Resonance . . . 24
- 2.3 The *BABAR* Detector . . . 29
  - 2.3.1 The Silicon Vertex Detector . . . 31
  - 2.3.2 The Drift Chamber . . . 32
  - 2.3.3 The Detector of Internally Reflected Cherenkov Radiation (DIRC) 34
  - 2.3.4 The Electromagnetic Calorimeter . . . 35
  - 2.3.5 The Instrumented Flux Return . . . 36
- 2.4 Trigger and Data Acquisition . . . 37

3 Event Selection and Analysis Method **41**
- 3.1 Partial Reconstruction . . . 41
- 3.2 Data Sample . . . 43
- 3.3 Fox-Wolfram Moments . . . 44
- 3.4 Event Selection . . . 47
- 3.5 Signal Definition . . . 52
- 3.6 Branching Fraction Determination . . . 53
- 3.7 Reconstruction Efficiency . . . 54
  - 3.7.1 The $\bar{B}^0 \to D^{*+}\ell\bar{\nu}_\ell$ efficiency . . . 54
  - 3.7.2 The $\bar{B}^0 \to D^{**+}\ell^-\bar{\nu}_\ell$ efficiency (Peaking Background) . . . 57

4 Backgrounds **59**
- 4.1 Continuum Background . . . 59
- 4.2 Combinatoric Background . . . 59
- 4.3 Peaking Background . . . 63
- 4.4 Radiative Corrections . . . 66
  - 4.4.1 PHOTOS . . . 69
- 4.5 Event Type Distributions . . . 70

5 Branching Fraction Extraction **74**
5.1 Raw Data and Monte Carlo . . . 74
5.2 Method 1 - Subtraction Method . . . 75
5.3 Method 2 - 1D Fitting Method . . . 81
5.4 Method 3 - 2D Fit Method . . . 92

6 Monte Carlo Adjustments **104**
6.1 Monte Carlo Tuning . . . 104
6.2 Monte Carlo Form Factor Reweighting . . . 114
6.2.1 Signal Form Factor Reweighting . . . 114
6.2.2 D^{**} Form Factor Reweighting . . . 117
6.3 PID Tweaking . . . 120
6.4 Track Killing . . . 125
6.5 Peaking Background Offset . . . 128

7 Systematic Errors **130**
7.1 PID Tweaking . . . 130
7.2 Track Killing . . . 133
7.3 Soft pion efficiency . . . 136
7.4 Radiative Corrections . . . 140
7.5 Background Shapes . . . 141
7.5.1 Continuum Background . . . 141
7.5.2 Peaking Background . . . 142
7.5.3 Combinatoric Background . . . 148
7.6 Fit Error . . . 148
7.7 Form Factor dependence . . . 149
7.7.1 Reweighting Effects . . . 149
7.7.2 Signal Extraction . . . 154

8 Results **156**
8.1 Branching Fraction Results . . . 156
8.2 Consideration of $|V_{cb}|$ . . . 159

List of Tables

1 Calculated production cross-sections at $\sqrt{s} = M(\Upsilon(4S))$ [2] 26
2 Some parameters of the silicon vertex tracker layout [2] 32
3 Properties of the Thallium-doped CsI [2] 36
4 Selection criteria for the $D^{*+}\ell^-\bar{\nu}$ decay 52
5 Efficiency Calculation Numbers 56
6 Calculated Efficiencies 57
7 Individual branching fractions for each contributing D^{**} mode 58
8 Event Type Classifications 71
9 Signal and Background Yields for Method 1 RS MC 77
10 Branching Fractions - Method 1 77
11 Signal and Comb. Background Yields for Method 1 WS MC and WS data 78
12 Signal and Background Yields for Method 2 - Both Leptons 84
13 Signal and Background Yields for Method 2 - Electrons Only 84
14 Signal and Background Yields for Method 2 - Muons Only 84
15 Branching Fractions Method 2 - Both Leptons 85
16 Branching Fractions Method 2 - Electrons Only 85
17 Branching Fractions Method 2 - Muons Only 85
18 Linear shape parameters for RS MC of Run 1 94
19 Signal and Background Yields for Method 3 - Run 1 RS MC with shaping 94
20 Signal and Background Yields for Method 3 - Both Leptons 95
21 Signal and Background Yields for Method 3 - Electrons Only 95
22 Signal and Background Yields for Method 3 - Muons Only 95
23 Branching Fractious Method 3 - Both Leptons 96
24 Branching Fractions Method 3 - Electrons Only 96
25 Branching Fractions Method 3 - Muons Only 96
26 Mean and RMS values of momentum and M_ν^2 shapes before and after Monte Carlo tuning 107
27 Form factor parameters [23] 116
28 D^{**} branching fractions for Monte Carlo 118
29 Tracking corrections for R22 data selected by GTL according to [64] . . . 126
30 Slope and offset parameters for track killing pull fits 127
31 Systematic Errors Method 3 (Method 2) 130
32 Signal and background yields for PID tweaking variations 132
33 Signal and background yields for track killing variations 134
34 Slope and offset parameters for track killing pull fits 135
35 Extraction yields for soft pion correction 138
36 Slope and offset parameters soft pion correction pull fits 139
37 Signal and background yields for a 30% variation on the photon admixture of the MC signal 140
38 Signal and background yields for the systematic variation on the peaking background 144
39 Signal yields of form factor variation in signal region 155
40 Signal yields of form factor variation in sideband region 155
41 Efficiencies and branching fractions after form factor variation 155

42 Branching fractions for both methods, both leptons and combined over both runs ($NDF = 58$) 158
43 $\mathcal{B}(\bar{B}^0 \to D^{*+}\ell^-\bar{\nu}_\ell)$ comparison with published results 158
44 $F(1)|V_{cb}|$ comparison with published results 160

List of Figures

1 Feynman diagram of B meson oscillation. 1
2 Feynman diagram for the B decay 7
3 Higher order Feynman diagrams for the B decay 8
4 Schematic diagram of the gluon field seen by the light degrees of freedom due to the current of the moving quark. The figure has been taken from [16]. 10
5 Schematic representation of the $\bar{B}^0 \to D^{*+}\ell^-\bar{\nu}_\ell$ decay through the reconstruction channel of $D^* \to D^0\pi^+$. The figure has been taken from [16]. . 15
6 Differential decay rate in phase space of w with (red) and without (black) the form factor contribution. The form factor contribution has been multiplied by a factor of 2 to make the shift in phase space more apparent. . 22
7 Shape of the form factor $\mathcal{F}^2(w)$ in phase space of w with the given parametrization in (39) (Form Factor 1) and with the parametrization given in (48) (Form Factor 2) 23
8 Simplest Feynman diagram of the $\Upsilon(4S)$ decay 25
9 Scan of the hadronic cross section of the e^+e^- annihilation process. The Υ resonances rise above a $q\bar{q}$ background. The figure has been taken from [31]. 26
10 The *BABAR* detector. Figure taken from [33] 30
11 General outline of the Silicone Vertex Tracker (SVT). The cross sectional view shows the five silicone strip layers surrounding the beam pipe. The high resolution hits are used for vertex detection. The figure has been taken from [2]. 31
12 Schematic side view of the Drift Chamber (DCH) showing the 40 layers of the wire chamber. Due to the asymmetric interaction beam energies the interaction point is shifted to the left. The figure has been taken from [35]. 33
13 Isochronous lines of a single cell of the DCH. The middle sense wire is surrounded by 6 field wires. The contours represent the 50 ns isochrones of the cell. The dimensions of the cell are about 12 mm by 18 mm. The figure has been taken from [35]. 34
14 Geometrical layout of the EMC crystals. The end cap is only necessary on the right due to the asymmetric beam energies. The figure has been taken from [39]. 36
15 Angular distribution of D^{*+} and π^+ momentum vectors for Partial Reconstruction 42
16 Momentum distribution between D^{*+} meson and soft pion (select data Run 2). Left: True distribution from Monte Carlo. Right: Distribution after partial reconstruction. The red line indicates the linear relation imposed by the partial reconstruction technique. 43

17 Second Fox-Wolfram moment H_2 for the e^+e^- annihilation process at $\sqrt{s} = 10$ GeV. The dotted line are $q\bar{q}$ "background" events and the dashed line are resonant events. It can be seen that this variable has good discrimination power for continuum background rejection. The solid line are $q\bar{q}$ events with the creation of an extra gluon. The figure has been taken from [46]. 46
18 χ spectrum for data and Monte Carlo: (left) Full χ spectrum of an earlier data set processed with the partial reconstruction technique taken from [47] for comparison. (right) χ spectrum of this analysis. The dotted curve (red) is data while the solid (black) curve and the shaded regions are the corresponding Monte Carlo constituents. 49
19 M_ν^2 spectrum for raw data: (left) M_ν^2 distribution for the $\chi < 0.3$ cut. (right) M_ν^2 distribution for the $\chi < 0.4$ cut. 50
20 Momentum spectra for the different χ cuts. Top: Pion momentum spectrum for $\chi < 0.3$ (left) and $\chi < 0.4$ (right). Bottom: Lepton momentum spectrum for $\chi < 0.3$ (left) and $\chi < 0.4$ (right). 51
21 Neutrino Mass Square, $\mathcal{M}_\nu^2$ spectrum from data. 53
22 Pure Monte Carlo Signal 56
23 Continuum and combinatoric background shapes: Top: (left) Continuum background from off resonance data. (right) RS MC Combinatoric Background. Bottom: (left) WS MC Combinatoric Background. (right) WS Data Combinatoric Background. 61
24 Combinatoric Background Comparisons: Top Row: (left) Superposition of Combinatoric Background shapes, (right) Difference of RS MC and WS MC comb. BG. Bottom: (left) Difference of RS MC and WS data comb. BG, (right) Difference of WS MC and WS data comb. BG. 62
25 Peaking background shapes for neutral B mesons. Top: (left) Cascade decays originating from charm states, (right) Cascade decays originating from tau decays. Bottom: (left) Peaking background from mis-identified pions, (right) $D^{**}/D^*(n)\pi$ decays. 64
26 Peaking background shapes for charged B mesons. Top: (left) Cascade decays originating from charm states, (right) Cascade decays originating from tau decays. Bottom: (left) Peaking background from mis-identified pions, (right) $D^{**}/D^*(n)\pi$ decays. 65
27 Photon energies and multiplicities for radiative D^* and D^{**} events: Left to right: Photon energies in C.M. frame, photon energies (log scale), photon multiplicities. Top to Bottom: D^* events, D^{**} events from neutral B mesons, D^{**} events from charged B mesons. 68
28 D^* signal shape for non-radiative events (black) and radiative events (red). 68
29 Event Type Distribution for neutral B mesons from Monte Carlo. 72
30 Event Type Distribution for charged B mesons from Monte Carlo 73
31 Comparison between raw data and raw Monte Carlo before adjusting and tuning techniques are applied. Top: Run 1 comparison of the histograms (left) and their pull values (right). Bottom: Run 2 comparison of the histograms (left) and their pull values (right). 75

32 Signal extraction summary plots for method 1 for Run 1: Top: (left) Raw data (black) and continuum background after luminosity and energy scaling (magenta). (right) Continuum background subtracted data (black) with RS MC combinatoric background fit to the sideband (red). Middle: (left) Combinatoric background subtracted data now containing signal and peaking background (black) and MC peaking background (blue). (right) Data composition from continuum background (magenta), RS MC combinatoric background (red), MC peaking background (blue) and the data signal (black). Bottom: (left) Data composition from continuum background (magenta), WS MC combinatoric background (red), MC peaking background (blue) and the data signal (black). (left) Data composition from continuum background (magenta), WS data combinatoric background (red), MC peaking background (blue) and the data signal (black). 79
33 Signal extraction summary plots for method 1 for Run 2: Top: (left) Raw data (black) and continuum background after luminosity and energy scaling (magenta). (right) Continuum background subtracted data (black) with RS MC combinatoric background fit to the sideband (red). Middle: (left) Combinatoric background subtracted data now containing signal and peaking background (black) and MC peaking background (blue). (right) Data composition from continuum background (magenta), RS MC combinatoric background (red), MC peaking background (blue) and the data signal (black). Bottom: (left) Data composition from continuum background (magenta), WS MC combinatoric background (red), MC peaking background (blue) and the data signal (black). (left) Data composition from continuum background (magenta), WS data combinatoric background (red), MC peaking background (blue) and the data signal (black). 80
34 Fit Results for RS MC signal extraction for Run 1. Left Column (top to bottom): M_ν^2 distributions for the fit and raw data for both lepton types, electrons only and muons only. The fit is sectioned into its contributions from continuum background (magenta), combinatoric background (red), peaking background (blue) and signal (green). Right Column (top to bottom): Pull of data to fit for both leptons, electrons only and muons only. 86
35 Fit Results for RS MC signal extraction for Run 2. Left Column (top to bottom): M_ν^2 distributions for the fit and raw data for both lepton types, electrons only and muons only. The fit is sectioned into its contributions from continuum background (magenta), combinatoric background (red), peaking background (blue) and signal (green). Right Column (top to bottom): Pull of data to fit for both leptons, electrons only and muons only. 87
36 Fit Results for WS MC signal extraction for Run 1. Left Column (top to bottom): M_ν^2 distributions for the fit and raw data for both lepton types, electrons only and muons only. The fit is sectioned into its contributions from continuum background (magenta), combinatoric background (red), peaking background (blue) and signal (green). Right Column (top to bottom): Pull of data to fit for both leptons, electrons only and muons only. 88

37 Fit Results for WS MC signal extraction for Run 2. Left Column (top to bottom): M_ν^2 distributions for the fit and raw data for both lepton types, electrons only and muons only. The fit is sectioned into its contributions from continuum background (magenta), combinatoric background (red), peaking background (blue) and signal (green). Right Column (top to bottom): Pull of data to fit for both leptons, electrons only and muons only. 89
38 Fit Results for WS data signal extraction for Run 1. Left Column (top to bottom): M_ν^2 distributions for the fit and raw data for both lepton types, electrons only and muons only. The fit is sectioned into its contributions from continuum background (magenta), combinatoric background (red), peaking background (blue) and signal (green). Right Column (top to bottom): Pull of data to fit for both leptons, electrons only and muons only. 90
39 Fit Results for WS data signal extraction for Run 2. Left Column (top to bottom): M_ν^2 distributions for the fit and raw data for both lepton types, electrons only and muons only. The fit is sectioned into its contributions from continuum background (magenta), combinatoric background (red), peaking background (blue) and signal (green). Right Column (top to bottom): Pull of data to fit for both leptons, electrons only and muons only. 91
40 Fit Results for RS MC signal extraction for Run 1 (left) and Run 2 (right) for both leptons in the M_ν^2 versus lepton momentum plane for data (black) and the Monte Carlo fit (red). 97
41 Fit Results for RS MC signal extraction for Run 1. Left Column (top to bottom): M_ν^2 distributions for the fit and raw data for both lepton types, electrons only and muons only. The fit is sectioned into its contributions from continuum background (magenta), combinatoric background (red), peaking background (blue) and signal (green). Right Column (top to bottom): Pull of data to fit for both leptons, electrons only and muons only. 98
42 Fit Results for RS MC signal extraction for Run 2. Left Column (top to bottom): M_ν^2 distributions for the fit and raw data for both lepton types, electrons only and muons only. The fit is sectioned into its contributions from continuum background (magenta), combinatoric background (red), peaking background (blue) and signal (green). Right Column (top to bottom): Pull of data to fit for both leptons, electrons only and muons only. 99
43 Fit Results for WS MC signal extraction for Run 1. Left Column (top to bottom): M_ν^2 distributions for the fit and raw data for both lepton types, electrons only and muons only. The fit is sectioned into its contributions from continuum background (magenta), combinatoric background (red), peaking background (blue) and signal (green). Right Column (top to bottom): Pull of data to fit for both leptons, electrons only and muons only. 100
44 Fit Results for WS MC signal extraction for Run 2. Left Column (top to bottom): M_ν^2 distributions for the fit and raw data for both lepton types, electrons only and muons only. The fit is sectioned into its contributions from continuum background (magenta), combinatoric background (red), peaking background (blue) and signal (green). Right Column (top to bottom): Pull of data to fit for both leptons, electrons only and muons only. 101

45 Fit Results for WS data signal extraction for Run 1. Left Column (top to bottom): M_ν^2 distributions for the fit and raw data for both lepton types, electrons only and muons only. The fit is sectioned into its contributions from continuum background (magenta), combinatoric background (red), peaking background (blue) and signal (green). Right Column (top to bottom): Pull of data to fit for both leptons, electrons only and muons only. 102
46 Fit Results for WS data signal extraction for Run 2. Left Column (top to bottom): M_ν^2 distributions for the fit and raw data for both lepton types, electrons only and muons only. The fit is sectioned into its contributions from continuum background (magenta), combinatoric background (red), peaking background (blue) and signal (green). Right Column (top to bottom): Pull of data to fit for both leptons, electrons only and muons only. 103
47 Pion Momentum Monte Carlo Tuning in the sideband region used to tune the combinatoric background: Left: Pion momentum spectrum of data (black line) versus Monte Carlo (red dots) before tuning (top) and after tuning (bottom). Right: Ratio of data to Monte Carlo for the pion momentum spectrum before tuning (top) and after tuning (bottom). . . 108
48 Lepton Momentum Monte Carlo Tuning in the sideband region used to tune the combinatoric background: Left: Lepton momentum spectrum of data (black line) versus Monte Carlo (red dots) before tuning (top) and after tuning (bottom). Right: Ratio of data to Monte Carlo for the lepton momentum spectrum before tuning (top) and after tuning (bottom). . . 109
49 Pion Momentum Monte Carlo Tuning in the signal region used to tune the signal and peaking background shapes: Left: Pion momentum spectrum of data (black line) versus Monte Carlo (red dots) before tuning (top) and after tuning (bottom). Right: Ratio of data to Monte Carlo for the pion momentum spectrum before tuning (top) and after tuning (bottom). . . 110
50 Lepton Momentum Monte Carlo Tuning in the signal region used to tune the signal and peaking background shapes: Left: Lepton momentum spectrum of data (black line) versus Monte Carlo (red dots) before tuning (top) and after tuning (bottom). Right: Ratio of data to Monte Carlo for the lepton momentum spectrum before tuning (top) and after tuning (bottom). 111
51 Monte Carlo Tuning for Peaking Shapes: Top: (left) Monte Carlo signal shape before and after tuning. (right): Ratio of Monte Carlo signal shape before to after tuning. Bottom: (left) $D^{**}/D^* n\pi$ Monte Carlo peaking distribution before and after tuning. (right) Ratio of $D^{**}/D^* n\pi$ Monte Carlo peaking distribution before to after tuning. 112
52 Monte Carlo Tuning for Combinatoric Background Shapes: Top: (left) RS MC combinatoric background shape before and after tuning. (right): Ratio of RS MC combinatoric background shape before to after tuning. Bottom: (left) WS MC combinatoric background shape before and after tuning. (right) Ratio of WS MC combinatoric background shape before to after tuning. 113
53 Form factor reweighting values for D^* signal Monte Carlo. 116

54 Left: Monte Carlo signal before (black) and after (red) form factor reweighting. Right: Ratio of the signal before to after form factor reweighting. . . 117
55 form factor reweighting values for D^{**} Monte Carlo modes. The top left plot does not decay to a D^{*+} meson and is therefore empty. 119
56 Monte Carlo D^{**} shape before (black) and after (red) form factor reweighting. 119
57 RS MC and WS MC combinatoric backgrounds before (black) and after (red) PID tweaking together with their pull plots. 123
58 MC Signal (top) and D^{**} peaking background (bottom) before (black) and after (red) PID tweaking together with their pull plots. 124
59 RS MC (top) and WS MC (bottom) combinatoric background before (black) and after (red) track killing together with their before to after pull plots. 126
60 MC Signal (top) and D^{**} peaking background (bottom) before (black) and after (red) track killing together with their before to after pull plots. . . . 127
61 Comparison between Monte Carlo signal and Monte Carlo peaking background. Left: Monte Carlo signal (black) and peaking background (red) scaled for comparison in arbitrary units for the M_ν^2 distribution. Right Monte Carlo signal (black) and peaking background (red) scaled in arbitrary units for the distributions in the lepton momentum. 129
62 Results of the variation of the PID tweaking error for unvaried (black) error added (red) and error subtracted (blue) shapes. 132
63 RS MC (top) and WS MC (bottom) combinatoric background before (black) and after (red) the systematic error was added to the track killing correction together with their before to after pull plots. 134
64 MC Signal (top) and D^{**} peaking background (bottom) before (black) and after (red) the systematic error was added to the track killing correction together with their before to after pull plots. 135
65 Differences in the relative soft pion turn (left) on curve for data (black) and Monte Carlo (red) and the pull between these values (right). 137
66 Comparison of the RS MC (top) and WS MC combinatoric background scaled to equal areas before (black) and after (red) the soft pion correction has been applied. 138
67 Comparison of the signal (top) and D^{**} peaking background scaled to equal areas before (black) and after (red) the soft pion correction has been applied. 139
68 Change of the MC signal shape due to a 30% radiative variation for more (top) and less (bottom) radiative contribution to the decay. 141
69 Variation of the $D1$ contribution to the D^{**} peaking background. Shown are the unvaried shape (black) and the total D^{**} shape with a variation of $+1\sigma$ (red) and -1σ. 145
70 Variation of the $D1'$ contribution to the D^{**} peaking background. Shown are the unvaried shape (black) and the total D^{**} shape with a variation of $+1\sigma$ (red) and -1σ. 146
71 Variation of the $D2$ contribution to the D^{**} peaking background. Shown are the unvaried shape (black) and the total D^{**} shape with a variation of $+1\sigma$ (red) and -1σ. 147

72 Form factor reweighting effects for the variation of ρ^2 by 1σ. All graphs are color codes as follows: Unvaried (black), $\rho^2+1\sigma$ (red), $\rho^2-1\sigma$ (blue): Top: (left) Effects of parameter variations on the $\mathcal{F}(w)^2$ versus w distribution. (right) Monte Carlo true signal for the form factor variations. Bottom: (left) Slow Pion momentum distribution for RS Monte Carlo form neutral B decays. (right) Lepton momentum distribution for RS Monte Carlo from neutral B decays. 151
73 Form factor reweighting effects for the variation of $R_1(1)$ by 1σ. All graphs are color codes as follows: Unvaried (black), $R_1(1)+1\sigma$ (red), $R_1(1)-1\sigma$ (blue): Top: (left) Effects of parameter variations on the $\mathcal{F}(w)^2$ versus w distribution. (right) Monte Carlo true signal for the form factor variations. Bottom: (left) Slow Pion momentum distribution for RS Monte Carlo form neutral B decays. (right) Lepton momentum distribution for RS Monte Carlo from neutral B decays. 152
74 Form factor reweighting effects for the variation of $R_2(1)$ by 1σ. All graphs are color codes as follows: Unvaried (black), $R_2(1)+1\sigma$ (red), $R_2(1)-1\sigma$ (blue): Top: (left) Effects of parameter variations on the $\mathcal{F}(w)^2$ versus w distribution. (right) Monte Carlo true signal for the form factor variations. Bottom: (left) Slow Pion momentum distribution for RS Monte Carlo form neutral B decays. (right) Lepton momentum distribution for RS Monte Carlo from neutral B decays. 153

1 Physics of B Decays and Theoretical Concepts

The $\bar{B}^0 \to D^{*+}\ell^-\bar{\nu}_\ell$ decay has the largest exclusive branching fraction of any B decay and is the basis for the determination of the weak mixing matrix element $|V_{cb}|$ and hadronic form factor parameters of B decays. This dissertation applies a novel technique of partial reconstruction to make the most precise statistical measurement of this branching fraction to date. This section is intended to give an overview of the theoretical concepts behind the decay under study. Presented are fundamental concepts of B physics with an emphasis on the importance of quantum chromo-dynamics (QCD) form factors to the measurement.

1.1 CP Violation

A major purpose of the *BABAR* detector is the measurement of CP violation in B meson decays. CP violation is the combination of charge conjugation and parity that, as a product, was postulated to be conserved until first deviations were found in kaon decays. This was first publicized in 1964 by James Cronin *et al.* and was observed indirectly in the oscillation of kaons into their anti-particles [1]. The paper showed the first measurement of the $K_L^0 \to \pi^+\pi^-$ decay, which was forbidden by CP symmetry, and showed that K_L^0 is not a true CP eigenstate. It is now a candidate for the explanation of the surplus of matter to anti-matter. The same behavior, though weaker, was later observed in the B meson system. Figure 1 shows a Feynman diagram of the neutral B oscillation.

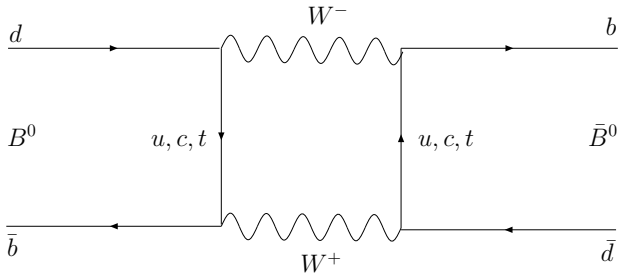

Figure 1: Feynman diagram of B meson oscillation.

Just as it is the case with the neutral kaon system, the B mesons are not mass eigenstates of the Lagrangian. However a linear combination of the B^0 and $\bar{B}^0$ meson

can be found to satisfy this requirement.

$$|B_L\rangle = p|B^0\rangle + q|\bar{B}^0\rangle$$
$$|B_H\rangle = p|B^0\rangle - q|\bar{B}^0\rangle \tag{1}$$

These are the light and heavy mass eigenstates of the B mesons. p and q are complex variables normalized by the relation $|p|^2 + |q|^2 = 1$ and obeying the time independent Schrödinger equation below [2]:

$$i\frac{d}{dt}\begin{pmatrix} p \\ q \end{pmatrix} = (M - \frac{i}{2}\Gamma)\begin{pmatrix} p \\ q \end{pmatrix} \tag{2}$$

The mass difference Δm_B between the light and the heavy state has been measured several times by *BABAR* , for example in [3], is currently cited in [4] to be $(0.507 \pm 0.005)\hbar s^{-1}$ and is responsible for the B meson oscillations. A neutral B meson starting in a defined state at time $t = 0$ will therefore oscillate between itself and its anti-particle with the following time dependence [2]:

$$|B^0_{phys}(t)\rangle = g_+(t)|B^0\rangle + (q/p)g_-(t)|\bar{B}^0\rangle$$
$$|\bar{B}^0_{phys}(t)\rangle = (p/q)g_-(t)|B^0\rangle + g_+(t)|\bar{B}^0\rangle \tag{3}$$

where

$$g_+(t) = e^{-iMt}e^{-\Gamma t/2}cos(\Delta m_B t/2)$$
$$g_-(t) = e^{-iMt}e^{-\Gamma t/2}i\ sin(\Delta m_B t/2) \tag{4}$$

and $M = \frac{1}{2}(M_H + M_L)$. The formalism therefore follows the known mathematical concepts from the neutral kaon system.

BABAR measures CP violation indirectly through the B meson oscillations and directly through several of its decay channels such as $B^0 \to \pi^+\pi^-$ or $B^0 \to K^+\pi^-$. The following paragraph is a brief overview of the origin of CP violation. First we need to take a look at the individual transformations. The C operator, or charge reversal, transforms a particle into its anti-particle. In case of an electromagnetic particle this means changing the sign of its charge and transforming the fields in the following manner [5].

$$\begin{aligned} \psi &\to -i(\bar{\psi}\gamma^0\gamma^2)^T \\ \bar{\psi} &\to -i(\gamma^0\gamma^2\psi)^T \\ A^\mu &\to -A^\mu \end{aligned} \tag{5}$$

This transformation however leaves the chirality of the particle untouched, transforming for example a left handed neutrino, into a left handed anti-neutrino which violates C symmetry. Only the application of the P operator, or space inversion, transforms the left handed anti-neutrino into a right handed one which then preserves CP symmetry. Geometrically a parity transformation can be seen as the mirroring of a coordinate system about a fixed point or turning a right handed coordinate system into a left handed one. Since CP violation occurs only in weak decays it is represented in the CKM matrix which is the mathematical construct of these decays. Since B mesons contain a decaying b quark, measurements of CP asymmetry gives details about the values in the third column of the CKM matrix. CP violation is introduced here with the use of phases on the amplitude of particle wave functions. Since the physically measurable quantity is only the absolute value of the amplitude, we distinguish between two types of phases. Arbitrary rotational phases that preserve the amplitude value and CP violating phases that do not. If we consider a particle/anti-particle pair we can write their decay amplitudes A and $\bar{A}$ respectively as follows [6]:

$$A = A_1 + ae^{i(\phi+\delta)}$$
$$\bar{A} = A_1 + ae^{i(-\phi+\delta)}$$
$$\Rightarrow |A| \neq |\bar{A}| \tag{6}$$

In this case CP symmetry is violated since the decay amplitude of the particle is larger than that of its anti-particle. In quantum field theory (QFT) there are several quantities that can be expressed in a phase independent way. One of these quantities useful for the measurement of CP violation in B decays is [2]:

$$\left|\frac{q}{p}\right|^2 = \left|\frac{M_{12}^* - \frac{i}{2}\Gamma_{12}^*}{M_{12} - \frac{i}{2}\Gamma_{12}}\right| \tag{7}$$

where M_{12} and Γ_{12} are the elements of the previously discussed hermitian matrices and represent the mass and the width of the particle. In case of CP conservation the mass states would also be CP eigenstates and there would not be a CP violating phase present between M_{12} and Γ_{12} and the above fraction would be equal to unity. This is an example of indirect CP violation in mixing. One possibility of measuring this effect is through the semi-leptonic decay of neutral B mesons using the asymmetry of their decay widths Γ, thus giving importance to the exact determination of such branching fractions [2]:

$$a_{sl} = \frac{\Gamma(\bar{B}^0 \to \ell^+\nu X) - \Gamma(B^0 \to \ell^-\nu X)}{\Gamma(\bar{B}^0 \to \ell^+\nu X) + \Gamma(B^0 \to \ell^-\nu X)} = \frac{1 - |q/p|^4}{1 + |q/p|^4} \tag{8}$$

1.2 The CKM Matrix

The CKM Matrix (named after the three physicists Cabibbo, Kobayashi and Maskawa who developed it in 1972) is a 3×3 unitary quark mixing matrix that describes the weak interactions and decays of the three generations of quarks [7]. It indicates how much of the coupling is shared between quarks of different flavor. It can be written as [8]:

$$V_{CKM} = \begin{pmatrix} V_{ud} = 0.974 & V_{us} = 0.227 & V_{ub} = 0.004 \\ V_{cd} = 0.227 & V_{cs} = 0.973 & V_{cb} = 0.042 \\ V_{td} = 0.008 & V_{ts} = 0.042 & V_{tb} = 0.999 \end{pmatrix} \tag{9}$$

The matrix contains off-diagonal elements since the mass eigenstates of the quarks are slightly different than their weak eigenstates. These elements are responsible for flavor changing decay processes between quarks. As before, the amplitudes of the decay processes are governed by the square of their absolute values $|V_{ab}|^2$, showing that generation changing decays are suppressed and that the third generation quarks are decoupled from the first and second generation quarks. The unitary CKM matrix can be expressed as a product of three rotational matrices. Constraints due to the redefinition of individual quark fields and unitarity give the complex parameters of the CKM matrix a total of four degrees of freedom defined as three angles $\theta_{12}, \theta_{13}, \theta_{23}$ and a phase δ. Thus the CKM matrix can be rewritten using these parameters [8]:

$$V_{CKM} = \begin{pmatrix} c_{12}c_{13} & s_{12}c_{13} & s_{13}e^{-i\delta} \\ -s_{12}c_{23} - c_{12}s_{23}s_{13}e^{i\delta} & c_{12}c_{23} - s_{12}s_{23}s_{13}e^{i\delta} & s_{23}c_{13} \\ s_{12}s_{23} - c_{12}c_{23}s_{13}e^{i\delta} & -c_{12}s_{23} - s_{12}c_{23}s_{13}e^{i\delta} & c_{23}c_{13} \end{pmatrix} \tag{10}$$

where $s_{ij} = sin(\theta_{ij})$ and $c_{ij} = cos(\theta_{ij})$. To this day, the values of the CKM matrix are determined purely by experiments. So far there is no reliable theoretical model to calculate its elements. Several ways exist to parameterize the CKM matrix. The most common way is an expansional form employing the four parameters λ, ρ, A and η and is called the Wolfenstein representation [9]:

$$V_{CKM} = \begin{pmatrix} 1 - \lambda^2/2 & \lambda & A\lambda^3(i\rho - i\eta) \\ -\lambda & 1 - \lambda^2/2 & A\lambda^2 \\ A\lambda^3(1 - \rho - i\eta) & -A\lambda^2 & 1 \end{pmatrix} \tag{11}$$

where

$$s_{12} = sin(\theta_c) = \lambda;\ s_{23} = A\lambda^2 \ll s_{12};\ s_{13}e^{-i\delta} = A\lambda^3(\rho - i\eta) \ll s_{23} \tag{12}$$

In this representation the power on λ is an indication for the strength of the coupling.

Experimentally, access to the CKM elements was achieved through a series of different particle decays. V_{ub} has been determined from nuclear β-decay and muon decay rates, V_{us} was determined in kaon decay channels and V_{ub} was measured by experiments such as *BABAR* through the semi-leptonic decay of the b quark to a u quark ($b \to u\ell\nu$). The quantity V_{cb} can be found through the semi-leptonic decay mode studied in this dissertation. Its relation to the branching fraction will be discussed in more detail later in this dissertation. V_{cd} was measured from the rate of single charmed particle production in high energy neutrino interactions such as [9]:

$$\nu_\mu + d \to \mu^- + c;\ c \to s + \mu^+ + \nu_\mu \tag{13}$$

V_{cs} can be obtained from D meson decays such as $D^+ \to \bar{K}^0 e^+ \nu_e$ [10] and is therefore also measurable by *BABAR* . The production of top quarks cannot be achieved in the *BABAR* detector due to energy constraints and is rare in other accelerators [11]. The quantities V_{td} and V_{ts} can be obtained from $B^0 - \bar{B}^0$ mixing rates. Besides measuring CP violation, current experiments are aimed at reducing the errors on these quantities of the CKM matrix and checking for its unity. The violation of unitarity may give rise to new physics.

1.3 The $\bar{B}^0 \to D^{*+}\ell^-\bar{\nu}_\ell$ Decay

The $\mathcal{B}(\bar{B}^0 \to D^{*+}\ell^-\bar{\nu}_\ell)$ [1] branching fraction was first exclusively measured in 1987 by the ARGUS collaboration [12] using a data sample with an integrated luminosity of 101 pb^{-1} on the $\Upsilon(4S)$ resonance reconstructing a total of 47$\pm$8 signal events. Other measurements followed in the coming years from the ARGUS, CLEO and Crystal Ball collaborations [4] including the only measurement conducted using a partial reconstruction technique [13] in 1994. That analysis used an integrated luminosity of 246 pb^{-1} to reconstruct a total of $2693 \pm 183 \pm 105$ signal event. However errors on the reported branching

[1] Charged conjugate states are always implied throughout the dissertation.

fraction remained large. Measurements in the following years started combining the branching fraction determination with other measurable quantities accessible through this decay mode. Although the decay under study has the largest exclusive branching fraction of any B decay, none of the measurements considered by [4] for the world average are dedicated precision measurements. All of these analyses focus on the determination of other measurements which also allow for the extraction of the branching fraction. Such analyses for example look for the semi-leptonic form factor parameters [14] or a multitude of branching fractions [15]. The analysis techniques chosen in these papers limit the amount of signal available for a branching fraction determination resulting in larger errors. The $\mathcal{B}(\bar{B}^0 \to D^{*+}\ell^-\bar{\nu}_\ell)$ branching fraction is directly linked to the weak mixing matrix element V_{cb}. A precise knowledge of this branching fraction can improve the measurement values of this matrix element. This analysis is the first dedicated precision measurement of this important branching fraction using large statistics and specific techniques to lower the systematic errors.

The decay under study is considered to be a semi-leptonic decay since the B meson, a hadron, undergoes a weak decay into a D meson by emitting a lepton and a neutrino. This is done through the decay of the b quark into a c quark which emits a W boson. The decay end products are therefore part hadronic and part leptonic, hence the name of the decay. Figure 2 shows the simplest Feynman diagram of this decay. Here one

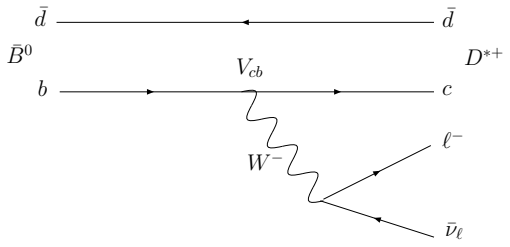

Figure 2: Feynman diagram for the B decay

can see that the weak decay vertex between the b and the c quark is coupled to the CKM matrix element V_{cb} which can be measured through this decay. The $\bar{d}$ quark is called a spectator quark since it is unchanged and does not interact during the decay

process. However since we are dealing with hadronic particles the decay process also has contributions from other diagrams containing gluon interactions. Unlike quantum electro-dynamics (QED) for which the coupling constant causes diagrams of higher order to become negligible, these QCD contributions remain important in higher orders. The theory is not resummable and the problem is addressed with the introduction of so called form factors, which are predicted by theory, but who's parameters have to be determined experimentally and incorporate our lack of knowledge of the hadronic field. Some of the gluonic diagrams are shown below in Figure 3:

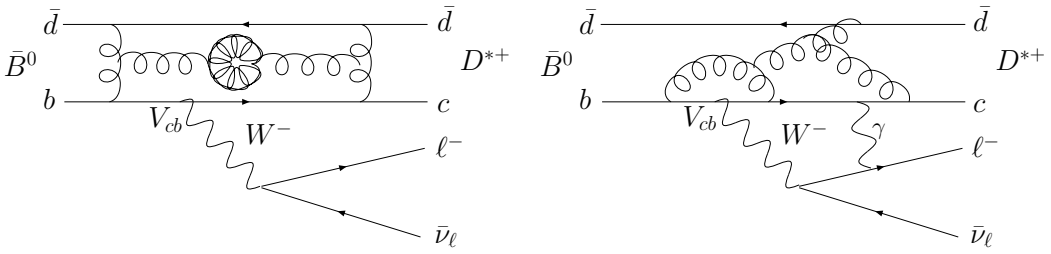

Figure 3: Higher order Feynman diagrams for the B decay

While the γ, which couples to the c quark and the lepton, belongs to a higher order QED process that only contributes to corrections, the gluon parts are ample and of equal importance. Several theories were developed to handle the hadronic decay processes in QCD, however they were all model dependent and limited in their predictive power due to high levels of uncertainties. The considerations of symmetries or pseudo-symmetries, which are symmetries to first order, has led to model independent predictions in the quark sector before. Such a symmetry for example is the previously known Chiral Symmetry, which assumes that the light quark masses (m_u, m_d, m_s) vanish to first order compared to their heavier counter parts. This causes the quarks of left and right helicities to decouple making the Lagrangian invariant under rotation among the helicity states (u_L, d_L, s_L) and (u_R, d_R, s_R). This gives rise to a $SU(3)_L \times SU(3)_R$ chiral flavor symmetry, which is a true symmetry of the Lagrangian. Corrections arise from the symmetry breaking conditions that the light quarks are not massless [2]. This method succeeded in making model independent prediction for light quarks and gave rise to a similar ansatz for the

heavy quark sector leading to the development of a Heavy Quark Symmetry (HQS) [16] which is described in section 1.4.

1.4 Heavy Quark Symmetry

In HQS one obtains an approximate symmetry by assuming an infinite mass limit for heavy quarks ($m_Q \to \infty$). In particular these are the c, b and t quarks. This forces the rest frame of a system with a light and a heavy quark, such as the system under study, to be the same as the frame of the heavy quark. Here only the electric color field of the quark is important for interactions making flavor and spin of hadronic systems irrelevant. However, unlike chiral symmetry, this consideration is not a symmetry of the Lagrangian. One reasons why heavy quarks can be treated in this manner is the fact that the strong coupling constant α_s decreases for large momentum transfer (Q^2) [16]:

$$\alpha_s = \frac{g_{eff}^2(Q^2)}{4\pi} = \frac{12\pi}{(33 - 2n_f)ln(Q^2)\Lambda_{QCD}^2} \tag{14}$$

where n_f is the number of quark flavors and $\Lambda_{QCD} \approx 0.2$ GeV is the energy at which the coupling constant becomes small. Therefore quarks with masses $m_Q \gg \Lambda_{QCD}$ are considered heavy quarks, others light quarks. This means that $\alpha_s(m_Q)$ is small for heavy quarks on length scales of the Compton wavelength $\lambda_Q \sim 1/m_Q$. This phenomenon is called asymptotic freedom. Here the interactions are similar to electromagnetic interactions where $\alpha_{em} \approx 1/137$.

1.5 Heavy Quark Effective Theory (HQET)

Since the system of interest here consists of one light and one heavy quark, the momentum transfer between them will be small and of order Λ_{QCD} leading to perturbative corrections of order Λ_{QCD}/m_Q for the theory due to the non infinite quark masses. In this limit however the QCD Lagrangian for heavy quarks still needs to be reformulated since it blows up for the heavy quark limit:

$$\mathcal{L}_Q = \bar{Q}(iD - m_Q)Q \tag{15}$$

For a hadron containing only one heavy quark it can be assumed that the heavy quark will only exchange small momenta with its lighter counter parts making it almost on-shell. It therefore travels with about the same velocity as the hadron itself. Its momentum can be expressed by the hadrons four velocity v^μ as [16]:

$$P_Q^\mu = m_Q v^\mu + k^\mu \tag{16}$$

where k is its small momentum correction due to non infinite mass and is of order Λ_{QCD}. Figure 4 shows what is seen by the light degrees of freedom due to the current of the moving heavy quark. The assumption of the momentum transfer allows for an approximation of the above Lagrangian in the heavy mass limit. This limit is a simplification of the above Lagrangian for one heavy quark which exchanges soft gluons with the light degrees of freedom. This is called Heavy Quark Effective Theory (HQET). As a first step one rewrites the above Lagrangian separated into heavy and light quark fields:

$$\mathcal{L}_{eff} = \bar{h}_v iv \cdot D h_v - \bar{H}_v(iv \cdot D + 2m_Q)H_v + \bar{h}_v i/D_\perp H_v + \bar{H}_v i/D_\perp h_v \tag{17}$$

were $H_v(h_v)$ is the field for the heavy (light) quark and D is the covariant derivative.

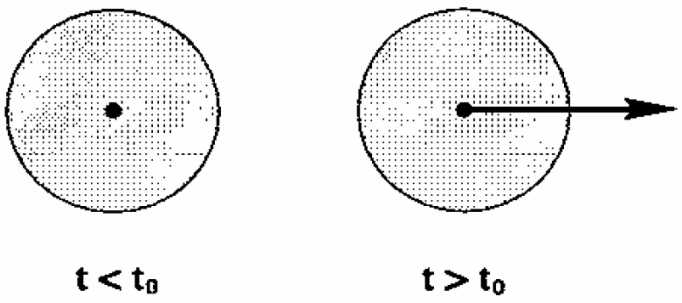

Figure 4: Schematic diagram of the gluon field seen by the light degrees of freedom due to the current of the moving quark. The figure has been taken from [16].

It can be seen that in this approximation the kinematics are related to the four velocity

of the hadron which is approximately the same for the heavy quark as mentioned above. The relation will also reoccur in the discussion of the form factors. However this still includes heavy quark fields which are to be eliminated in the heavy quark mass limit in order to describe the system based solely on its light degrees of freedom. In order to do this one looks at the relation between the heavy and light fields. Using the QCD equation of motion one finds:

$$H_v = \frac{1}{iv \cdot D + 2m_Q - i\varepsilon} i/D_\perp h_v \tag{18}$$

This shows that the heavy quark fields have a dependence of $1/m_Q$ and vanish in the limit of $m_q \to \infty$ as intended. Substitution into equation (17) yields the Lagrangian of the Heavy Quark Effective Theory (HQET):

$$\mathcal{L}_{eff} = \bar{h}_v iv \cdot D h_v + \bar{h}_v i/D_\perp \frac{1}{iv \cdot D + 2m_Q - i\varepsilon} i/D_\perp h_v \tag{19}$$

which now only depends on light degrees of freedom.

1.6 The Isgur-Wise function

The correct mathematical description of events in the hadron sector in the light of certain symmetries has been greatly investigated in the literature. One such investigation was done by N. Isgur and M. Wise in 1989 [17] and 1990 [18] focusing on weak transitions of a pseudoscalar to a pseudoscalar or a pseudoscalar to a vector meson for mesons with one single heavy quark. The results presented lead to a model independent prediction in the heavy quark limit [18]. Transitions of such systems can then be described with a single one parameter function $\xi(t)$ which is called the Isgur-Wise function where $t = (p_i - p'_j)^2$ is the momentum transfer between quarks and $i, j \in \{1, 2\}$. Normalization of $\xi(t)$ demands that $\xi(0) = 1$. According to [18] the symmetries present in such systems are beyond QCD predictions. Here the b and the c quark of the B and D^* meson can be approximated to hold the same mass giving rise to a $b \leftrightarrow c$ symmetry for the light degrees of freedom.

The consideration of such symmetries allows for the treatment of the decay in an theory in which the heavy quarks of infinite mass are considered at rest in the hadron's rest frame and solely serves as a provider of color fields. Therefore, in case of a transition of a quark Q_1 of velocity v into quark Q_2 of velocity v', the light degrees of freedom only see the color fields of the quarks which are now moving and depend on the color fields of the rest frame through their Lorentz boosts. This results in a mass independent symmetry of velocities instead of momenta which allows the combination of all arising form factors of both pseudoscalar and meson final states into the Isgur-Wise function $\xi(t)$. Although the Isgur-Wise function relates all hadronic form factors of this weak decay, it cannot predict their values. Since the symmetry depends on the velocities of the heavy quarks before and after transition v and v' it is often convenient to describe the Isgur-Wise function in terms of the boost between the initial and final rest frame $w = v \cdot v'$. Hence the normalization of the Isgur-Wise function demands $\xi(w = 1) = 1$.

1.7 Form Factors

Since the hadronic contributions in determining the decay rate are not resummable, the exact prediction from QCD is not possible. The momentum space of the partial decay width is therefore modeled with the use of form factors (FF) which depend on the momentum transfer q^2 to the virtual W boson in the decay. Since it is more convenient to express the kinematics of the meson with its velocity rather than its momentum, the form factors will be expressed with these variables. During the decay process of the meson the exchange of soft gluons rearranges the light degrees of freedom, changing its initial velocity v to its final one v'. In the heavy quark limit this only depends on the Lorentz boost $w = v \cdot v'$. Therefore the hadronic matrix element describing this transition can also be expressed as a velocity dependent quantity:

$$\langle P(v')|\bar{h}_{v'}\gamma^{\mu}h_v|P(v)\rangle = \xi(v \cdot v')(v + v')^{\mu} \tag{20}$$

The mass independent function $\xi(v \cdot v')$ is the universal form factor for HQT and is the Isgur-Wise function. From kinematic observations in the zero recoil limit for which $v \cdot v' = 1$ it can be shown that $\xi(1) = 1$.

For semi-leptonic decays, the matrix element M of the decay process can be expressed with a leptonic and a hadronic current [19]:

$$M(B \to D^* \ell \nu) = -i \frac{G_F}{\sqrt{2}} V_{cb} L_\mu H^\mu \tag{21}$$

The leptonic current L_μ is well known and can be directly obtained from QED without corrections. The hadronic part of the current H^μ however has to be obtained from the previously discussed symmetry assumptions of QCD. HQET models the general case of the hadronic current H^μ of a pseudoscalar meson decaying to a vector meson with a set of generic form factors for which the heavy mass limit has been broken perturbatively in powers of Λ_{QCD}/m_Q based on (19). These can be related to the Isgur-Wise function in the HQT limit. The hadronic part of the decay under study can therefore be expressed as:

$$\begin{aligned} H^\mu &= \langle D(p', \varepsilon) | \bar{c} \gamma^\mu (1 - \gamma_5) b | B(p) \rangle = \frac{2i\epsilon^{\mu\nu\alpha\beta}}{m_B + m_{D^*}} \varepsilon^*_\nu p'_\alpha p_\beta V(q^2) \\ &\quad -(m_B + m_{D^*}) \varepsilon^{*\mu} A_1(q^2) + \frac{\varepsilon^* \cdot q}{m_B + m_{D^*}} (p + p')^\mu A_2(q^2) \\ &\quad +2m_{D^*} \frac{\varepsilon^* \cdot q}{q^2} q^\mu A_3(q^2) - 2m_{D^*} - \frac{\varepsilon^* \cdot q}{q^2} q^\mu A_0(q^2) \end{aligned} \tag{22}$$

where V and A_i are vector and axial form factors [20]. The form factor $A_3(q^2)$ is not an independent quantity and simply introduced for convenience. It can be expressed as a linear combination of the other factors [16]:

$$\begin{aligned} A_3(q^2) = \frac{m_B + m_{D^*}}{2m_{D^*}} A_1(q^2) - \frac{m_B - m_{D^*}}{2m_{D^*}} A_2(q^2) \\ A_0(0) = A_3(0) \end{aligned} \tag{23}$$

leaving the expression with a total of four independent form factors. In the above relation ε is the polarization of the D^* vector meson. In the limit of infinite heavy quark mass the independent factors relate to the Isgur-Wise function (for $m \to \infty$) [16]:

$$\xi(v \cdot v') = R^* V(q^2) = R^* A_0(q^2) = R^* A_2(q^2) = R^* \left[1 - \frac{q^2}{(m_B + m_{D^*})^2}\right]^{-1} A_1(q^2) \quad (24)$$

where $R^* = 2\sqrt{m_B m_{D^*}}/(m_B + m_{D^*})$ is a simple mass ratio. This makes it possible in the limit of heavy quark symmetry (HQS) to describe the hadronic part of the decay under study with only one form factor as opposed to four in the general case.

1.7.1 Differential Decay Rates

Another simplification for HQET that can be made in the study of the differential semi-leptonic decay rate of the decay $B \to D^* \ell \nu$ is the assumption of massless leptons. In this case, where the leptons consists of electrons or muons this simplification is quite valid. The differential decay rate can then be expressed with three form factors related to the invariant helicity amplitudes of the D^* meson $H_{\pm,0}(q^2)$, which refer to the different polarizations [19]. They are defined as linear combinations of the axial and vector form factors [21]:

$$\begin{aligned} H_\pm(q^2) &= (m_B + m_{D^*}) A_1(q^2) \mp \frac{2 m_B |\vec{p}_{D^*}|}{m_B + m_V} V(q^2) \quad (25) \\ H_0(q^2) &= \frac{1}{2 m_{D^*} \sqrt{q^2}} \left[(m_B + m_{D^*})(m_B^2 - m_{D^*}^2 - q^2) A_1(q^2) - \frac{4 m_B^2 |\vec{p}_{D^*}|}{m_B + m_{D^*}} A_2(q^2)\right] \end{aligned}$$

The differential decay rate related to phase space and all three angles then becomes:

$$\begin{aligned}
\frac{d^4\Gamma(B \to D^*\ell\nu)}{dq^2 dcos\theta_\ell dcos\theta_V d\chi} &= |V_{cb}|^2 \frac{3G_F^2 |\vec{p_D}| q^2}{8(4\pi)^4 m_B^2} \times (1-cos\theta_\ell)^2 sin^2\theta_V |H_+(q^2)|^2 \\
&+(1+cos\theta_\ell)^2 sin^2\theta_V |H_-(q^2)|^2 + 4sin^2\theta_\ell cos^2\theta_V |H_0(q^2)|^2 \\
&-4sin^2\theta\ell(1-cos\theta_\ell) sin\theta_V cos\theta_V cos\chi H_+(q^2) H_0(q^2) \\
&+4sin^2\theta\ell(1+cos\theta_\ell) sin\theta_V cos\theta_V cos\chi H_-(q^2) H_0(q^2) \\
&-2sin^2\theta\ell sin^2\theta_V cos2\chi H_+(q^2) H_-(q^2) \qquad (26)
\end{aligned}$$

The semi-leptonic decay $B \to D^*\ell\nu$ can be fully described by three angles and one momentum transfer variable. The B meson in its rest frame decays back-to-back into a W and the D^*. The W will further decay into a lepton ℓ and a neutrino back-to-back in the W rest frame. The angle θ_ℓ is then defined as the angle between the thrust axis of the W and the lepton. Likewise, the D^* meson decays into a D and a π back-to-back in the D^* rest frame. The angle θ_V is the angle between the thrust axis of the D^* and the D. χ is then the angle between the two decay planes of the W and the D^*. The last quantity is the invariant mass square of the virtual W boson [19]. Figure 5 shows the angular relations of the decay.

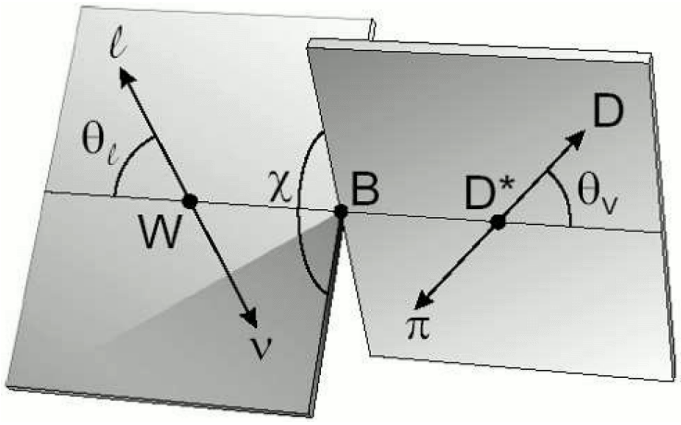

Figure 5: Schematic representation of the $\bar{B}^0 \to D^{*+}\ell^-\bar{\nu}_\ell$ decay through the reconstruction channel of $D^* \to D^0\pi^+$. The figure has been taken from [16].

Often only the dependence on q^2 of the differential decay rate is of interest. Integrating over all the angles one obtains:

$$\frac{d\Gamma(B \to D^* \ell \nu)}{dq^2} = |V_{cb}|^2 \frac{G_F^2 |\vec{p_D}| q^2}{96\pi^3 m_B^2} \times \sum_{i=\pm,0} |H_i|^2 \tag{27}$$

In the decay under study the boost variable w describes the relation between the initial B meson and the final D^* meson and is the product of their four velocities $w = v_B \cdot v_{D^*}$. Its relation to the momentum transfer of the B meson to the lepton pair originating from the virtual W boson can be expressed through simple mass relations:

$$w = \frac{m_B^2 + m_{D^*}^2 - q^2}{2 m_B m_{D^*}} \tag{28}$$

Since w is a more convenient variable it will be used to describe the momentum space from now on. This relation can be studied to obtain the range of w in momentum space:

$$w_{max} = \frac{m_B^2 + m_{D^*}^2}{2 m_B m_{D^*}} = 1.504 \tag{29}$$

In the case of zero recoil in which no momentum is transferred from the B meson to the D^* meson, the maximum momentum transferred to the lepton pair can be determined as well. In this case $w_{min} = 1$:

$$q_{max}^2 = m_B^2 + m_{D^*}^2 - 2 m_B m_{D^*} = 10.69 \text{ GeV}^2 \tag{30}$$

1.7.2 HQET Form Factors

From now on it is more convenient to represent the differential decay rate with the boost variable w instead of the momentum transfer q^2. The simple relation (28) allows for a transformation of the decay rate and helicity amplitudes to this value. HQET for this purpose introduces another set of form factors $h_{A/V_i}(w)$ which only depend on the boost variable w and fully describe the hadronic part of the current in the Lagrangian by replacing the previous axial and vector form factors A_i and V. This description away from the direct momentum dependence of the D meson to the meson form factors $h_i(w)$ proves more useful. This allows for a redefinition of the hadronic current H^μ in terms of

w. Splitting the current into $V^\mu = \bar{c}\gamma^\mu b$ and $A^\mu = \bar{c}\gamma^\mu\gamma^5 b$ one obtains [22]:

$$\begin{aligned} H^\mu = \langle D(v',\varepsilon')|V^\mu - A^\mu|B(v)\rangle &= ih_V(w)\epsilon^{\mu\nu\alpha\beta}\varepsilon'^*_\nu v'_\alpha v_\beta - h_{A_1}(w)(w+1)\varepsilon'^*\mu \\ &\quad + \left[h_{A_2}(w)v^\mu + h_{A_3}(w)v'^\mu\right]\varepsilon'^*\cdot v \end{aligned} \tag{31}$$

where ε' represents the polarization of the D^* meson and $\epsilon^{\mu\nu\alpha\beta}$ is the complete anti-symmetric tensor. Simple relations exist to convert between the two sets of form factors. They can be found by comparing the new hadronic current (31) to the previous one definition in (22) [16]:

$$\begin{aligned} R^*V(q^2) &= h_V(w) \\ R^{*-1}A_1(q^2) &= \frac{w+1}{2}h_{A_1}(w) \\ R^*A_2(q^2) &= h_{A_3}(w) + \frac{m_{D^*}}{m_B}h_{A_2}(w) \end{aligned} \tag{32}$$

where R^* is the same mass ratio as previously defined. It can also be seen, by comparison to (24) together with (28), that the HQET form factors either vanish or reduce to the Isgur-Wise function in the HQS limit at zero recoil as is expected:

$$\begin{gathered} \xi(w) = h_V(w) = h_{A_1}(w) = h_{A_3}(w) \\ h_{A_2}(w) = 0 \\ w \approx 1 \end{gathered} \tag{33}$$

In the context of the new HQET form factors h_{V/A_i}, one can rewrite the helicity amplitudes in w instead of q^2. Factoring out the meson form factor $h_{A_1}(w)$ one can define the reduced helicity amplitudes $\tilde{H}_i(w)$ [16]:

$$|H_i|^2 = (m_B - m_{D^*})^2\frac{m_B m_{D^*}}{q^2}(w+1)^2|h_{A_1}(w)|^2|\tilde{H}_i(w)|^2 \tag{34}$$

The differential decay rate integrated over all angles becomes [16]:

$$\begin{aligned}\frac{d\Gamma(B \to D^* \ell \nu)}{dw} &= |V_{cb}|^2 \frac{G_F^2}{48\pi^3}(m_B - m_{D^*})^2 m_{D^*}^3 \sqrt{w^2-1}(w+1)^2 \\ &\quad \times |h_{A_1}(w)|^2 \sum_{i=\pm,0} |\tilde{H}_i(w)|^2 \end{aligned} \tag{35}$$

The definition of reduced helicity amplitudes then allows the exact description of $|\tilde{H}(i)(w)|^2$ based on the ratios of meson form factors $R_i(w)$. These ratios arise due to the fact that the HQET form factor h_{A_1} has been factored out in the definition. This is desirable because it is the only form factor that, in the case of zero recoil, shows a dependence of $1/m^2$ instead of $1/m$ to the next leading order [16]. The ratios are useful, since in their chosen form they only show a very weak phase space dependence and most of the form factor phase space dependence is carried by $h_{A_1}(w)$. The ratios are related to both sets of form factors in the following way [16]

$$\begin{aligned} R_1(w) &= \left[1 - \frac{q^2}{(m_B + m_{D^*})^2}\right] \frac{V(q^2)}{A_1(q^2)} = \frac{h_V(w)}{h_{A_1}(w)} \\ R_2(w) &= \left[1 - \frac{q^2}{(m_B + m_{D^*})^2}\right] \frac{A_2(q^2)}{A_1(q^2)} = \frac{h_{A_3}(w) + (m_{D^*}/m_B) h_{A_2}(w)}{h_{A_1}(w)} \end{aligned} \tag{36}$$

Using a shorthand for the mass ratio $r = m_{D^*}/m_B$ the reduced helicity amplitudes can be expressed as:

$$\begin{aligned} |\tilde{H}_\pm(w)|^2 &= \frac{1 - 2wr + r^2}{(1-r)^2} \left[1 \mp \sqrt{\frac{w-1}{w+1}} R_1(w)\right]^2 \\ |\tilde{H}_0(w)|^2 &= \left[1 + \frac{w-1}{1-r}\left(1 - R_2(w)\right)\right]^2 \end{aligned} \tag{37}$$

This fully describes the differential decay rate in w based on the meson form factor $h_{A_1}(w)$ and the two meson form factor ratios $R_1(w)$ and $R_2(w)$. Equation (35) is generally rewritten summarizing the form factors in a single factor $\mathcal{F}(w)$. A phase space factor

is incorporated into $\mathcal{F}(w)$ so that the $\mathcal{F}(w)$ completely includes the deviations of the differential decay rate from the heavy quark symmetry limit [16] which in the limit of zero corrections becomes the Isgur-Wise function. This leads to the final notation of the differential decay rate:

$$\begin{aligned}\frac{d\Gamma(B \to D^*\ell\nu)}{dw} &= \frac{G_F^2}{48\pi^3}(m_B - m_{D^*})^2 m_{D^*}^3 \sqrt{w^2-1}(w+1)^2 \\ &\quad \times \left[1 + \frac{4w}{w+1}\frac{1-2wr+r^2}{(1-r)^2}\right] |V_{cb}|^2 \mathcal{F}^2(w) \end{aligned} \tag{38}$$

Summing the contributions of the reduced helicities $\tilde{H}_i$ in (35) the form factor $\mathcal{F}(w)$, now including the inverted phase space factor of (38), in its final representation becomes:

$$\begin{aligned}\mathcal{F}^2(w) &= |h_{A_1}(w)|^2 \times \left\{ 2\frac{1-2wr+r^2}{(1-r)^2}\left[1 + \frac{w-1}{w+1}R_1(w)^2\right] + \left[1 + \frac{w-1}{1-r}(1-R_2(w))\right]^2 \right\} \\ &\quad \times \left[1 + \frac{4w}{1+w}\frac{1-2wr+r^2}{(1-r)^2}\right]^{-1} \end{aligned} \tag{39}$$

The form factor $\mathcal{F}(w)$ directly affects the shape of the partial decay width (38). The precise knowledge of its shape is therefore essential for reliable simulations. The exact functions $h_{A_1}(w), R_1(w)$ and $R_2(w)$ cannot yet be calculated, but a successful attempt to estimate their shapes using simple polynomial expansions with phase space variables has been presented in [22]. The expansions show less than 2% deviation over the entire phase space region and are therefore well suited for Monte Carlo modeling of the decay. In [22] the authors limit bounds on the form factor shapes by applying previous results from a dispersion technique to the full spin symmetry of $B^{(*)}$ and $D^{(*)}$ mesons and considering all effects of heavy quark symmetry. By looking at all relevant spin-parity channels of the $B^{(*)}$ to $D^{(*)}$ transitions [22] finds the optimal constraints on the form factors by intersecting the resulting four domains of the spin parity channels. This results in well constrained form factors over the whole semi-leptonic phase space. The results of this analysis are used in this dissertation to model the form factor shape. The expansion for

the form factor ratios $R_i(w)$ are given by [22]:

$$\begin{aligned} R_1(w) &\approx R_1(1) - 0.12(w-1) + 0.05(w-1)^2 \\ R_2(w) &\approx R_2(1) + 0.11(w-1) + 0.06(w-1)^2 \end{aligned} \tag{40}$$

The measurement of the values around $R_i(1)$ at zero recoil have been improved by several analyses. For this analysis they will be take from the most recent *BABAR* measurements [23]. The quoted values in [23] to the date of this analysis are:

$$R_1(1) = 1.429 \pm 0.061 \pm 0.044 \quad \textit{and} \quad R_2(1) = 0.827 \pm 0.038 \pm 0.022 \tag{41}$$

where the quoted errors are statistical and systematic, respectively. The expansion of $h_{A_1}(w)$ is obtained by relating it to other form factors directly constrained by the method employed in [22] which gives the following result:

$$h_{A_1}(w) \approx h_{A_1}(1) \times (1 - 8\rho^2_{A_1} z + (53\rho^2_{A_1} - 15)z^2 - (231\rho^2_{A_1} - 91)z^3) \tag{42}$$

Besides its value at zero recoil $h_{A_1}(1)$ also depends on a second parameter $\rho^2_{A_1}$ which describes the slope of $h_{A_1}(w)$ at zero recoil [20].

$$\frac{dh_{A_1}(w)}{dw}|_{w=1} = -\rho^2_{A_1} \tag{43}$$

It should be noted, that the w dependence of (42) is hidden in the variable $z(w)$. An expansion of $h_{A_1}(w)$ in powers of $(w-1)$, as done in (40), was not chosen in order to avoid dependence of the result on sub-threshold singularities [22]. The presented expansion is independent of such effects and z is given by:

$$z = \frac{\sqrt{w+1} - \sqrt{2}}{\sqrt{w+1} + \sqrt{2}} \tag{44}$$

While the dispersive method provides upper and lower bounds on $\rho^2_{A_1}$, these are quite

large and do not provide sufficient binding for this analysis ($0.14 < \rho^2_{A_1} < 1.54$ [22]). Therefore, its value is again taken from [23] and is, at the present time of the analysis, quoted to be:

$$\rho^2_{A_1} = 1.191 \pm 0.048 \pm 0.028 \tag{45}$$

where quoted uncertainties again are statistical and systematic, respectively. Contrary to the expansions of $R_i(w)$, the zero recoil value of $h_{A_1}(w)$ simply acts as a scale factor and does not alter its shape. For this analysis it is therefore not considered to be a shaping parameter of $\mathcal{F}(w)$. Its value is directly taken from lattice QCD calculations [24], which calculate the value using a quenched approximation including a mixed symposium of $1/m_q^2$ and $1/m_Q^3$ corrections:

$$h_{A_1}(1) = 0.931^{\pm 0.029}_{\pm 0.034} \tag{46}$$

where the quoted uncertainties represent the individual uncertainties added in quadrature. The presented concepts allow for a concise representation of the form factor $\mathcal{F}(w)$ based on three measured parameters $\mathcal{F}(w|\rho^2_{A_1}, R_1(1), R_2(1))$. The parametrization of this function can then directly be applied to the differential decay rate in (38) for further study. In this analysis the reshaping of the phase space due to $\mathcal{F}(w)$ directly impacts the momentum distributions of the decay particles. Its effect therefore will have to be carefully studied in order to assess proper systematic errors due to form factor variations. Figure 6 shows the differential decay rate with and without the form factor contribution, using the parametrization given in (39) and the quoted parameter values. It can be seen that the introduction of the form factor skews the differential decay rate towards lower values in w. The form factor reweighted phase space in this figure has been multiplied by a factor of two in order to make the shift in phase space more apparent. Figure 7 shows the shape of $\mathcal{F}(w)$ in its current parameterization. The total branching fraction can be obtained through integration of the partial decay width (38) and the B^0 lifetime τ_{B^0}:

$$\mathcal{B}(\bar{B}^0 \to D^{*+}\ell^-\bar{\nu}_\ell) = \tau_{B^0} \int_{w_{min}}^{w_{max}} \frac{d\Gamma(\bar{B}^0 \to D^{*+}\ell^-\bar{\nu}_\ell)}{dw} dw \tag{47}$$

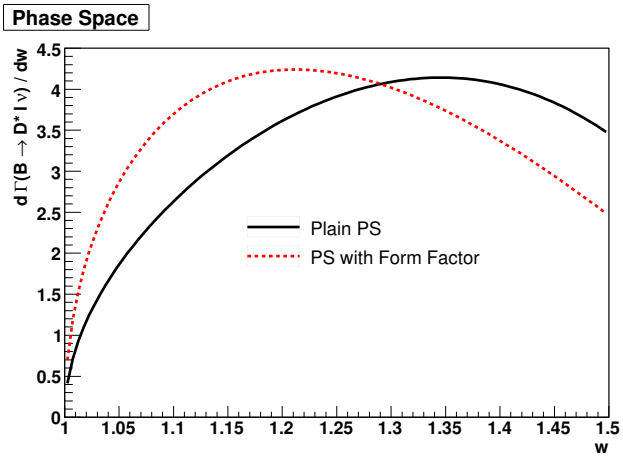

Figure 6: Differential decay rate in phase space of w with (red) and without (black) the form factor contribution. The form factor contribution has been multiplied by a factor of 2 to make the shift in phase space more apparent.

1.7.3 Generic Form Factor Expansion

Another parameterization of the form factor used in the literature [25], [26] is a direct expansion of $\mathcal{F}(w)$ in powers of $(w-1)$ in the form of:

$$\mathcal{F}(w) = \mathcal{F}(1) \times (1 + \rho^2_{\mathcal{F}}(1-w) + c(1-w)^2 + \mathcal{O}(1-w)^3) \tag{48}$$

Here $\rho^2_{\mathcal{F}}$ again is the slope of the expansion and c its curvature. This expansion is feasible since the form factor ratios $R_i(w)$ are much less dependent on w than $h_{A_1}(w)$. R_i show a maximum deviation from their value at zero recoil of less than 5%, while h_{A_1} shows a change of over 30% from its value at zero recoil in the valid kinematic range. The expansion therefore roughly follows the shape of $h_{A_1}(w)$. Higher order terms are possible but generally not used [20]. [26] underwent an extensive study of the parameter bounds for this expansion. It shows that the curvature parameter c of the expansion is not independent of the slope parameter $\rho^2_{\mathcal{F}}$. It is bound by the linear relation:

$$c = 0.66\rho^2_{\mathcal{F}} - 0.11 + \mathcal{O}(\Lambda_{QCD/m_Q}) \tag{49}$$

However these relations were calculated for the proximity of the zero recoil limit with one loop corrections. Further deviation in larger ranges of w is therefore expected. The value of $\mathcal{F}(w)$ at zero recoil is the same as $h_{A_1}(1)$ which follows from (39). Figure 7 shows the comparison of this expansion to the previous expansion (39). The value of $\rho^2_{\mathcal{F}}$ has to be obtained experimentally. Here simply the previous value of ρ_{A_1} is used since this is the curvature of the form factor at zero recoil. It can be seen that (48) deviates from (39) at high values of w, but that they are considerably close in the area of zero recoil. In this analysis the more precise form factor expansion (39) based on $h_{A_1}(w), R_1(w)$ and $R_2(w)$ is used.

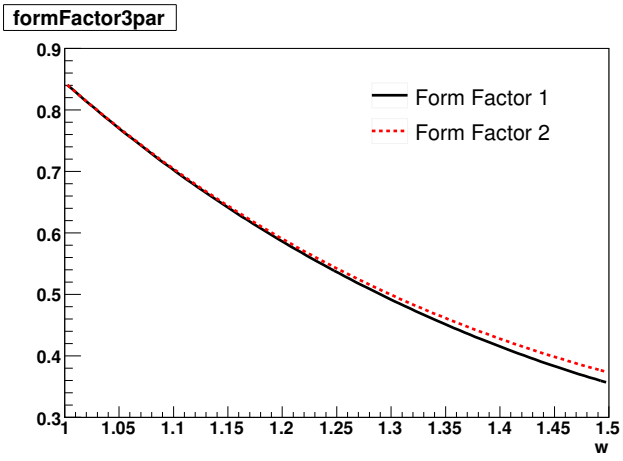

Figure 7: Shape of the form factor $\mathcal{F}^2(w)$ in phase space of w with the given parametrization in (39) (Form Factor 1) and with the parametrization given in (48) (Form Factor 2)

2 The *BABAR* Experiment at SLAC

2.1 SLAC

The PEP-II collider at the Stanford Linear Accelerator Center (SLAC) located in Menlo Park, California, is an electron - positron collider tuned to the $\Upsilon(4S)$ resonance to produce B mesons [27]. Its primary purpose is the study of CP violation in B meson decays to test the Standard Model. Previous experiments such as CLEO at Cornell, ARGUS at DESY (Germany) and UA1 at CERN (Switzerland) have measured numerous B-Decays and have discovered several interesting aspects of B physics such as B-mixing between the B^0 and $\bar{B}^0$ meson [28]. One aspect of CP violation can be found in the difference of decay rates between the meson and anti-meson. However the short travel distance of the B mesons made it impossible to separate the decay vertices of the B mesons in those previous experiments. For this reason the *BABAR* detector and its Japanese counterpart $BELLE$ were constructed incorporating asymmetric beam energies to overcome this problem. The relativistic boost of the B mesons into the lab frame makes the measurement of a travel distance of such small magnitude possible [29].

The experiment consists of a linear accelerator which accelerates the electrons and positrons to the desired energies of 9.0 GeV and 3.1, GeV respectively. The accelerated beams then get injected into the PEP-II storage ring which consists of two rings: A High Energy Ring (HER) holding the electrons and a Low Energy Ring (LER) holding the positrons. The beams circulate in PEP-II until they are brought to a collision in the interaction point inside the *BABAR* detector. The center of mass energy of the collision is tuned to the $\Upsilon(4S)$ resonance, a highly unstable state that almost immediately decays to B mesons.

2.2 The $\Upsilon(4S)$ Resonance

BABAR 's beam energies are tuned to operate at the $\Upsilon(4S)$ resonance, a highly unstable state that almost immediately decays into B mesons with an inclusive branching fraction

of more than 96% [4]. It is the first $b\bar{b}$ quark resonance to produce B mesons with an available mass difference of merely 20.4 MeV/c^2 causing the resulting B mesons to emerge almost at rest from the decay. Figure 8 shows the simplest Feynman diagram of the $\Upsilon(4S) \rightarrow B^0\bar{B}^0$ decay.

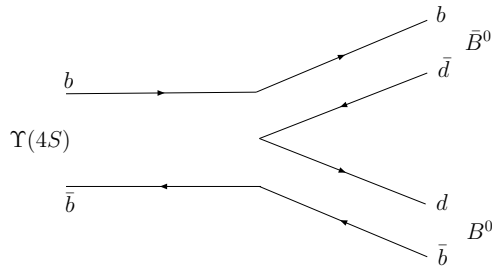

Figure 8: Simplest Feynman diagram of the $\Upsilon(4S)$ decay

Decays to less massive D meson pairs are doubly V_{cb} suppressed making the B hadronization the dominant mode despite the limited phase space. The cross section of the $\Upsilon(4S)$ resonance follows a relativistic Breit-Wigner shape when neglecting radiative corrections and the spread of the beam energy [30]:

$$\sigma_0 = 12\pi \frac{\Gamma^0_{ee}\Gamma_{tot}(s)}{(s-M^2)^2 + M^2\Gamma^2_{tot}(s)} \tag{50}$$

Here M is the $\Upsilon(4S)$ mass, Γ^0_{ee} is the partial decay width for electron-positron scattering, Γ_{tot} is the total decay width and s is the square of the center of mass beam energy. The total decay width was measured in [30] to be about $\Gamma_{tot} = 21$ MeV while the energy spread of the beam is always less than 5 MeV. This ensures that the *BABAR* detector always operates around the peak of the resonance. Figure 9 shows the hadronic cross section of the e^+e^- collision based on its center of mass energy. It can be seen that the $\Upsilon(4S)$ resonance is a weak one giving only a maximum cross section of about 4.5 nb where about 3.5 nb come from the $q\bar{q}$ background. Table 1 shows the calculated hadronic and leptonic cross sections for individual particle/anti-particle pairs at the $\Upsilon(4S)$ center of mass energy. From this it becomes apparent that the collision is dominated by the leptonic mode $e^+ + e^- \rightarrow e^+ + e^-$ which is referred to as Bhabha scattering. In the

experiment these events are suppressed by certain energy and geometry cuts on the reaction products therefore making the $\Upsilon(4S)$ resonance the dominant occurrence. The cut procedure is described later in this dissertation.

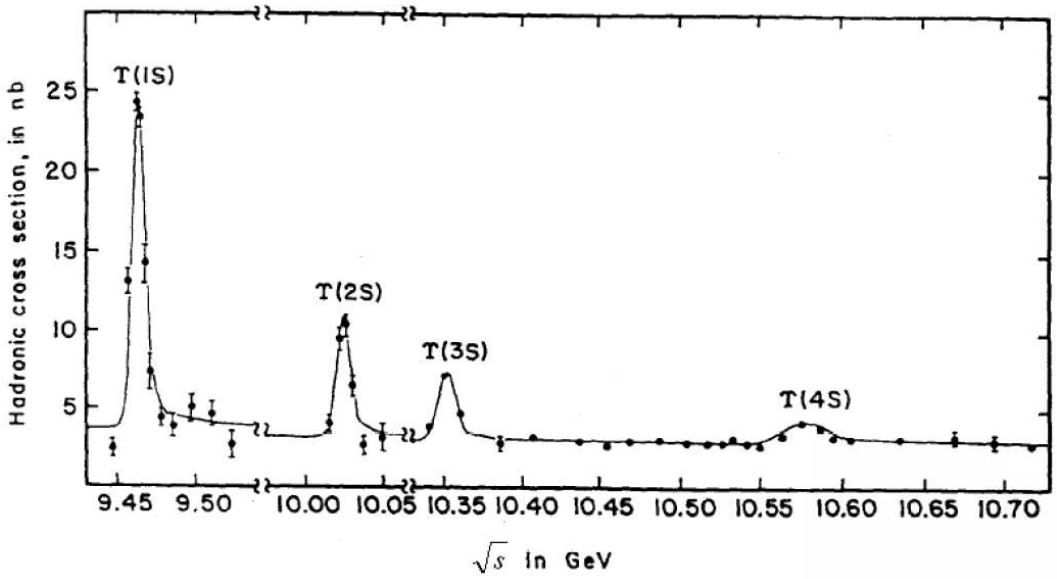

Figure 9: Scan of the hadronic cross section of the e^+e^- annihilation process. The Υ resonances rise above a $q\bar{q}$ background. The figure has been taken from [31].

Table 1: Calculated production cross-sections at $\sqrt{s} = M(\Upsilon(4S))$ [2]

$e^+ + e^- \rightarrow$	Cross-section (nb)
$b\bar{b}$	1.05
$c\bar{c}$	1.30
$s\bar{s}$	0.35
$u\bar{u}$	1.39
$d\bar{d}$	0.35
$\tau^+\tau^-$	0.94
$\mu^+\mu^-$	1.16
e^+e^-	~ 40

By using the Lorenz invariance of the square of the four momentum one can see that the chosen beam energies in *BABAR* yield the $\Upsilon(4S)$ rest mass in the center of mass frame of 10.58 GeV/c^2. This procedure is shown below in equation (51).

$$\begin{aligned} p_\mu p^\mu &= (p_{e^-} + p_{e^+})_\mu (p_{e^-} + p_{e^+})^\mu \\ 2m_e^2 + E_{e^-,Lab}E_{e^+,Lab} - \vec{p}_{e^-,Lab}\vec{p}_{e^+,Lab} &= 2m_e^2 + \tfrac{1}{2}E_{e^-,cm}\tfrac{1}{2}E_{e^+,cm} - \vec{p}_{e^-,cm}\vec{p}_{e^+,cm} \\ E_{cm} &= 2\sqrt{E_{e^-,Lab}E_{e^+,Lab}} = 10.58 \text{ GeV} \end{aligned} \tag{51}$$

Further the introduced relativistic boost into the lab frame of the B mesons makes it possible to measure the relative B meson decay times. The B mesons are created almost at rest in the center of mass frame making this measurement impossible for previous symmetric colliders. The lifetime of the B meson is determined to be $\tau = 1.53 \times 10^{-12} s$ [4]. In a collider with equal beam energies like the the former CLEO experiment at Cornell, where the center of mass frame corresponds to the lab frame, the B mesons are created with little momentum almost at rest. In order to obtain a lifetime measurement the separation between the decay vertexes has to be measured. The relativistic transformation factors are small and can be found using the energy and momentum of the B meson:

$$\begin{aligned} E_B &= \frac{E_{cm}}{2} = 5.29 \text{ GeV} \\ p_B &= \sqrt{E_B^2 - m_B^2} = 0.34 \text{ GeV/c} \end{aligned} \tag{52}$$

$$\begin{aligned} E_B &= \gamma_B m_B \Rightarrow \gamma_B = 1.0020 \\ p_B &= (\gamma\beta)_B m_B \Rightarrow (\gamma\beta)_B = 0.0644 \end{aligned} \tag{53}$$

Using relativistic transformations one can find the separation between the two B mesons.

$$t = \gamma(t - \vec{\beta} \cdot \vec{x})$$
$$\vec{x'} = \vec{x} + \frac{\gamma - 1}{\beta^2}(\vec{\beta} \cdot \vec{x})\vec{\beta} - \gamma\vec{\beta}t \tag{54}$$

Since the two B mesons separate in the center of mass frame in opposite directions, the above equation can be reduced to a one dimensional case. If we consider the distance of the first B meson from the common vertex of creation to be z_1 with z_2 being the equivalent for the second meson one can calculate the maximum separation to be:

$$\Delta z = z_1 + z_2 = \gamma\beta(\tau_1 + \tau_2) = 59\mu m \tag{55}$$

here having used the average lifetime for both mesons for the sake of the argument. This lies below the measurement resolution of the DCH and challenges the capabilities of the SVT of the *BABAR* detector. The boost however, due to asymmetric beam energies, makes it possible to measure this decay vertex separation of the two decaying B mesons in the lab frame. Since here the $\Upsilon(4S)$ resonance is not at rest, the boost of the B mesons depends on the decay angle θ from the z-axis in the center of mass frame. The boost of the $\Upsilon(4S)$ resonance in the lab frame is:

$$\begin{aligned} \gamma &= \frac{E_{\Upsilon(4S)}}{m_{\Upsilon(4S)}} = \frac{\sqrt{p_{e^-} - p_{e^+}}}{m_{\Upsilon(4S)}} = 1.14 \\ \gamma\beta &= \frac{p_{\Upsilon(4S)}}{m_{\Upsilon(4S)}} = \frac{p_{e^-} - p_{e^+}}{m_{\Upsilon(4S)}} = 0.56 \end{aligned} \tag{56}$$

The x and y directions remain unchanged by the boost, but the z direction becomes elongated. In the CM frame the z separation between the two B mesons is anti-parallel. Using the proper time and the CM boost values of the B one can write the position and time doublets of the B mesons in the CM frame as [6]:

$$
\begin{aligned}
(z_1^*, t_1^*) &= ((\gamma\beta)_B \tau_1 cos\theta,\ \gamma_B \tau_1) \\
(z_2^*, t_2^*) &= (-(\gamma\beta)_B \tau_2 cos\theta,\ \gamma_B \tau_2)
\end{aligned} \tag{57}
$$

Now boosting the z coordinate into the lab frame denoting γ and β as the lab frame boost variables one gets

$$
\begin{aligned}
z_1 = \gamma(z_1^* + \beta t_1^*) &= \gamma(\gamma\beta)_B \tau_1 cos\theta + \gamma\beta\gamma_B \tau_1 \\
z_2 = \gamma(z_2^* + \beta t_2^*) &= -\gamma(\gamma\beta)_B \tau_2 cos\theta + \gamma\beta\gamma_B \tau_2
\end{aligned} \tag{58}
$$

which gives a final z separation in the lab frame of

$$
\Delta z = \gamma(\gamma\beta)_B(\tau_1 + \tau_2) cos\theta + \gamma\beta\gamma_B(\tau_1 - \tau_2) \tag{59}
$$

As was shown above, $\gamma\beta\gamma_B$ is about 10 times larger that $\gamma(\gamma\beta)_B$ therefore elongating the z difference. The average z separation in *BABAR* is around $\Delta z \approx 256\mu m$ making it well measurable in the *BABAR* detector. The proper lifetime difference can be obtained from this measurement as:

$$
\Delta\tau = \frac{\Delta z}{\gamma\beta} \tag{60}
$$

More detailed information on the vertex separation can be found in [31].

2.3 The *BABAR* Detector

The *BABAR* detector is a standard barrel detector with five significant detection layers encompassing the beam pipe. Starting with the inner most layer these components are the Silicon Vertex Tracker (SVT), the Drift Chamber (DCH), the DIRC, which stands for Detection of Internally Reflected Cherenkov light, the Electromagnetic Calorimeter

(EMC) and the Instrumented Flux Return (IRF). Each component plays a significant role in the reconstruction of the decay particles. The distinct difference of the *BABAR* detector in comparison to common barrel detectors is the asymmetric shapes of its components. The small but significant boost of the decay products due to the asymmetric beam energies leads to an asymmetric detector design in order to achieve maximum acceptance in the center of mass (CM) frame. The boost lies parallel to the beam pipe favoring decay products to spray forward in the detector. The coordinate system used in the *BABAR* detector is pseudo-spherical. The beam pipe denotes the z-axis while positioning in the detector barrel and endcap are given by the polar angle θ and the azimuthal angle ϕ. The asymmetry can be seen in the one sided calorimeter endcap of Figure 10. The advantage of the boost for the determination of the B lifetime differences was explained before. Below is a detailed description of the sub-detectors. A more detailed description is provided in [32]. Figure 10 shows a cross sectional overview of the *BABAR* detector with its sub-components.

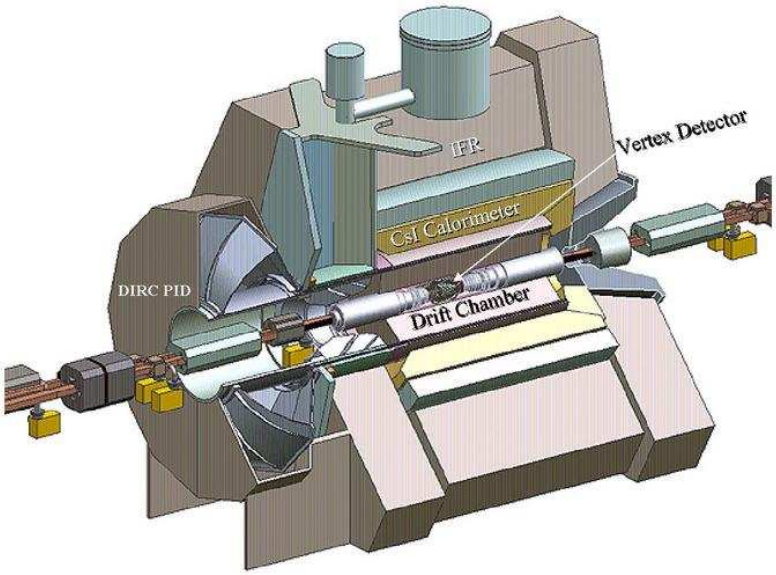

Figure 10: The *BABAR* detector. Figure taken from [33]

2.3.1 The Silicon Vertex Detector

The design of the SVT is shown in Figure 11. It consists of five concentric cylindrical double sided silicon detector layers which are further divided into individual modules. Each module consists of a forward and backward half-module. The inner side of the detectors are outfitted with strips that are oriented perpendicular to the beam pipe, which allows for the measurement of the z-component of a particle. The outer side contains longitudinal strips which are used to measure the ϕ-component. Each half-module contains between two and four detectors giving the *BABAR* detector a total of 340 silicon detectors spanning an area of about 1 m^2 with approximately 150000 readout channels. Table 2 summarizes some parameters of the silicon vertex layout. This design gives the Silicon Vertex Detector an intrinsic resolution of less than 30 μm which is necessary to resolve the individual vertexes of the B mesons.

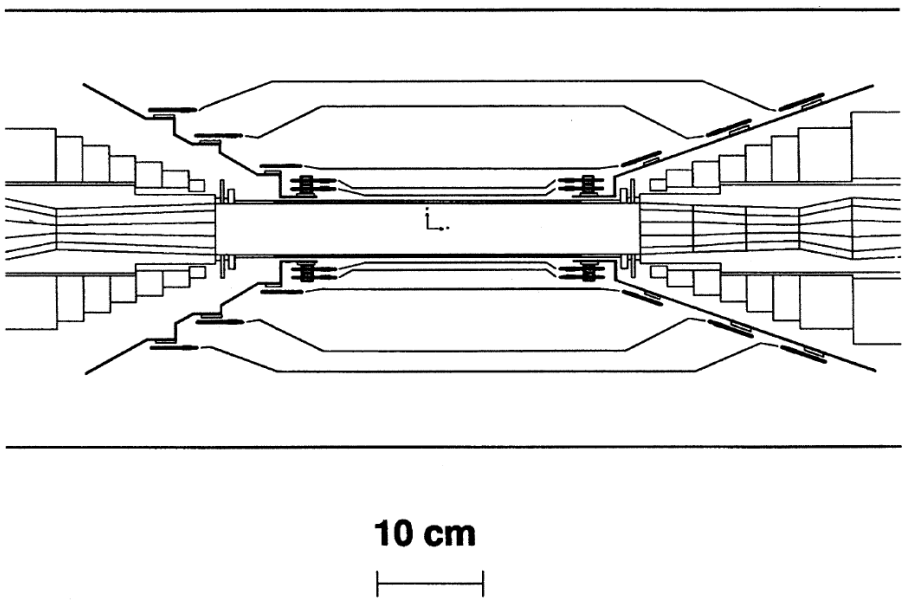

Figure 11: General outline of the Silicone Vertex Tracker (SVT). The cross sectional view shows the five silicone strip layers surrounding the beam pipe. The high resolution hits are used for vertex detection. The figure has been taken from [2].

Table 2: Some parameters of the silicon vertex tracker layout [2]

	Layer 1	Layer 2	Layer 3	Layer 4a	Layer 4b	Layer 5a	Layer 5b
Radius (mm)	32	40	54	124	127	140	144
Modules/Layers	6	6	6	8	8	9	9
Wafers/Modules	4	4	6	7	7	8	8
Readout pitch (μm)							
ϕ	50	55	55	80-100		80-100	
z	100	100	100	210		210	
Floating Strips							
ϕ	-	-	-	1		1	
z	1	1	1	1		1	
Intrinsic Resol. (μm)							
ϕ	10	10	10	10-12		10-12	
z	12	12	12	25		25	

2.3.2 The Drift Chamber

The Drift Chamber is the next layer of the *BABAR* detector and responsible for the main reconstruction of the charged particle tracks. This wire chamber consists of 40 concentric cylindrical layers capable of producing up to 40 hits of spatial coordinates per track for particles with a transverse momentum over 100 MeV/c. The system is used in combination with the Silicon Vertex Tracker to provide optimal spatial resolution for the particle tracks. The helium-isobutane gas filled Drift Chamber incorporates a light weight design in order to minimize multiple scattering introduced by the chamber achieving an average vertex resolution of 125 μm which is less than the proposed 140 μm in the design plans [34]. Figure 12 shows a schematic side view of the Drift Chamber. Due to the asymmetry of the beam energies, the interaction point is shifted towards the +z direction. By using materials such as 1mm thick beryllium for the inner cylinder, which corresponds to 0.28% of a radiation length, and two layers of carbon fiber on a Nomex core corresponding to 1.5% of a radiation length, the distortion of the particle trajectory is kept to a minimum. The chamber consists of 20 μm gold-plated tungsten-

rhenium sense wires which are responsible for the detection of ionization electrons. These wires are surrounded by six 120 μm and 80 μm gold-plated aluminum field wires used to produce the electric field. Figure 13 shows the isochronous lines around the sense wire. The ionized gas molecules created by a passing charged particle drift towards the field wires while the loose electrons create a cascade towards the sense wires. Since the drift velocity of the electron cascade is known, the sense wire provides a timing measurement which provides a positioning of the track relative to the sense wire. This relative positioning of isochronous lines is circular close to the sense wire and becomes distorted in the proximity of the field wires as shown in Figure 13. A fitting algorithm will later analyze these positioning circles to reproduce the particle trajectory. The voltages applied to the sense and field wires are 340 V and 1960 V, respectively, with slight deviations of the field wire voltage depending on the time and date of the run.

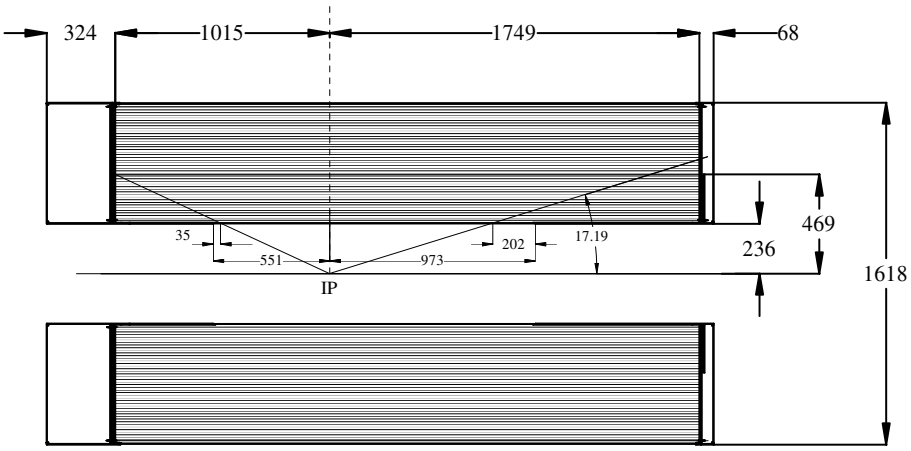

Figure 12: Schematic side view of the Drift Chamber (DCH) showing the 40 layers of the wire chamber. Due to the asymmetric interaction beam energies the interaction point is shifted to the left. The figure has been taken from [35].

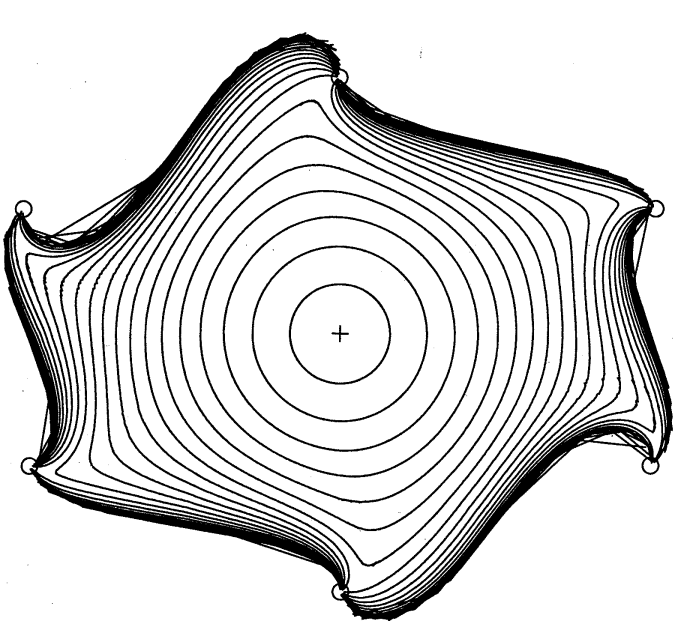

Figure 13: Isochronous lines of a single cell of the DCH. The middle sense wire is surrounded by 6 field wires. The contours represent the 50 ns isochrones of the cell. The dimensions of the cell are about 12 mm by 18 mm. The figure has been taken from [35].

2.3.3 The Detector of Internally Reflected Cherenkov Radiation (DIRC)

The DIRC, which is a sub-type of a Ring Imaging Cherenkov counter (RICH), is the next layer in the detectors geometry. Its main purpose is devoted to the particle identification (PID). The radiative material is made of synthetic quartz. The 144 elongated bars are arranged in a 12-sided polygonal barrel. The quartz fulfills two purposes: First as a radiator and second as a light-guide using total internal reflection to transport the Cherenkov light to the approximately 11,000 photomultiplier tubes (PMT) located on a disk on the side of the detector. The DIRC is necessary for the *BABAR* experiment to provide a clear separation between kaon and pion decay channels so that the B decay channels such as $B^0 \to \pi^+\pi^-$ and $B^0 \to K^+\pi^-$ can be clearly separated. It is also used for muon identification below 750 MeV/c where the IFR is still inefficient. The DIRC uses its grid of PMTs to measure the Cherenkov angle of a charged particle, which is related to its velocity:

$$cos\theta_c = \frac{1}{n\beta} \tag{61}$$

In combination with the momentum measurements of the DCH and the SVT, the mass of the particle can be determined and therefore its identity. Since the DCH is only able to separate pions from kaons up to a momentum of 700 MeV/c, the DIRC is solely responsible for the PID in the regions of 0.7 GeV/c to 4.2 GeV/c where the upper limit mainly pertains in the forward direction due to the relativistic boost of the particles. The DIRC is able to distinguish between pions and kaons with a separation of over 2σ above 0.7 GeV/c. Detailed information on the DIRC can be found in [36].

Other types of Cherenkov detectors have also been used in previous experiments such as a silica aerogel system at the BELLE experiment [37] or a gas Cherenkov counter [38]. The latter however fills a larger volume which is not available at the *BABAR* detector.

2.3.4 The Electromagnetic Calorimeter

The EMC of the *BABAR* detector is made of 6580 CsI(Tl) crystals and spans a polar angle of $-0.775 \leq cos\theta \leq 0.962$ in the laboratory frame. Incoming electromagnetic particles such as electrons and photons will be absorbed and produce narrow showers of secondary particles which will create photons in the vicinity of the incident particle. These photons are detected by photodiodes instead of PMTs, due to the presence of the strong magnetic field in this area. Hadronic particles are not easily absorbed, but leave a wider electromagnetic plus hadronic shower in the calorimeter. Together with the PID properties of the DIRC, hadronic particles can be characterized without the need of a separate hadronic calorimeter. The basic properties of the CsI(Tl) crystals are summarized in Table 3. The geometry of the EMC is depicted in Figure 14. The EMC is used to identify electrons as well as uncharged particles such as photons and neutral pions, which are essential for most analysis. The efficiency achieved for photons above 20 MeV was measured to be more than 96%. The angular energy resolution of the calorimeter was measured using π^0 and η control samples to be $\sigma_{\theta,\phi} = \frac{(3.87\pm0.07)mrad}{\sqrt{E(\mathrm{GeV})}} + (0.00 \pm 0.04)mrad.$ Another use of the EMC is the separation of electromagnetic from hadronic particles and the distinction between K_L^0 and muons together with the IFR.

Table 3: Properties of the Thallium-doped CsI [2]

Properties	CsI(Tl)
Radiation Length (cm)	1.85
Moliere Radius (cm)	3.6
Absorption Length for 5 GeV pions (cm)	41.7
Density (g/cm^3)	4.53
$dE/dx\|_{mip}$ (MeV/cm)	5.6
Light Yield (Photons/MeV $\times 10^3$)	40-50
Light Yield Temperature Coef. (%/C)	0.1
Peak Emission (nm)	565
Refractive Index at Emission Maximum	1.79
Decay Time (ns)	940
Hygroscopic	slight
Radiation Hardness (rad)	$10^3 - 10^4$

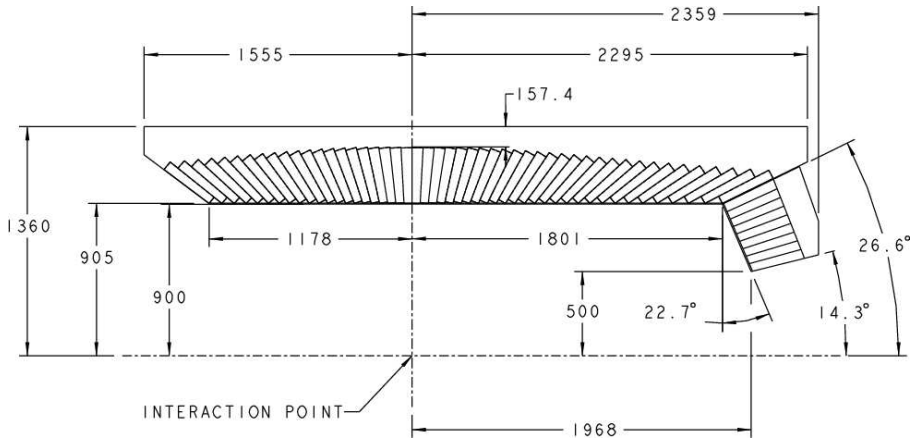

Figure 14: Geometrical layout of the EMC crystals. The end cap is only necessary on the right due to the asymmetric beam energies. The figure has been taken from [39].

2.3.5 The Instrumented Flux Return

The IFR is the last layer in the detector layout. Its purpose is to trace particles which have made it through the previous sub-detectors such as muons, neutron and K_L^0 particles. Muons are the only charged particles which pass through the EMC with only minimal ionization loss therefore making the IFR necessary. The iron layers serve the purpose of a magnetic flux return for the solenoid and together with the brass layers act as absorbers for the particle detection. The 65cm thick sextant, each section segmented

into 18 plates, is filled with an equal mixture of Argon and Freon gas and a small part of Isobutane between the absorption plates. The detection efficiencies reached with control samples at an operating voltage of 8000V was 97.2% during initial testing. Since pions get absorbed more quickly than muons, the IFR provides good discrimination between pions and muons.

2.4 Trigger and Data Acquisition

The event trigger at the *BABAR* experiment is a two stage trigger system consisting of a Level 1 (L1) hardware and a Level 3 (L3) software trigger with L3 being conditional on L1. A second stage trigger was conceived for more complicated trigger requirements, but not implemented. Unless stated otherwise the information presented in this section is a direct summary of [40]. The overall trigger efficiency achieved with this setup in *BABAR* is above 99% for $B\bar{B}$ events. The L1 trigger response latency typically lies below 12 μs and its overall trigger rate is about 1 kHz. A fast control and timing system (FCTS) collects information from the individual L1 sub-triggers and formulates the final trigger response, which is fed forward to the L3 trigger. The L3 trigger presents a secondary event reduction trigger for selection of physics events and rejection of Bhabha and other background events. Using L1 trigger and complete event information it filters proper physics events and stores them at a rate of up to 120 Hz. Further data processing is then performed offline using computer farms [41]. Data acquisition is propagated through special crate based readout modules over 1 GBits/s ethernet connections to servers dedicated to online event processing which monitor the data quality, combine the multiple data output streams and write the selected events to a file [32]. Detector calibration data is stored in a separate conditions database.

The FCTS formulates the trigger response based on 24 input lines originating from the Global Trigger (GLT). Since spacing between beam bunch crossings at *BABAR* are nearly continuous at 4.2 ns [32] these input lines provide the FCTS with almost continuous information. The GLT trigger is formed from information of charged tracks in the DCH

beyond a certain transverse momentum, shower responses in the EMC, and reported hits in the IFR layers. Each of these system provide information on "trigger primitives", a type of estimated event signatures reported from the systems sub-triggers. These sub-triggers are named the drift chamber trigger (DCT), the electromagnetic calorimeter trigger (EMT), and the instrumented flux return trigger (IFT). Sub trigger primitives are processed by the GLT every 134 ns. The DCT provides hit information on each of the 7104 DCH cells every 269 ns. The trigger then formulates its response based on a three stage algorithm. In a first stage DCH track segments are found together with their azimuthal positioning and timing estimates. In a second stage a Binary Link Tracker (BLT) combines the previously found track segments into complete tracks. A last step selects tracks above a certain transverse momentum. The EMT divides the information in the EMC into 280 towers, each consisting of 24 crystals. Energies in each tower are summed and provided to the EMT every 269 ns if exceeding a minimum level of 15 MeV per tower. The IFT processes hit signal from the ten sectors of the IFR. Hit data from the readout strips in all eight layers are processed through a majority logic requiring at least four hits in the eight layers of a particular detector segment within a time window of 134 ns. The ten sectors are then combined to a common trigger word. The GTL combines information from these sub-triggers and sends this to the FCTS every 67 ns. L1 does not perform any event identification.

The framework of Online Event Processing (OEP) implements the L3 software trigger, which primarily categorizes and filters the physics events. It is the first part of the DAQ system and is the first stage which is able to look at complete events. It operates at a logging rate of about 120 Hz. The reduction in rate to the L1 trigger is achieved through the rejection of BhaBha events, which constitute the majority of the L1 triggered events. At the L3 level data is preliminarily reconstructed from EMC and DCH information and trigger decisions are fed forward to the main offline event filters DigiFilter and BGFilter. The sub classes of the L3 trigger, such as the L3Dch and L3Emc are responsible for reconstructing the event signatures of their corresponding sub-detectors and perform

parallel to each other. Normally a L3 trigger decision is based on the L3Dch, L3Emc and one filter. The L3 information includes DCH tracks and EMC clusters. Tracks are returned from the Track Segment Finder (TSF) which returns estimates of track crossings in the DCH superlayers in form of ϕ positioning values. This information is combined with drift times from the individual DCH wires to form and store a transient event. This is done in three stages. First the 10 DCH superlayers are divided into 120 cells in ϕ. A track candidate is postulated if a sequence of close DCH cells have responded. The candidates are then matched against templates of precomputed track patterns. Also long tracks are required to produce at least 8 hits in the 10 DCH layers, shorter tracks need to show a response in 5 out of 6 layers. A next stage estimates timing values from DCH drift times which then are, in a last step, converted to positioning measurements. Track fitting is performed iteratively which allows for the addition and removal of track points. Generally poorly correlated hit points are removed from the fit. The fitting algorithm employs a 5 parameter χ^2 minimization fit on the helix curvature, the distance of closest approach to the coordinate origin in the (x, y) plane, the azimuth of the particle's momentum vector in the (x, y) plane at the point of closest approach to the origin of that plane, the z coordinate of the track's point of closest approach to the z-axis, and the tangent of the angle between the particle's direction and the z-axis. The information from the track fitting is then passed on to L3 trigger filters. The L3Emc module processes the information from the EMT and checks the 6580 individual crystals for recorded energy depositions of 20 MeV or more above the 0.5 MeV noise level. Since particle showers show a mean timing distribution in the EMC of 6 μs, an additional timing window between 5.7 μs and 7.0 μs is applied which limits passing crystals to a few dozen per event. EMC hits are then processed through a clustering algorithm and stored as clusters if the cluster energy sum exceeds 100 MeV.

The previously preliminarily reconstructed tracks and clusters are then processed through filters which categorize the physics event. These filters process the event by counting the number of good tracks or requiring a minimum EMC cluster energy or

combinations of both. Good tracks are generally required to pass certain vertexing or transverse momentum cuts among other requirements. A primary stage selects events through four Level 3 filters which loosely look for $B\bar{B}$, $c\bar{c}$, $\tau^+\tau^-$ and 2 γ events. These filters put loose requirements on the data such as minimum transverse momentum for tracks or maximum vertex separation. Additional Bhabha filters are used to veto the otherwise high contamination of Bhabha and muon pairs by specifically looking for two or one track events with high Bhabha characteristics. A second stage of offline filters is run in Prompt Reconstruction (PR) and is the last level of selection before full event reconstruction takes place. These filters are the DigiFilter and the BGFilter. The DigiFilter uses information from the L1 and L3 trigger words only to select events for further full reconstruction. About 35% of events which pass L1 and L3 triggering are passed on by the DigiFilter. Further information of the trigger bitmaps for this filter can be found in [40]. The BGFilter performs a part of the offline reconstruction and combines this information with the DCH hist and EMC cluster responses to select events for full reconstruction. For this it only passes tracks with a transverse momentum above 0.1 GeV/c and a certain number of drift chamber hits while also requiring a certain separation between tracks in the transverse plane and in z from their interaction point. Events which pass this filter are then stored in event lists such as "RecoGoodTracksLoose" or "RecoGoodTracksTight" for final analysis. Several other filters on this level are applied in parallel for event specification in other lists. A detailed summary of the available filter list can be found in [40].

3 Event Selection and Analysis Method

3.1 Partial Reconstruction

The $\mathcal{B}(\bar{B}^0 \to D^{*+}\ell^-\bar{\nu})$ branching fraction measurements currently included in the world average [4] have all been measured using a full reconstruction technique as presented in [14] [15], in which the decay products were reconstructed through the end products of a specific decay chain such as:

$$\bar{B}^0 \to D^{*+}\ell^-\bar{\nu}$$

$$D^{*+} \to D^0\pi^+$$

$$D^0 \to K^-\pi^+,\ K^-\pi^+\pi^-\pi^+,\ K^-\pi^+\pi^0.$$

A skim will select events which show the distinct signature of two pions and one kaon to reconstruct the original event. This was done for example in [15]. While background contamination is low in such techniques, the limiting branching fractions such as $\mathcal{B}(D^0 \to K^-\pi^+) = (3.80 \pm 0.07)\%$ [4], which is the largest mode of this channel, makes a high statistics measurement difficult. The partial reconstruction technique, which was successfully employed in earlier experiments at *ARGUS* [42], *CLEO* [43] and *DELPHI* [44] as well as *BABAR* [45], performs the reconstruction at an earlier stage by estimating the 4-momentum of the D^{*+} meson from the soft pion of its decay. This is possible because the available phase space in the decay $D^{*+} \to D^0\pi^+$ is minimal (~ 6 MeV/c^2). The resulting soft pion in the lab frame will travel in the approximate direction of the excited D^{*+} meson allowing for an estimation of its four momentum. This technique will increase the amount of selected events between 10 to 20 times compared to previous techniques allowing for a minimization of the statistical error while also possibly lowering the systematic error due to the absence of the $\mathcal{B}(D^0 \to K^-\pi^+)$ branching fraction. The estimation of the D^{*+} meson four momentum is done by a linear slope and offset relation of the soft pion three momentum to the D^{*+} momentum. The energy is then calculated relativistically from the momentum estimate as follows:

$$p_{D^*} = \alpha + \beta \times p_{\pi_s} \tag{62}$$

$$E_{D^*} = \sqrt{p_{D^*}^2 + m_{D^*}^2} \tag{63}$$

These relations can be evaluated in either frame. Here the quantities are evaluated in the $\Upsilon(4S)$ rest frame. The offset and slope parameters α and β were determined from Monte Carlo to be $\alpha = 0.2$ GeV/c and $\beta = 12.3$ for the CM frame system. The direction of the D^{*+} meson is assumed to be collinear with the slow pion. The directional error observed in Monte Carlo studies of the tagged soft pion peaks in a cone around the D^{*+} direction in the CM frame of about 13°. The error on the D^* energy averages around 400 MeV. The uncertainty introduced due to the momentum estimation will result in a widening of the signal peak which has been observed in Monte Carlo studies. Certain momentum and fitting constraints help limit this spread as will be presented later. Uncorrelated background events are distributed over the whole range of the angle. Figure 15 shows the distribution of the angular error in degrees for a select sample of Run 2 Monte Carlo data showing the distinct peak for true D^* events and their tail towards higher values, which is responsible for the widening of the signal peak in the M_ν^2 spectrum.

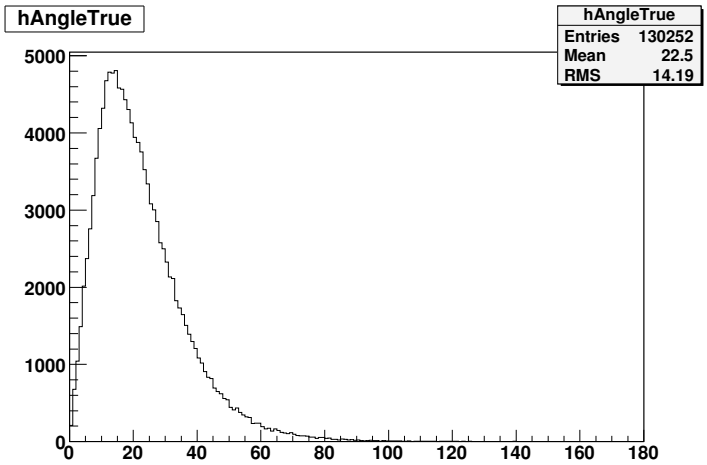

Figure 15: Angular distribution of D^{*+} and π^+ momentum vectors for Partial Reconstruction

Equation (62) employs a linear relation between the momentum of the soft pion and the momentum of the D^{*+} meson. In reality, signal events are distributed around this line with background spanning the full momentum range of both mesons. Figure 16 shows the relation of real D^{*+} momenta versus soft pion momenta based on select Monte Carlo data of Run 2 before and after partial reconstruction without background. The contour diagram shows the accumulation of signal in a peaking distribution of D^{*+} momenta in the area around the linear relation (indicated by a red line). After partial reconstruction has taken place all momenta show this linear relation.

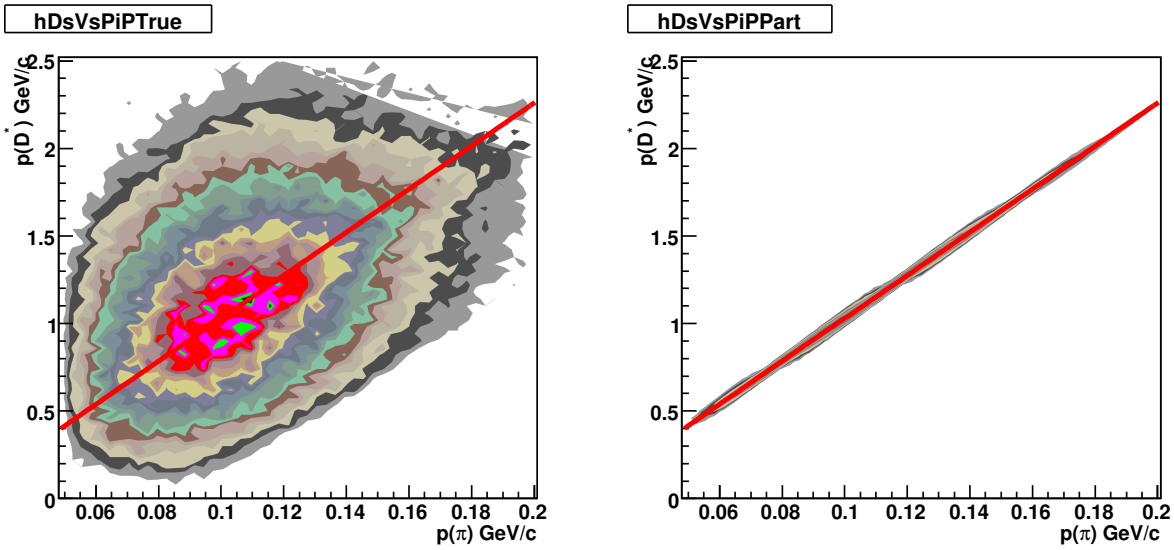

Figure 16: Momentum distribution between D^{*+} meson and soft pion (select data Run 2). Left: True distribution from Monte Carlo. Right: Distribution after partial reconstruction. The red line indicates the linear relation imposed by the partial reconstruction technique.

3.2 Data Sample

The data used in this analysis was collected by the *BABAR* experiment at SLAC through collisions of two counter rotating e^- and e^+ beams with asymmetric beam energies tuned to produces B mesons through the decay of the $\Upsilon(4S)$ resonance. The decay end products of the collisions are recorded by the *BABAR* detector, reconstructed and stored on an event by event basis. This analysis uses data collected between the years 2000 and 2002

with an available integrated luminosity of 81.47 fb^{-1}. In addition a total of 9.54 fb^{-1} of data was collected 40 MeV below the $\Upsilon(4S)$ resonance as a control sample of non-resonant $q\bar{q}$ background. This corresponds to the full data set of Run 1 and Run 2. Generic *BABAR* SP8 Monte Carlo is also available with an integrated luminosity of $190 fb^{-1}$ for both charged and neutral B mesons. Separate signal Monte Carlo data for the specific decay chain $\bar{B}^0 \rightarrow D^{*+}\ell^-\bar{\nu}_\ell$ was not created for this analysis since all necessary information can be extracted from the generic Monte Carlo data set. All applicable data sets of Run 1 trough 6 have been processed for both data and generic Monte Carlo and are available, but inclusion of the later runs does not significantly contribute to the reduction of either statistical or systematic errors. They are therefore not included in this analysis. Quarterly skims preselect events based on analysis type and the skimmed events are stored in nTuples for further analysis. Data used in this analysis has been processed through level 1 and 2 skims and is currently, at the time of this analysis, available at the computing grid *GridKa* in Karlsruhe, Germany. The analysis is based on the *Inclusive Semileptonic Skim* processed with analysis release 22.3.d. A work directory was created at GridKa and source code was written to further process the nTuples to histograms used in the analysis. All major adjustments, such as Monte Carlo tuning and luminosity weighting, as well as systematic error studies such as form factor reweighting and soft pion efficiency testing is done on this level.

3.3 Fox-Wolfram Moments

Goeffrey C. Fox and Stephen Wolfram have published an extensive study of event shapes for the e^+e^- annihilation process in [46]. Their work aimed to formulate features to help distinguish between jet-like and isotropic events of the e^+e^- annihilation process inspired by the expected decay structure of the ψ and Υ resonances. These particles were predicted to show a three jet decay structure coming from the dominant formation of three gluons. The paper [46] focuses on describing event shape functions, the Fox-Wolfram moments, which help distinguish between event types. The studies presented

in their paper are well suited for distinguishing events of this analysis from background hadronization processes. Since this non-resonant continuum background consists of $q\bar{q}$ pairs, which show a directional, jet-like decay structure and most $\Upsilon(4S)$ events are uniformly distributed in the detector, a measure for isotropy of the decay can be used as a selection feature between continuum background and $\Upsilon(4S)$ resonant decay events. Such a measure can be obtained from the ratio R_2 of second-to-zeroth Fox-Wolfram moments [46], calculated using the momenta of all charged and neutral particles in the event. The Fox-Wolfram moments H_l are axial independent observables expanded in spherical harmonics which characterize the shapes of the final states of the e^+e^- annihilation process defined as:

$$H_l = \frac{4\pi}{2l+1} \sum_{m=-l}^{+l} |\sum_i Y_l^m(\Omega_i) \frac{|p_i|}{E_{tot}}|^2 \tag{64}$$

Previous measures relied on finding a common axis between jets which made the classification dependent on the choice of coordinates while here all moments are rotationally invariant. In their discussion Fox and Wolfram consider the expansion to describe a sphere which tags event points which pierce through the sphere with its weight in the summation proportional to the absolute momentum of the particle piercing the sphere. Conservation of momentum centers the event in the middle of the sphere. A more general representation of the Fox-Wolfram moments can be obtained by introducing a mass density $\rho(\Omega)$ on the sphere and generalizing (64) to the continuum:

$$H_l = \frac{4\pi}{2l+1} \sum_{m=-l}^{+l} |\int \rho(\Omega) Y_l^m(\Omega) d\Omega|^2 \tag{65}$$

Since this analysis deals with discrete distributions of measured particles, the discrete representation of (64) will be used. Detailed investigations for a variety of event shapes have been performed in [46]. From this follows that the second Fox-Wolfram ratio $R_2 = H_2/H_0$ is a good discriminant to distinguish between the jet like continuum background of $q\bar{q}$ events and the more isotropic $\Upsilon(4S)$ decay products. This can be shown from ideal, theoretical considerations. From energy-momentum conservation it follows $H_0 \simeq 1$. The

process $e^+e^- \to q\bar{q}$ ideally gives $H_l = 1$ for even l and $H_l = 0$ for odd l. For uniformly distributed events we expect that ideally $H_2 = 0$, making the second Fox-Wolfram ratio $R_2 = H_2/H_0$ a good discriminant for continuum background rejection. R_2 is a standard discriminant used in most *BABAR* analyses. The Fox-Wolfram moments and ratios for different event shapes have been graphed and their average values tabulated for reference purposes in [46]. Tabulation was preformed for different center of mass energies to account for differences in event shape. Figure 17 was taken from [46] and shows the distribution of H_2 for a center of mass energy of 10 GeV, which is close to the *BABAR* energy. Among the shapes investigated, the dashed line shows the ratio for resonant decays and the dotted line shows the ratio for $q\bar{q}$ events. It can be seen that a cut value of $R_2 < 0.5$ would be able to reject half of the continuum background while maintaining most of the resonant signal.

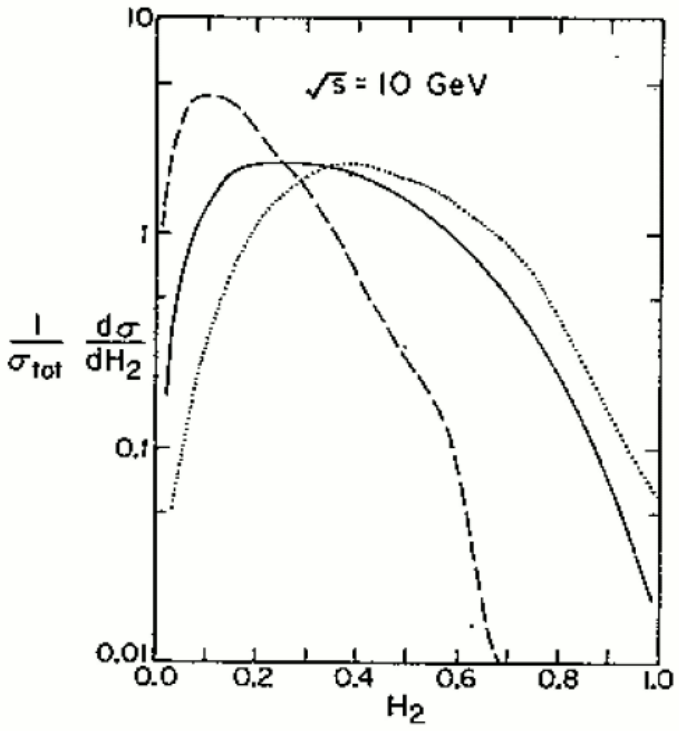

Figure 17: Second Fox-Wolfram moment H_2 for the e^+e^- annihilation process at $\sqrt{s} = 10$ GeV. The dotted line are $q\bar{q}$ "background" events and the dashed line are resonant events. It can be seen that this variable has good discrimination power for continuum background rejection. The solid line are $q\bar{q}$ events with the creation of an extra gluon. The figure has been taken from [46].

3.4 Event Selection

Events are selected with the following bounds and requirements on the overall event and the individual reconstructed particles during the skim. A detailed description can also be found in [47]. In order to limit Bhabha scattering and muon pair events, the SVT and the DCH are required to show at least four tracks to originate from charged particles. This helps the selection of hadronic events. Muons are required to pass the neural network based *muNNLoose* selector. This provides an average muon identification efficiency of about 80% with an average pion mis-identification rate of about 1%. The exact rates depend on the momentum of the muon, its angle to the detector and year of the run. A detailed map of the efficiencies spit up into angles, momentum and years can be found in [48]. This muon selector is required to keep the pion mis-identification rate at a minimum since the analysis heavily relies on correctly reconstructed and identified pions. Electrons are required to pass the likelihood based *PidLHElectrons* selector. The electron efficiency based on this selector is about 90% with a negligible pion mis-identification rate. Details on this selector can be found in [49]. Furthermore, since soft pions are used for the reconstruction of the decay all pions are required to fall within a momentum window in the CM frame of 0.05 GeV/c $\leq p_{\pi_s} \leq$ 0.20 GeV/c. The upper bond limits background contamination while the lower bound is manly due to detector capabilities. Leptons are require to fall within a momentum window in the CM frame of 1.4 GeV/c $\leq p_\ell \leq$ 2.5 GeV/c where this bound applies for both electrons and muon candidates. The upper bound is due to the kinematic range of the decay while the lower bound helps reduce "peaking background" from $D^{**}/D^* n\pi$ events (see section 3.7). Background rejection based on the sphericity and isotropy of the events are performed by requiring the second Fox Wolfram ratio of each event to be less than one half ($R_2 < 0.5$). This suppresses jet like background events from $q\bar{q}$ production.

After reconstruction another cut is applied to improve background rejection in the sample focusing on combined properties of the soft pion and the lepton in the decay. As described below, this χ cut is based on probability ratios $r(x) = s(x)/b(x)$ depicting

whether an input x belongs to a signal event or background event. Pure signal would result in an infinite ratio ($r(x) \to \infty$) and pure background returns a value of zero ($r(x) = 0$). A probability density whether a lepton (pion) is part of a signal (background) decay is computed on the appropriate momentum range. For each lepton (pion) momentum range $x = p_{\ell,(\pi)} + \delta p_{\ell,(pi)}$ a probability density $s(x)(b(x))$ is computed whether this lepton (pion) belongs to signal (background) events. Probability ratios are computed for the lepton and the pion based on their momenta and from their probability to originate from a common vertex ($r(p_\ell), r(p_\pi), r(\Pi_V)$). More detailed information can be found in [47]. The common vertex fit of the lepton and pion Π_V is constrained to the x-y plane with a softening in the y direction of $50\mu m$ to account for B motion. The probability densities are computed from Monte Carlo data by fitting a polynomial expansion to the resulting shape. The expansions are given by:

$$\begin{aligned} r(\Pi_V) &= 0.507 + 5.791 \times \Pi_V - 27.69 \times \Pi_V^2 + 61.86 \times \Pi_V^3 - 61.98 \times \Pi_V^4 + 22.61 \times \Pi_V^5 \\ r(p_\ell) &= -276.7 + 656.6 \times p_\ell - 579.0 \times p_\ell^2 + 224.7 \times p_\ell^3 - 32.27 \times p_\ell^4 \\ r(p_\pi) &= -2.002 + 78.00 \times p_\pi - 589.0 \times p_\pi^2 + 1309. \times p_\pi^3 \end{aligned} \tag{66}$$

The product of the likelihood ratios of the lepton, pion and their common vertex then has decisional capabilities whether the event should be included or cut from the data: $r = r(p_\ell) \cdot r(p_\pi) \cdot r(\Pi_V)$. To limit this number to a probability range from 0 to 1 a χ variable is introduced which is comprised of the ratios:

$$\chi = \frac{r}{r+1} \tag{67}$$

As a preliminary selection criteria events were rejected on a $\chi < 0.3$ basis in addition to the hard momentum cuts and recorded into the nTuples. The χ spectrum for the data set can be seen in Figure 18 for data compared to the equivalent combination of Monte Carlo data consisting of charged and neutral Monte Carlo signal, combinatoric Monte

Carlo background and continuum background from on resonance data [47]. It can be seen that the cut criteria tag about 18 % of the data as background in addition to the hard momentum cuts. The figure on the left shows the full χ distribution for an earlier data set processed in this way and was taken from [47] for comparison. The figure on the right shows the χ distribution of the data set at hand. The region of $\chi < 0.3$ was excluded at the skimming level and cannot be reproduced from the nTuple of this data set. The Monte Carlo data shown is raw data without modification such as tuning. Scaling was only performed on the luminosity level. It can be seen that the Monte Carlo (black solid curve) depicts the data quite well only undershooting a little in the low χ peak. This deficiency will be addressed later by slightly rescaling the Monte Carlo through a fit in the sideband region. All data shown here was taken from Run 1 and Run 2 for both electrons and muons.

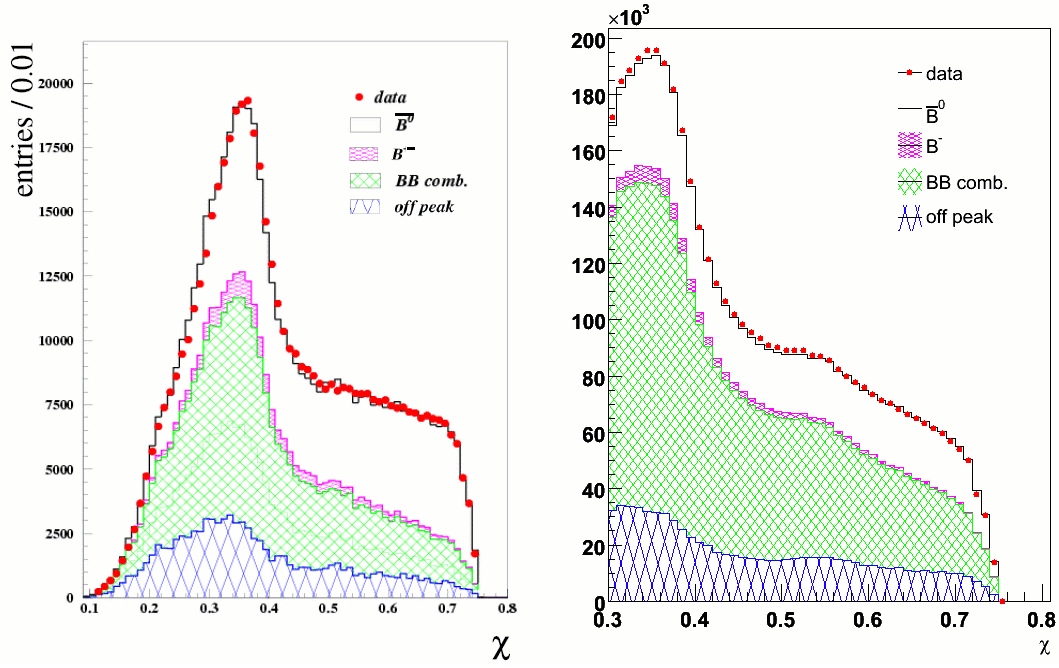

Figure 18: χ spectrum for data and Monte Carlo: (left) Full χ spectrum of an earlier data set processed with the partial reconstruction technique taken from [47] for comparison. (right) χ spectrum of this analysis. The dotted curve (red) is data while the solid (black) curve and the shaded regions are the corresponding Monte Carlo constituents.

Only two more cuts were implemented at the nTuple level during histogramming. In addition to the hard momentum cut in the CM frame, pions are also rejected if falling below 80 MeV/c in momentum in the lab frame ($p_{\pi,lab}$). It should be noted that this is the absolute momentum as opposed to the transverse momentum. This cut limits the dependence of the analysis to the soft pion turn-on differences between detector and Monte Carlo. Details on efficiencies and data rates can be found in the section on systematic errors of this dissertation. During histogramming it also proved more beneficial to raise the cut level of the χ variable to 0.4. Events are rejected if $\chi < 0.4$. The tighter requirement for the likelihood ratio eliminates about another 35% of raw data but improves the signal to background ratio from about 46% to 53%. Figure 19 shows a comparison of the resulting neutrino missing mass square (described in section 3.5) before and after the tighter cut. It can be seen that the combinatoric background contributions have been lowered and the signal to background ratio was improved.

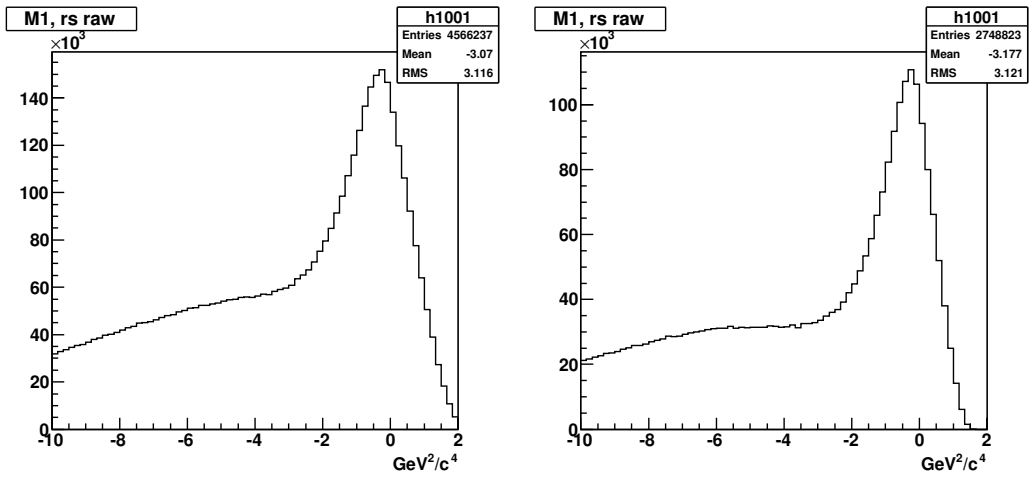

Figure 19: M_ν^2 spectrum for raw data: (left) M_ν^2 distribution for the $\chi < 0.3$ cut. (right) M_ν^2 distribution for the $\chi < 0.4$ cut.

Figure 20 shows the lepton and pion momentum distributions after this cut. While the decline in the pion momentum bins at low momenta is due to the rapidly shrinking detector efficiency for slow pions in that region, the upper momentum region is clearly dominated by the hard cut and seems unaffected in shape by the tightening of the χ

variable. For the lepton momentum distribution one can see that the decline of entries in the higher momentum regions is due to phase space limitation and remains unaffected by the tighter χ criteria. The low momentum edge however is significantly altered by this cut. The left plot shows a strong dependence of the lepton momentum spectrum on the hard lepton cut. After tightening the lepton momentum plot on the right shows a relatively soft edge in the low momentum region. The lepton momentum is therefore dominated by the χ cut and only softly correlated to the hard lepton cut. The χ selection criterion therefore helps soften the dependence on theoretical models. Table 4 shows a summary of the main selection criteria applied in this analysis.

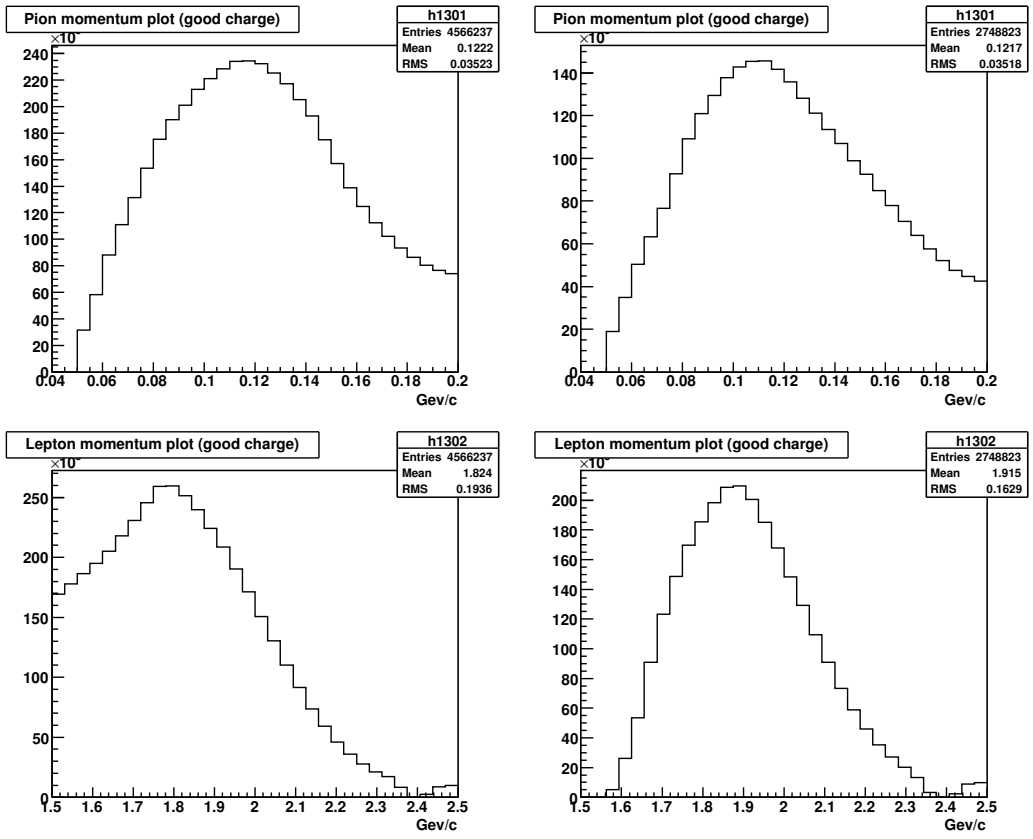

Figure 20: Momentum spectra for the different χ cuts. Top: Pion momentum spectrum for $\chi < 0.3$ (left) and $\chi < 0.4$ (right). Bottom: Lepton momentum spectrum for $\chi < 0.3$ (left) and $\chi < 0.4$ (right).

Table 4: Selection criteria for the $D^{*+}\ell^-\bar{\nu}$ decay

Variable	**Cut**	**Description**
SVT/DCH	# Tracks ≥ 4	Removes Bhabha and muon pairs
p_ℓ	1.4 GeV/c $\leq p_\ell \leq$ 2.5 GeV/c	Suppresses leptons from charm decays
p_π	50 MeV/c $\leq p_\pi \leq$ 200 MeV/c	Soft pion selection
$p_{\pi,lab}$	$p_{\pi,lab} \geq$ 80 MeV/c	Reduces soft pion turn on dependence
List	PidLHElectrons	Electron Selection Tool.
List	muNNLoose	Muon Selection Tool
R_2	$R_2 = H_2/H_0 \leq 0.5$	Fox-Wolfram moments to limit cont. Bg.
p_ℓ, p_π, Π_V	$\chi > 0.4$	Event Probability Cut

3.5 Signal Definition

The reconstruction of the signal is based on the concept that the neutrino in the decay leaves the detector undetected. The reconstruction of the invariant mass of this missing particle from the other decay products present in the decay can then be used to separate signal from background events according to:

$$\mathcal{M}_\nu^2 = (E_{beam} - E_{D^*} - E_\ell)^2 - (\vec{p}_{D^*} + \vec{p}_\ell)^2 \tag{68}$$

The signal reconstruction is done by selecting events which contain leptons identified in the electromagnetic calorimeter (electrons) or in the IFR (muons) as well as soft pions. A proper signal decay will produce one lepton and one soft pion from the $D^{*+} \rightarrow D^0\pi^+$ decay, but other pions and leptons from secondary decays or the other B mesons might be present in the data sample. The neutrino mass is reconstructed for each pair of one lepton and one pion. Events that did not originate from the signal will show a neutrino rest mass different from zero, while signal events will be distributed around the zero value due to statistical fluctuations as well as the spread introduced in the partial reconstruction technique. Figure 21 shows the raw signal peak for a combined sample of Run 1 and 2 for both lepton types.

One can clearly see the signal peak around zero mass as well as the background dominated area. The signal to background ratio is approximately 1 to 1. Based on previous studies [43] we define the region in which a signal should be found to be the

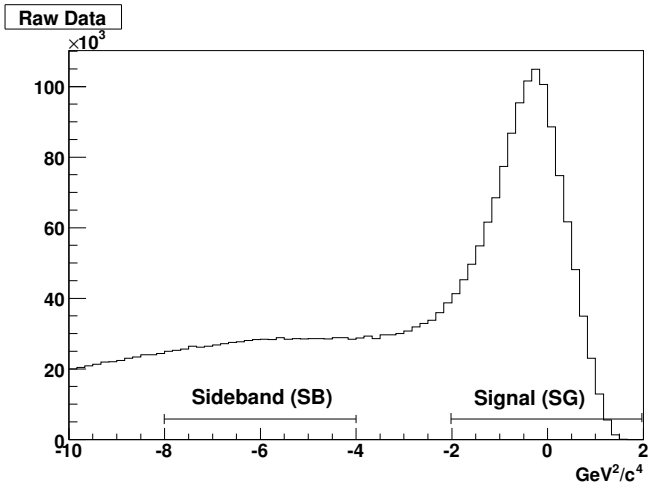

Figure 21: Neutrino Mass Square, $\mathcal{M}_\nu^2$ spectrum from data.

signal region $-2\ \mathrm{GeV}^2/\mathrm{c}^4 \leq M_\nu^2 \leq 2\ \mathrm{GeV}^2/\mathrm{c}^4$ while the region dominated by background is defined as the sideband region $-8\ \mathrm{GeV}^2/\mathrm{c}^4 \leq M_\nu^2 \leq -4\ \mathrm{GeV}^2/\mathrm{c}^4$. The plot shown in Figure 21 contains about 700,000 signal events in the signal region which demonstrates the statistical advantage of the partial reconstruction method. It represents the raw data after reconstruction for Run 1 and Run 2 with both lepton samples combined. Comparable analyses using full reconstruction have reconstructed up to 70,000 signal events for the same integrated luminosity of data [14].

3.6 Branching Fraction Determination

The branching fraction can be determined by either integrating the partial decay width of equation (38) or through a more straightforward extraction of the signal events from raw data presented below. Since the distribution in phase space is effectively integrated out for the determination of the branching fraction, the latter method will be applied as described below. This method allows one to desensitize the data to very low momentum pions by introducing the low pion momentum cut in the lab frame as mentioned before. This was not done in other analysis techniques for the low momentum region is needed for measurement of other quantities such as the form factor parameters or V_{cb}. The number of pure signal events, N_D, found in the data after all backgrounds have been removed

is related to the total amount of data B meson pairs, $N_{B\bar{B}}$, which is obtained from B counting methods provided by *BABAR* software in the following way:

$$N_D = 2 \times N_{B\bar{B}} f_{00} \times \mathcal{B}\left(\bar{B}^0 \to D^{*+}\ell^-\bar{\nu}_\ell\right) \times \mathcal{B}\left(D^{*+} \to D^0\pi^+\right) \times \epsilon \tag{69}$$

The branching fractions $\mathcal{B}\left(D^{*+} \to D^0\pi^+\right)$ and f_{00} are known and taken from the current value of the PDG [4]. Here f_{00} is the branching fraction of the $\Upsilon(4S)$ resonance to decay into neutral B mesons $\mathcal{B}(\Upsilon(4S) \to B^0\bar{B}^0)$. The efficiency ϵ is obtained through Monte Carlo simulations for the data set being used.

3.7 Reconstruction Efficiency

The determination of the reconstruction efficiency of the analysis for the decay under study is essential for the proper extraction of the branching fraction. Several aspects determine this value for the specific techniques applied in this analysis. To obtain this relative value one needs to find the ratio of the number of reconstructed signal events for the decay in question to the number of signal events which were originally created. Events are not reconstructed, for example, due to detector uncertainties, momentum cuts, background rejection techniques and other effects that limit the extraction of real signal events. This is determined from Monte Carlo simulations.

3.7.1 The $\bar{B}^0 \to D^{*+}\ell\bar{\nu}_\ell$ efficiency

Compared to the raw produced B meson events, this efficiency ε has the following relation to the found signal events:

$$N_D^{MC} = 2 \times N_{B\bar{B}}^{MC} \times f_{00} \times \mathcal{B}^{\mathcal{MC}}\left(\bar{B}^0 \to D^{*+}\ell^-\bar{\nu}_\ell\right) \times \mathcal{B}^{\mathcal{MC}}\left(D^{*+} \to D^0\pi^+\right) \times \varepsilon^{MC} \tag{70}$$

Here N_D^{MC} is the amount of signal in the signal region, f_{00} is the branching fraction of the $\Upsilon(4S)$ resonance to decay into neutral B mesons and $N_{B\bar{B}}^{MC}$ is the amount of B mesons produced in the Monte Carlo event. The factor of two is due to the fact that

both B mesons are capable of producing signal events. Since this extraction requires a proper knowledge of the $\mathcal{B}^{\mathcal{MC}}\left(\bar{B}^0 \to D^{*+}\ell^-\bar{\nu}_\ell\right)$ branching fraction, the efficiency can only be determined from pure Monte Carlo simulations. This technique however is deemed to be suitable since ample data is available to tune the Monte Carlo samples to the corresponding data shapes as is described later on in this dissertation. Therefore it is believed that the uncertainty due to M_ν^2 shape differences between Monte Carlo and data is negligible and that other systematic errors outweigh this effect. Also the definition of the signal region is taken into account in the determination of the efficiency. The number of produced Monte Carlo events is given as a integrated luminosity $\mathcal{L}_{MC}$. In general the B meson count can also be found through the corresponding cross section and the relation:

$$N_{B\bar{B}}^{MC} = \mathcal{L}_{MC} \times \sigma_{MC} \tag{71}$$

However the proper number of B mesons is more accurately known in the event of Monte Carlo data based on the R22 simulations using the available collections from the run files. The yields are quoted in Table 5. The number of signal events is taken from the Monte Carlo signal plot shown in Figure 22 in the signal region by simply counting the histogram entries. The signal region again is defined as events satisfying the mass constraint -2 GeV/c^2 $\leq M_\nu^2 \leq 2$ GeV/c^2. All relevant figures for this calculation are summarized in Table 5. Since the Monte Carlo data is processed through the same level of skims and signal selection cuts as the data, the efficiency changes with any modification in the signal extraction technique, making it possible to study the behavior of, for example, different cut levels on the corresponding signal. Solving for the efficiency in equation (70) one finds:

$$\varepsilon^{MC} = \varepsilon = (22.96 \pm 0.01)\% \tag{72}$$

as the overall efficiency for combined Run 1 and 2 using electron and muon samples. This efficiency is taken to also be the detector efficiency for real data. Since the efficiency is

determined purely from Monte Carlo data, it is also sensitive to effects from model dependent form factors. For this reason it will also have to be recalculated in the study of form factor dependencies, which is described later, as well as other systematic error studies.

Table 5: Efficiency Calculation Numbers

	Run 1	Run 2	Run 1+2
N_D^{MC}	662400 ± 814	1814307 ± 1347	2476707 ± 1574
$N_{D,e}^{MC}$	384814 ± 620	1052028 ± 1026	1436842 ± 1199
$N_{D,\mu}^{MC}$	277585 ± 527	762279 ± 873	1039864 ± 1020
$N_{B^0\bar{B}^0}^{MC}$	36594586 ± 6019	103124000 ± 10155	139718586 ± 11820
$N_{B^+B^-}^{MC}$	37200000 ± 6099	103356000 ± 10166	140556000 ± 11856
$\mathcal{B}^{\mathcal{MC}}\left(\bar{B}^0 \to D^{*+}\ell^-\bar{\nu}_\ell\right)$		5.7%	
$\mathcal{B}^{\mathcal{MC}}\left(D^{*+} \to D^0\pi^+\right)$		67.7%	

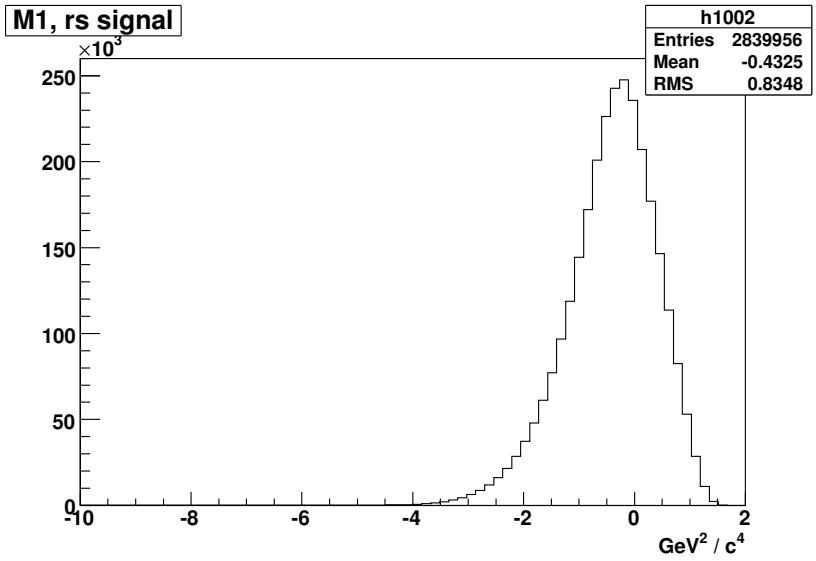

Figure 22: Pure Monte Carlo Signal

The efficiency is an essential part in the determination of the branching fraction of this decay channel. It can alternatively be determined by considering double tag events, where both B mesons decay into the correct semi-leptonic channel. This technique is described in [50] and can be used for verification purposes. However, Monte Carlo dependence still exists indirectly through an efficiency correlation factor shadowing the advantage of obtaining the efficiency from data. It is believed that the single tag determination is

accurate for this analysis, so that it is chosen to be the sole determination of the efficiency here.

The quoted efficiency above was obtained with a combined sample of electrons and muons taken from both Runs (1 and 2). It therefore is the average reconstruction efficiency for this data set and can be used whenever all data is considered. However in order to more closely consider the effects of different run conditions and differences between the detection of muons and electrons it is useful to calculate the individual efficiencies per lepton and run condition. These efficiencies are later used for the individual calculation of the branching fraction as a cross check to using combined data. Since the final result should be unaffected by this technique, any differences can be attributed to the systematic error. The values used for the efficiency calculations are summarized in Table 5 and are split into runs. The resulting efficiencies based on lepton kind and run number are displayed in Table 6. The table shows the efficiency of electron only data to be higher than the one obtained from muon samples, which reflects the higher efficiency of the ECAL for electron as opposed to the IFR used for muon detection.

Table 6: Calculated Efficiencies

	Run 1	Run 2	Run 1+2
$\varepsilon_{e+\mu}$	$(23.46 \pm 0.03)\%$	$(22.80 \pm 0.02)\%$	$(22.96 \pm 0.01)\%$
ε_e	$(13.63 \pm 0.02)\%$	$(13.22 \pm 0.01)\%$	$(13.32 \pm 0.01)\%$
ε_μ	$(9.83 \pm 0.02)\%$	$(9.58 \pm 0.01)\%$	$(9.64 \pm 0.01)\%$

3.7.2 The $\bar{B}^0 \to D^{**+}\ell^-\bar{\nu}_\ell$ efficiency (Peaking Background)

Another efficiency of interest is the reconstruction efficiency of the excited D^{**} charm mesons since these states constitute the majority of the "peaking background" in the analysis. The efficiency referred to here is the amount of D^{**} peaking events which pass selection cuts and are present in the raw $\bar{B}^0 \to D^{*+}\ell^-\bar{\nu}_\ell$ M_ν^2 distribution. The lepton momentum cut was introduced to maximize the rejection of such decays. By calculating the efficiency from Monte Carlo simulations one can verify the validity of the lepton momentum cut. Since these are background events, a very low efficiency is

desired in this case. The D^{**} mesons and its decay branching fractions have been recently measured [51] and a theoretical model for Monte Carlo modeling of these decays has been recently updated [52]. The D^{**} meson is a pair of the two charm meson doublets $[D_1(2420), D_2^*(2460)]$ with angular momentum $j = 3/2$ and $[D_0^*(2400), D_1'(2430)]$ with angular momentum $j = 1/2$ where the first doublet represents narrow resonances and the second two are very broad [51]. However the $D_0^*(2400)$ state does not decay into a $D^{*+}(2010)$ meson and will therefore be omitted from this consideration. Since D^{**} contributions to the peaking background originate from both neutral and charged B mesons we calculate the overall branching fraction of the D^{**} resonance by summing the individual contributions to be $\mathcal{B}(B \to D^{**}\ell^-\bar{\nu}_\ell) = 3.50\%$. The individual branching fractions, after reweighting in the Monte Carlo, are summarized in Table 7 [53]. Applying equation (70) together with the values of Table 5 we find the efficiency for the combined neutral and charged sample for both runs and with electrons and muons combined to be $(2.013 \pm 0.004)\%$. This number is roughly 10 times smaller than the efficiency determined above for the signal decay under study. This result is a promising cross check for the validity of the background rejecting cuts applied in this analysis.

Table 7: Individual branching fractions for each contributing D^{**} mode

Decay Mode	BF
$B^- \to D_1^0\ell^-\bar{\nu}_\ell$	$0.54 \pm 0.06)\%$
$B^- \to D_1'^0\ell^-\bar{\nu}_\ell$	$(0.85 \pm 0.20)\%$
$B^- \to D_2^{*0}\ell^-\bar{\nu}_\ell$	$(0.42 \pm 0.08)\%$
$\bar{B}^0 \to D_1^+\ell^-\bar{\nu}_\ell$	$(0.50 \pm 0.08)\%$
$\bar{B}^0 \to D_1'^+\ell^-\bar{\nu}_\ell$	$(0.80 \pm 0.20)\%$
$\bar{B}^0 \to D_2^{*+}\ell^-\bar{\nu}_\ell$	(0.39 ± 0.07) %
Total	$(3.50 \pm 0.32)\%$

4 Backgrounds

Three major background categories accompany the signal: 1) Continuum background, 2) Combinatoric background, and 3) Peaking background. A combination of simulated Monte Carlo events and real data, where possible, is used in the analysis to properly describe this background contamination.

4.1 Continuum Background

Continuum background events which accompany $\Upsilon(4S)$ decays are non-resonant quark/anti-quark events of first and second generation quark pairs which are seen as jets of particles in the detector. The majority of these jet-like events are suppressed by the introduced cut on the Fox-Wolfram ratios. A measurement of the continuum background is obtained from off resonance data at the *BABAR* PEP-II collider by operating 40 MeV below the $\Upsilon(4S)$ resonance. The resulting data is then scaled to the luminosity of the "on peak" data as well as to the difference in energies according to:

$$S_{cont} = \frac{\mathcal{L}_{on}}{\mathcal{L}_{off}} \cdot \frac{E_{off}^2}{E_{on}^2} \tag{73}$$

where S is the scale factor, $\mathcal{L}$ are the luminosities and E are the beam energies of the on and off resonance runs. This is done to find the contribution of continuum background in the on peak data sample. The luminosity scaled data is directly subtracted from the "on peak" missing mass square data in Figure 21 during the analysis.

4.2 Combinatoric Background

The combinatoric background dominates the sideband region and consists of random combinations of leptons from B decays paired with right sign (RS) soft pions $(\ell^{\pm}, \pi^{\mp})$ originating from the same B meson of the decay. The study of wrong signed (WS) combinations $(\ell^{\pm}, \pi^{\pm})$ allows to investigate the background shape in the full M_{ν}^2 region from data. Thus we use combinations of both RS and WS to study the combinatoric

background.

Three models of combinatoric background can be constructed. First, the combinatoric background shape is obtained from RS Monte Carlo data. The RS lepton-pion pairs are chosen from the tracks list, excluding the true decay candidates. The lepton-pion pairs are required to originate from a common vertex. Second, WS combinatoric background is obtained from the Monte Carlo data in a similar fashion. The lepton-pion pairs are required not to originate from a common vertex. Third, WS lepton-pion candidates are obtained from the data. Again the lepton-pion pairs are required not to originate from a common vertex. Combinatoric background can originate from both charged and neutral B decays.

Since the sideband is dominated by combinatoric background, these backgrounds can be fit to the sideband and extended into the signal region for background subtraction/fitting. The study of the three types of combinatoric backgrounds is used in the analysis to estimate a systematic error on the final result.

Figure 23 shows the shape of of the continuum background as well as the three shapes of combinatorial background for the inclusive data set of Run 1 and Run 2 and both leptons. All figures shown in this section have been adjusted with the Monte Carlo tuning technique described in section 6.

Combinatoric Background Comparison

The combinatoric background is the only background shape which is available from three different sources, RS MC, WS MC and WS data. All three sources agree well in their shapes but slight differences exist. These differences will be attributed to the systematic error in the analysis. To investigate the deviation, a study to compare the three shapes with each other was performed. The ratios between the shapes were taken to illustrate the deviations. These ratios also give insight in the disagreement between data and Monte Carlo since wrong sign combinations are available from both sources. This section focuses on the comparison and differences of these line shapes. Figure 24 shows the

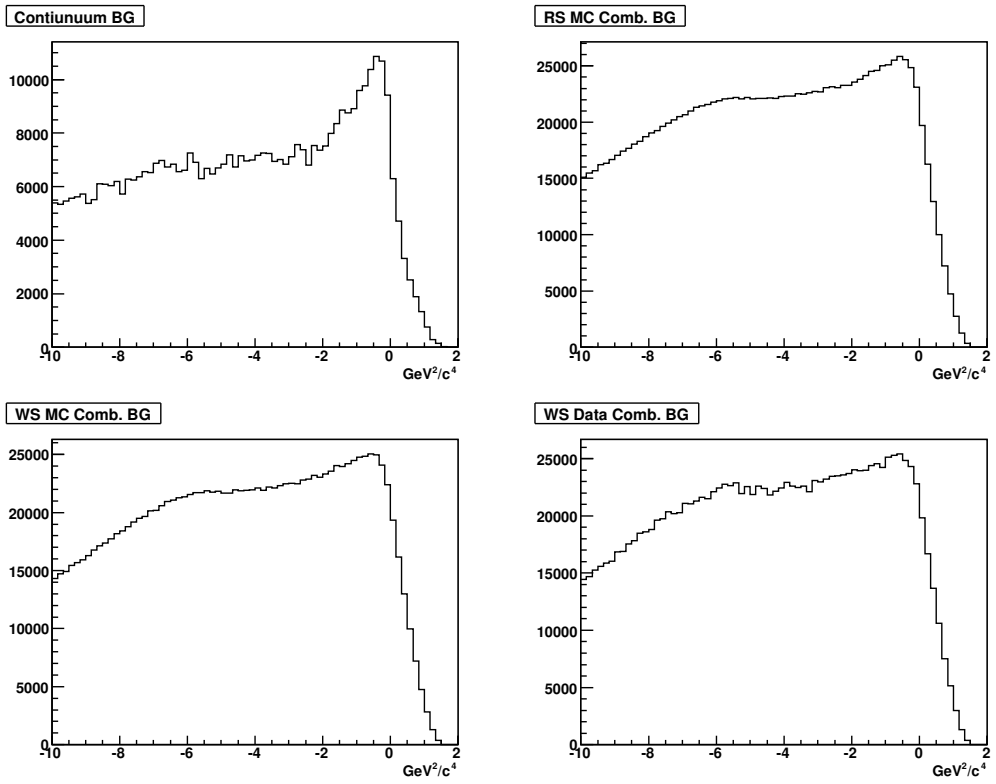

Figure 23: Continuum and combinatoric background shapes: Top: (left) Continuum background from off resonance data. (right) RS MC Combinatoric Background. Bottom: (left) WS MC Combinatoric Background. (right) WS Data Combinatoric Background.

superposition as well as the ratios of the different combinatoric background shapes. All shapes were arbitrarily scaled to a best fit in the sideband region where agreement is expected to be high.

The three shapes show good agreement with each other. Deviations are visible for the RS MC shape in low M_ν^2 region and between Monte Carlo and data in the signal region. The slightly worse agreement in the low M_ν^2 region shaped the definition of the sideband region in the range of -8 GeV^2/c^4 $\leq M_\nu^2 \leq -4$ GeV^2/c^4 instead of the full regime. Slight differences between RS MC and data are expected since they are accumulated from different selections. Figure 24 shows good agreement between WS MC and WS data except for a slight overshooting of the MC data in the signal region which is clearly visible in the difference plot. The difference between the shapes in this region is about 0.8%. This difference is currently still under study. To account for this phenomena all

background shapes are applied separately in the analysis and the difference considered to be a systematic error.

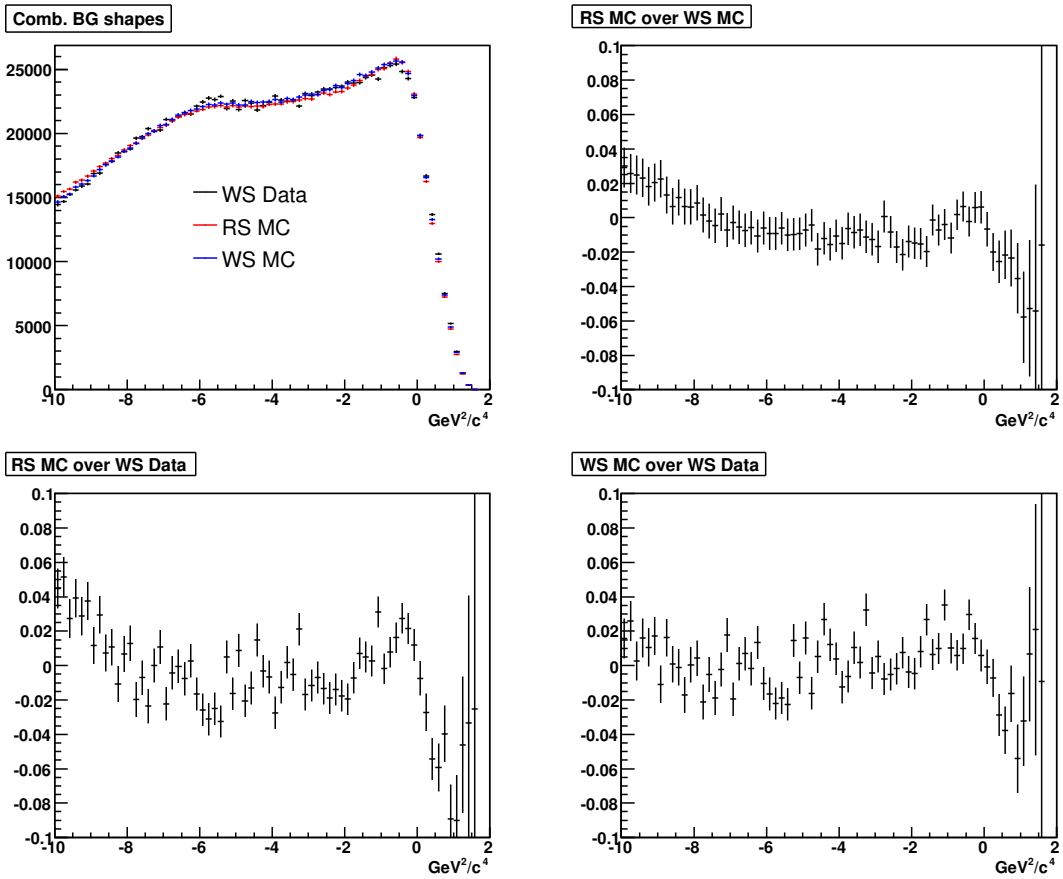

Figure 24: Combinatoric Background Comparisons: Top Row: (left) Superposition of Combinatoric Background shapes, (right) Difference of RS MC and WS MC comb. BG. Bottom: (left) Difference of RS MC and WS data comb. BG, (right) Difference of WS MC and WS data comb. BG.

4.3 Peaking Background

Peaking backgrounds are small topological backgrounds similar to the decay under study whose missing mass-squared primarily peaks in the signal region. The lepton momentum cut is used to limit the contribution of the majority of peaking background. Most contributions of the peaking background come from decays of the type $\bar{B} \to D^{*+} n(\pi) \ell^- \bar{\nu}_\ell$ through the channels $B^- \to D^{*+} n(\pi) \ell^- \bar{\nu}_\ell$ and $\bar{B}^0 \to D^{*+} n(\pi) \ell^- \bar{\nu}_\ell$ where the $D^* n(\pi)$ may or may not come from an orbitally excited charm resonance (D^{**}) [54]. The peaking background is small compared to the previously mentioned backgrounds. Other contributing decay channels include cascade decays such as $\bar{B}^0 \to D^{*+} \tau / X_c \, (\tau / X_c \to \ell^- X)$, in which a tau or charm state decays into a lepton and $\bar{B}^0 \to D^{*+} \pi^-$, with the π^- mis-identified as a lepton, which occurs about 1% of the time in the *BABAR* detector. Both neutral and charged B mesons contribute to this background. The peaking background shapes are obtained from *BABAR* Monte Carlo data and are expected to be small. It is the only background which cannot be measured directly. The lepton momenta of the peaking background are generally smaller causing the M_ν^2 distribution to be shifted slightly towards higher values. This shift relative to the signal peak allows for extraction of the peaking background through fitting methods.

The peaking background is the smallest of all backgrounds with a contamination of around 5% in the signal region. To address this uncertainty the peaking background is varied during the analysis. Details can be found in the section on systematic errors. Figure 25 shows histograms of the four major peaking background shapes for neutral B mesons from Monte Carlo. Charged contributions are shown in Figure 26. Resonant and non-resonant $D^{**}/D^*(n)\pi$ states are combined in this analysis. It can be seen that this mode is clearly dominating in the peaking background compilation. For this reason shape and scale adjustments will primarily be performed on this mode while other peaking background is considered sufficiently modeled by Monte Carlo and applied directly to the data set.

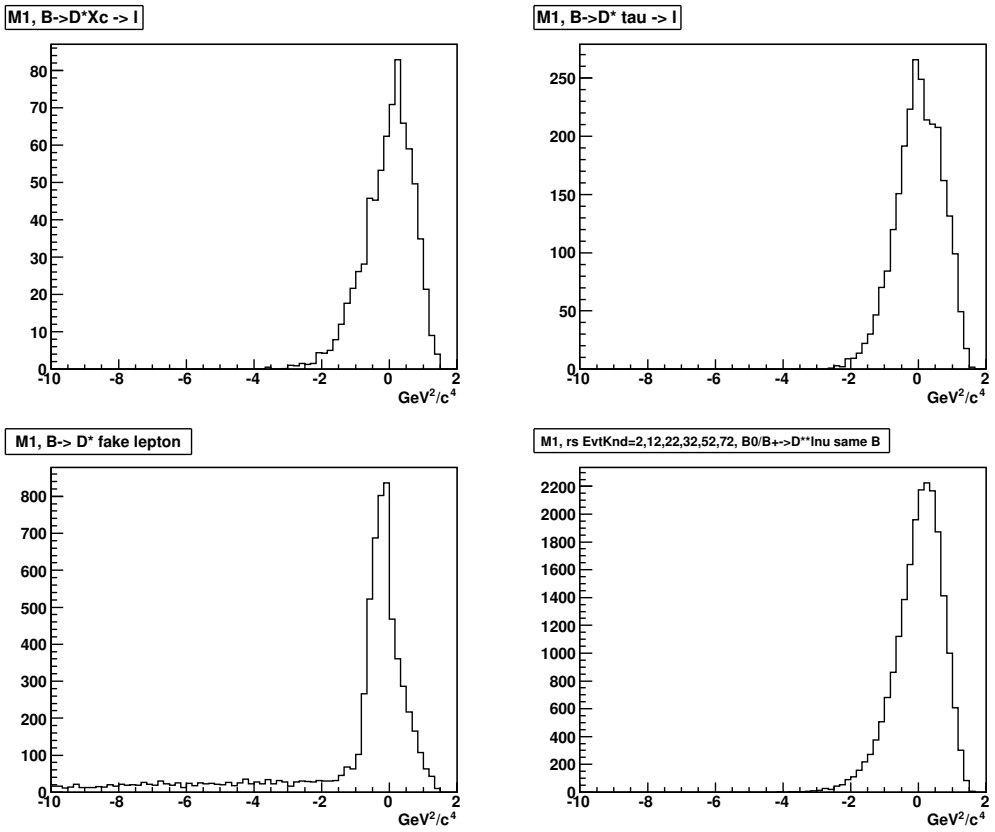

Figure 25: Peaking background shapes for neutral B mesons. Top: (left) Cascade decays originating from charm states, (right) Cascade decays originating from tau decays. Bottom: (left) Peaking background from mis-identified pions, (right) $D^{**}/D^{*}(n)\pi$ decays.

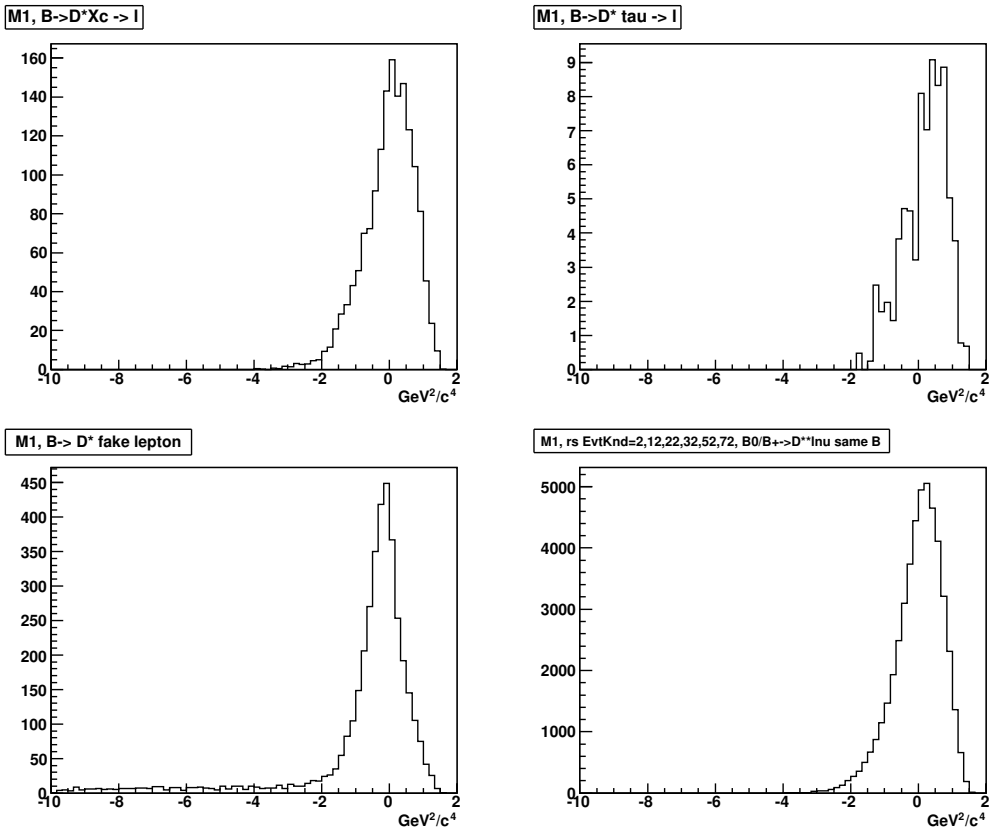

Figure 26: Peaking background shapes for charged B mesons. Top: (left) Cascade decays originating from charm states, (right) Cascade decays originating from tau decays. Bottom: (left) Peaking background from mis-identified pions, (right) $D^{**}/D^{*}(n)\pi$ decays.

4.4 Radiative Corrections

Radiative decays such as $\bar{B}^0 \to D^{*+}(n)\gamma\ell^-\bar{\nu}_\ell$ for the signal decay or $\bar{B}^0 \to D^{**}(n)\gamma\ell^-\bar{\nu}_\ell$ for peaking events are included as signal/background for their respective non-radiative event types. Radiative decays are modeled by $PHOTOS$ [55] in the Monte Carlo release SP8 used in this analysis. About 85% of these radiative photons are emitted at energies of 20 MeV or below and contribute to a small but significant distortion in the M_ν^2 mass distribution plot. Higher energetic events are rarer but contribute to higher distortions. To further study corrections due to radiative decays the photon energies and their multiplicities per event have been extracted from Monte Carlo data in the C.M. frame for both D^* and D^{**} events. Figure 27 shows the photon energies and their multiplicity distribution for signal D^* events (top row) and for D^{**} events originating from neutral B mesons (middle row) and charged B mesons (bottom row). It can be seen that multiple photon events are rare in all cases and that radiative corrections should be minor. Since signal and peaking backgrounds produce similar event shapes in the M_ν^2 mass distribution it is vital to study possible changes in this distribution due to corrections for the later extraction of the peaking background through fits (see section 5.3). Since the radiated photons are not considered in the M_ν^2 spectrum the resulting histogram will experience a shift towards higher values. Examining (68) one can estimate this shift:

$$M_\nu^2 = (E_{beam} - \tilde{E}_{D^*} - \tilde{E}_\ell)^2 - (\tilde{\vec{p}}_{D^*} + \tilde{\vec{p}}_\ell)^2 \tag{74}$$

where $\tilde{E}_{D^*}, \tilde{E}_\ell, \tilde{\vec{p}}_{D^*}$ and $\tilde{\vec{p}}_\ell$ are the actual measured quantities of the particles. Since the photon has been neglected in the calculation the result will be non zero. In order to estimate the shift ΔM_ν^2 we add an extra photon into the reconstruction of a regular signal decay:

$$-\Delta M_\nu^2 = (E_{beam} - E_{D^*} - E_\ell - E_\gamma)^2 - (\vec{p}_{D^*} + \vec{p}_\ell + \vec{p}_\gamma)^2$$
$$= (E^* - E_\gamma)^2 - (\vec{p^*} + \vec{p}_\gamma)^2 \quad (75)$$

where E^* and $\vec{p^*}$ are the summed energy and momentum of the event which ideally equal the neutrino values and reconstruct to a neutrino mass of zero. Assuming $E^* >> E_\gamma$ we can estimate ΔM_ν^2 to first order:

$$-\Delta M_\nu^2 = (E^*)^2 \left(1 - \frac{E_\gamma}{E^*}\right)^2 - (p^*)^2 \left(1 + \frac{p_\gamma cos(\theta)}{p^*}\right)^2$$
$$\Delta M_\nu^2 \leq 4 E^* E_\gamma \quad (76)$$

Here we have made the assumptions that $E^* = |\vec{p^*}|$ since they represent the neutrino and θ is the angle between the photon and the neutrino. Furthermore we find the average energies of the D^* mesons and the lepton from Monte Carlo to be about $\bar{E}_{D^*} = 2.4$ GeV and $\bar{E}_\ell = 1.9$ GeV. Since $E^* = E_{beam} - E_{D^*} - E_\ell$ we can estimate the average energy to be $E^* \approx 1.0$ GeV. Considering that 85% of the radiated photons possess an energy below 20 MeV the possible shift in the M_ν^2 will be less than 0.08 GeV^2/c^4 which corresponds to about 1/2 of a binning width in this histogram. To study this behavior signal candidates from non-radiative and radiative decays were accumulated in Monte Carlo, scaled to equal size and superimposed for comparison. The results are shown in Figure 28. (Non-) radiative signal decays are depicted in red (black). The shift towards higher values is clearly visible. The actual differences in means of both histograms is 0.069 GeV^2/c^4 which is below the maximum estimate. However, since the shift is visible it was included in the systematic error estimation (see section 7).

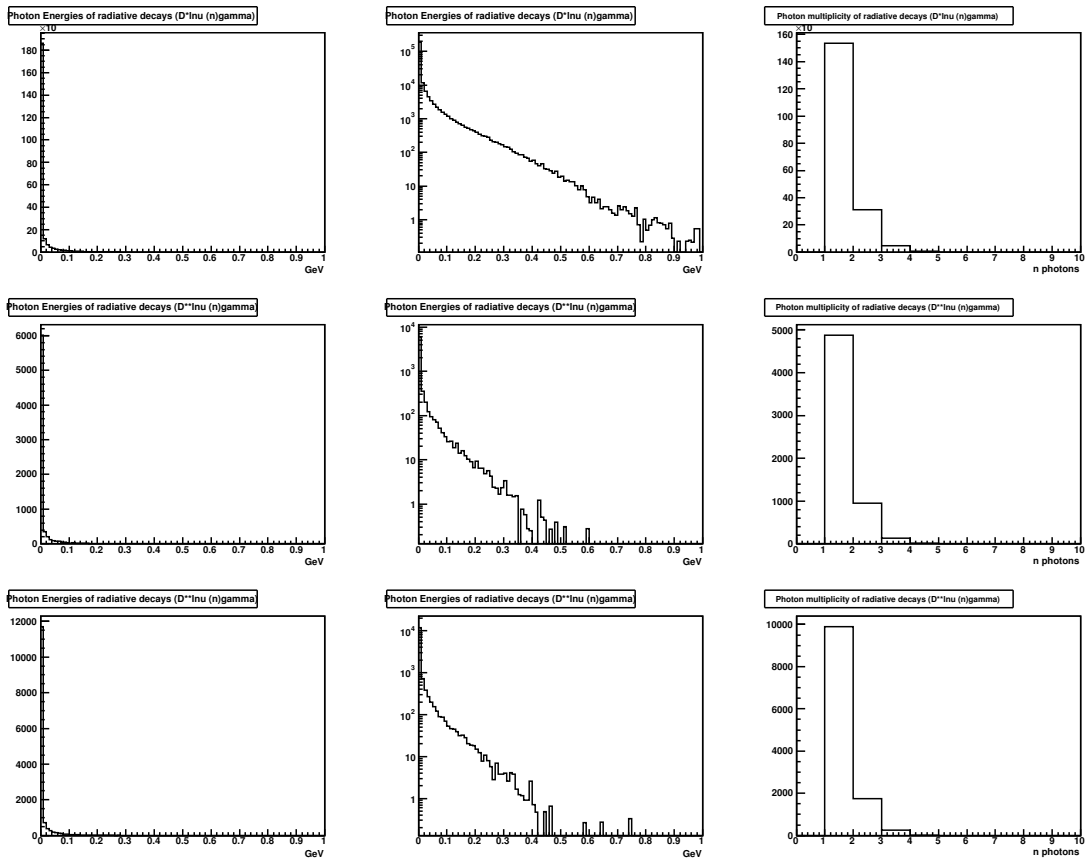

Figure 27: Photon energies and multiplicities for radiative D^* and D^{**} events: Left to right: Photon energies in C.M. frame, photon energies (log scale), photon multiplicities. Top to Bottom: D^* events, D^{**} events from neutral B mesons, D^{**} events from charged B mesons.

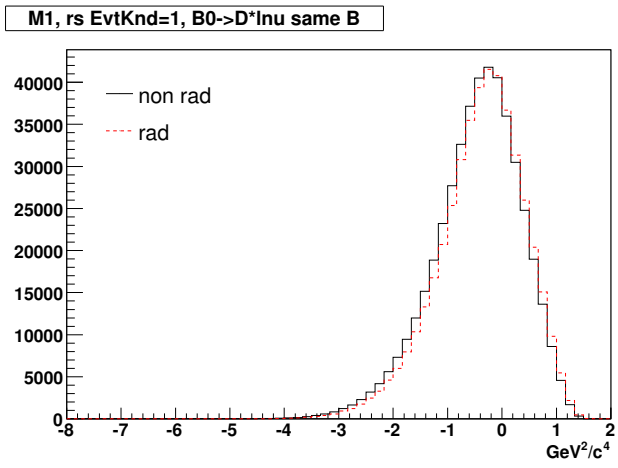

Figure 28: D^* signal shape for non-radiative events (black) and radiative events (red).

4.4.1 PHOTOS

The signal shape of the $\bar{B}^0 \to D^{*+}\ell^-\bar{\nu}_\ell$ decay can be slightly altered when accompanied by an additional photon. The emitted photon of these $\bar{B}^0 \to D^{*+}\gamma\ell^-\bar{\nu}_\ell$ decays is called bremsstrahlung. Bremsstrahlung is the emission of extra photons during a decay process. These photons are usually emitted with relatively low energies, but the presence of hard photons can influence the measured shape of a decay process. The effect of bremsstrahlung on this measurement will be discussed later in this dissertation. The emission of extra photons during decay processes in generic *BABAR* Monte Carlo are modeled by the PHOTOS package [55] in an attempt to model such alterations. PHOTOS, a universal package to simulate bremsstrahlung using QED considerations, was developed by E. Barberio *et al.* in 1990 and has been integrated into the *BABAR* Monte Carlo production. This paragraph is intended to give a brief overview of the functionality and limitations of PHOTOS presented in [55]

The QED based algorithm was developed to model bremsstrahlung present in production and decay as well as its effect on detector properties. The algorithm is process independent and models the decay of a mother particle into one main charged particle and a multitude of neutral or other charged particles where charged particles are required to be of low momentum. The charged particle is initially assumed to be of spin 1/2. Decay cross sections are calculated in the leading logarithmic approximation. The decays are modeled in phase space. Exact formulas of the decay phase space for this procedure can be found in [55]. Bremsstrahlung is generated by fragmenting the parent decay into a daughter mass and a photon, adjusting the four momenta to obey momentum-energy conservation. This fragmentation is governed by the spin and charge of the main charged particle of the decay only and independent of other processes. In case of multiple high momentum charged particles in the decay, the PHOTOS procedure is applied iteratively to the individual charged particles. The model to data agreement is improved in a final step through the application of weights to correct the distribution of low energetic photons and allow for variable spin values. Bremsstrahlung emission in the PHOTOS

package is performed through phase space considerations only. A systematic uncertainty study of this algorithm is also performed in [55]. Comparisons to previous simulations such as KORALZ [56] and MUSTRAL [57] are made in the paper and show good agreement. An estimate of maximum error is performed in channels of known uncertainty, such as the $\tau \to \pi\bar{\nu}$ decay, for which the algorithm could show deviations of up to 30% [55] in production rate. This error will be considered in the systematic studies of this analysis.

4.5 Event Type Distributions

During histogramming the Monte Carlo data events are identified as pertaining to categories such as signal or a specific type of background and distributed into their corresponding histograms for further study. The distribution is based on Pythia numbers of event kinds which split the data sample into its sub-categories which consist of the following. (1) Pure $\bar{B}^0 \to D^{*+}\ell^-\bar{\nu}_\ell$ signal decays, (2) $\bar{B}^0 \to D^{**+}/D^*(n)\pi\ell^-\bar{\nu}_\ell$ peaking background, (3) correlated $\bar{B}^0 \to D^{*+}\bar{X}_c(\to \ell^-)$ peaking background, (4) $\bar{B}^0 \to D^{*+}\tau^-\bar{\nu}_\tau$ peaking background, (5) fake lepton peaking background, events of leptonic decaying D mesons ($D^0 \to X\ell$) originating from B mesons (6) and $c\bar{c}$ (7) decays, (8) combinatoric events and (9) a rest class of unclassified events (ROE). In addition events which have been mis-associated as combinatorial background during the analysis are flagged by adding the integer 50 to their event numbers (+50) and recovered to their correct histograms. Events occurring from pions which decayed in flight are tagged through addition of 10 (+10) as well as events with radiative photons through addition of 20 (+20). A complete list of possible event numbers and their associations to the histograms of this analysis is shown in Table 8.

While mis-associated and in-flight decaying pion events are minor and together represent less than 0.8% of the total data sample they are included in the event shapes to allow for a precision measurement. Figure 29 also shows the distribution of event type numbers from Monte Carlo for neutral B decays in a regular and logarithmic scale. It can

be seen that the dominating modes are combinatoric events followed by $\bar{B}^0 \to D^{*+}\ell^-\bar{\nu}_\ell$ signal decays. The figure also shows that radiative decays constitute about 30% of the D^* and D^{**} decays. The minimum detection threshold of the electromagnetic calorimeter at *BABAR* is quoted in [39] to be above 10 MeV. Since about 80% of the photons in radiative decays fall beyond this threshold they will remain undetected and the decay will be classified as a non-radiative decay in real data. Therefore radiative decays are included in their respecting histograms in this analysis. Figure 30 shows the event type distributions for Monte Carlo from charged B mesons and resembles the previous figure closely except for the absence of signal decays.

Table 8: Event Type Classifications

Event	Event number
Signal	1, 11, 21, 31, 51, 71
$\bar{B}^0 \to D^{*+}\bar{X}_c(\to \ell^-)$	3, 13, 23, 33, 53, 73
$\bar{B}^0 \to D^{*+}\tau^-\bar{\nu}_\tau$	4, 54
fake lepton	5, 55
$\bar{B}^0 \to D^{**+}/D^*(n)\pi\ell^-\bar{\nu}_\ell$	2, 12, 22, 32, 52, 72
combinatoric events	6, 7, 8, 9

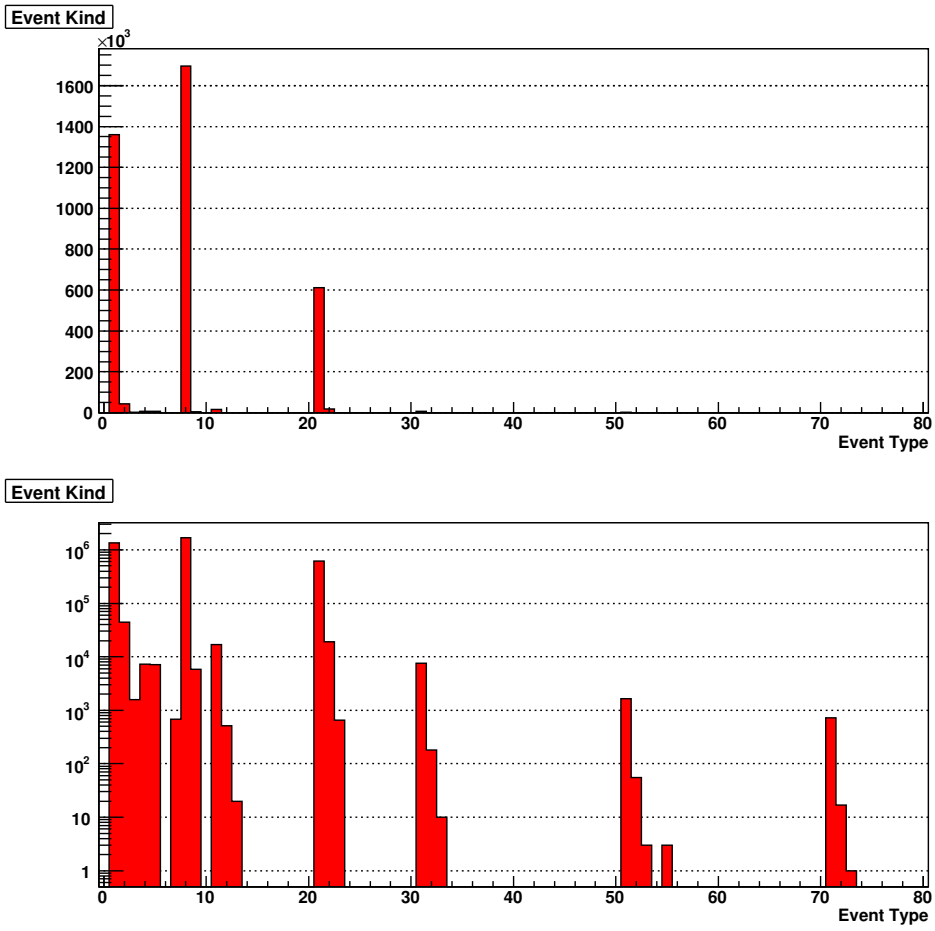

Figure 29: Event Type Distribution for neutral B mesons from Monte Carlo.

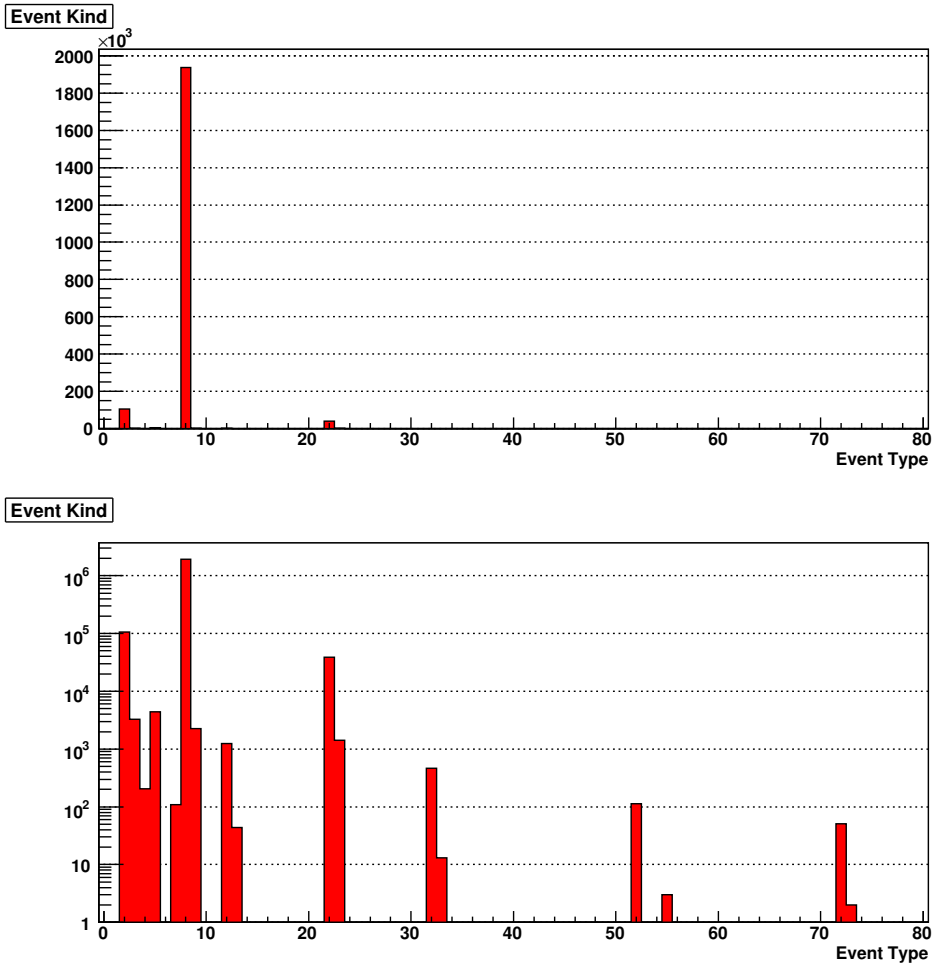

Figure 30: Event Type Distribution for charged B mesons from Monte Carlo

5 Branching Fraction Extraction

The challenge of this analysis lies in the proper determination of the signal yields after background subtraction. The signal to background ratio in the release 22 data set from the inclusive semi-leptonic skim used here is about 1 to 1. This constitutes a higher background contamination than other measurements based on full reconstruction. However a signal extraction of comparable quality is possible due to the large Monte Carlo control samples of about $190 fb^{-1}$ for charged and neutral generic B mesons respectively. The background behavior has been well studied before [50] [47] [58]. The branching fraction extraction in this analysis was performed according to (69) of section 3.6. All Monte Carlo control samples have been scaled to their appropriate luminosities and to fit the sideband region of the data, reweighted according to the newest form factor values and have been adjusted by the Monte Carlo tuning procedure (see section 6). The branching fraction determination was performed using three different extraction techniques based on subtraction and fitting methods. The small differences which arise from the different techniques were attributed to the systematic error. More emphasis is given to the fitting methods while the pure subtraction method was used as a cross check.

5.1 Raw Data and Monte Carlo

Before a branching fraction extraction was performed, the raw data was compared to raw Monte Carlo simulated data. A good up front agreement is essential for the success of a precision measurement. Since no off resonance Monte Carlo data has been created, the raw data was first continuum subtracted in the usual manner before a comparison was performed. The final Monte Carlo shape was composed of an equal amount of RS combinations of leptons and pions which is the equivalent to the data sample. No tagging into categories such as signal or peaking background was considered since only the overall raw agreement is of interest. The Monte Carlo data was not fit to the data. Figure 31 shows the superposition of Monte Carlo and data for Run 1 and Run 2, respectively,

together with the pull, the ratio of data over Monte Carlo. It can be seen that agreement is already very good before tuning methods are applied. Run 1 data shows a flat fluctuation of the pull data without noticeable bias. Run 2 data is also in very good agreement except for a slight underestimation of the Monte Carlo data in the signal region. Based on these observation, tuning effects are expected to be minor. The agreement provides a good basis for a precision measurement.

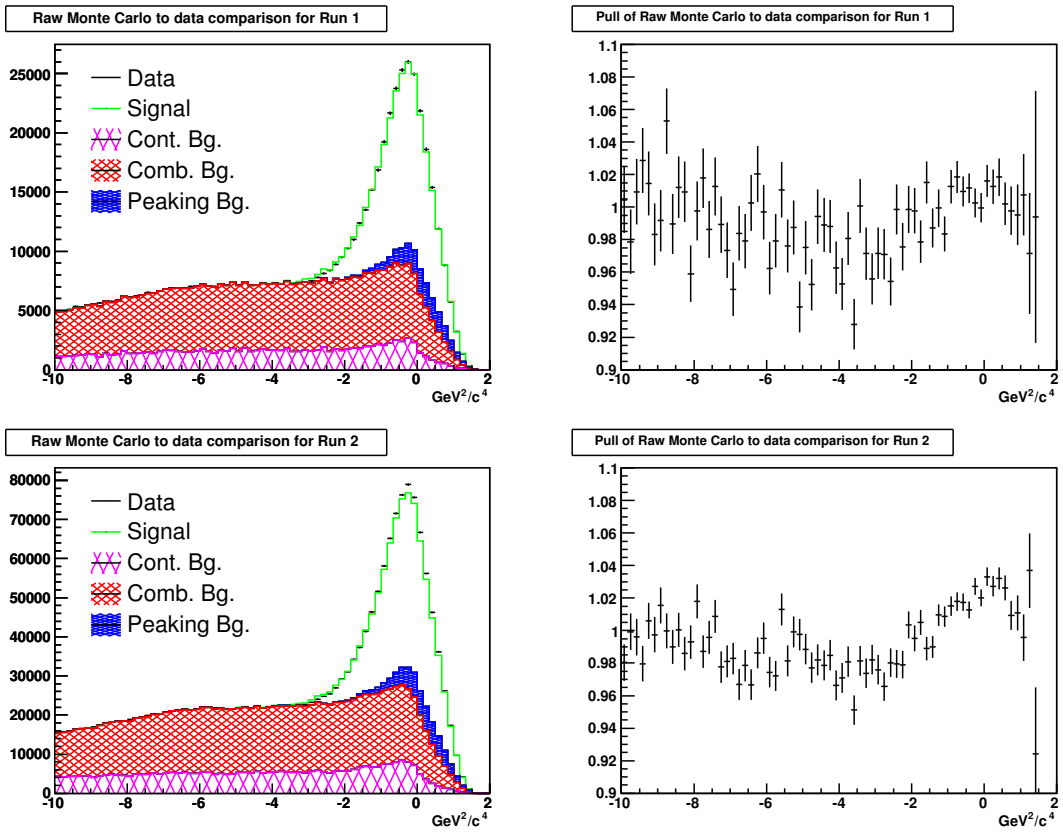

Figure 31: Comparison between raw data and raw Monte Carlo before adjusting and tuning techniques are applied. Top: Run 1 comparison of the histograms (left) and their pull values (right). Bottom: Run 2 comparison of the histograms (left) and their pull values (right).

5.2 Method 1 - Subtraction Method

The subtraction method provides a first look at the branching fraction measurement using solely the M_ν^2 distribution in one dimension and subtracting background histograms one at a time. The remaining data is considered the signal. The subtraction follows the

following scheme. The continuum background, which has been luminosity and energy weighted during histogramming, is directly subtracted from the raw data. The statistical bin error is properly propagated through scaling and subtraction.

The combinatoric background is then subtracted from the resulting data histogram in the following way. Since after continuum subtraction the sideband region is dominated by combinatoric background the RS MC combinatoric background is fit to the sideband region using a χ^2 binned fit and scaled to fit the sideband. It is then subtracted in the full region from the remaining M_ν^2 data distribution. The sideband fit is used to determine the proper amount of combinatoric background contamination in the signal region. Since three types of combinatoric backgrounds are available, RS MC, WS MC and WS data, the branching fraction determination is repeated with each background and the difference is used for a systematic error estimate.

The remaining data is now a combination of signal and peaking background. The peaking background is generated from the appropriate histograms from charged and neutral B Monte Carlo and added as described in section (4.3). No scaling or fitting is performed at this point. The peaking background is then directly subtracted from the data. Since peaking background contamination in the signal region is around 5% of the raw data this method is considered a good estimate of the branching fraction which is to be determined. However since the generation of the peaking background decays in Monte Carlo include large uncertainties on the branching fractions, the result is only considered an estimate and not a measurement.

The analysis is repeated for each run separately. Detailed results of this method using the RS MC combinatoric background sample together with summary plots for the other backgrounds are shown in Figures 32 and 33 for Run 1 and Run 2, respectively. It can be seen that after tuning and form factor reweigthing the combinatoric background fits well in the sideband with fit values for the χ^2/NDF of 1.06 and 1.23 for Runs 1 and 2. The signal yield in the sideband is zero within its error. Table 9 shows a summary of the yields for the signal and the specific backgrounds in the signal and sideband region.

Table 9: Signal and Background Yields for Method 1 RS MC

	Run 1		Run 2	
Type	Signal Region	Sideband Region	Signal Region	Sideband Region
Cont. BG	30821 ± 488	39454 ± 553	101515 ± 943	128176 ± 1059
Comb. BG RS MC	91122 ± 302	131098 ± 362	273344 ± 523	393746 ± 627
Peaking BG	20142 ± 142	146 ± 12	61939 ± 249	611 ± 24
Signal	165218 ± 811	-415 ± 779	494461 ± 1468	-941 ± 1428

Using the previously determined efficiencies the branching fraction was calculated from values of Table 9 using equation (69) for each run and then added according to their luminosities. Since this method is not considered a measurement, no further splitting into lepton type was performed. The results are given below where the error is the statistical error:

$$\begin{aligned} Run1 \quad \mathcal{B}(\bar{B}^0 \to D^{*+}\ell^-\bar{\nu}_\ell) &= (4.80 \pm 0.01)\% \\ Run2 \quad \mathcal{B}(\bar{B}^0 \to D^{*+}\ell^-\bar{\nu}_\ell) &= (4.91 \pm 0.01)\% \\ Run1\&2 \quad \mathcal{B}(\bar{B}^0 \to D^{*+}\ell^-\bar{\nu}_\ell) &= (4.88 \pm 0.01)\% \end{aligned}$$

The low statistical error which was achieved here reflects the advantages of partial reconstruction for this measurement. An interpretation of the result will be postponed to the actual measurements. The branching fractions together with the fit value determined by the other background types are summarized in Table 10. The different background yields for these backgrounds are summarized in Table 11

Table 10: Branching Fractions - Method 1

Run #	BG Type	$\mathcal{B}(\bar{B}^0 \to D^{*+}\ell^-\bar{\nu}_\ell)$	χ^2/NDF
Run 1	RS MC	$(4.80 \pm 0.01)\%$	1.06
	WS MC	$(4.80 \pm 0.01)\%$	1.10
	WS data	$(4.78 \pm 0.01)\%$	1.74
Run 2	RS MC	$(4.91 \pm 0.01)\%$	1.23
	WS MC	$(4.91 \pm 0.01)\%$	1.25
	WS data	$(4.95 \pm 0.01)\%$	1.95
Run 1+2	RS MC	$(4.88 \pm 0.01)\%$	
	WS MC	$(4.88 \pm 0.01)\%$	
	WS data	$(4.91 \pm 0.01)\%$	

Table 11: Signal and Comb. Background Yields for Method 1 WS MC and WS data

	Run 1		Run 2	
Type	Signal Region	Sideband Region	Signal Region	Sideband Region
Comb. BG WS MC	91077 ± 302	131158 ± 362	273740 ± 523	393813 ± 628
Signal WS MC	165264 ± 811	-475 ± 779	494066 ± 1468	-1007 ± 1428
Comb. BG WS data	91727 ± 503	131177 ± 617	269651 ± 951	393905 ± 1137
Signal WS MC	164613 ± 905	-493 ± 926	498155 ± 1669	-1100 ± 1714

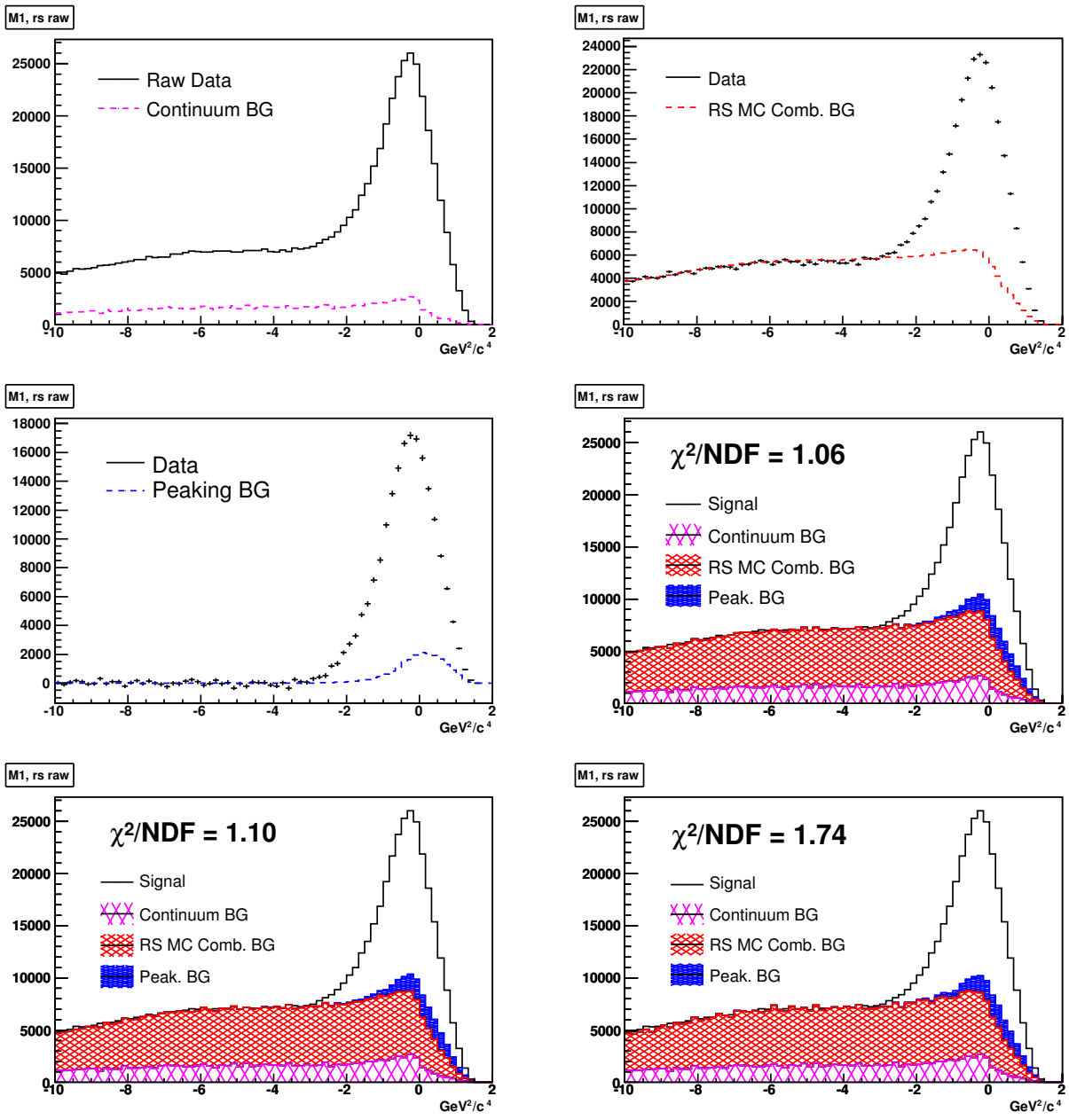

Figure 32: Signal extraction summary plots for method 1 for Run 1: Top: (left) Raw data (black) and continuum background after luminosity and energy scaling (magenta). (right) Continuum background subtracted data (black) with RS MC combinatoric background fit to the sideband (red). Middle: (left) Combinatoric background subtracted data now containing signal and peaking background (black) and MC peaking background (blue). (right) Data composition from continuum background (magenta), RS MC combinatoric background (red), MC peaking background (blue) and the data signal (black). Bottom: (left) Data composition from continuum background (magenta), WS MC combinatoric background (red), MC peaking background (blue) and the data signal (black). (left) Data composition from continuum background (magenta), WS data combinatoric background (red), MC peaking background (blue) and the data signal (black).

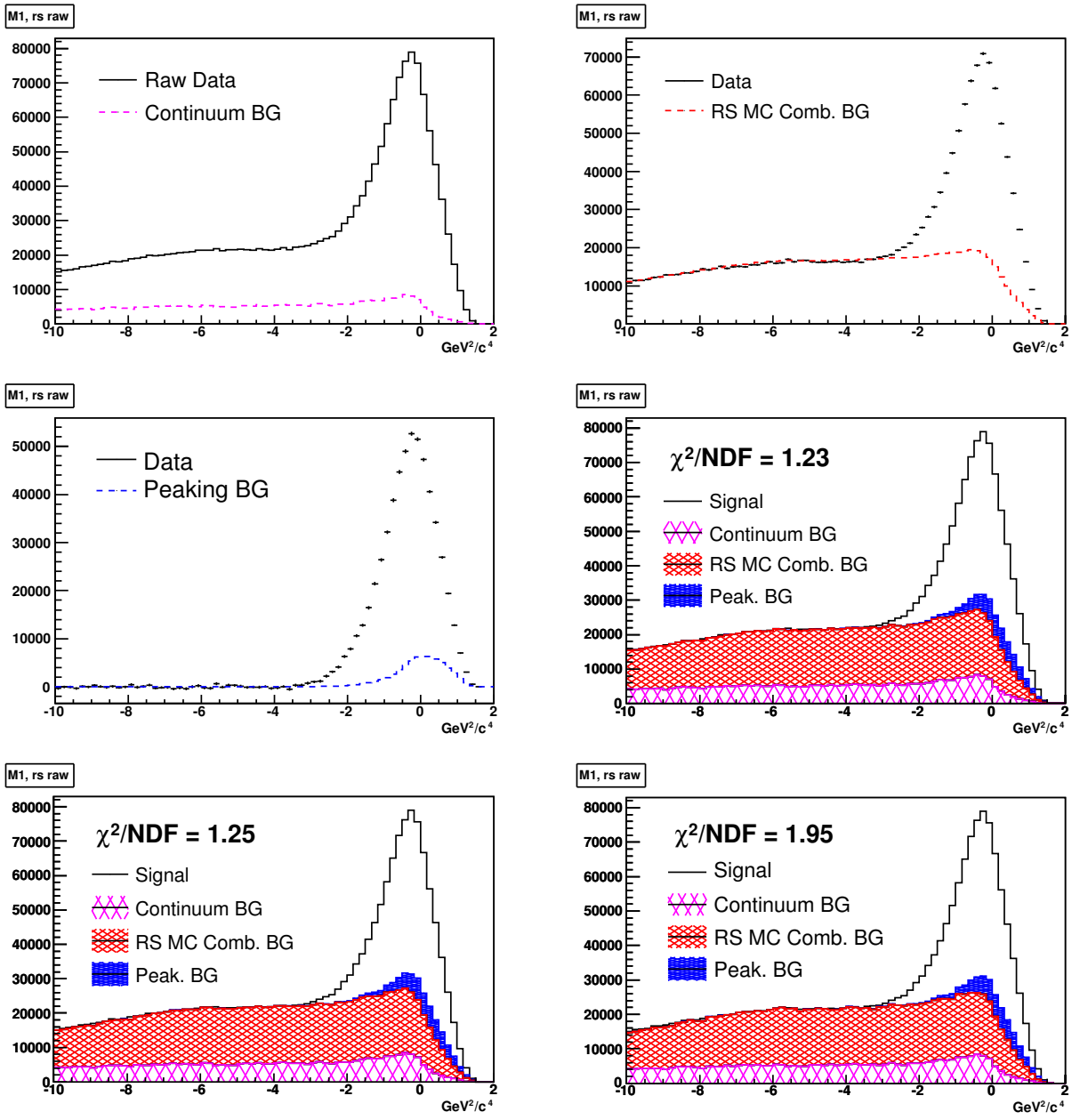

Figure 33: Signal extraction summary plots for method 1 for Run 2: Top: (left) Raw data (black) and continuum background after luminosity and energy scaling (magenta). (right) Continuum background subtracted data (black) with RS MC combinatoric background fit to the sideband (red). Middle: (left) Combinatoric background subtracted data now containing signal and peaking background (black) and MC peaking background (blue). (right) Data composition from continuum background (magenta), RS MC combinatoric background (red), MC peaking background (blue) and the data signal (black). Bottom: (left) Data composition from continuum background (magenta), WS MC combinatoric background (red), MC peaking background (blue) and the data signal (black). (left) Data composition from continuum background (magenta), WS data combinatoric background (red), MC peaking background (blue) and the data signal (black).

5.3 Method 2 - 1D Fitting Method

The previous calculation was based on the peaking background yields actually predicted by Monte Carlo. To desensitize the analysis to these predictions the signal is determined in an overall fit in which the background yields are left floating. A fit technique using probability density functions (PDF) obtained from the corresponding histograms for signal, peaking background and combinatoric background is employed. Since the continuum background is obtained from off-resonance data scaled to the energies and luminosity of the on resonance data, it is still subtracted in this technique from the raw data. The resulting histogram includes the signal together with combinatoric and peaking background with floating yields. The peaking background is composed of the same histograms as before and the combinatoric background is taken from one of the three choices (RS or WS Monte Carlo or WS data). Instead of subtracting the backgrounds individually, a fit is employed to extract the yields of combinatoric background, peaking background and signal in the data sample according to (77).

$$F = N_{sig}H_{sig} + N_{comb}H_{comb} + N_{peak}H_{peak} \tag{77}$$

The range of the fit is extended over the full region of interest (-8.0 GeV^2/c^4 $\leq M_\nu^2 \leq$ 2.0 GeV^2/c^4) and therefore includes both the signal and sideband region. Fitting is performed by the ROOFIT toolkit for data modeling [59] using a maximum likelihood technique. The fact that all shapes, background and signal, are fit simultaneously makes this method independent of prior assumptions of distributions in the sideband and signal regions. Signal leakage into the sideband region will automatically be considered. However due to the higher complexity of the fit, we may expect slightly larger fit errors. It should be noted that the D^{**}, here symbolic for both resonant and non-resonant decays, constitute about 85% of the peaking background. It is also the contribution that clearly separates itself from the signal in the neutrino mass spectrum by a shift of about 0.5 GeV^2/c^4 towards higher values. Therefore, the fit allows only the D^{**} yield to float while keeping the rest of the peaking background constant to the values predicted by the

Monte Carlo simulation.

The final fit function is then a combination of histograms. To access a value for the goodness of the fit, the resulting histogram is compared with data by the Pearson's chi-squared test. Since both data and fit histogram have associated bin errors, they both need to be considered in the goodness of fit determination. This is done according to (78):

$$\chi^2 = \sum_i \frac{(d_i - f_i)^2}{\sigma_{d_i}^2 + \sigma_{f_i}^2} \tag{78}$$

Here i is the bin number of the histogram, d_i is the i^{th} bin of the data histogram, f_i is the i^{th} bin of the fit histogram, σ_{d_i} is the i^{th} bin error of the data histogram and σ_{f_i} is the i^{th} bin error of the fit histogram.

Signal extraction was performed separately for each run and for each combinatoric background for systematic error studies. To cross check the validity of the result the fit was repeated separately with samples split into electron only and muon only contributions of data. The results are shown in the following figures. The goodness of fit is quoted as the χ^2/NDF where NDF stands for the number of degrees of freedom which were determined as the number of bins of the histogram minus the limiting degrees of freedom defined as the number of fit parameters plus one (par + 1). Figures 34 and 35 show the fit histogram (green) separated into its contributions from continuum background, RS MC combinatoric background, peaking background and signal superimposed onto the raw data. It can be seen that through the reweighting and tuning procedures applied on the Monte Carlo a good agreement between the fit and the data could be reached. The χ^2/NDF values all indicate good agreement. The pulls are somewhat noisy for Run 1 also do to the lower statistics, but do not show a significant slope. They are all reasonably flat in the signal region for which the signal extraction is performed. Figures 36 and 37 as well as Figures 38 and 39 show the same plots for the case of WS MC combinatoric background and WS data combinatoric background respectively.

The resulting signal and background yields for the different background types for

both signal and sideband region are shown in Tables 12 through 14 for both leptons, electrons only and muons only respectively. The quoted errors include statistical and fit errors. Tables 15 through 17 show a summary of the resulting branching fractions from these yields. The difference between the determined branching fractions due to different combinatoric backgrounds will be considered as a systematic error due to these background shapes. This is explained in the section of systematic errors.

The signal extraction error, which is reported by the fit, can be separated into a statistical error and a systematic fit error ($\sigma_{fit}^2 = \sigma_{stat}^2 + \sigma_{syst}^2$). These errors are considered in the signal region since this is the only region which contributes to the branching fraction result. For statistical consideration the counting error σ_{data} on the raw data (before continuum subtraction), as seen in Figure 21 in the signal region, is combined in quadrature with the error on the continuum background σ_{cont} to obtain the full statistical error on the continuum subtracted data ($\sigma_D^2 = \sigma_{data}^2 + \sigma_{cont}^2$). The signal portion of σ_D is found by taking the signal fraction, $f_{sig} = N_{sig}/(N_{sig} + N_{comb} + N_{peak})$, of σ_D:

$$\sigma_{stat} = \sqrt{f_{sig}}\ \sigma_D \tag{79}$$

The systematic fit error is described in section 7.6 on systematic errors.

Table 12: Signal and Background Yields for Method 2 - Both Leptons

	Run 1		Run 2	
Type	Sideband Region	Signal Region	Sideband Region	Signal Region
Cont. BG	39454 ± 553	30821 ± 488	128176 ± 1059	101515 ± 943
Comb. BG RS MC	124534 ± 353	90326 ± 301	374152 ± 612	271036 ± 521
Peaking BG	145 ± 12	20359 ± 881	609 ± 25	63145 ± 1545
Signal RS MC	70 ± 8	165630 ± 1083	219 ± 15	495655 ± 1893
Comb. BG WS MC	124269 ± 353	90105 ± 300	373488 ± 611	270935 ± 521
Peaking BG	145 ± 12	19503 ± 882	609 ± 25	60495 ± 1546
Signal WS MC	71 ± 8	166755 ± 1082	220 ± 15	498499 ± 1892
Comb. BG WS data	124091 ± 352	90637 ± 301	374071 ± 612	267379 ± 517
Peaking BG	145 ± 12	18027 ± 884	608 ± 25	53399 ± 1539
Signal WS data	71 ± 8	167909 ± 1083	225 ± 15	508782 ± 1883

Table 13: Signal and Background Yields for Method 2 - Electrons Only

	Run 1		Run 2	
Type	Sideband Region	Signal Region	Sideband Region	Signal Region
Cont. BG	20455 ± 398	15267 ± 344	59679 ± 723	47036 ± 642
Comb. BG RS MC	70017 ± 265	51102 ± 226	208602 ± 457	151659 ± 389
Peaking BG	40 ± 6	10860 ± 690	177 ± 13	32302 ± 1189
Signal RS MC	36 ± 6	96640 ± 843	122 ± 11	287246 ± 1453
Comb. BG WS MC	69905 ± 264	51047 ± 226	208101 ± 456	152397 ± 390
Peaking BG	40 ± 6	10164 ± 691	177 ± 13	30776 ± 1190
Signal WS MC	36 ± 6	97414 ± 843	122 ± 11	288032 ± 1453
Comb. BG WS data	69841 ± 264	51365 ± 227	209116 ± 457	150112 ± 387
Peaking BG	40 ± 6	9270 ± 692	176 ± 13	27071 ± 1184
Signal WS data	37 ± 6	98084 ± 843	124 ± 11	293963 ± 1447

Table 14: Signal and Background Yields for Method 2 - Muons Only

	Run 1		Run 2	
Type	Sideband Region	Signal Region	Sideband Region	Signal Region
Cont. BG	18999 ± 384	15554 ± 347	68496 ± 774	54479 ± 691
Comb. BG RS MC	54510 ± 233	39220 ± 198	165563 ± 407	119390 ± 346
Peaking BG	105 ± 10	9530 ± 544	432 ± 21	31154 ± 982
Signal RS MC	34 ± 6	69045 ± 676	95 ± 10	208092 ± 1206
Comb. BG WS MC	54378 ± 233	39222 ± 198	165358 ± 407	119075 ± 345
Peaking BG	105 ± 10	9307 ± 545	432 ± 21	30017 ± 983
Signal WS MC	35 ± 6	69292 ± 677	96 ± 10	209629 ± 1205
Comb. BG WS data	54259 ± 233	39270 ± 198	164962 ± 406	117280 ± 342
Peaking BG	105 ± 10	8776 ± 548	432 ± 21	26716 ± 979
Signal WS data	35 ± 6	69906 ± 678	98 ± 10	214431 ± 1199

Table 15: Branching Fractions Method 2 - Both Leptons

Run #	BG Type	$\mathcal{B}(\bar{B}^0 \to D^{*+}\ell^-\bar{\nu}_\ell)$	χ^2/NDF	CL (%)
Run 1	RS MC	$(4.81 \pm 0.01)\%$	0.82	83
	WS MC	$(4.84 \pm 0.01)\%$	0.97	54
	WS data	$(4.88 \pm 0.01)\%$	0.98	52
Run 2	RS MC	$(4.92 \pm 0.01)\%$	0.97	53
	WS MC	$(4.95 \pm 0.01)\%$	1.23	11
	WS data	$(5.05 \pm 0.01)\%$	0.93	63
Run 1+2	RS MC	$(4.89 \pm 0.01)\%$		
	WS MC	$(4.92 \pm 0.01)\%$		
	WS data	$(5.01 \pm 0.01)\%$		

Table 16: Branching Fractions Method 2 - Electrons Only

Run #	BG Type	$\mathcal{B}(\bar{B}^0 \to D^{*+}\ell^-\bar{\nu}_\ell)$	χ^2/NDF	CL (%)
Run 1	RS MC	$(4.83 \pm 0.02)\%$	0.80	86
	WS MC	$(4.87 \pm 0.02)\%$	0.96	56
	WS data	$(4.90 \pm 0.02)\%$	0.92	65
Run 2	RS MC	$(4.92 \pm 0.01)\%$	1.11	26
	WS MC	$(4.93 \pm 0.01)\%$	1.22	12
	WS data	$(5.04 \pm 0.01)\%$	1.00	47
Run 1+2	RS MC	$(4.90 \pm 0.01)\%$		
	WS MC	$(4.92 \pm 0.01)\%$		
	WS data	$(5.00 \pm 0.01)\%$		

Table 17: Branching Fractions Method 2 - Muons Only

Run #	BG Type	$\mathcal{B}(\bar{B}^0 \to D^{*+}\ell^-\bar{\nu}_\ell)$	χ^2/NDF	CL (%)
Run 1	RS MC	$(4.78 \pm 0.02)\%$	0.87	75
	WS MC	$(4.80 \pm 0.02)\%$	0.98	51
	WS data	$(4.84 \pm 0.02)\%$	1.02	44
Run 2	RS MC	$(4.92 \pm 0.01)\%$	1.00	48
	WS MC	$(4.95 \pm 0.01)\%$	1.02	42
	WS data	$(5.07 \pm 0.01)\%$	0.90	68
Run 1+2	RS MC	$(4.88 \pm 0.01)\%$		
	WS MC	$(4.92 \pm 0.01)\%$		
	WS data	$(5.01 \pm 0.01)\%$		

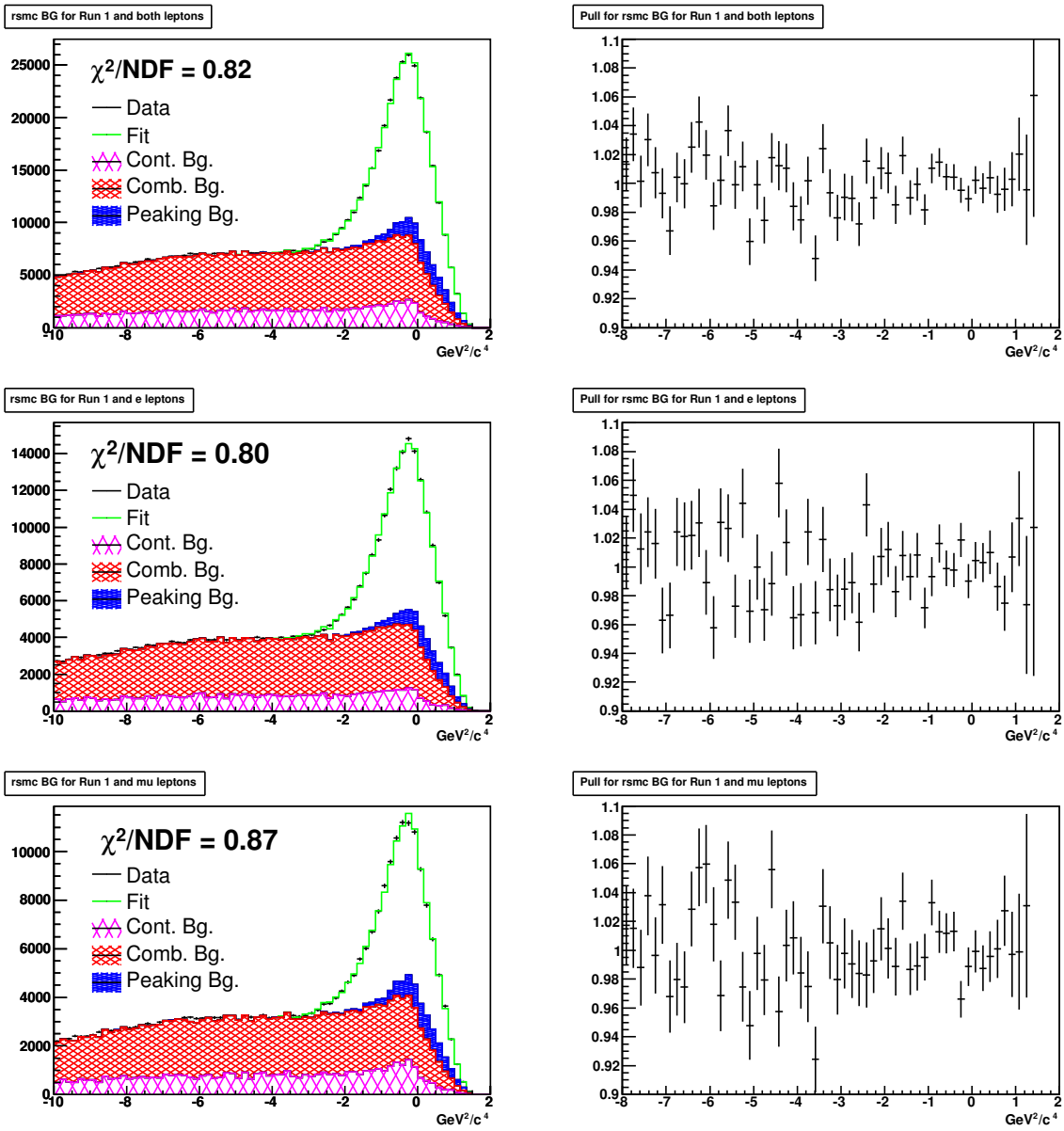

Figure 34: Fit Results for RS MC signal extraction for Run 1. Left Column (top to bottom): M_ν^2 distributions for the fit and raw data for both lepton types, electrons only and muons only. The fit is sectioned into its contributions from continuum background (magenta), combinatoric background (red), peaking background (blue) and signal (green). Right Column (top to bottom): Pull of data to fit for both leptons, electrons only and muons only.

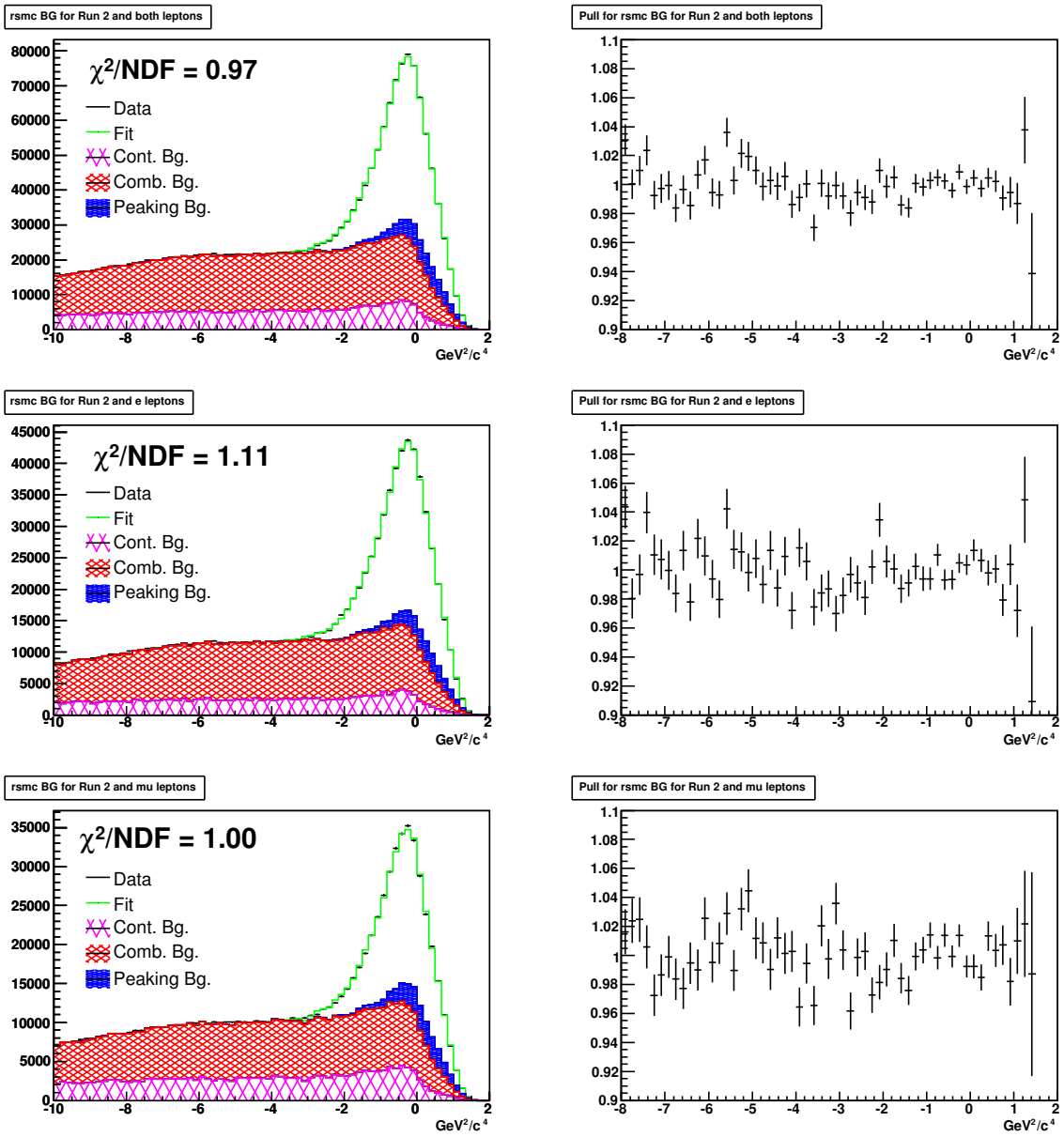

Figure 35: Fit Results for RS MC signal extraction for Run 2. Left Column (top to bottom): M_ν^2 distributions for the fit and raw data for both lepton types, electrons only and muons only. The fit is sectioned into its contributions from continuum background (magenta), combinatoric background (red), peaking background (blue) and signal (green). Right Column (top to bottom): Pull of data to fit for both leptons, electrons only and muons only.

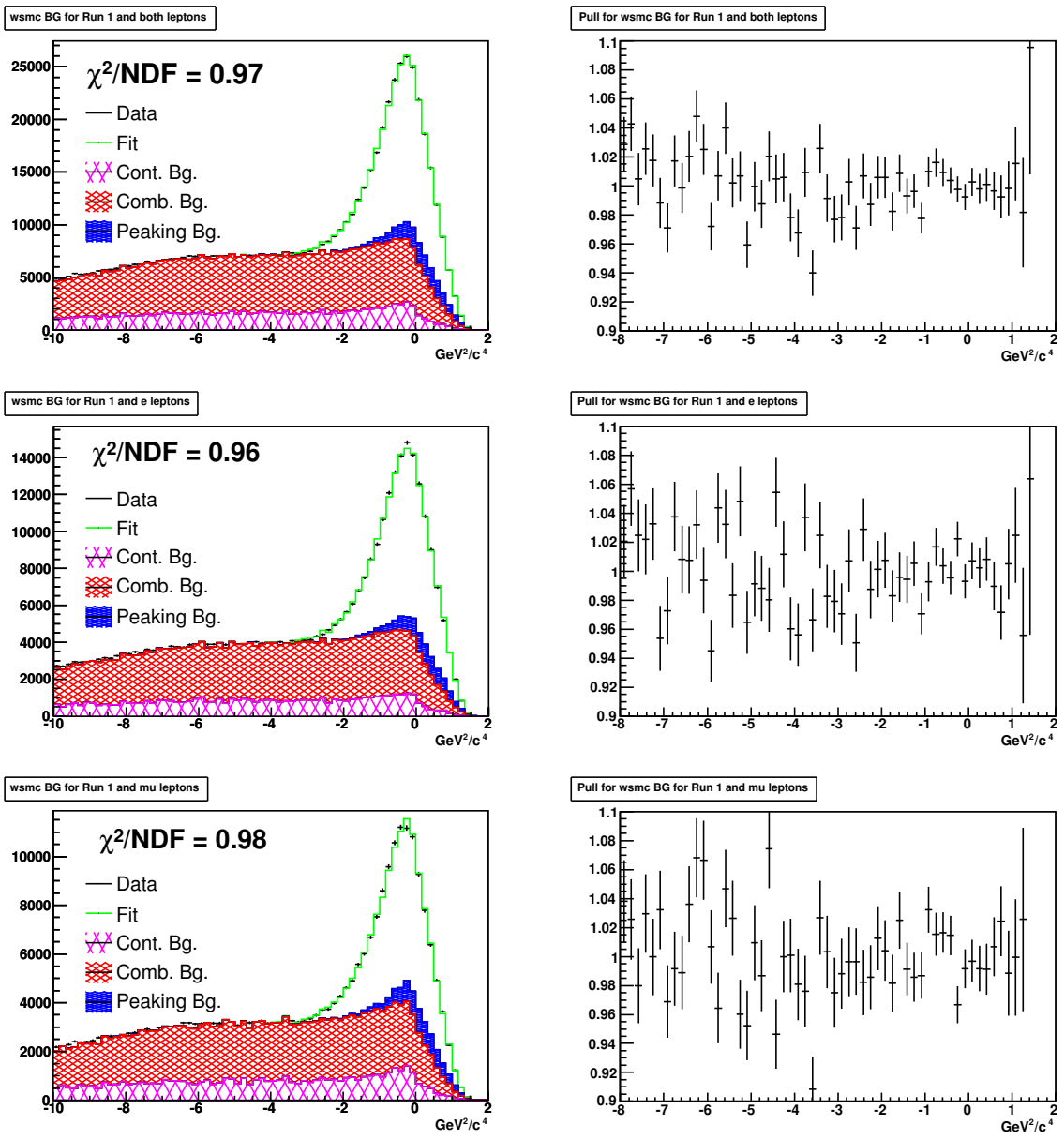

Figure 36: Fit Results for WS MC signal extraction for Run 1. Left Column (top to bottom): M_ν^2 distributions for the fit and raw data for both lepton types, electrons only and muons only. The fit is sectioned into its contributions from continuum background (magenta), combinatoric background (red), peaking background (blue) and signal (green). Right Column (top to bottom): Pull of data to fit for both leptons, electrons only and muons only.

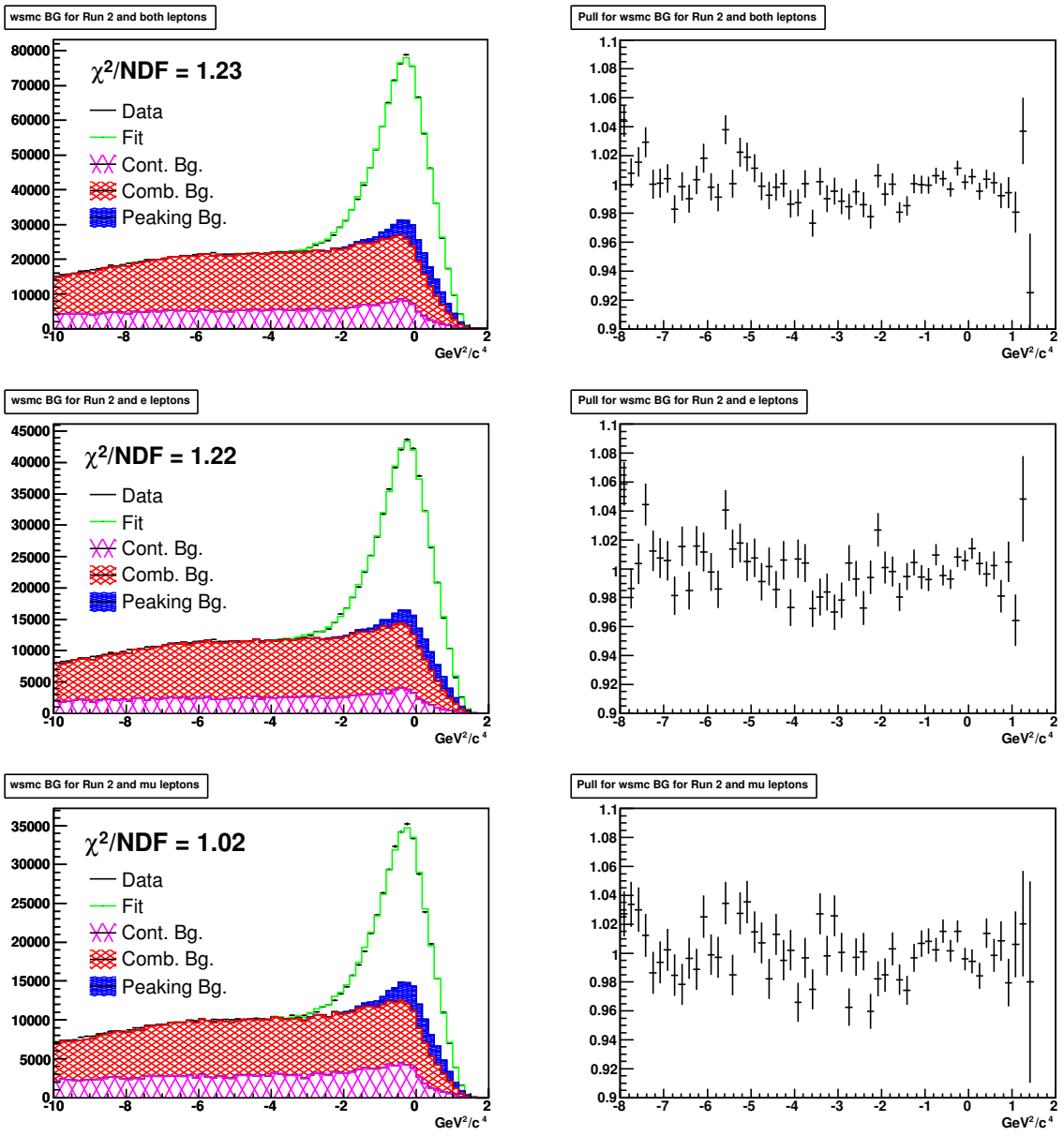

Figure 37: Fit Results for WS MC signal extraction for Run 2. Left Column (top to bottom): M_ν^2 distributions for the fit and raw data for both lepton types, electrons only and muons only. The fit is sectioned into its contributions from continuum background (magenta), combinatoric background (red), peaking background (blue) and signal (green). Right Column (top to bottom): Pull of data to fit for both leptons, electrons only and muons only.

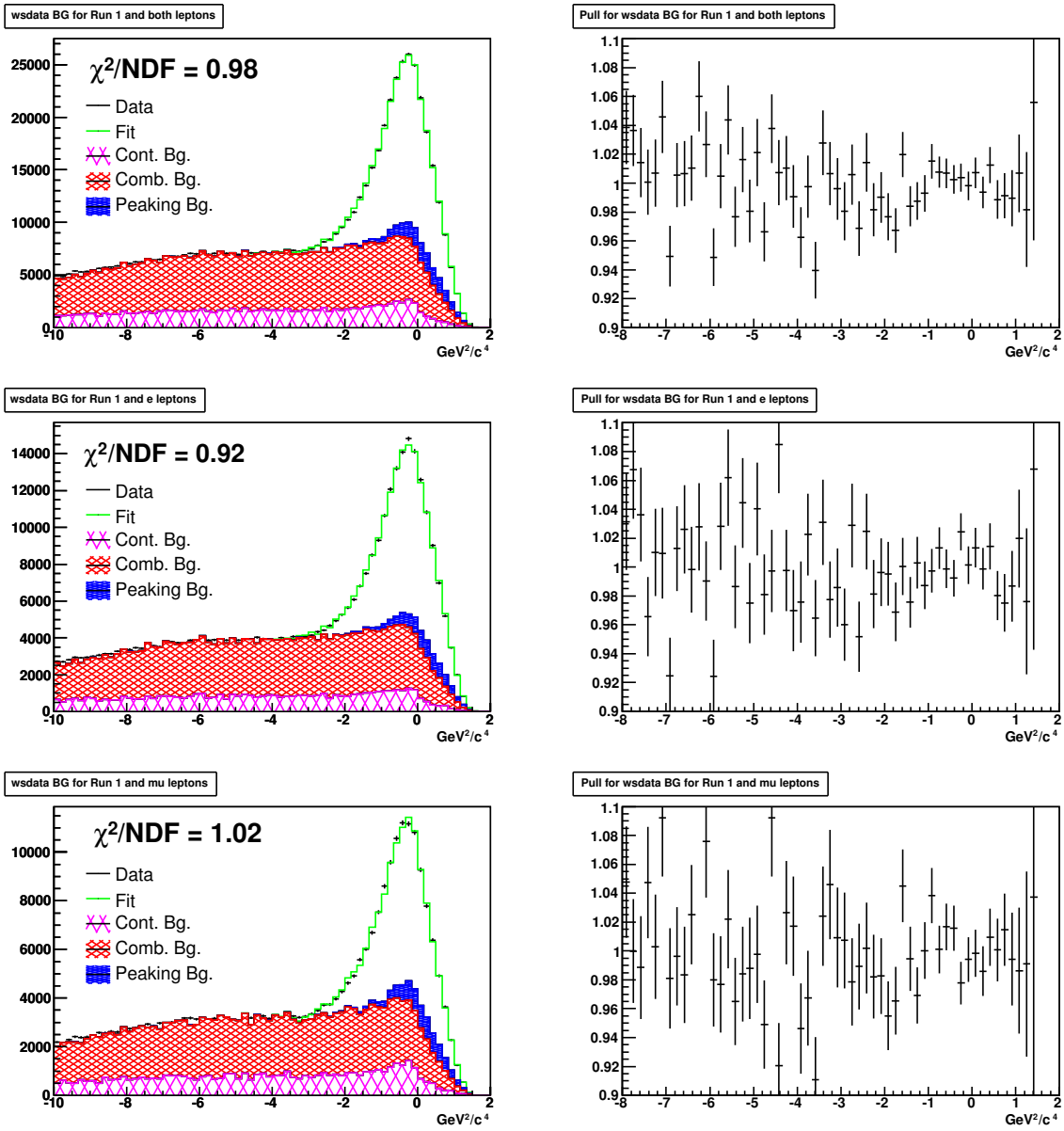

Figure 38: Fit Results for WS data signal extraction for Run 1. Left Column (top to bottom): M_ν^2 distributions for the fit and raw data for both lepton types, electrons only and muons only. The fit is sectioned into its contributions from continuum background (magenta), combinatoric background (red), peaking background (blue) and signal (green). Right Column (top to bottom): Pull of data to fit for both leptons, electrons only and muons only.

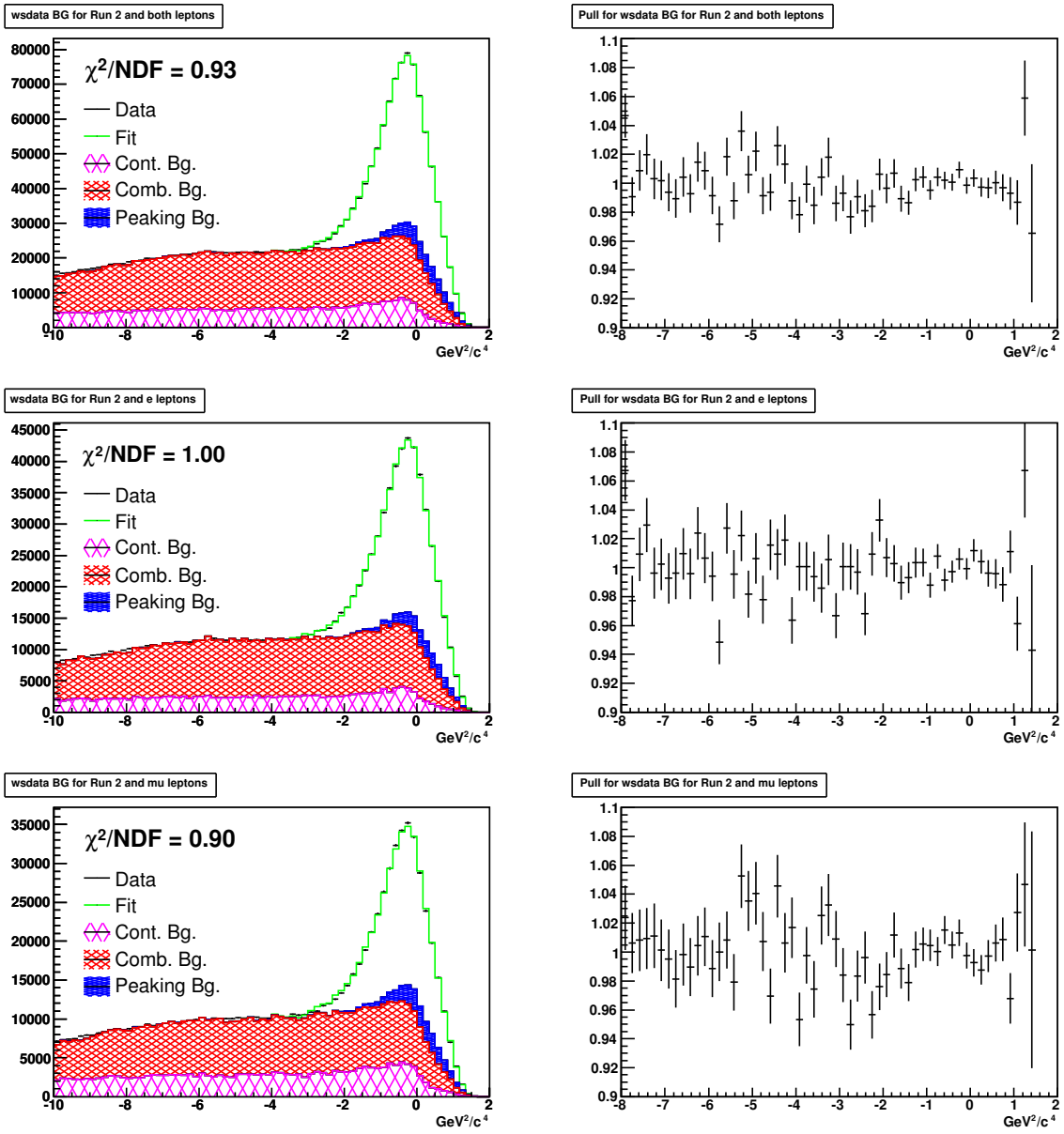

Figure 39: Fit Results for WS data signal extraction for Run 2. Left Column (top to bottom): M_ν^2 distributions for the fit and raw data for both lepton types, electrons only and muons only. The fit is sectioned into its contributions from continuum background (magenta), combinatoric background (red), peaking background (blue) and signal (green). Right Column (top to bottom): Pull of data to fit for both leptons, electrons only and muons only.

5.4 Method 3 - 2D Fit Method

The 2D fitting method is an extension of the previous one dimensional fit to M_ν^2 in an attempt to achieve better separation between peaking background and the signal. As shown in section 6.5, a similar separation between these types of data as seen in the M_ν^2 spectrum is also observed in their lepton momenta. For this reason two dimensional histograms with a combination of the M_ν^2 spectrum and the lepton momentum are accumulated for the data, the signal and the different types of background as was used in the one dimensional case. The two dimensional histogram consists of ten equally spaced momentum bins on the x-axis which hold the lepton momentum in the range of 1.5 GeV/c $\leq p_\ell \leq$ 2.5 GeV/c and 72 equally spaced bins on the y-axis which hold the corresponding neutrino mass in the full range of -10 GeV^2/c^4 $\leq M_\nu^2 \leq$ 2 GeV^2/c^4. The Monte Carlo pion and lepton momentum spectra have already been adjusted in the Monte Carlo tuning section to more closely mimic data. However tuning was performed on a combined sample of all data present in the signal region. Initially a further separation was considered to allow for fine tuning of the lepton momentum spectrum during the fitting and yield extractions. The lepton momenta of the signal, the combinatoric background and the D^{**} contribution to the peaking background are adjusted by a linear relation during fitting. Its slope is determined during the fit according to the event weight:

$$w_{\ell,j}(p_\ell) = a_{\ell,j} \times (1 + b_{\ell,j} \times (p_\ell - 1.85 \text{ GeV/c})) \tag{80}$$

were j is either the Monte Carlo signal, the combinatoric background or D^{**} events. The midpoint of 1.85 GeV/c for the linear fit is extracted experimentally. The parameter $a_{\ell,j}$ therefore determines the scale or yield of the histogram shape and the parameter $b_{\ell,j}$ can be considered a normalized slope of its skew. All weight functions are evaluated at their bin center. The data was analyzed using this technique, but results have shown that this method does not show improvement over the regular Monte Carlo tuning technique. Table 18 shows the slope parameters of the above relation for Run 1 data and RS MC combinatoric background applied to both leptons and their separations. One can see

that the slope parameters are zero within error thus the weight functions are basically flat suggesting that further reshaping is not needed. Table 19 shows the signal and background yields for these fits. Compared to the previous method, one can see that the errors introduced from the reshaping option are larger, thus overshadowing the advantage of further separation in the lepton momenta of signal and peaking background. Since reshaping does not seem necessary it is no longer considered and yield extraction is performed similarly to method 2 but in two dimensions.

A combination of Monte Carlo data is composed to mimic the shape of data. The signal extraction is then obtained from a two dimensional maximum likelihood fit. The continuum background obtained from the off resonance run, scaled to luminosity and energy difference, is first subtracted from the raw data as before. The combined Monte Carlo histogram is composed of the sum of the the signal, combinatoric background and, the D^{**} contributions. Again, all peaking background shapes, except the D^{**} simulated events, are considered to be accurate to the order needed for this analysis and are added into the shape after luminosity adjustment.

During fitting the three floating parameters are determined in a maximum likelihood minimization fit of the accumulated Monte Carlo shape to the data using the ROOT [60] data analysis framework according to:

$$F = N_{sig}H_{sig} + N_{comb}H_{comb} + N_{peak}H_{peak} \tag{81}$$

The fit is performed for the combined sample of electrons and muons for Run 1 and 2 separately as well as on a lepton separated sample for cross check. For better comparison the two dimensional fit is then projected onto the neutrino mass axis effectively reproducing the one dimensional histograms used in the previous discussion. Figure 40 shows the two dimensional fit shapes for Run 1 and Run 2 and both leptons to the data. Figures 41 through 46 show the one dimensional projection of the two dimensional fits onto the neutrino axis as well as their pull plots for Run 1 and Run 2 separately. Fitting is repeated for the three types of combinatoric background. The resulting signal and back-

ground yields for the different background types for both signal and sideband region are shown in Tables 20 through 22 for both leptons, electrons only and muons only respectively. The quoted errors include statistical and fit errors. Tables 23 through 25 show a summary of the resulting branching fractions from these yields. The difference between the determined branching fractions due to different combinatoric backgrounds will be considered as a systematic error due to these background shapes. This is explained in the section of systematic errors.

Table 18: Linear shape parameters for RS MC of Run 1

BG type	lep type	b_{sig}	$b_{D^{**}}$	b_{comb}
RS MC	e + μ	-0.0260 ± 0.0627	-1.0507 ± 0.7049	-0.0423 ± 0.0346
RS MC	e	0.0895 ± 0.0844	-1.3232 ± 0.9215	-0.0404 ± 0.0443
RS MC	μ	-0.1455 ± 0.0950	-1.1146 ± 1.1253	0.0100 ± 0.0539

Table 19: Signal and Background Yields for Method 3 - Run 1 RS MC with shaping

	Run 1	
Type	Sideband Region	Signal Region
Comb. e + μ	130270 ± 652	90637 ± 453
Peaking e +μ	147 ± 12	17127 ± 2018
Signal e + μ	102 ± 10	168840 ± 2709
Comb. e only	73583 ± 467	51504 ± 327
Peaking e only	40 ± 6	9882 ± 1597
Signal e only	51 ± 7	96677 ± 2052
Comb. μ only	57082 ± 453	39355 ± 312
Peaking μ only	105 ± 10	7676 ± 1252
Signal μ only	51 ± 7	71515 ± 1782

Table 20: Signal and Background Yields for Method 3 - Both Leptons

	Run 1		Run 2	
Type	Sideband Region	Signal Region	Sideband Region	Signal Region
Cont. BG	39454 ± 553	30821 ± 488	128176 ± 1059	101515 ± 943
Comb. BG RS MC	129838 ± 360	90246 ± 300	390579 ± 625	271146 ± 521
Peaking BG	148 ± 12	20142 ± 628	613 ± 25	63192 ± 1109
Signal RS MC	100 ± 10	165992 ± 800	314 ± 18	495099 ± 1396
Comb. BG WS MC	129711 ± 360	90072 ± 300	390192 ± 625	271223 ± 521
Peaking BG	147 ± 12	18994 ± 628	612 ± 25	59214 ± 1107
Signal WS MC	101 ± 10	167263 ± 797	316 ± 18	498730 ± 1391
Comb. BG WS data	128876 ± 359	90118 ± 300	390656 ± 625	267427 ± 517
Peaking BG	147 ± 12	17239 ± 627	611 ± 25	52923 ± 1104
Signal WS data	102 ± 10	169488 ± 793	323 ± 18	508512 ± 1389

Table 21: Signal and Background Yields for Method 3 - Electrons Only

	Run 1		Run 2	
Type	Sideband Region	Signal Region	Sideband Region	Signal Region
Cont. BG	20455 ± 398	15267 ± 344	59679 ± 723	47036 ± 642
Comb. BG RS MC	72925 ± 270	50996 ± 226	217567 ± 466	151593 ± 389
Peaking BG	40 ± 6	10528 ± 495	179 ± 13	32004 ± 859
Signal RS MC	52 ± 7	97121 ± 625	173 ± 13	287572 ± 1082
Comb. BG WS MC	72972 ± 270	50929 ± 226	217143 ± 466	152059 ± 390
Peaking BG	40 ± 6	9721 ± 494	178 ± 13	29267 ± 859
Signal WS MC	53 ± 7	97951 ± 623	175 ± 13	289810 ± 1085
Comb. BG WS data	72386 ± 269	51022 ± 226	218086 ± 467	149932 ± 387
Peaking BG	40 ± 6	9125 ± 495	178 ± 13	26646 ± 854
Signal WS data	53 ± 7	98555 ± 623	177 ± 13	294134 ± 1075

Table 22: Signal and Background Yields for Method 3 - Muons Only

	Run 1		Run 2	
Type	Sideband Region	Signal Region	Sideband Region	Signal Region
Cont. BG	18999 ± 384	15554 ± 347	68496 ± 774	54479 ± 691
Comb. BG RS MC	56809 ± 238	39176 ± 198	172723 ± 416	119355 ± 345
Peaking BG	106 ± 10	9803 ± 398	433 ± 21	31323 ± 711
Signal RS MC	48 ± 7	68720 ± 507	141 ± 12	207789 ± 894
Comb. BG WS MC	56699 ± 238	39112 ± 198	173114 ± 416	119196 ± 345
Peaking BG	106 ± 10	9438 ± 397	433 ± 21	30896 ± 690
Signal WS MC	48 ± 7	69154 ± 505	141 ± 12	207683 ± 826
Comb. BG WS data	56200 ± 237	38891 ± 197	171610 ± 414	116833 ± 342
Peaking BG	106 ± 10	8743 ± 398	432 ± 21	27016 ± 705
Signal WS data	49 ± 7	70287 ± 505	145 ± 12	214340 ± 883

Table 23: Branching Fractious Method 3 - Both Leptons

Run #	BG Type	$\mathcal{B}(\bar{B}^0 \to D^{*+}\ell^-\bar{\nu}_\ell)$	χ^2/NDF	CL (%)
Run 1	RS MC	$(4.82 \pm 0.01)\%$	0.86	76
	WS MC	$(4.86 \pm 0.01)\%$	1.02	43
	WS data	$(4.92 \pm 0.01)\%$	1.41	3
Run 2	RS MC	$(4.92 \pm 0.01)\%$	1.00	47
	WS MC	$(4.95 \pm 0.01)\%$	1.29	8
	WS data	$(5.05 \pm 0.01)\%$	1.34	5
Run 1+2	RS MC	$(4.89 \pm 0.01)\%$		
	WS MC	$(4.93 \pm 0.01)\%$		
	WS data	$(5.02 \pm 0.01)\%$		

Table 24: Branching Fractions Method 3 - Electrons Only

Run #	BG Type	$\mathcal{B}(\bar{B}^0 \to D^{*+}\ell^-\bar{\nu}_\ell)$	χ^2/NDF	CL (%)
Run 1	RS MC	$(4.86 \pm 0.02)\%$	0.85	77
	WS MC	$(4.90 \pm 0.02)\%$	1.02	44
	WS data	$(4.93 \pm 0.02)\%$	1.29	8
Run 2	RS MC	$(4.93 \pm 0.01)\%$	1.18	18
	WS MC	$(4.96 \pm 0.01)\%$	1.30	7
	WS data	$(5.04 \pm 0.01)\%$	1.39	3
Run 1+2	RS MC	$(4.91 \pm 0.01)\%$		
	WS MC	$(4.95 \pm 0.01)\%$		
	WS data	$(5.01 \pm 0.01)\%$		

Table 25: Branching Fractions Method 3 - Muons Only

Run #	BG Type	$\mathcal{B}(\bar{B}^0 \to D^{*+}\ell^-\bar{\nu}_\ell)$	χ^2/NDF	CL (%)
Run 1	RS MC	$(4.76 \pm 0.02)\%$	0.92	64
	WS MC	$(4.79 \pm 0.02)\%$	1.04	40
	WS data	$(4.87 \pm 0.02)\%$	1.52	1
Run 2	RS MC	$(4.91 \pm 0.01)\%$	1.05	37
	WS MC	$(4.91 \pm 0.01)\%$	1.11	27
	WS data	$(5.07 \pm 0.01)\%$	1.37	4
Run 1+2	RS MC	$(4.87 \pm 0.01)\%$		
	WS MC	$(4.88 \pm 0.01)\%$		
	WS data	$(5.02 \pm 0.01)\%$		

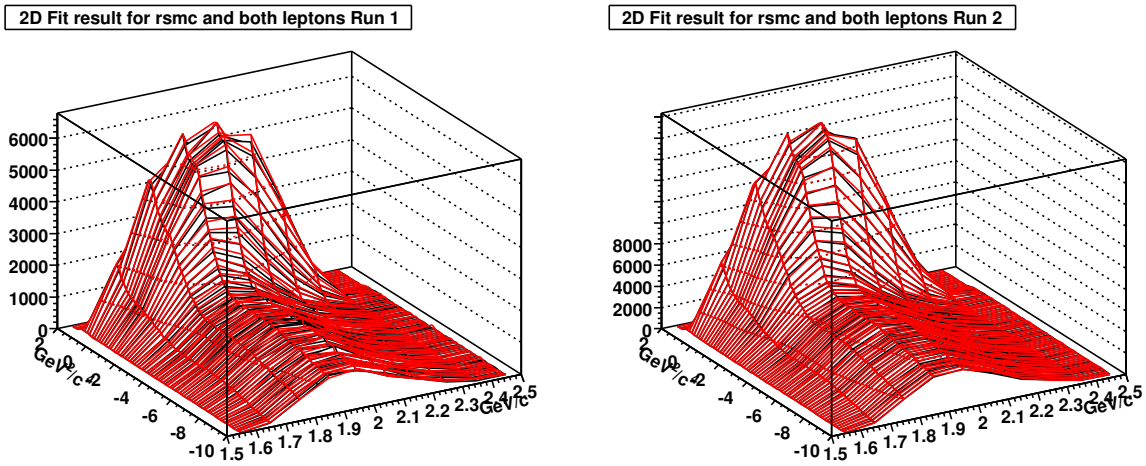

Figure 40: Fit Results for RS MC signal extraction for Run 1 (left) and Run 2 (right) for both leptons in the M_ν^2 versus lepton momentum plane for data (black) and the Monte Carlo fit (red).

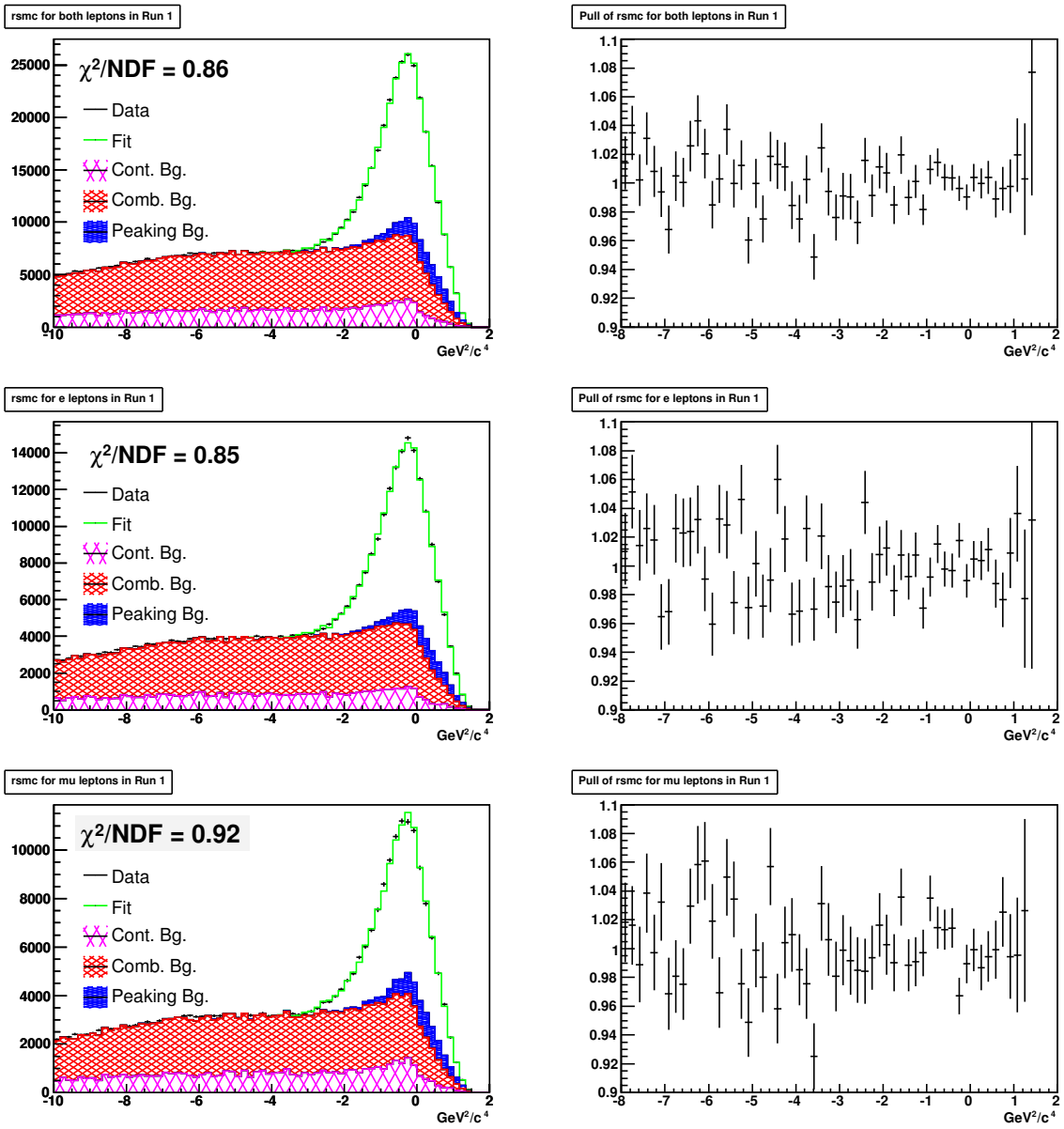

Figure 41: Fit Results for RS MC signal extraction for Run 1. Left Column (top to bottom): M_ν^2 distributions for the fit and raw data for both lepton types, electrons only and muons only. The fit is sectioned into its contributions from continuum background (magenta), combinatoric background (red), peaking background (blue) and signal (green). Right Column (top to bottom): Pull of data to fit for both leptons, electrons only and muons only.

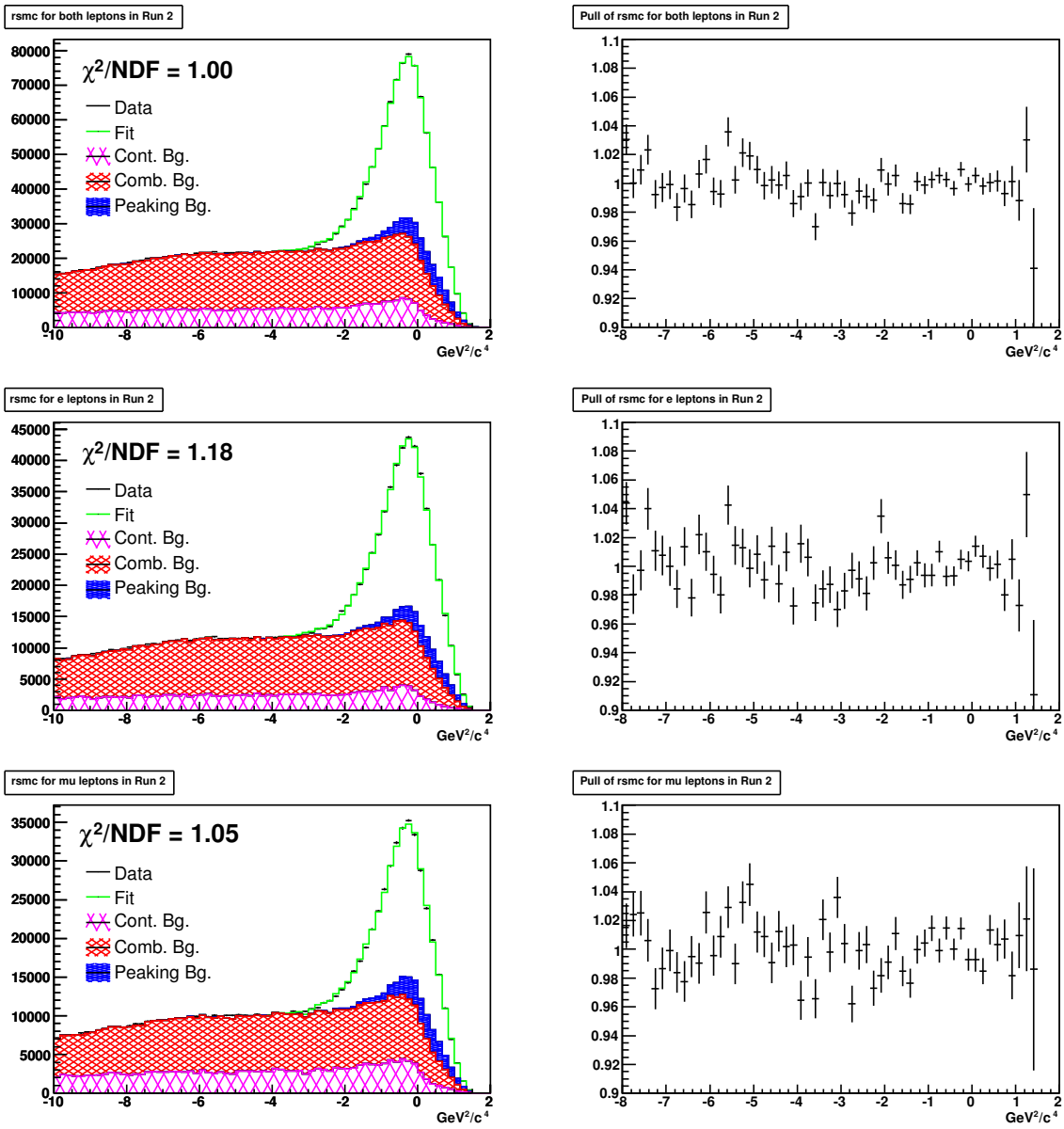

Figure 42: Fit Results for RS MC signal extraction for Run 2. Left Column (top to bottom): M_ν^2 distributions for the fit and raw data for both lepton types, electrons only and muons only. The fit is sectioned into its contributions from continuum background (magenta), combinatoric background (red), peaking background (blue) and signal (green). Right Column (top to bottom): Pull of data to fit for both leptons, electrons only and muons only.

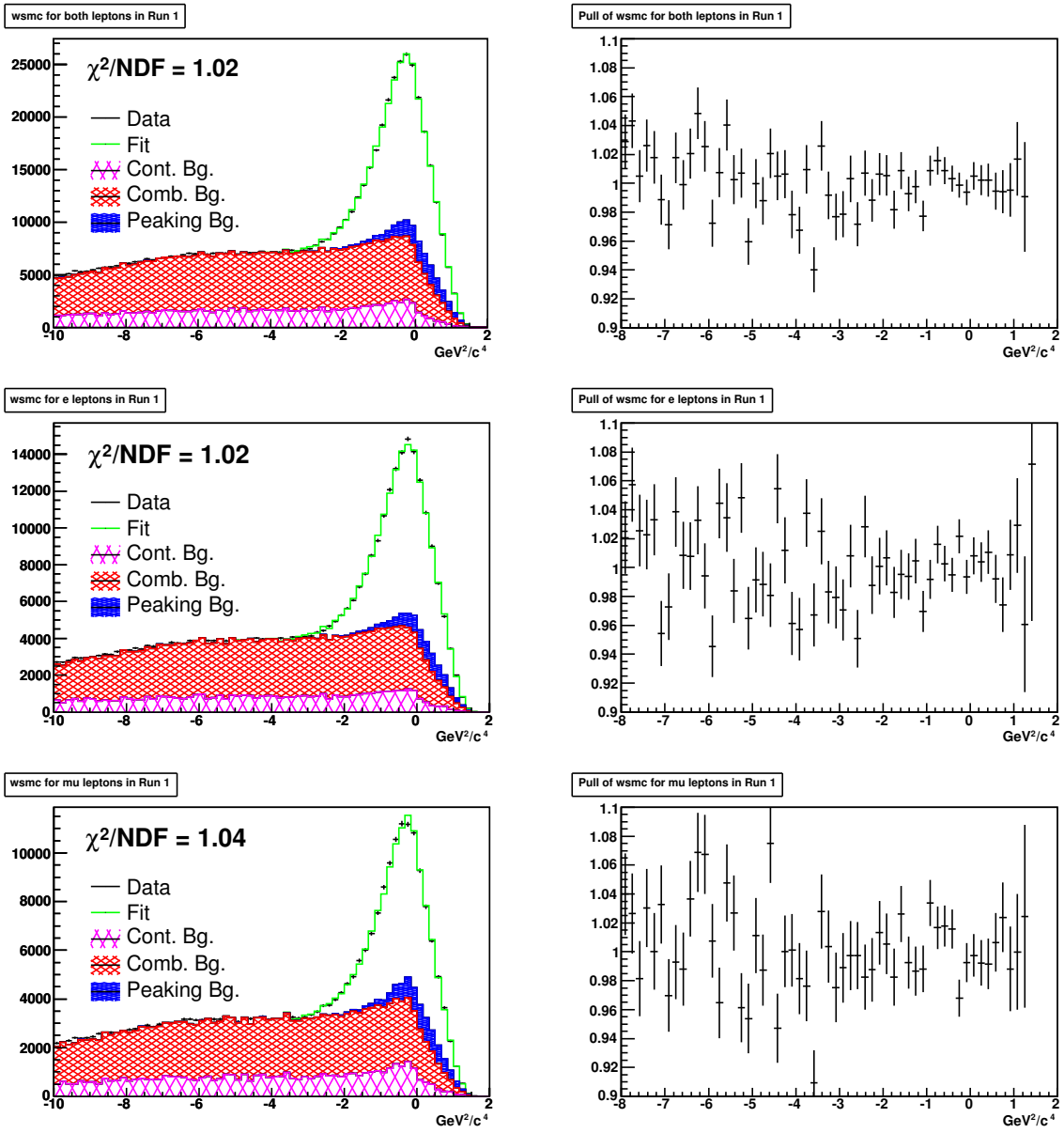

Figure 43: Fit Results for WS MC signal extraction for Run 1. Left Column (top to bottom): M_ν^2 distributions for the fit and raw data for both lepton types, electrons only and muons only. The fit is sectioned into its contributions from continuum background (magenta), combinatoric background (red), peaking background (blue) and signal (green). Right Column (top to bottom): Pull of data to fit for both leptons, electrons only and muons only.

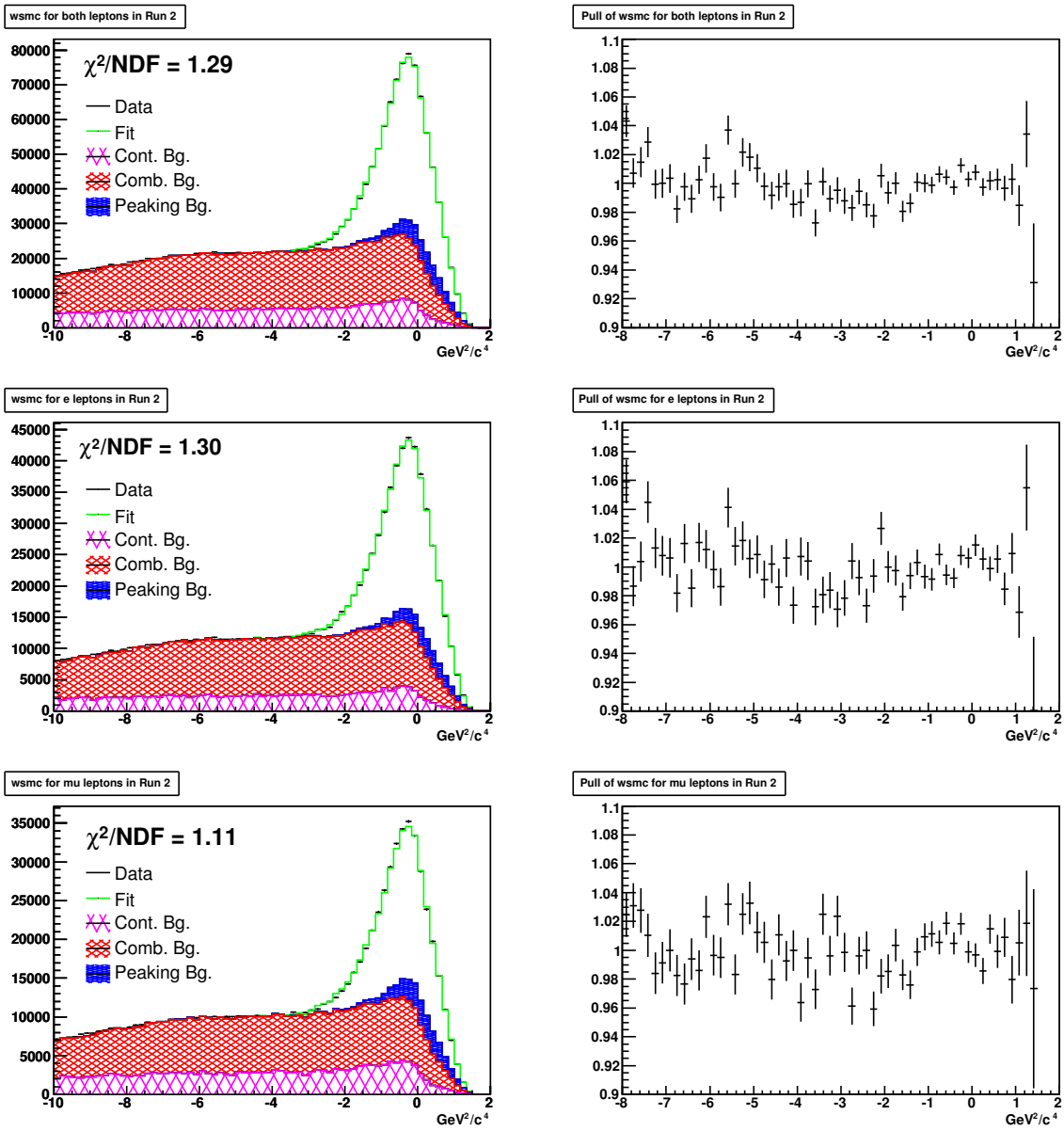

Figure 44: Fit Results for WS MC signal extraction for Run 2. Left Column (top to bottom): M_ν^2 distributions for the fit and raw data for both lepton types, electrons only and muons only. The fit is sectioned into its contributions from continuum background (magenta), combinatoric background (red), peaking background (blue) and signal (green). Right Column (top to bottom): Pull of data to fit for both leptons, electrons only and muons only.

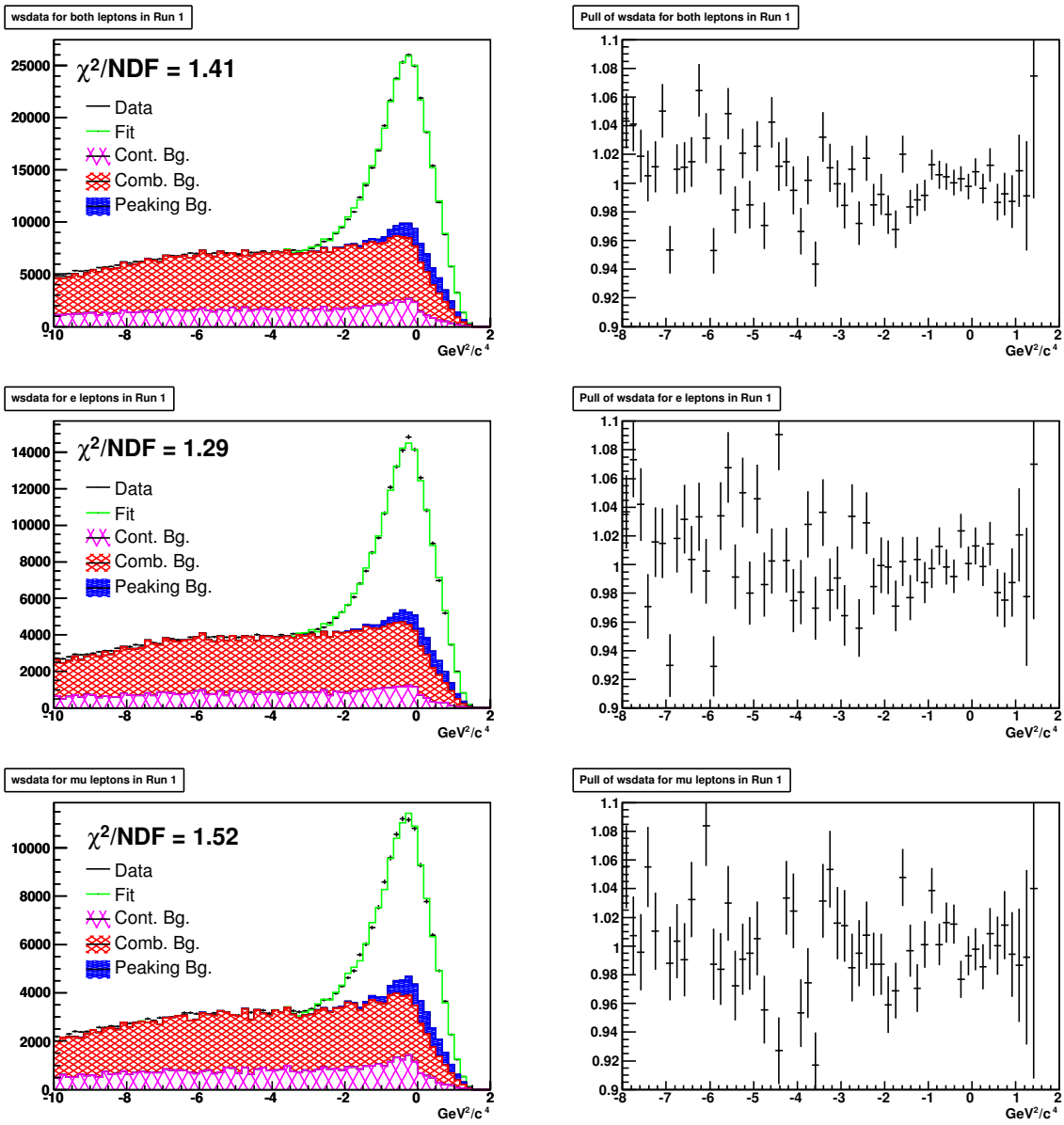

Figure 45: Fit Results for WS data signal extraction for Run 1. Left Column (top to bottom): M_ν^2 distributions for the fit and raw data for both lepton types, electrons only and muons only. The fit is sectioned into its contributions from continuum background (magenta), combinatoric background (red), peaking background (blue) and signal (green). Right Column (top to bottom): Pull of data to fit for both leptons, electrons only and muons only.

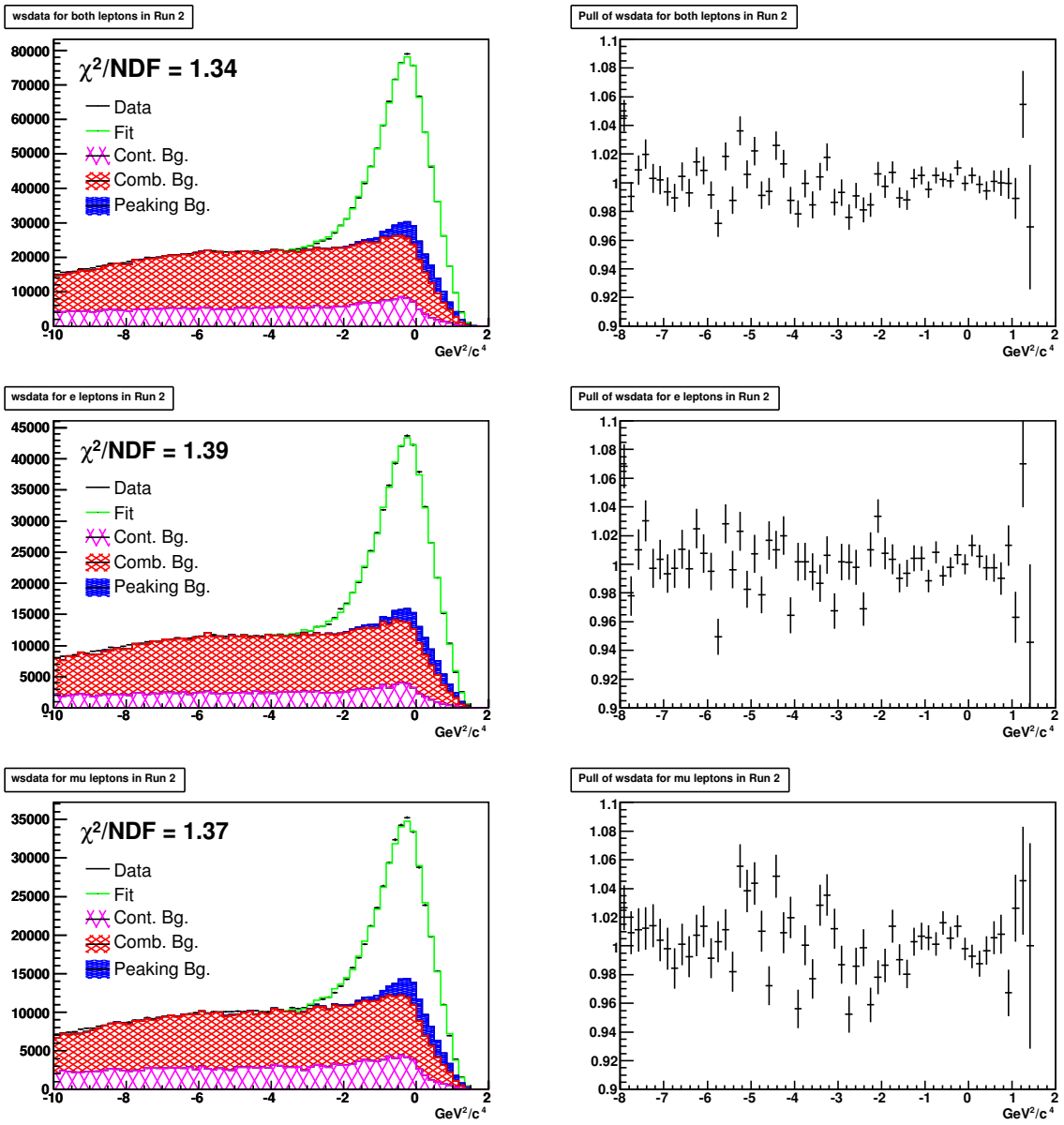

Figure 46: Fit Results for WS data signal extraction for Run 2. Left Column (top to bottom): M_ν^2 distributions for the fit and raw data for both lepton types, electrons only and muons only. The fit is sectioned into its contributions from continuum background (magenta), combinatoric background (red), peaking background (blue) and signal (green). Right Column (top to bottom): Pull of data to fit for both leptons, electrons only and muons only.

6 Monte Carlo Adjustments

6.1 Monte Carlo Tuning

Since in the partial reconstruction technique M_ν^2 is constructed solely through the lepton and the soft pion of the decay, the shape of the mass distribution depends heavily on the soft pion and lepton momentum spectra. In order to achieve a better agreement between data and Monte Carlo control samples, a Monte Carlo tuning is applied to the Monte Carlo lepton and soft pion momentum spectra before partial reconstruction takes place to improve Monte Carlo to data agreement. Tuning is preformed in two regions depending on the type of Monte Carlo which dominates that region. The pion and lepton momenta are accumulated in histograms of 32 equal bins in their full kinematic range of 40 MeV/c $\leq p_{pi} \leq$ 200 MeV/c for the pion and 1.5 GeV/c $\leq p_\ell \leq$ 2.5 GeV/c for the lepton momenta. Two histograms for leptons and pions each are generated in the sideband and signal neutrino mass region to separate between background and signal dominated tuning.

The Monte Carlo data is tuned by using bin-by-bin weights in the specific momentum spectra. The histograms for lepton and pion momenta for data and Monte Carlo are first scaled to equal areas. This avoids introducing scaling into the reweighting process and only reshapes the Monte Carlo data. Then the ratio of data to Monte Carlo for each momentum bin is computed and stored into a reweighting array for the 32 bins. An array is filled for the pion momentum, the electron and the muon momentum spectra, respectively. Since only the soft pion and lepton are used to reconstruct the decay, the tuning of their momentum spectra is sufficient to also tune the M_ν^2 spectra who's weight is computed from the product of the individual weights:

$$w_{M_\nu^2}(p_\pi, p_\ell) = w_\pi(p_\pi) \times w_\ell(p_\ell) \tag{82}$$

The weighting procedure undergoes two main steps. First the pion and lepton weights from the sideband region are calculated and the MC combinatoric background is reweighted

during histogramming. The sideband weights are used since this area is predominately filled with combinatoric background events. Reweighting is applied on the full M_ν^2 spectrum. In a second step, the reweighted momentum histograms for pion and lepton momenta of the combinatoric background are subtracted from the pion and lepton momentum histograms accumulated in the signal region. After subtraction these histograms show the lepton and pion momentum distribution of data and Monte Carlo of the combined sample of the signal and peaking background. Tuning weights are calculated by taking the ratio of each bin of the momentum histograms between Monte Carlo and data which are used to reweigh the signal and peaking background histograms. This separation allows for the separate tuning of signal and background dominated contributions. Again tuning is performed in the whole M_ν^2 spectrum.

On the nTuple level each histogram is filled with the corresponding weight from the weighting array. Figures 47 and 49 shows the agreement of the pion momentum in the sideband and signal regime for data and Monte Carlo before and after tuning as well as the data to Monte Carlo ratios before and after tuning. It shows that the pion momenta in Monte Carlo seem to favor more low momentum pions in the Monte Carlo than compared to data. It should be noted that this effect is due to modeling differences such as form factors and not different slow pion efficiency curves between data and Monte Carlo since the additional low pion lab-momentum cut desensitizes the data to systematic errors in this region. The effect of form factors on the analysis is separately considered and discussed in section 7.7. After the tuning both spectra are in good agreement, which can be seen from the plot of ratios of data to Monte Carlo. After tuning the pull is flat within error. Figures 48 and 50 show the agreement of the lepton momentum in the sideband and signal regime for data and Monte Carlo before and after tuning as well as the data to Monte Carlo ratios before and after tuning. After the tuning both spectra are in good agreement.

The signal extraction for the branching fraction measurement mainly depends on the M_ν^2 distributions. Since the signal shape and shapes for peaking background are solely

obtained from Monte Carlo data, we also investigate the shape change of the Monte Carlo signal as well as the major contributor to the peaking background, the $D^* n\pi / D^{**}$ shape, due to the tuning process. Figure 51 shows the Monte Carlo signal shape before and after tuning as well as the data to Monte Carlo ratio of this shape. It can be seen that differences are small but beyond the statistical error of the shape. Also shown is the $D^* n\pi / D^{**}$ peaking background shape as well as its ratio of data to Monte Carlo before and after tuning. The differences again are small but beyond statistical error. The overall changes in event number for both signal and peaking background are 0.28% and 0.71%, respectively. However only the absolute change in events of the signal shape directly influences the analysis since this shape is used to calculate the efficiency. The combinatoric and peaking backgrounds will only contribute due to their change in shape, but not absolute event number, since their scale is determined by fits to data. The overall systematics of the Monte Carlo tuning technique will be accounted for by repeating the analysis with tuned data and will be discussed in detail in section 7. For consistency we also examine the RS and WS Monte Carlo combinatoric background shapes. Figure 52 shows the shape of RS and WS Monte Carlo combinatoric background in the full range before and after Monte Carlo tuning as well as the ratios between data and Monte Carlo. The effect of the tuning mechanism on these shapes is also minor and similar to the signal shape.

To compare the changes in shape introduced from the Monte Carlo tuning the mean and RMS of the corresponding shapes before and after the tuning procedure were calculated and are summarized in Table 26. This table summarizes the kinematic impact of the Monte Carlo tuning technique on the discussed shapes. As mentioned, the pion momentum spectrum is skewed to slightly higher momenta in order to match data. This is supported by the increase in its mean after tuning while maintaining a relatively constant RMS as can be seen in Table 26. The distribution of lepton momenta is not quite as clear as in the case of pions. This is mainly due to the fact that leptons are strongly correlated to the effect of the χ probability cut, which solely shapes the bell shape distribution.

From examining the plot one can see that the tuning results in a tightening of the lepton spectra which is supported by its relatively constant mean and decreasing RMS value. The tuning technique also seems to have a similar effect on the Monte Carlo signal and the $D^{**}/D^{*}n\pi$ peaking distribution respectively. Both show tightening in shape represented by a decreasing RMS value. This is also shown in the pull plots of these shapes. Both follow a slight parabola shape indicating decreasing numbers towards the edges of the shape. Both the signal and the $D^{**}/D^{*}n\pi$ distribution show a distinct change in shape from the pull plots and a slight shift to lower values in the M_{ν}^{2} distribution represented by decreasing mean values which is expected from the following. Examining the neutrino missing mass square formula (68) it becomes clear that higher values of momenta for the soft pion, which also results in higher values of energy, will skew the M_{ν}^{2} distribution towards lower values. A shift in mean for shapes dependent on this value is therefore expected. This effect is best seen by examining the combinatoric background shapes for which the mean decreases after tuning in both cases. These shapes also show a visible skew in their distributions over the full kinematic range following this trend which is not so obvious in peaking distributions due to the limited range. This trend is also reflected in the pull plots of the combinatoric background graphs which show a general positive linear skew beyond the statistical error indicating a shift to lower values after tuning.

Table 26: Mean and RMS values of momentum and M_{ν}^{2} shapes before and after Monte Carlo tuning

Source	Before Tuning		After Tuning		Unit
	mean	RMS	mean	RMS	
$p(\pi)$ SB	0.1250	0.0369	0.1266	0.0366	GeV/c
$p(\ell)$ SB	1.9042	0.1497	1.9036	0.1479	GeV/c
$p(\pi)$ SG	0.1162	0.0334	0.1169	0.0332	GeV/c
$p(\ell)$ SG	1.8903	0.1490	1.8911	0.1475	GeV/c
MC Signal	-0.4411	0.8072	-0.4391	0.8033	$\mathrm{GeV}^2/\mathrm{c}^4$
$D^{**}/D^{*}n\pi$	-0.0039	0.7132	-0.0037	0.7096	$\mathrm{GeV}^2/\mathrm{c}^4$
RS MC Comb. Bg.	-4.3503	2.9816	-4.3732	2.9837	$\mathrm{GeV}^2/\mathrm{c}^4$
WS MC Comb. Bg.	-4.3285	2.9713	-4.3516	2.9742	$\mathrm{GeV}^2/\mathrm{c}^4$

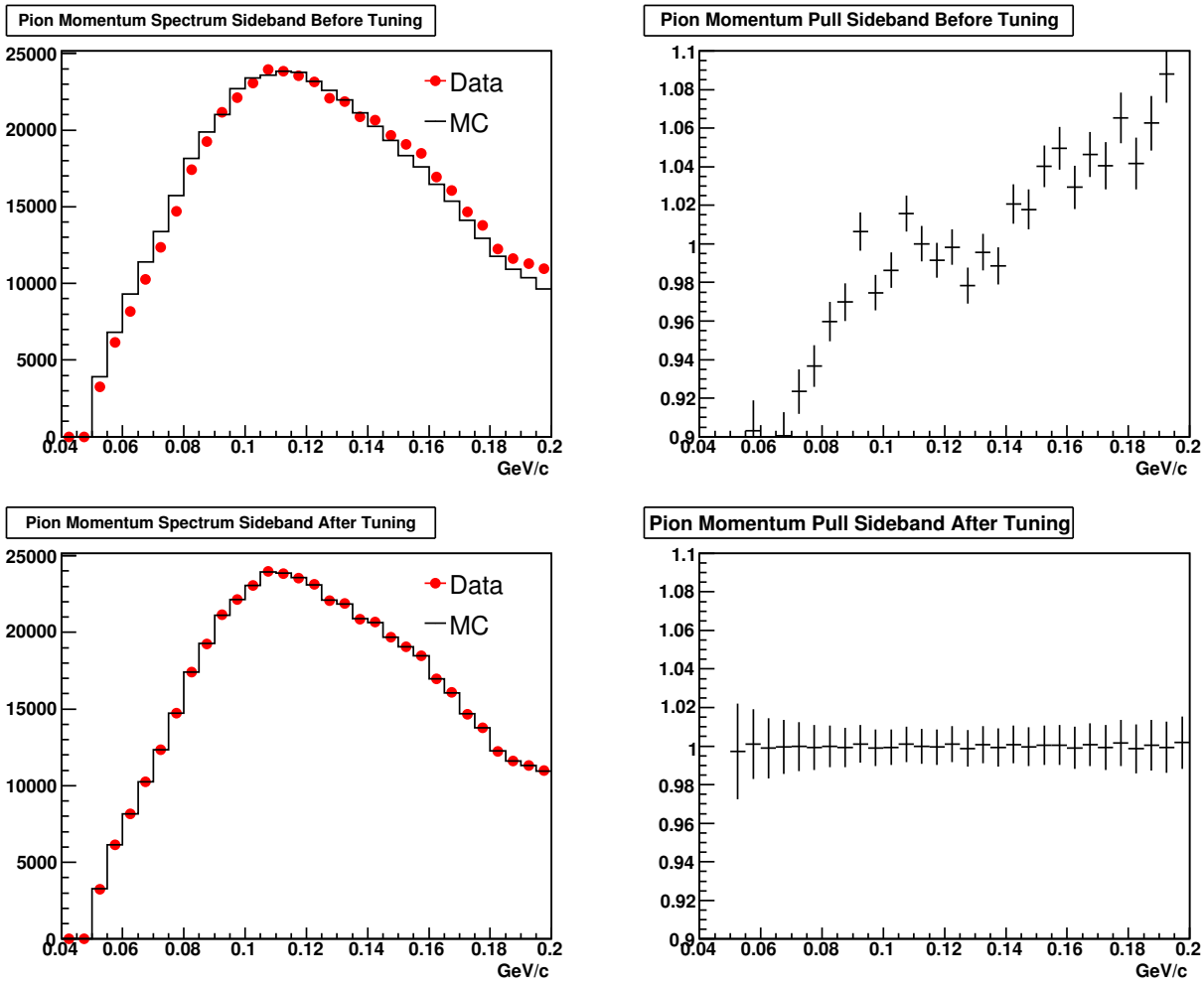

Figure 47: Pion Momentum Monte Carlo Tuning in the sideband region used to tune the combinatoric background: Left: Pion momentum spectrum of data (black line) versus Monte Carlo (red dots) before tuning (top) and after tuning (bottom). Right: Ratio of data to Monte Carlo for the pion momentum spectrum before tuning (top) and after tuning (bottom).

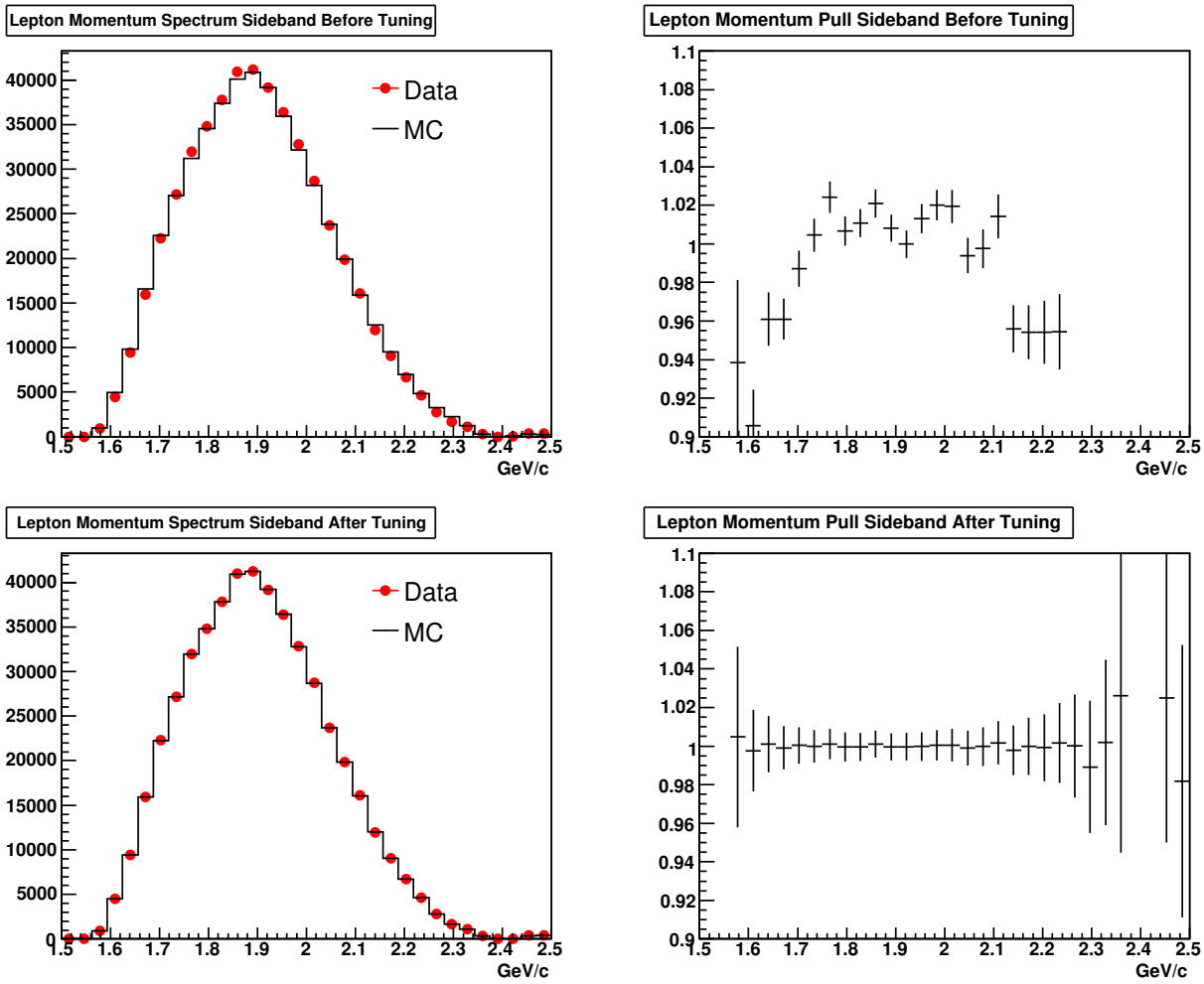

Figure 48: Lepton Momentum Monte Carlo Tuning in the sideband region used to tune the combinatoric background: Left: Lepton momentum spectrum of data (black line) versus Monte Carlo (red dots) before tuning (top) and after tuning (bottom). Right: Ratio of data to Monte Carlo for the lepton momentum spectrum before tuning (top) and after tuning (bottom).

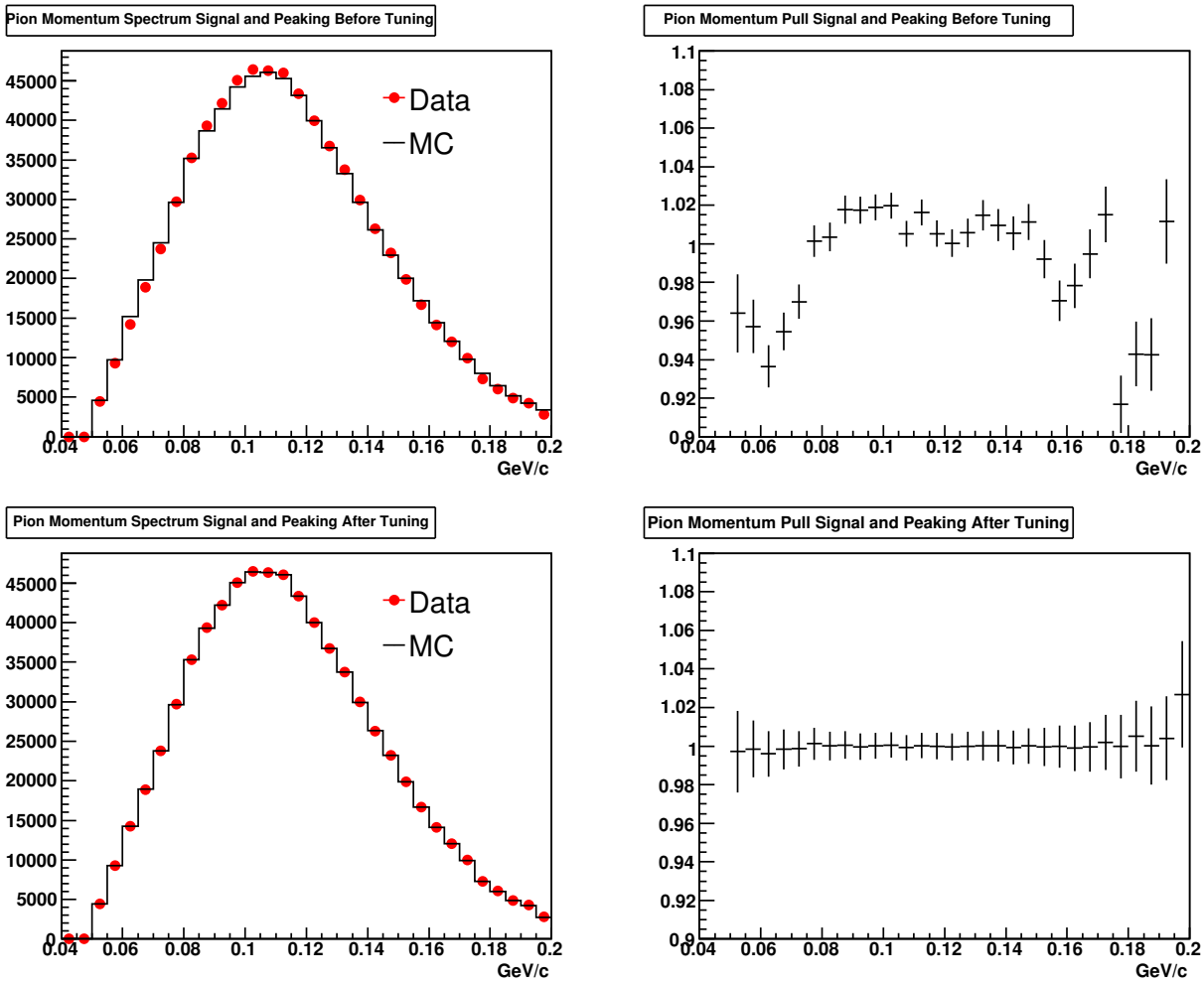

Figure 49: Pion Momentum Monte Carlo Tuning in the signal region used to tune the signal and peaking background shapes: Left: Pion momentum spectrum of data (black line) versus Monte Carlo (red dots) before tuning (top) and after tuning (bottom). Right: Ratio of data to Monte Carlo for the pion momentum spectrum before tuning (top) and after tuning (bottom).

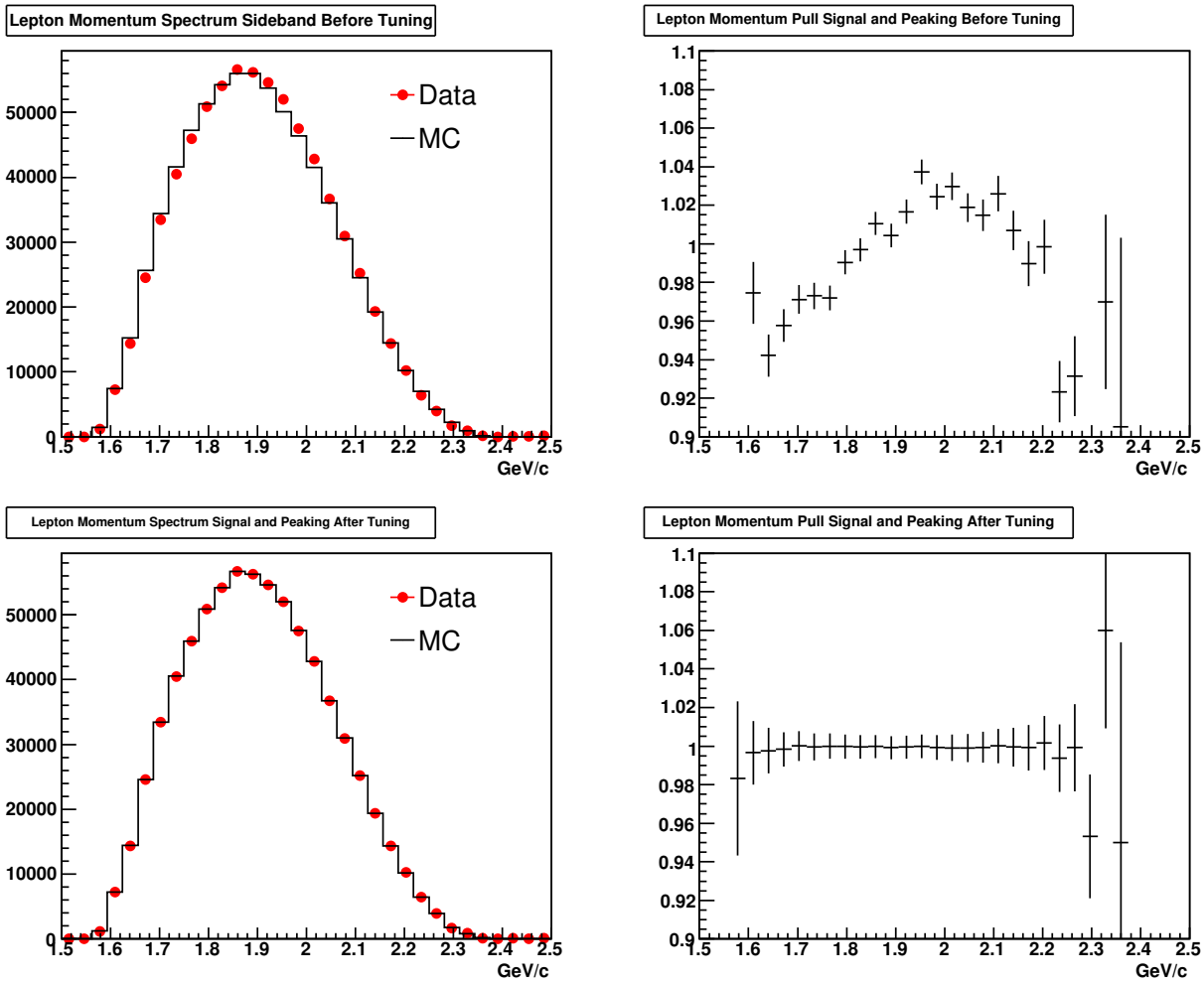

Figure 50: Lepton Momentum Monte Carlo Tuning in the signal region used to tune the signal and peaking background shapes: Left: Lepton momentum spectrum of data (black line) versus Monte Carlo (red dots) before tuning (top) and after tuning (bottom). Right: Ratio of data to Monte Carlo for the lepton momentum spectrum before tuning (top) and after tuning (bottom).

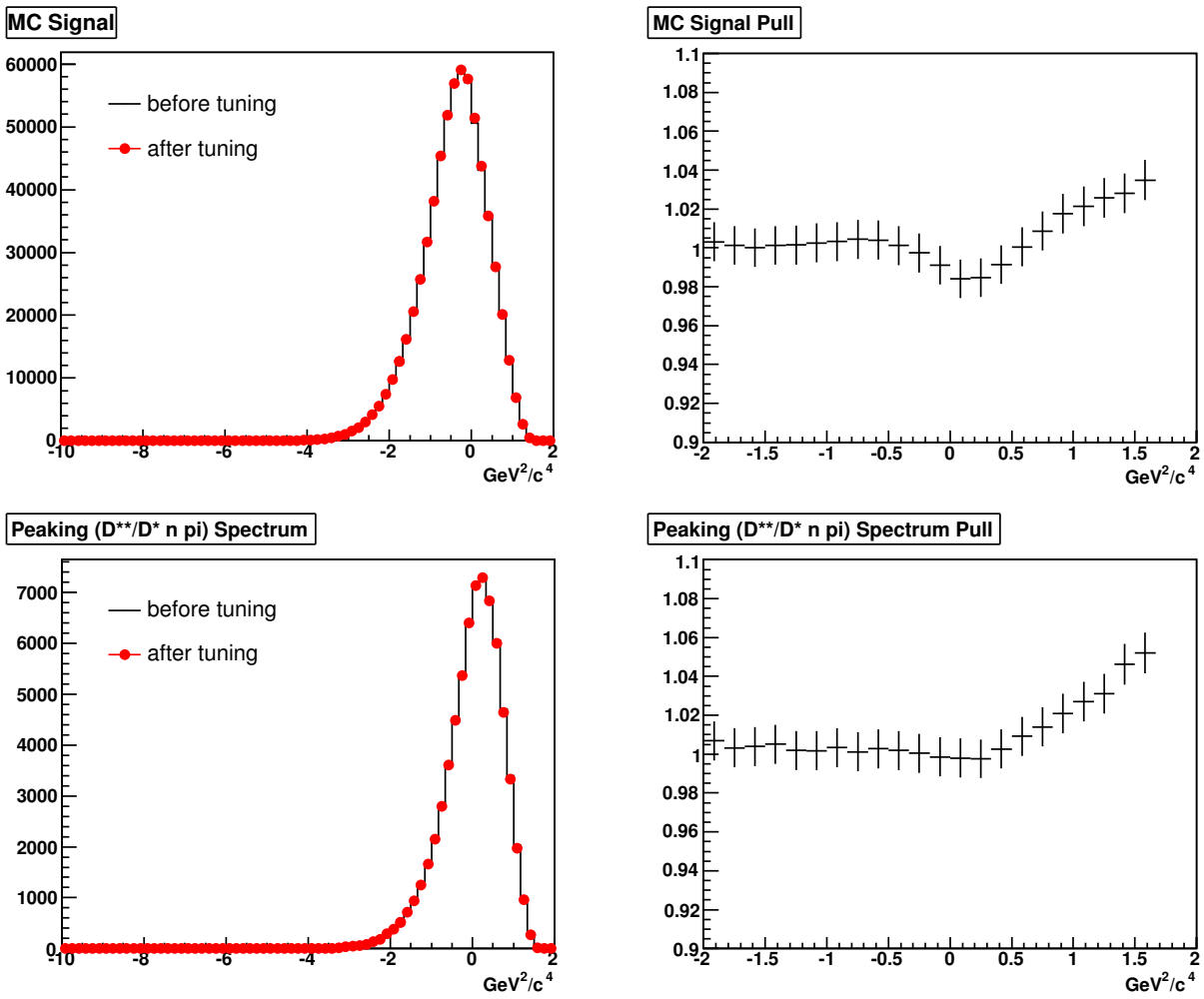

Figure 51: Monte Carlo Tuning for Peaking Shapes: Top: (left) Monte Carlo signal shape before and after tuning. (right): Ratio of Monte Carlo signal shape before to after tuning. Bottom: (left) $D^{**}/D^{*}n\pi$ Monte Carlo peaking distribution before and after tuning. (right) Ratio of $D^{**}/D^{*}n\pi$ Monte Carlo peaking distribution before to after tuning.

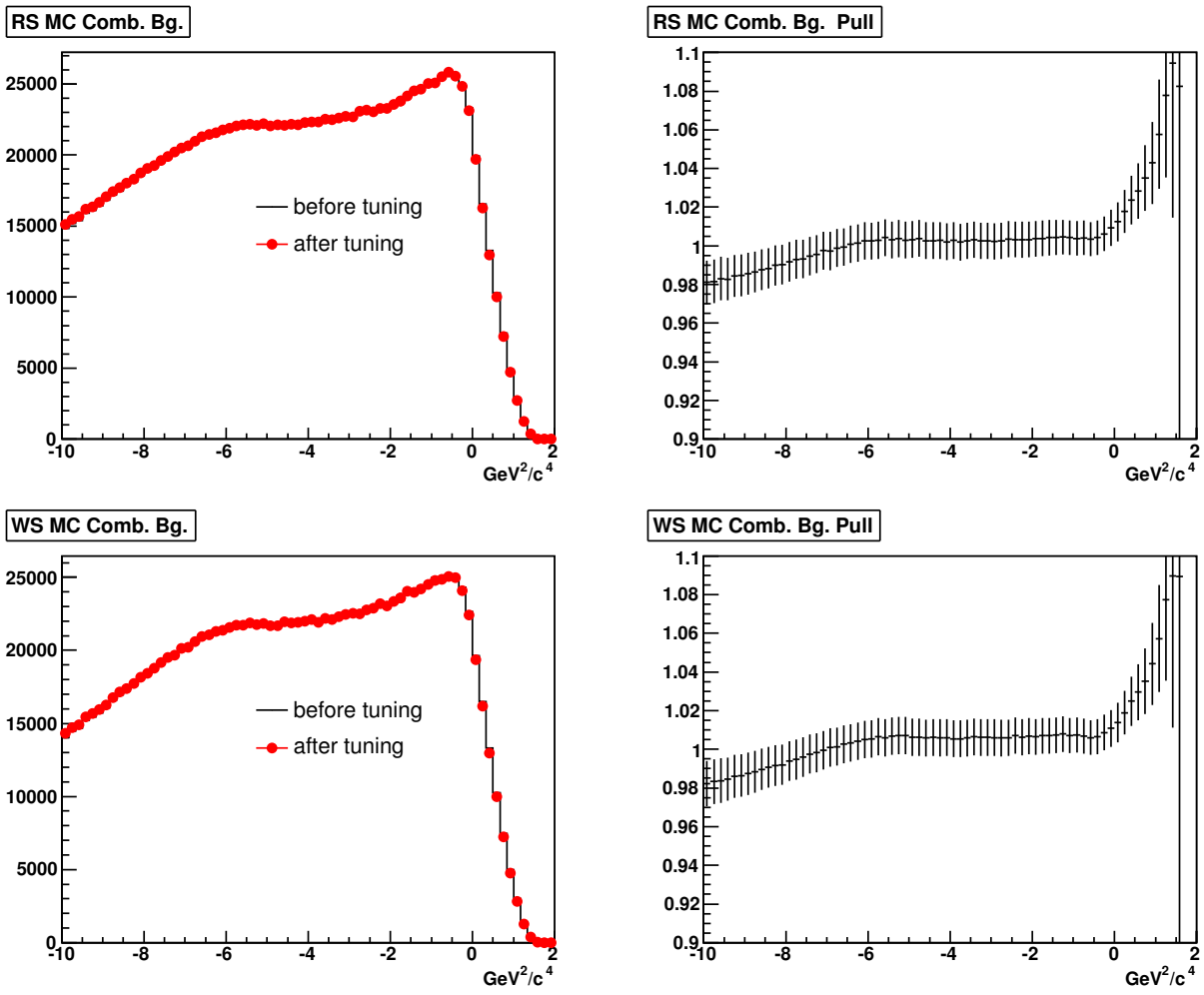

Figure 52: Monte Carlo Tuning for Combinatoric Background Shapes: Top: (left) RS MC combinatoric background shape before and after tuning. (right): Ratio of RS MC combinatoric background shape before to after tuning. Bottom: (left) WS MC combinatoric background shape before and after tuning. (right) Ratio of WS MC combinatoric background shape before to after tuning.

6.2 Monte Carlo Form Factor Reweighting

One of the possible systematic uncertainties for this analysis is the dependence on the Monte Carlo data. Since peaking background and signal are not directly accessible from data, fits of Monte Carlo produced signal and peaking background to the data signal candidates are necessary to extract the proper number of signal events in the data. The shape of the Monte Carlo signal histogram depends on the distribution of the momenta of the leptons and pions which are influenced by the form factor used during production of the Monte Carlo data.

6.2.1 Signal Form Factor Reweighting

As mentioned in the section on form factors, the semi-leptonic form factor can be expressed by the three constants R_1, R_2 and ρ^2 which have been measured by *BABAR* [23] and other experiments. As the knowledge of these constants changes with time it may be necessary to regenerate Monte Carlo data with the new values to account for model dependencies in the signal extraction. While effects due to the form factor uncertainties are expected to be very small, indirect dependencies of the momentum spectra due to the employed cuts may show bigger effects. The study of these effects is described below.

Instead of having to rerun *BABAR* Monte Carlo, the repository provides a form factor reweighting package which allows one to apply weights to the already available *BABAR* Monte Carlo data to force its momentum spectra to fit the new form factor values. The reweighting functions are located in the *XslFFReweighting* package and can be checked out from the repository. The reweighting procedure described here is based on [19].

The package provides reweighting functions for a variety of B meson decays. The function used in this analysis is based on the CLN model, but a linear version is also available. Other reweighting functions can be generically derived from the *XSLPseudoScalarFF* and *XSLVectorFF* classes which are provided in this package. The weighting function returns a single weight based on the four vectors of the particles participating in the decay. These are the B and D^* mesons as well as the lepton and the soft pion.

Below is the syntax of the function used:

```
XSLBToDstrlnu_DstrToDpi_CLN w( B04v,      // B0
                               Lep4v,     // Lep
                               Dstar4v,   // Dstar
                               Pst4v,     // Pion
                               R1, R2, rho2 ) ;

return (Float_t)w.FromSP7ToThisModel() ;
```

Here R1, R2 and rho2 are the constants of the form factor which can be chosen by the user. The function *FromSP7ToThisModel()* calculates the transfer weight of the generic *BABAR* Monte Carlo data for this particular event to the model specified by the user defined values. Functions for data created earlier than SP7 are also available. SP7 can also be used for *BABAR* Monte Carlo created with SP8 or SP9 since none of the changes affect the reweighting technique. However, in order to properly use this reweighting tool for the purpose of this analysis, a small change needs to be made to the *XSLBToDstrlnu_DstrToDpi_CLN* class. The change described here is in conformity with standard practice of the Semileptonic Working Group. The output needs to be adjusted to reflect the square of the form factor and should look as shown below:

```
double
XSLBToDstrlnu_DstrToDpi_CLN::FromSP7ToThisModel(){
  double wLinear=XSLBToDstrlnu_DstrToDpi_LinearQ2::FromSP7ToThisModel();

  double z=(sqrt(_w+1.)-sqrt(2.))/(sqrt(_w+1.)+sqrt(2.));
  double hA1_CLN= 1. -8.*_rho2*z +(53.*_rho2 - 15.)*z*z
                    -(231.*_rho2 - 91.)*z*z*z;

  double hA1_linear_new= 1. -(_w-1.)*_rho2;
  double rw = 1.196; // Renormalisation weight determined by data
  double w = wLinear*hA1_CLN*hA1_CLN/(hA1_linear_new*hA1_linear_new)/rw;

  return w;
}
```

The variable *rw* is a normalization constant which centers the reweighting peak at 1. It needs to be determined separately for each new data set. This necessary change narrows

and centers the resulting form factor weights. Figure 53 shows the resulting weight distribution after this modification. The form factor parameters used are the most recent reported by *BABAR* [23] and are listed in Table 27. Currently only the signal decay can be directly reweighted by available *BABAR* software. Figure 54 shows a comparison of the Monte Carlo signal before and after the application of the form factor weights for a combined sample of electrons and muons of Run 1 and 2. The error bars shown on the pull plot are arbitrary since no weighting errors are returned from the reweighting function. The change in signal shape is small, but the negative parabolic shape of the pull plot indicates a slight widening of the signal shape. Since a good MC signal shape is needed for the analysis, reweighting is a necessary step for a precision measurement of this kind.

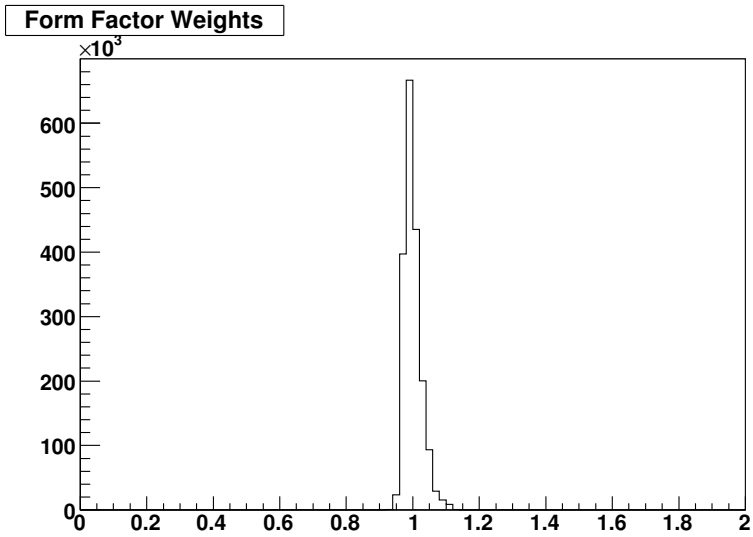

Figure 53: Form factor reweighting values for D^* signal Monte Carlo.

Table 27: Form factor parameters [23]

R_1	$1.191 \pm 0.048 \pm 0.028$
R_2	$1.429 \pm 0.061 \pm 0.044$
ρ^2	$0.827 \pm 0.038 \pm 0.022$

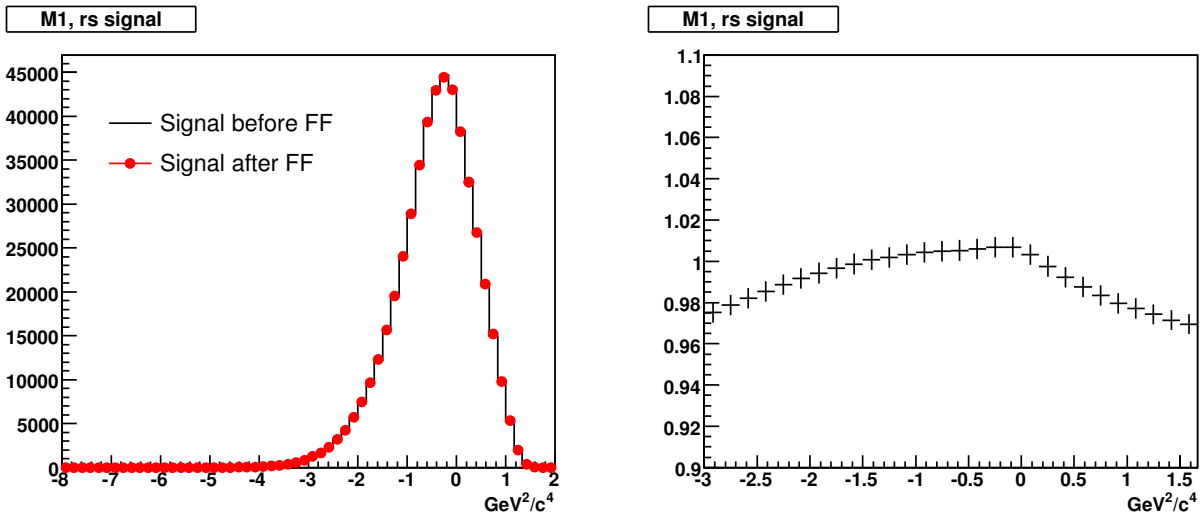

Figure 54: Left: Monte Carlo signal before (black) and after (red) form factor reweighting. Right: Ratio of the signal before to after form factor reweighting.

6.2.2 D^{**} Form Factor Reweighting

Similar to the MC signal shape, the analysis also relies on a proper histogram template for peaking background. Since D^{**} decays constitute the majority of the peaking background, reshaping of its sub-modes is performed to mimic the most recent measurements. Two types of modifications are done to the SP8 Monte Carlo data. First the branching fractions used to produce the narrow doublet and broad doublets, $[D_1(2420), D_2^*(2460)]$ and $[D_0^*(2400), D_1'(2430)]$, are reweighted to match the most recent measurements. The values are based on a reweighting note produced by the AWG [61]. Table 28 shows the branching fraction values used in SP8 compared to the new values that represent an average over heavy flavor averaging group (HFAG) 2006, PDG 2006 and recent *BABAR* measurements [61]. The individual modes are reweighted with the ratios of the new to old branching fractions on an event by event basis during histogramming. The quoted errors are used to assess a systematic error due to the peaking background shape (see section on systematics).

Besides the adjustment on the branching fractions, the D^{**} narrow and wide modes are also reweighted to match a recent form factor HQET model. Measurements of the parameters of the formulated form factors have recently become available in [52]. In

Table 28: D^{**} branching fractions for Monte Carlo

Mode	SP 8 $B^{\pm}$	new value $B^{\pm}$	SP 8 B^0	new value B^0
D_1	0.56	0.54 ± 0.06	0.52	0.50 ± 0.08
D_2	0.30	0.42 ± 0.08	0.23	0.39 ± 0.07
D_0^*	0.49	0.45 ± 0.09	0.45	0.43 ± 0.09
$D_1^{'}$	0.90	0.85 ± 0.20	0.83	0.80 ± 0.20

analogy to the D^* reweighting, each mode has its own form factor with a variety of parameters. The formulation of these form factors goes beyond the scope of this dissertation and can be found in great detail in [52]. Phase space is reweighted during histogramming to convert from the ISGW2 model used in the SP8 Monte Carlo to the new HQET model. *BABAR* software does not yet provide standard techniques for this reweighting, so analysis code written by D. Lopez Pegna [62] was amended for use for this reweighting. The code calculates ratios in w space between the ISGW2 and HQET models based on the decay products similar to the D^* reweighting technique. Figure 55 shows the reweighting ratios for each of the four D^{**} decay modes. The ratios show a wide spread, but are relatively symmetric resulting in only small changes in the D^{**} peaking background template. As expected, the weighting histogram for the D_0^* mode is empty since it does not produce a D^{*+} meson in its decay. Figure 56 shows the difference between the D^{**} Monte Carlo template before and after form factor reweighting. The error bars shown on the pull plot are arbitrary since no weighting errors are returned from the reweighting function. Changes in the event shape are minor, but the figure shows a tendentious widening of the shape towards lower values in the M_ν^2 distribution. Since peaking background to signal ratios in the analysis are about 1 to 10, it is less sensitive to this observed shape change. However, for completeness this reweighting was included in the analysis.

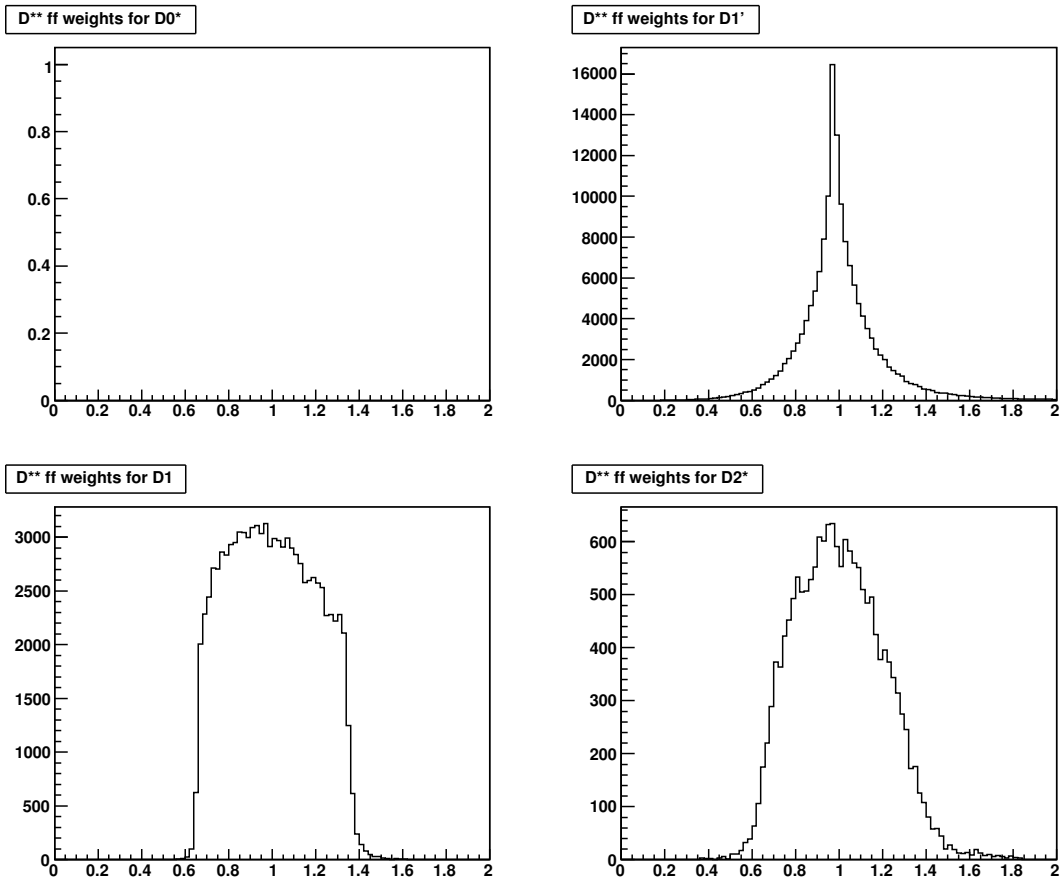

Figure 55: form factor reweighting values for D^{**} Monte Carlo modes. The top left plot does not decay to a D^{*+} meson and is therefore empty.

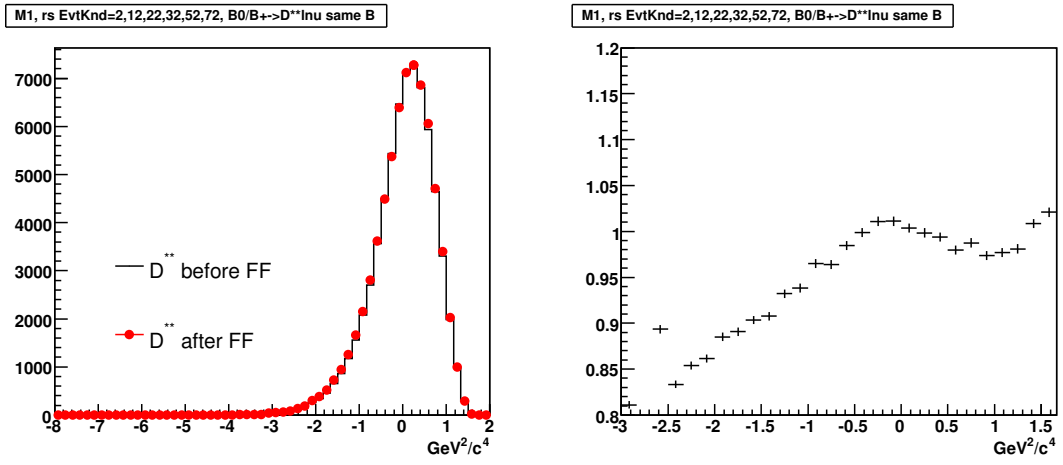

Figure 56: Monte Carlo D^{**} shape before (black) and after (red) form factor reweighting.

6.3 PID Tweaking

Besides Monte Carlo tuning, another procedure to improve data to Monte Carlo agreement is PID tweaking. This selector based procedure is aimed to improve selection efficiency differences between data and Monte Carlo based on the selectors at hand. It is observed that the available particle selectors at *BABAR* show slightly different performances between data and Monte Carlo. Several procedures on the Monte Carlo level are available to bridge these differences such as *PID killing, PID tweaking* and *PID weighting*. The chosen recipe for this analysis is PID tweaking. A detailed summary of this and the other procedures can be found in [63].

In the analysis the available generic *BABAR* Monte Carlo is treated *as data* and is therefore processed through the same particle id (PID) selectors as real data. These are the *PidLHElectrons* and the *muNNLoose* selectors for electrons and muons, respectively. However differences exist in the selection efficiencies of these selectors between data and Monte Carlo. These differences depend on the particle momentum p and its angular position in the detector θ and ϕ. For this reason the PID group has accumulated efficiency tables binned in p, θ and ϕ taken from very clean control data that show the selection efficiency for a particular range in the (p, θ, ϕ) space. These *PID tables* are accumulated for each selector individually, for data and Monte Carlo separately as well as for each run condition. Each selector itself has at least ten different tables associated with it for electrons, muons, kaons, pions and protons. In case of the *PidLHElectrons* selector, the electron table would depict the selection efficiencies, while the other tables show the misidentification probabilities. There are separate tables for positive and negative charges. Since run conditions have changed for the data set at hand during a run period, such as the DCH voltage for Run 1 and the run year for Run 2, the correct PID tables are identified by the time stamp of each individual event in the data. Each PID table has ten columns depicting the following data (random example):

```
1.500000 1.600000 32.77 37.51 -180.00 180.00 0.960674 0.010575  342  356
1.600000 1.700000 32.77 37.51 -180.00 180.00 0.959551 0.009531  427  445
1.700000 1.800000 32.77 37.51 -180.00 180.00 0.951175 0.009282  526  553
1.800000 1.900000 32.77 37.51 -180.00 180.00 0.947748 0.009556  526  555
1.900000 2.000000 32.77 37.51 -180.00 180.00 0.936893 0.009858  579  618
```

The first two columns are the momentum interval, followed by the interval for θ and the interval for ϕ. Columns 7 and 8 are the selection efficiency and its error. Column 9 is the number of control sample tracks passing the selector and column 10 is the original number of control sample tracks. The ϕ bins are very large indicating isotropy in the ϕ angle which is expected since the detector is symmetrical in this angle. Momentum and θ binning are different for each selector and particle depending on the rate of change in these variables. PID tweaking is usually performed during skimming, but is done after the fact in this analysis since it was not used during the creation of the nTuple. PID tweaking is based on randomly accepting a track rejected by the selector for the Monte Carlo sample if the Monte Carlo selection efficiency falls short of data or randomly rejecting an accepted track if the Monte Carlo selection efficiency exceeds data. The rejection (acceptance) probabilities are constructed from the PID tables as follows [63]:

$$\begin{aligned} P_{rejection} &= 1 - \frac{\varepsilon_{data}}{\varepsilon_{MC}} \quad if \quad \varepsilon_{data} < \varepsilon_{MC} \\ P_{acceptance} &= \frac{\varepsilon_{data} - \varepsilon_{MC}}{1 - \varepsilon_{MC}} \quad if \quad \varepsilon_{data} > \varepsilon_{MC} \end{aligned} \tag{83}$$

One advantage of PID tweaking over PID killing is that in case of equality of efficiencies no tracks get rejected or accepted while during PID killing selections are solely based on rejecting tracks randomly. This can cause a good track to be rejected which would have been accepted with high certainties by the selector.

The tweaking procedure described above is normally applied during skimming and can only be used in a modified way on the nTuples. While it is possible to reject tracks from the nTuple, previously rejected tracks cannot be accepted anymore since their information

has not been saved in the nTuple. The recipe has therefore been modified to a reweighting algorithm on accepted and recorded tracks only. Each track fitting a certain (p, θ, ϕ) bin is then reweighted according to a ratio of

$$w(p, \theta, \phi) = \frac{\varepsilon_{data}}{\varepsilon_{MC}} \tag{84}$$

therefore giving less weight to tracks which are accepted with an excessive efficiency in Monte Carlo and more weight to the ones that are not. This technique should yield the same result as the original tweaking recipe in case of a large data sample, which is the case for this analysis. The errors associated with each PID table bin are later used to determine the systematic error due to the particle ID process (see section on systematic errors).

Since this PID tweaking reweights Monte Carlo over the full data range, it impacts the shapes of all histograms. Figures 57 and 58 show the impact of PID tweaking on the RS MC and WS MC combinatoric background, the signal and the D^{**} contribution to the peaking background. The figures show that the tweaking procedure manly causes a rescaling of the shapes without introducing much skew to them. This is supported by the reasonably flat pull plots of the shapes. The errors shown are arbitrarily chosen to represent the mean error of the tweaking procedure. Linear fits have been performed to the pulls. It can be seen that especially the plots in the signal region (signal and D^{**}) show a slight positive slope indicating a minor shift of the shapes towards lower values in the M_ν^2 axis. However scaling effect by far outweigh shaping effects. Since the analysis is only sensitive to shape changes, the effect of PID tweaking is expected to be small.

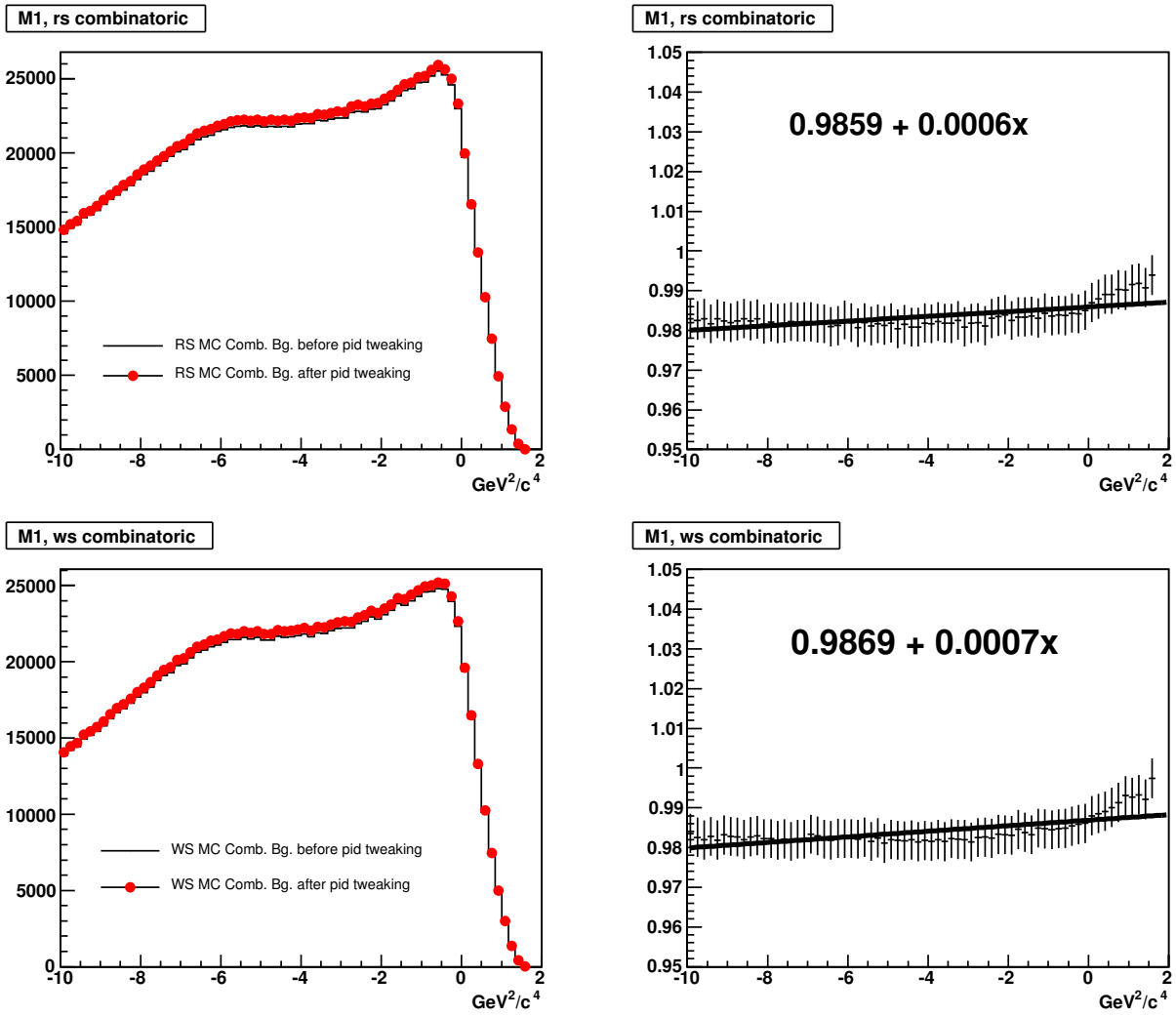

Figure 57: RS MC and WS MC combinatoric backgrounds before (black) and after (red) PID tweaking together with their pull plots.

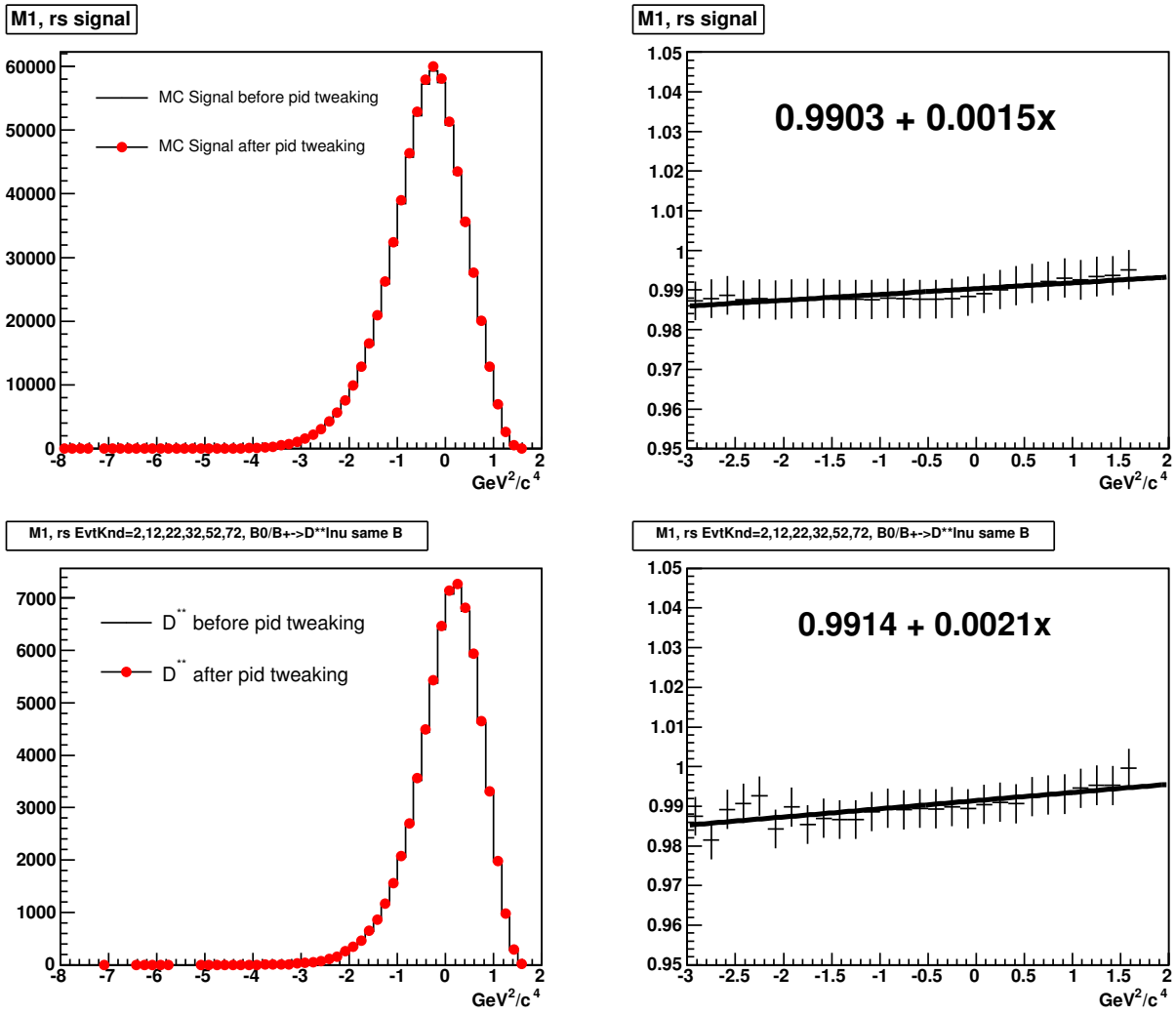

Figure 58: MC Signal (top) and D^{**} peaking background (bottom) before (black) and after (red) PID tweaking together with their pull plots.

6.4 Track Killing

Tracking refers to the track reconstruction in the detector before the track is associated with a particular particle. Depending on the criteria imposed on the goodness of a reconstructed track, more or fewer tracks generally get reconstructed. Tracks identified in this analysis are required to fulfill *BABAR* 's GTL (Good Tracks Loose) criteria. It is observed that Monte Carlo generally accepts more tracks than data. For this reason a track killing algorithm is implemented on the Monte Carlo data to match the Monte Carlo tracking efficiency closer to data. The procedure described here can be found in more detail in [64]. Since tracking is performed before the particle that caused the track is identified by a selector, all tracks are treated the same in this procedure. An investigation of the tracking task force for the R22 data set has resulted in a list of percentages of overestimation of the Monte Carlo together with systematic errors associated to these numbers. The list can be seen in Table 29. To apply the track killing, each track present in an event is rejected with the given probability shown in Table 29 according to the run number independent of the type of particle which caused the track. Since Monte Carlo always overestimates, this can be implemented on the nTuple level as a true track killing. During histogramming flagged tracks are ignored. Lepton-pion pairs used during partial reconstruction are ignored if at least one of the tracks has been flagged by the killing algorithm. This simple procedure should be unbiased over the full data range, therefore changing only the scale and not the shape of the individual histograms. Figures 59 and 60 show the Monte Carlo combinatoric background, the signal and the D^{**} peaking background before and after the tracking correction. The errors on the pulls are the average tracking errors, luminosity weighted by run number. Linear fits have been performed on the pull plots. The scale parameters show a slight downscaling in all the plots while the slope parameters are zero within error. The parameters are summarized in Table 30. This supports that track killing is mainly a downscaling of the data. The associated errors are used to assess a systematic error to the analysis due to track killing. This error is expected to scale linearly. The systematics study is presented in the section

for systematic errors.

Table 29: Tracking corrections for R22 data selected by GTL according to [64]

Run Number	Correction Factor (%)	Systematic Uncertainty per track (%)
Run 1	0.181	0.652
Run 2	0.014	0.377
Run 3	0.033	0.476
Run 4	0.260	0.620
Run 5	0.378	0.678
Run 6	0.335	0.277
Avg.	0.276	0.236

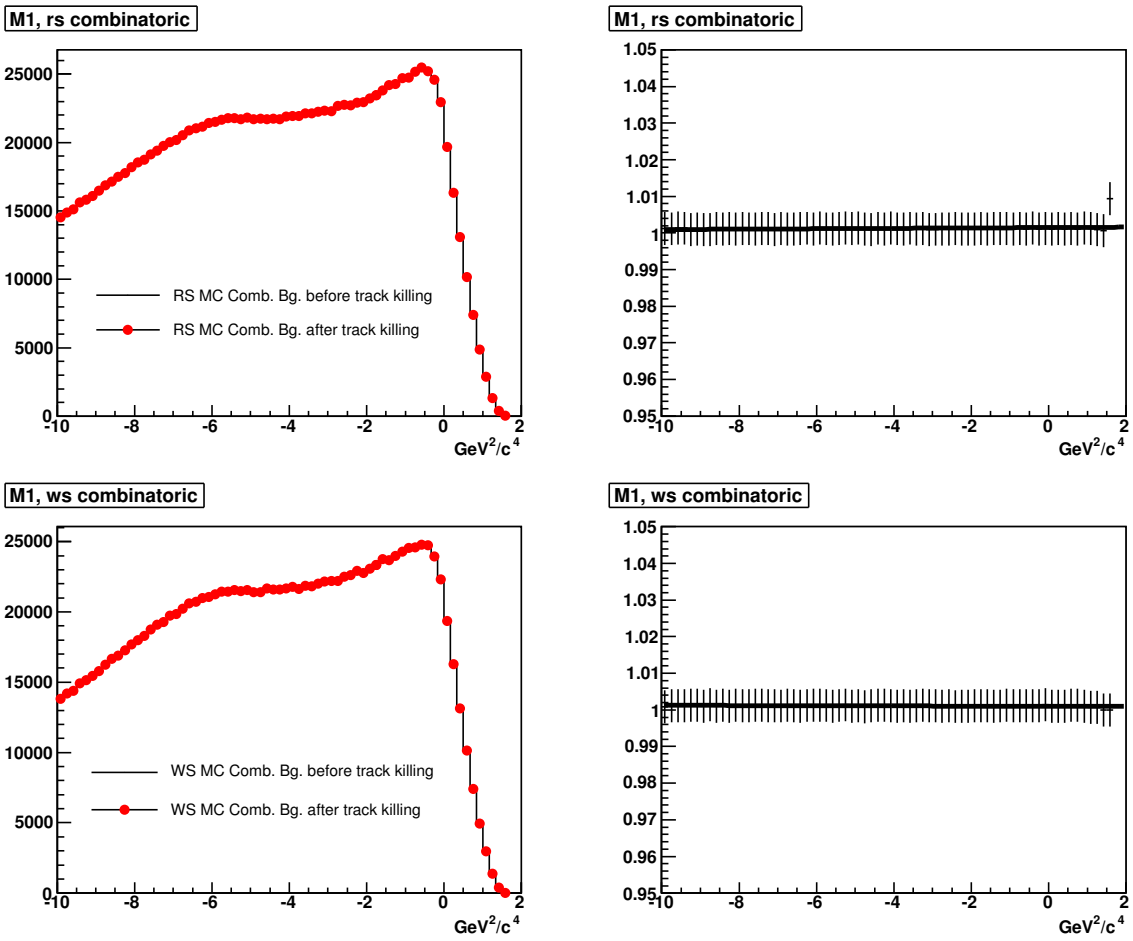

Figure 59: RS MC (top) and WS MC (bottom) combinatoric background before (black) and after (red) track killing together with their before to after pull plots.

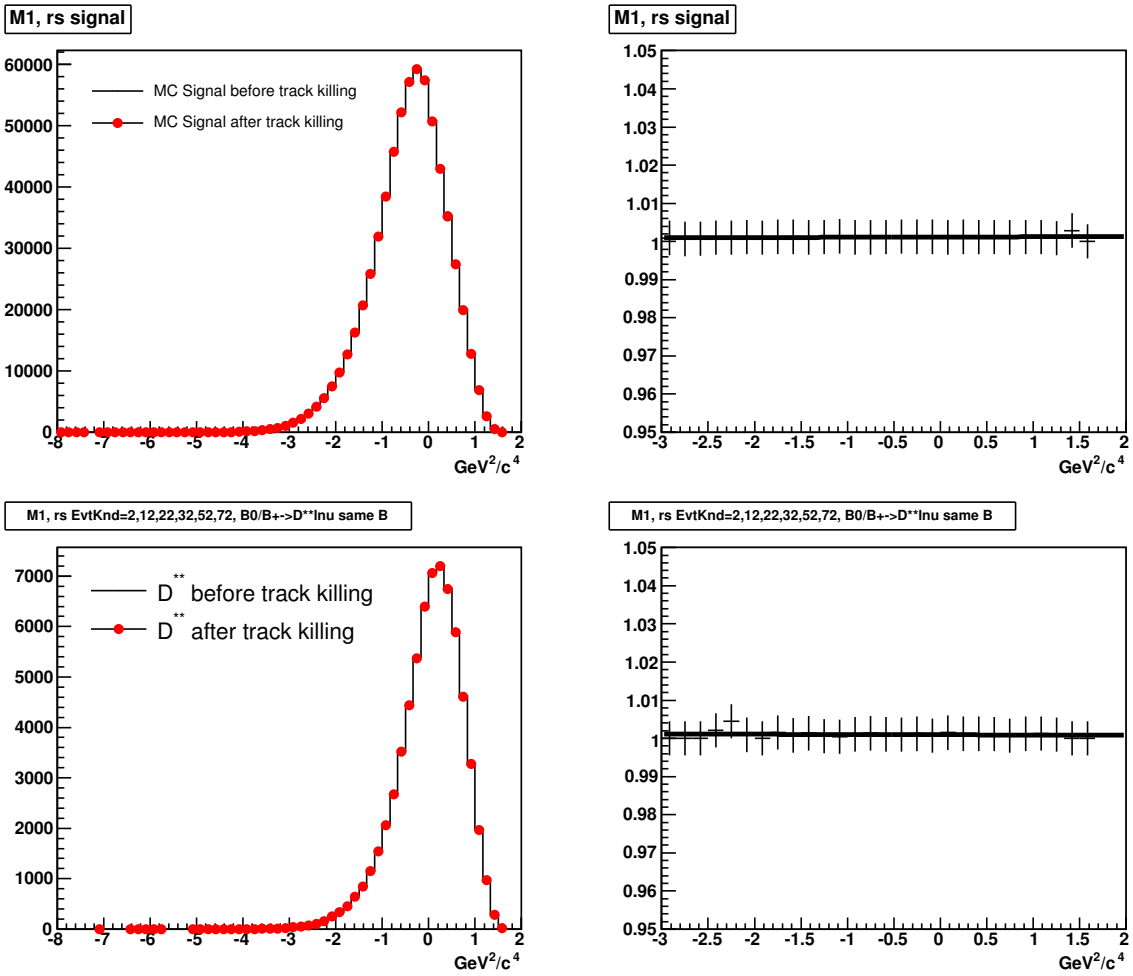

Figure 60: MC Signal (top) and D^{**} peaking background (bottom) before (black) and after (red) track killing together with their before to after pull plots.

Table 30: Slope and offset parameters for track killing pull fits

Histogram	Offset	Slope (%)
RS MC Comb. BG.	1.0015 ± 0.0009	$(0.6 \pm 1.6) \times 10^{-4}$
WS MC Comb. BG.	1.0010 ± 0.0009	$(-0.3 \pm 1.6) \times 10^{-4}$
Signal	1.0012 ± 0.0010	$(0.6 \pm 6.3) \times 10^{-4}$
D^{**} BG.	1.0010 ± 0.0009	$(-0.7 \pm 6.3) \times 10^{-4}$

6.5 Peaking Background Offset

As discussed in section 4.3 the contamination of the signal with peaking background can only be determined with Monte Carlo data since this background is almost completely contained within the signal region of the M_ν^2 distribution. Peaking events from resonant or non-resonant decays are characterized by the presence of extra particles, mainly pions, in the semi-leptonic decay chain. These particles limit the available phase space in the decay chain. Below is an example for M_ν^2 of a decay of the type $\bar{B}^0 \to D^{*+}\ell^-\pi^0\bar{\nu}_\ell$:

$$M_\nu^2 = (E_{beam} - E_{D^*} - E_\ell - E_\pi)^2 - (\vec{p}_{D^*} + \vec{p}_\ell + \vec{p}_\pi)^2 \tag{85}$$

The above construct is the correct reconstruction of the neutrino mass. However in the analysis method, the energy and momentum of the extra pion is not included since the decay satisfies the characteristics of a signal decay with the presence of one charged lepton and one charged pion which is used for the reconstruction of the D^{*+} meson. The absence of the extra pion results in an over estimation of the neutrinos energy and an underestimation of its momentum therefore shifting the M_ν^2 distribution towards higher values. Figure 61 shows the signal M_ν^2 distribution and the peaking background distribution of Monte Carlo data for Run 2 for both electron and muon samples, scaled in arbitrary units for better display. It shows that the peaks of both distributions are roughly separated by 0.5 $\mathrm{GeV}^2/\mathrm{c}^4$. This separation allows for the extraction of peaking background contamination of the measured signal through a proportionality fit. Figure 61 also shows the distribution of the Monte Carlo signal and the peaking background in the lepton momentum. Here the separation between the means of the distributions is roughly 0.1 GeV/c. The consideration of the lepton momentum distribution as done in the two dimensional signal extraction algorithm therefore adds further discriminatory power to the proportionality fit. The shift in the mean of the peaking background towards lower values in the lepton momentum is caused by the limitation of the available phase space for the decay products. The presence of extra pions in the decay forces the average momenta of the other particles to be lower.

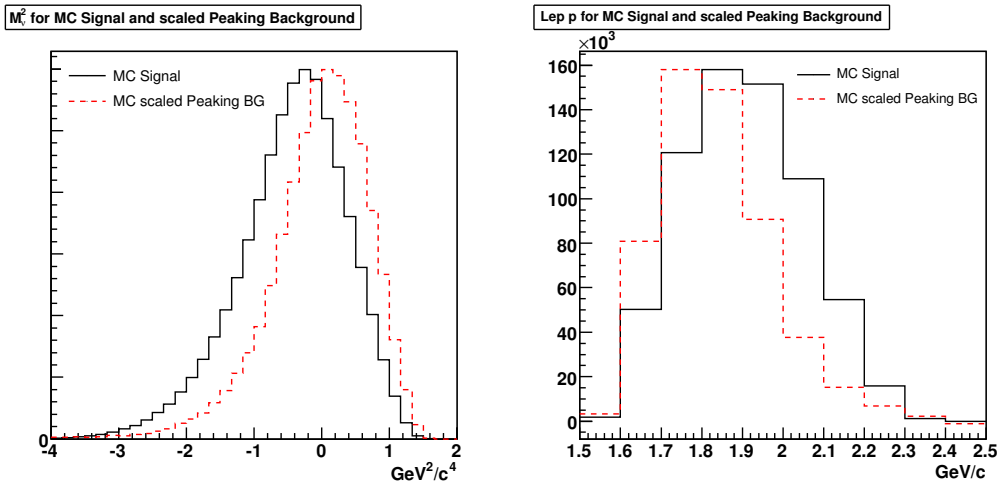

Figure 61: Comparison between Monte Carlo signal and Monte Carlo peaking background. Left: Monte Carlo signal (black) and peaking background (red) scaled for comparison in arbitrary units for the M_ν^2 distribution. Right Monte Carlo signal (black) and peaking background (red) scaled in arbitrary units for the distributions in the lepton momentum.

7 Systematic Errors

This section discusses the systematic errors considered in the analysis. Since the partial reconstruction technique is able to produce ample statistical data, the analysis is dominated by its systematics. Several systematic errors were considered in the analysis and are believed to adequately and completely describe the main sources of uncertainty on the analysis. Table 31 shows a summary of the systematic errors and their weight on the branching fraction measurement. Most errors are equal for both fitting methods. Errors which differ for each method are quoted for method 3 followed by the errors for method 2 in parentheses. The following sub-sections will describe in detail how these errors were determined.

Table 31: Systematic Errors Method 3 (Method 2)

Error Type	Error (%)	Source
PID	1.35%	PID Tweaking
Tracking efficiency	0.91%	Track Killing
Soft pion efficiency	0.53%	eff. variation
Radiative corrections	0.99%	rad. variation
Continuum Background	0.06%	$\pm 1\%$ on $\sigma_{q\bar{q}}$
Peaking Background	0.14%	D^{**} BF uncertainty
Combinatoric Background	0.72% (1.52%)	Shape Variation
Extraction fit	0.20% (0.30%)	fit error
B-Counting	1.1%	*BABAR*
$\mathcal{F}(w)$	1.02%	FF studies
$\mathcal{B}(D^{*+} \to D^0\pi^+)$	0.8%	[4]
f_{00}	1.2%	[4]
Total	**3.0% (3.3%)**	

7.1 PID Tweaking

The PID tweaking procedure was applied to reweight selection efficiencies in Monte Carlo due to the selectors used in the analysis to match the identification efficiency of data for these selectors. Selection efficiencies are reweighted in bins of track momentum p, polar angle θ and azimuthal angle ϕ. Each of the (p, θ, ϕ) bins have an associated error. This error is mainly governed by the amount of control data available in this channel and is

assessed in the PID tables by the PID group. Most PID tables have a very fine binning where bin numbers often reach 1900 bins per table and beyond. The result of this binning is that variations between individual bins are minor and the number of events in the control sample used to assess efficiency values for each bin become small. Errors quoted in the PID tables have been calculated using the binomial error on the efficiency ratio:

$$\Delta\varepsilon = \sqrt{\left(\frac{\varepsilon(1-\varepsilon)}{N}\right)} \tag{86}$$

where N is the number of events of the control sample in this bin. This assessment often leads to an inflated error such that the quoted errors in the PID tables cannot be used directly for a proper assessment of the systematic error. Instead a flat correction per particle type per track is assessed in this analysis for each efficiency in the PID tables. The general conservative consensus in *BABAR* is that PID tables can be trusted to about 1% accuracy [65]. A conservative study has been performed [66] examining PID uncertainties using alternately created PID tables from different control samples for this study. Based on this study we apply a symmetric uncertainty per track of 1% for electrons and 2% for muons (here ignoring a inflated statistical error on the muon sample in [66]). To assess a systematic uncertainty due to the PID, the tweaking procedure is repeated with the bin-by-bin error added, or subtracted, to the reweighting weights. The resulting data is then processed through the Monte Carlo tuning technique and analysis method 2 is repeated for the combined data set of Run 1 and 2 with both leptons choosing the RS MC combinatoric background. The difference in branching fraction compared to the unvaried result is considered the systematic uncertainty. Table 32 shows the background and signal yields for the up and downward variation of the PID tweaking error. The data here also shows that the PID error mainly results in a rescaling instead of a reshaping. Therefore, most of the uncertainty comes from the changing reconstruction efficiency. The efficiencies yielded 23.26% for the added and 22.66% for the subtracted error. The resulting branching fractions are $(4.83 \pm 0.01)\%$ for the added error and $(4.96 \pm 0.01)\%$ for the subtracted error where the quoted uncertainties are the statistical ones. This

yields a total systematic PID uncertainty of 1.35%. Figure 62 shows the comparison of the Monte Carlo combinatoric backgrounds, the signal and the D^{**} peaking background before and after the error variations. Similar to the systematic study on the tracking correction, the histograms show a slight rescaling while remaining constant in shape.

Table 32: Signal and background yields for PID tweaking variations

variation	type	signal region	sideband region
unvaried	Comb. Bg.	361367 ± 601	498676 ± 706
	Peaking Bg.	83603 ± 1778	754 ± 27
	Signal	661330 ± 2180	295 ± 17
$+1\sigma$	Comb. Bg.	361355 ± 601	498687 ± 706
	Peaking Bg.	83729 ± 1778	756 ± 27
	Signal	661199 ± 2180	295 ± 17
-1σ	Comb. Bg.	361380 ± 601	498665 ± 706
	Peaking Bg.	83460 ± 1779	752 ± 27
	Signal	661478 ± 2180	296 ± 17

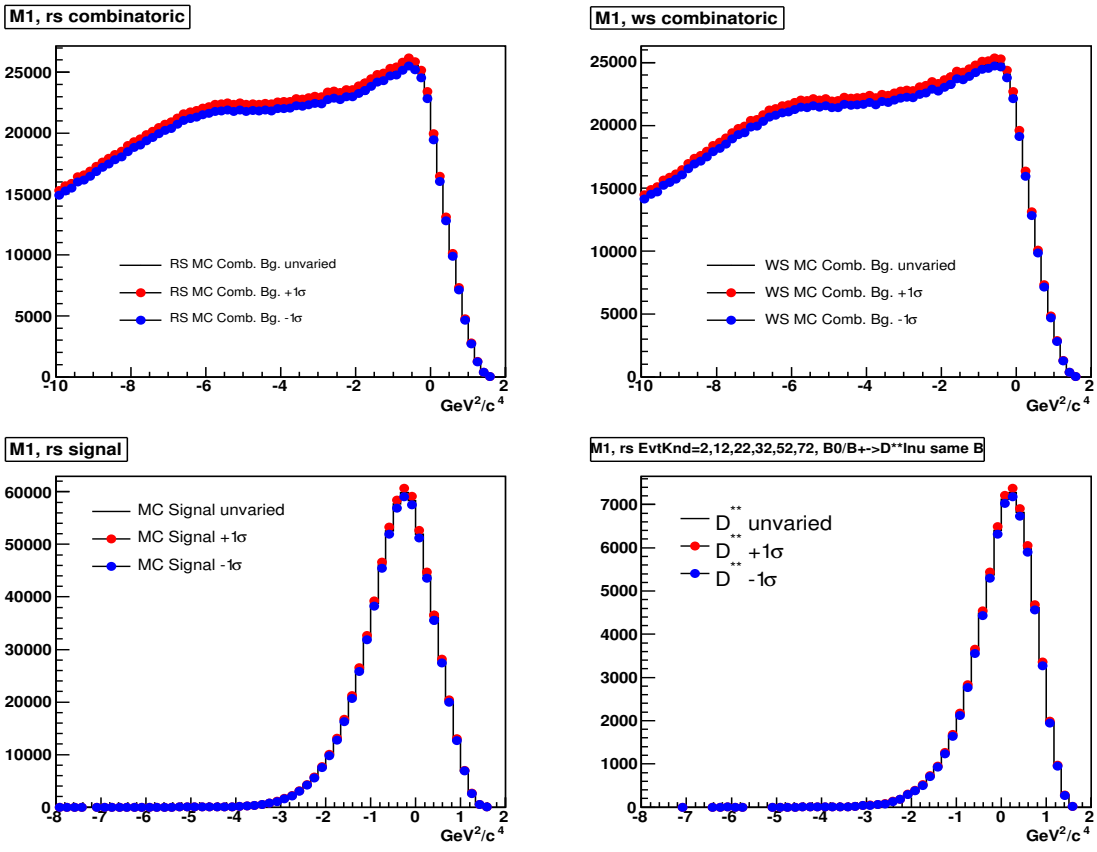

Figure 62: Results of the variation of the PID tweaking error for unvaried (black) error added (red) and error subtracted (blue) shapes.

7.2 Track Killing

As shown in Table 29 the tracking task force has determined systematic uncertainties due to track killing on a run by run basis. In the section on track killing in this dissertation it was shown that the tracking correction results merely in a rescaling and not reshaping of the overall data. Most of the analysis is only sensitive to reshaping effects except for the determination of the overall reconstruction efficiency. Since this efficiency scales linearly with the amount of Monte Carlo data accepted, it should scale linearly with the tracking error. The track killing procedure is implemented on the nTuple level as a true track killing and not reweighting. Since the systematics are larger than the actual killing percentage it is only possible to vary the systematic error downward, resulting in more tracks being killed since similar to the PID tweaking procedure tracks which were ignored on the skimming level cannot be reconstructed on the nTuple level. However, as described above, scaling is flat, so the error can be regarded as symmetric. Therefore the error will only be varied downward and considered symmetric in both directions. To assess a systematic error due to tracking, the track killing algorithm was rerun with the added systematic errors. The data was then processed through the Monte Carlo tuning technique and the analysis was repeated with the one dimensional fitting method (method 2) for the combined Runs 1 and 2 and both leptons. The difference in branching fraction is considered a systematic error. Table 33 shows the resulting signal and background yields. It can be seen that the signal yield remains almost unchanged since track killing only rescales and not reshapes. The main difference comes from the change in efficiencies which is sensitive to rescaling. The reconstruction efficiency changed from 22.96% from the unvaried case to 22.75%. The corresponding branching fraction is $(4.94 \pm 0.01)\%$ where the quoted error is the statistical error. Compared to the unvaried case this translates to a systematic uncertainty due to tracking of 0.91%. Figures 63 and 64 show the comparison of the Monte Carlo combinatoric backgrounds, the signal and the D^{**} peaking background before and after the error was varied. For the pull plots again the average track killing error was chosen weighted by the run luminosities. Variations are

mainly from scaling as before. Table 34 shows the offset and slope parameters showing slight scaling and flatness within error.

Table 33: Signal and background yields for track killing variations

variation	type	signal region	sideband region
unvaried	Comb. Bg.	361367 ± 601	498676 ± 706
	Peaking Bg.	83603 ± 1778	754 ± 27
	Signal	661330 ± 2180	295 ± 17
$+1\sigma$	Comb. Bg.	361337 ± 601	498657 ± 706
	Peaking Bg.	83650 ± 1780	768 ± 27
	Signal	661329 ± 2181	295 ± 17

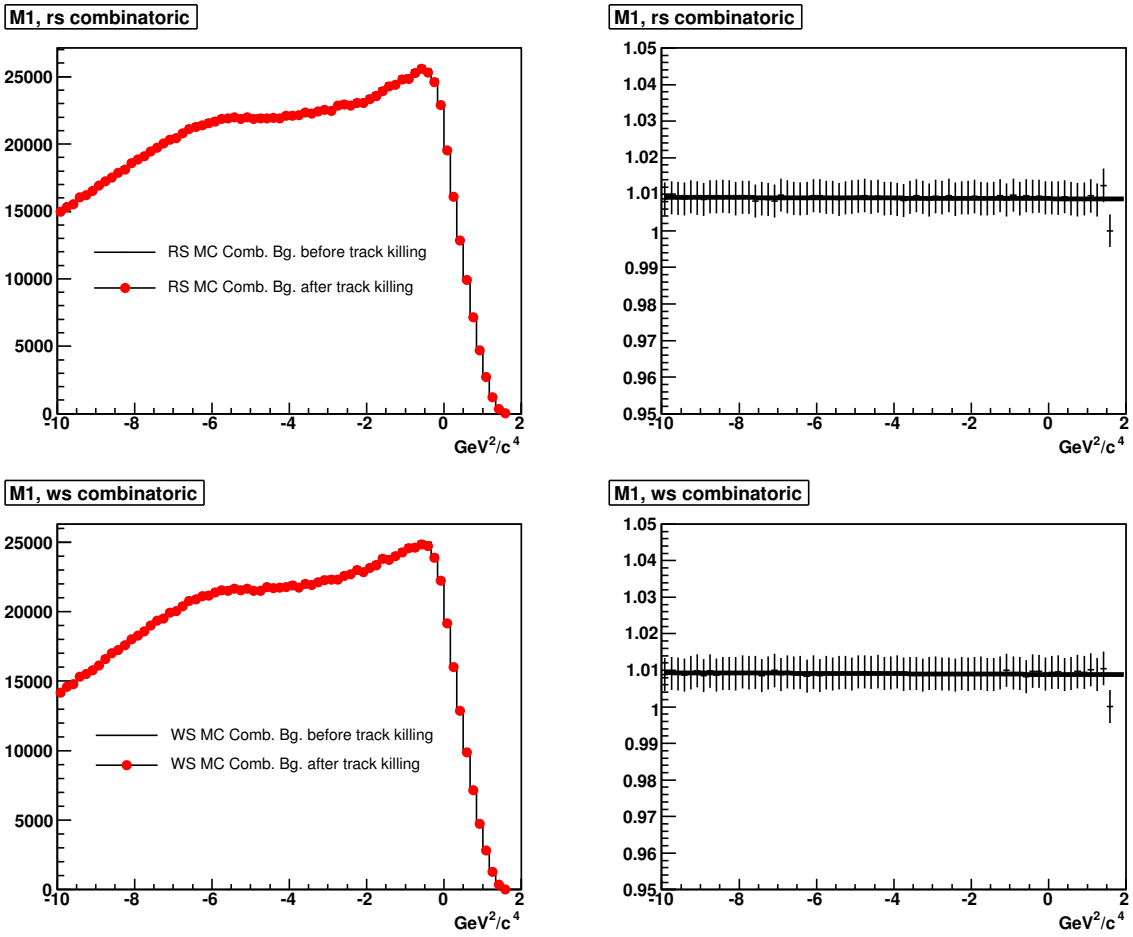

Figure 63: RS MC (top) and WS MC (bottom) combinatoric background before (black) and after (red) the systematic error was added to the track killing correction together with their before to after pull plots.

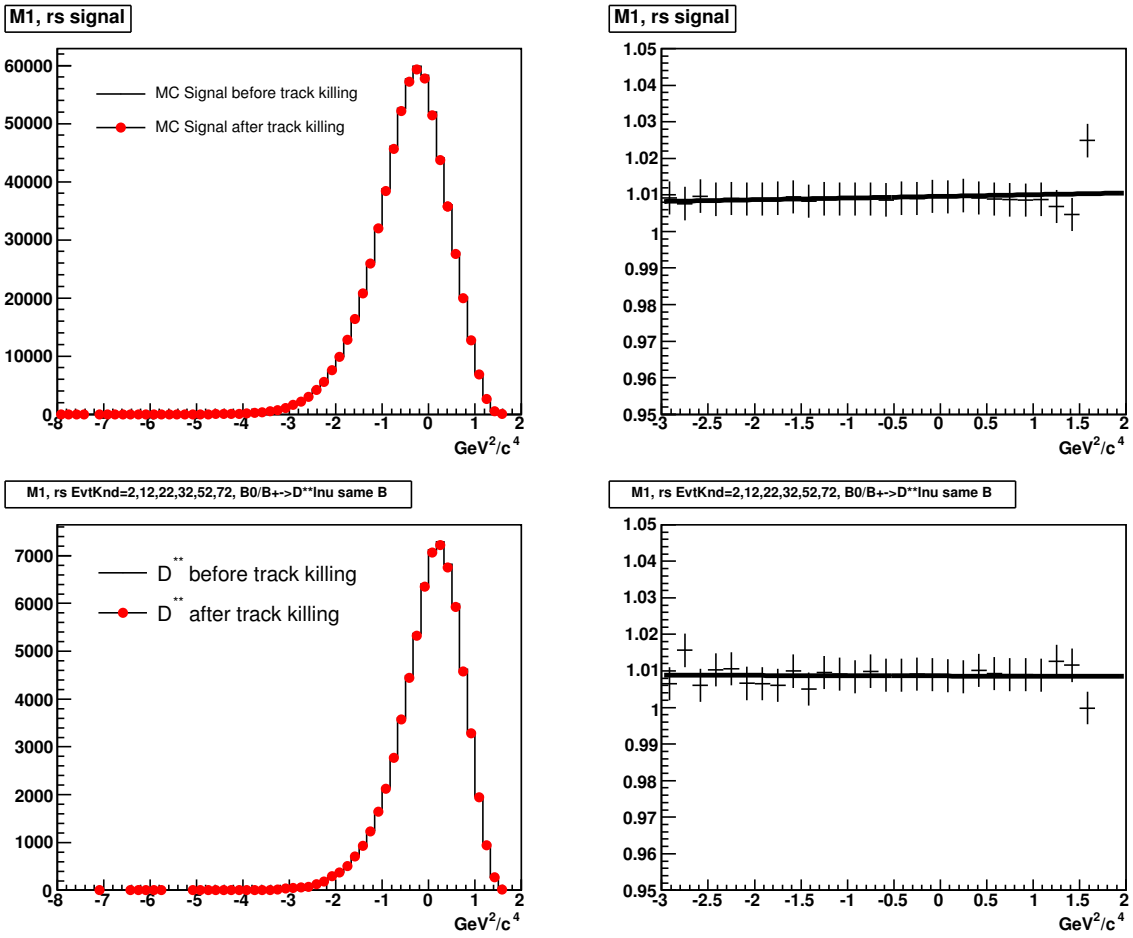

Figure 64: MC Signal (top) and D^{**} peaking background (bottom) before (black) and after (red) the systematic error was added to the track killing correction together with their before to after pull plots.

Table 34: Slope and offset parameters for track killing pull fits

Histogram	Offset	Slope (%)
RS MC Comb. BG.	1.0088 ± 0.0009	$(-0.4 \pm 1.6) \times 10^{-4}$
WS MC Comb. BG.	1.0089 ± 0.0009	$(-0.5 \pm 1.6) \times 10^{-4}$
Signal	1.0096 ± 0.0010	$(4.6 \pm 6.4) \times 10^{-4}$
D^{**} BG.	1.0086 ± 0.0010	$(-0.7 \pm 6.4) \times 10^{-4}$

7.3 Soft pion efficiency

One of the differences between data and Monte Carlo control samples is the modeled behavior of the detector for very slow pions at the limit of detectability. These slow pions curl up inside the SVT and have high errors associated with their reconstruction. For this reason a separate study to the PID and tracking study is performed to assess a systematic error to the low pion turn on efficiency dependence between data and Monte Carlo. The relative detector soft pion turn on efficiency, which describes the probability to detect a slow pion according to its momentum, can be adequately modeled by a two parameter function [67]:

$$\varepsilon_p = \begin{cases} 1 - \frac{1}{\beta(p-p_0)+1} & \text{if } p > p_0 \\ 0 & \text{otherwise} \end{cases} \tag{87}$$

Here β describes the steepness of the turn on curve and p_0 the turn on point. Values for these parameters have been recently determined by [68] for R22 data and Monte Carlo to be $\beta = 21.0713 \pm 0.2206$ and $p_0 = (0.0269 \pm 0.0001)$ GeV/c for data and $\beta = 17.5988 \pm 0.1180$ and $p_0 = (0.0260 \pm 0.0001)$ GeV/c for Monte Carlo using a helicity distribution method. Details on this method can be found in [67]. Figure 65 shows the shape of the soft pion turn on curve for data and Monte Carlo together with a pull plot between their differences where the errors have been properly propagated from the uncertainties on the parameters. The plot shows that the introduced cut in the lab frame of the pion momentum at $p_\pi(lab) < 80$ MeV/c eliminates data from the area in which data and Monte Carlo differ the most. This area is depicted in the pull plot by its steepness. The soft pion momentum range chosen for the analysis therefore only contains the area in which Monte Carlo and data start to agree well indicated by the relative flatness of the pull plot above 80 MeV/c. Again of interest is only the slope of the pull since rescaling effects are absorbed during yield extraction fits. The pull plot shows a slight shallowing negative slope in the area of interest which gives rise to a systematic dependence of the analysis to the soft pion efficiencies. To assess an error on this effect, Monte Carlo data has been reweighted with the ratio of data to Monte Carlo

soft pion efficiencies and the analysis has been repeated. The ratios were also varied by parameter errors causing maximum deviation by varying the β and p_0 parameters for Monte Carlo and data anti-parallel in each respect (example: β_{MC} up and β_{data} down and vice versa) and the analysis was repeated. The one dimensional fitting method for the RS MC combinatoric background, both runs and both leptons was again chosen for this assessment. The average deviation in branching fractions is then considered the systematic error. The reconstruction efficiency does not need to be reevaluated with this technique, since the above efficiency relation (87) is valid for the relative and not absolute efficiency. Table 35 shows the extraction yields as well as the efficiencies obtained for each variation. The resulting systematic uncertainty assessed for this effect is 0.53%. Figures 66 and 67 show the shape changes of the RS MC and WS MC combinatoric background, the MC signal, the D^{**} peaking background as well as their pulls before and after variation. Each shape shows non negative slopes above error. The strongest reshaping occurs on the D^{**} peaking background since this decay produces the most soft pions. This is also the shape which contributes the most to the systematic error of this section.

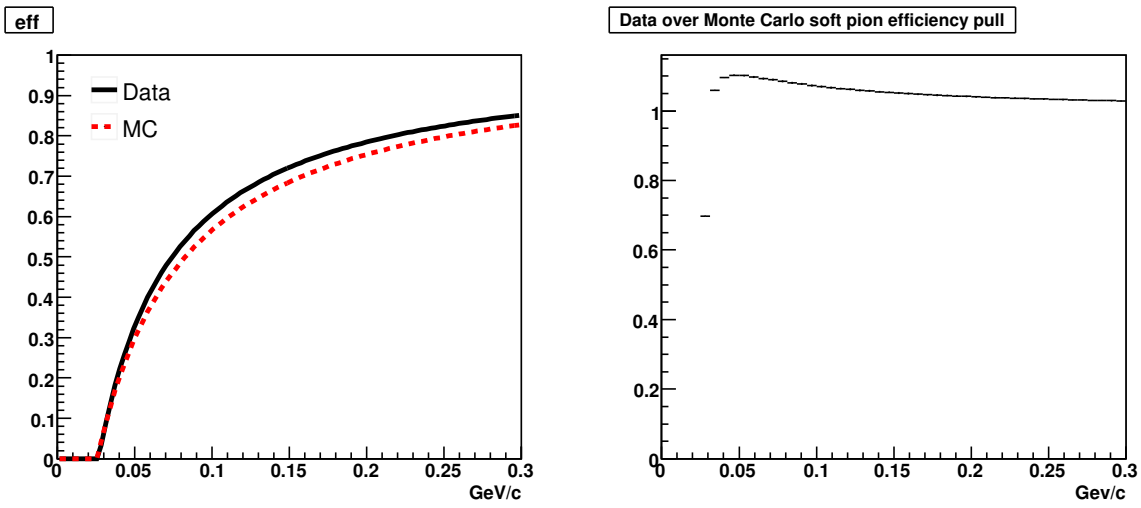

Figure 65: Differences in the relative soft pion turn (left) on curve for data (black) and Monte Carlo (red) and the pull between these values (right).

Table 35: Extraction yields for soft pion correction

variation	type	signal region	sideband region
unvaried	Comb. Bg.	361367 ± 601	498676 ± 706
	Peaking Bg.	83603 ± 1778	754 ± 27
	Signal	661330 ± 2180	295 ± 17
normal weight	Comb. Bg.	360980 ± 601	498637 ± 706
	Peaking Bg.	80482 ± 1759	793 ± 28
	Signal	664865 ± 2163	296 ± 17
Data: β up, p_0 down	Comb. Bg.	360955 ± 601	498675 ± 706
MC: β down, p_0 up	Peaking Bg.	80750 ± 1758	798 ± 28
	Signal	664606 ± 2163	296 ± 17
Data: β down, p_0 up	Comb. Bg.	361004 ± 601	498599 ± 706
MC: β up, p_0 down	Peaking Bg.	80211 ± 1759	789 ± 28
	Signal	665127 ± 2164	297 ± 17

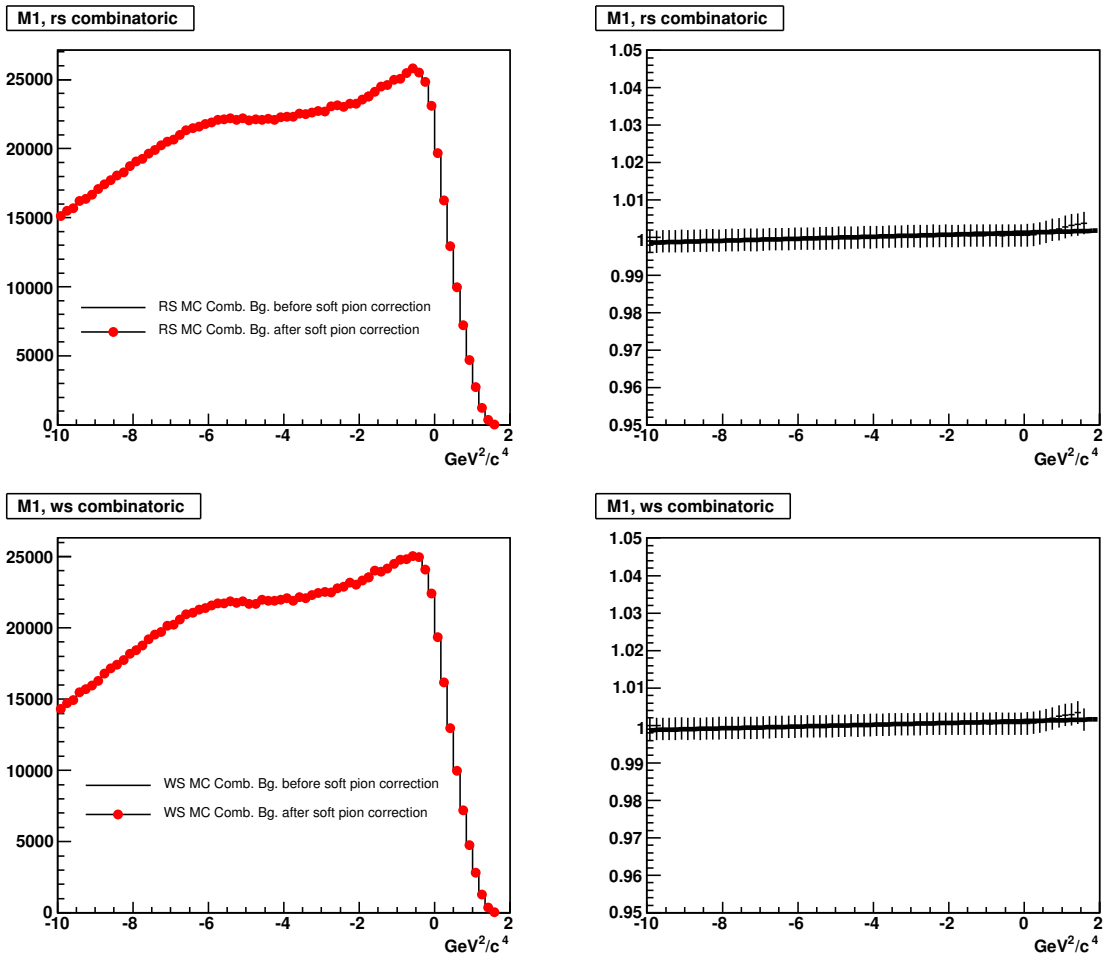

Figure 66: Comparison of the RS MC (top) and WS MC combinatoric background scaled to equal areas before (black) and after (red) the soft pion correction has been applied.

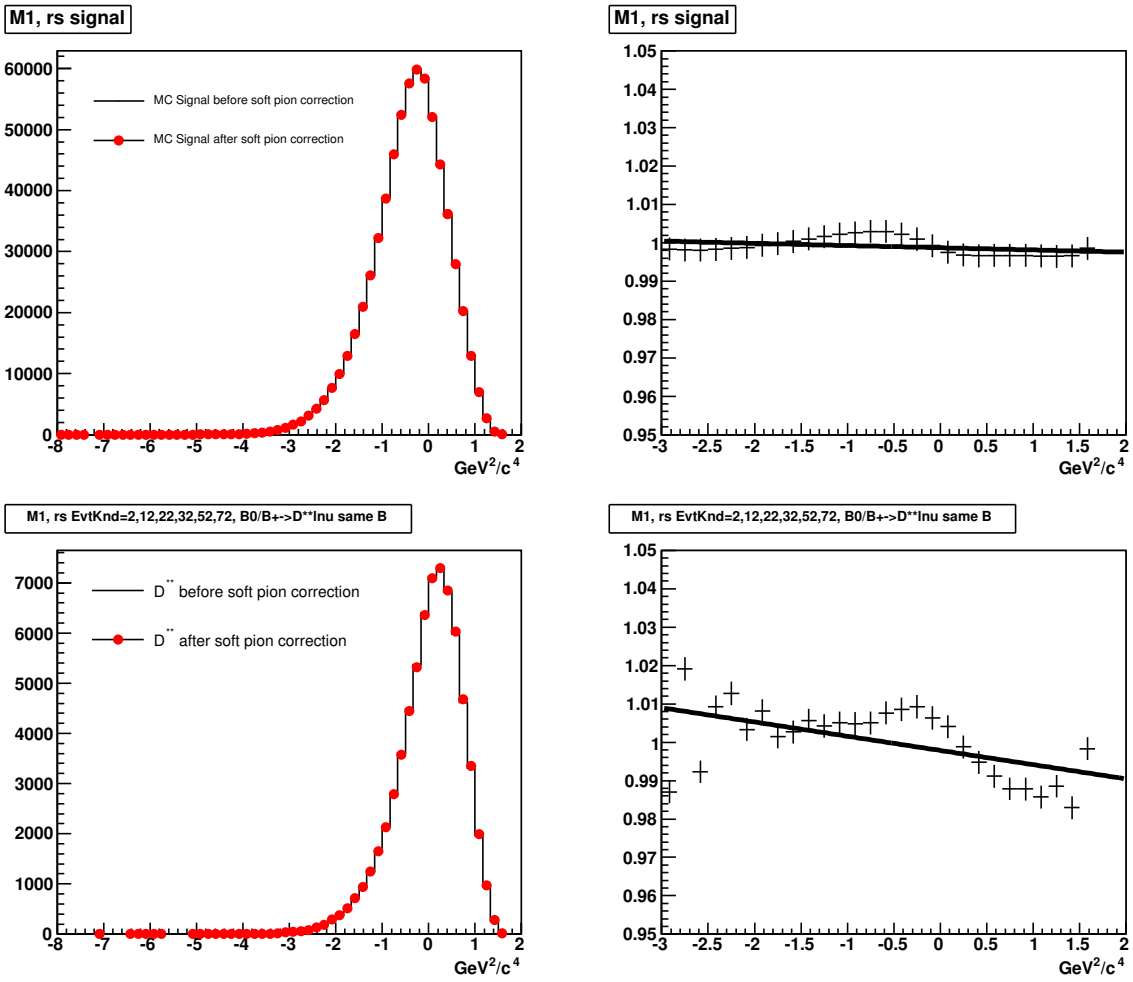

Figure 67: Comparison of the signal (top) and D^{**} peaking background scaled to equal areas before (black) and after (red) the soft pion correction has been applied.

Table 36: Slope and offset parameters soft pion correction pull fits

Histogram	Offset	Slope (%)
RS MC Comb. BG.	1.0013 ± 0.0006	$(2.7 \pm 1.1) \times 10^{-4}$
WS MC Comb. BG.	1.0012 ± 0.0006	$(2.4 \pm 1.1) \times 10^{-4}$
Signal	0.9987 ± 0.0006	$(-5.8 \pm 4.2) \times 10^{-4}$
D^{**} BG.	0.9979 ± 0.0006	$(-37.0 \pm 4.2) \times 10^{-4}$

7.4 Radiative Corrections

In the *BABAR* Monte Carlo bremsstrahlung is described by the PHOTOS package [55]. According to the LUND truth tables, in about 30% of the cases one or more photons are produced in addition to the other particles. The energy of the emitted photon(s) is large enough that the M_ν^2 distribution is somewhat altered as was shown earlier. To assess a systematic uncertainty due to these radiative decays the analysis was repeated varying the amount of radiative decays of the signal decay by 30% [69] up and down. This variation causes a slight shift in the M_ν^2 distribution of the signal. Signal extraction was performed using the one dimensional fitting method with a combined sample of both runs and both leptons. The difference in branching fraction is considered the systematic error due to photon uncertainties and is determined to be 0.99%. Table 37 shows the signal and background yields for the two variations. Differences are fairly similar so that the error is considered to be symmetric. Figure 68 shows the change in the signal shape due to the variations. While changes are minor a slight shift in the signal can be observed due to the radiative variations. This shift can be clearly seen in the pull plots which shows a shift of the signal towards lower (higher) values on the M_ν^2 mass axis for less (more) photon admixture. This is expected from the previous energy-momentum considerations of section 4.4. Errors on the pull plots are arbitrary since no error is considered on the amount of the variation.

Table 37: Signal and background yields for a 30% variation on the photon admixture of the MC signal

variation	type	signal region	sideband region
unvaried	Comb. Bg.	361367 ± 601	498676 ± 706
	Peaking Bg.	83603 ± 1778	754 ± 27
	Signal	661330 ± 2180	295 ± 17
$+1\sigma$	Comb. Bg.	361585 ± 601	498976 ± 706
	Peaking Bg.	76729 ± 1797	754 ± 27
	Signal	667887 ± 2202	290 ± 17
-1σ	Comb. Bg.	361155 ± 601	498384 ± 706
	Peaking Bg.	90375 ± 1760	755 ± 27
	Signal	654863 ± 2158	300 ± 17

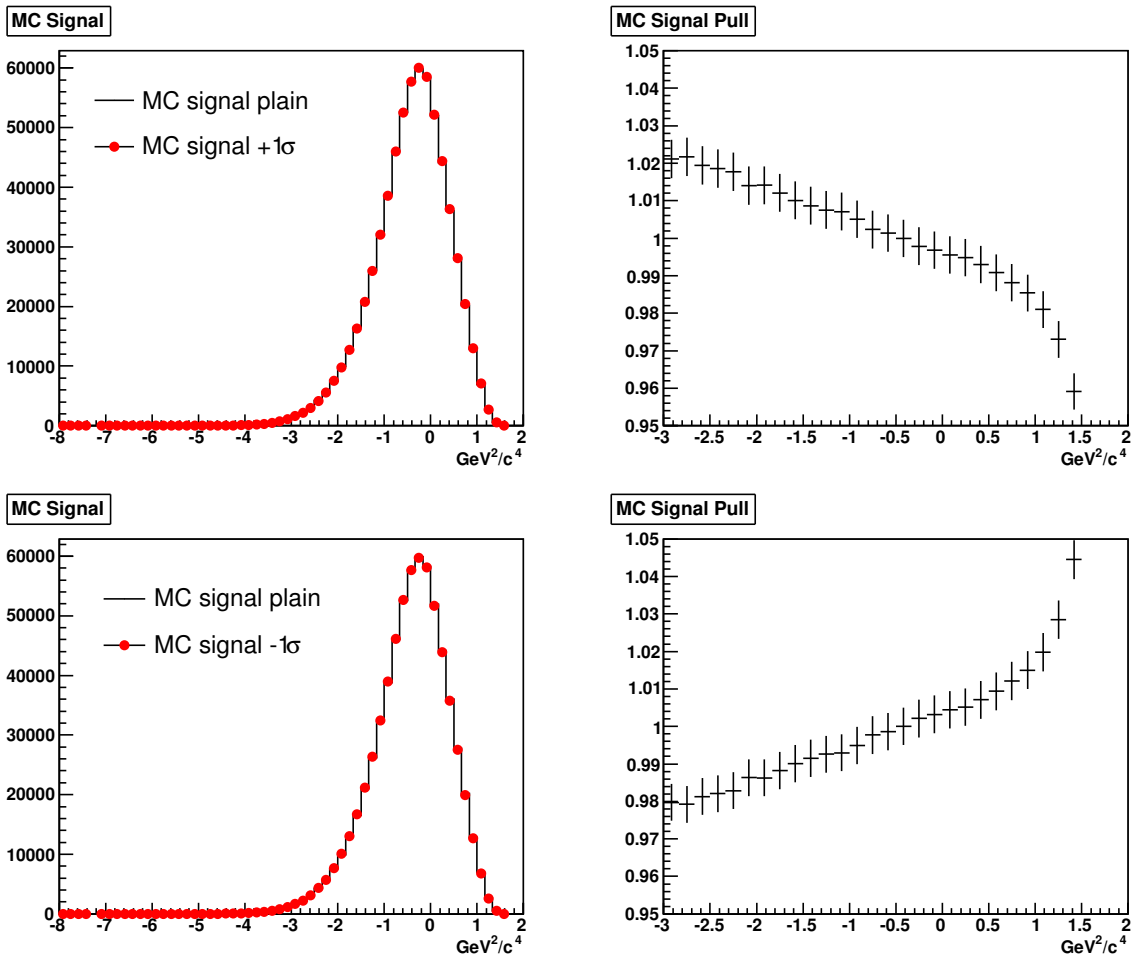

Figure 68: Change of the MC signal shape due to a 30% radiative variation for more (top) and less (bottom) radiative contribution to the decay.

7.5 Background Shapes

Different methods were applied to access the systematic uncertainty on the analysis due to the different background shapes.

7.5.1 Continuum Background

The continuum background for this analysis is obtained from a direct measurement with beam energies tuned away from the $\Upsilon(4S)$ resonance. No Monte Carlo data is generated nor needed for this background. For this reason no shape adjustments between data and Monte Carlo have to be considered. Since this was the dominant reason for systematics in the previous sections the error due to the uncertainty on the continuum background is

the smallest of the considered errors. To assess an error to this background the number of events of continuum background obtained from the off resonance measurement was varied by 1% according to the error on the on-peak over the off-peak cross section for continuum events [47]. This ratio is responsible for the energy dependence of the luminosity scale factor applied to the continuum background. Therefore, the error translates directly into a scale error and the continuum background scale factor can be varied instead. This is done in this analysis and the one dimensional fit method with the RS MC combinatoric background for a combined sample of both runs and leptons is repeated as before. Since the continuum background does not contribute to the determination of the reconstruction efficiency, no change in efficiency needs to be considered. The reweighted data set also does not need to be processed with different Monte Carlo tuning parameters since the Monte Carlo remains unchanged in this error assessment. The difference in branching fraction from the variation of the continuum background by $\pm 1\sigma$ is considered to be its systematic error on this analysis. The resulting error was determined to be 0.06%. Due to the similarity in shapes of the continuum and the combinatoric background, the refitting of the combinatoric background during the signal extraction fit makes up most of the difference introduced from the continuum background variation. Hence the dependence on this error is very small, as was expected.

7.5.2 Peaking Background

The dominant contribution to the peaking background decays coming from the charm meson doublets $[D_1(2420), D_2^*(2460)]$ and $[D_0^*(2400), D_1'(2430)]$ are used to assess a systematic error to the analysis due to the uncertainty on the peaking background. Since these contributions constitute about 85% of the total peaking background, the other shapes are again kept constant in this assessment. Also the $D_0^*(2400)$ mode is ignored in this study since it does not decay into the signal decay products. The error is assessed by varying each D^{**} state by one σ of its error up and down while keeping the others at their nominal value. The analysis is repeated and the difference in branching fraction recorded.

This step is repeated for each D^{**} mode individually. The differences in the branching fractions are summed in quadrature and the result is considered the systematic error. It should be noted that variation of the peaking background does not change the overall reconstruction efficiency which only depends on signal decays. Variation only results in a different admixture of states in the D^{**} peaking background, thus slightly varying its shape. This shape variation is responsible for the systematic error since rescaling will be compensated by the signal extraction fit. The branching fractions are again determined by the one dimensional fit method using the RS MC combinatoric background and data from both runs and both leptons. Since the reconstruction efficiency remains unaffected by this technique systematics are small. The overall systematic error assessed due to the uncertainty on the peaking background is 0.14%. Table 38 shows a summary of the signal and peaking background extraction yields for the different variations. The combinatoric background remained constant through the extractions except for minor statistical fluctuations. Figures 69 through 71 show the shape and scale variation of the D^{**} peaking background due to these admixture variations. The errors on the pull plots are chosen arbitrarily. The figures again show that although varying the admixture results can result in large rescaling effects, reshaping is only minor indicated by the flat slope of the pull plots. This is the reason for the only minor dependence on peaking background branching fractions of this analysis.

Table 38: Signal and background yields for the systematic variation on the peaking background

variation	type	signal region	sideband region
unvaried	Peaking Bg.	83603 ± 1778	754 ± 27
	Signal	661330 ± 2180	295 ± 17
$D_1 + 1\sigma$	Peaking Bg.	83223 ± 1770	754 ± 27
	Signal	661738 ± 2172	295 ± 17
$D_1 - 1\sigma$	Peaking Bg.	84019 ± 1788	754 ± 27
	Signal	660884 ± 2189	295 ± 17
$D_1' + 1\sigma$	Peaking Bg.	84249 ± 1794	755 ± 27
	Signal	660648 ± 2194	295 ± 17
$D_1' - 1\sigma$	Peaking Bg.	82765 ± 1759	754 ± 27
	Signal	662216 ± 2162	296 ± 17
$D_2^* + 1\sigma$	Peaking Bg.	83619 ± 1779	754 ± 27
	Signal	661306 ± 2180	295 ± 17
$D_2^* - 1\sigma$	Peaking Bg.	83587 ± 1778	754 ± 27
	Signal	661356 ± 2179	295 ± 17

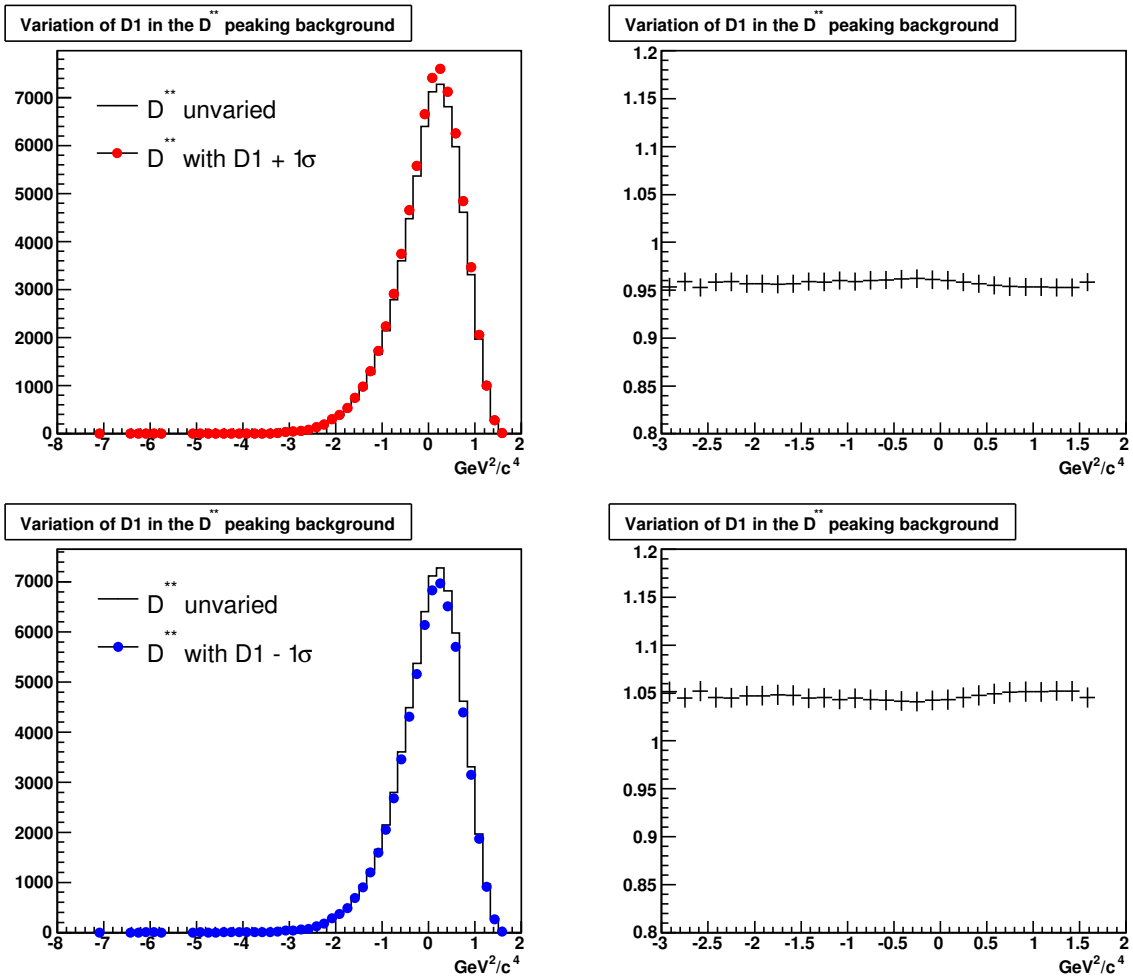

Figure 69: Variation of the $D1$ contribution to the D^{**} peaking background. Shown are the unvaried shape (black) and the total D^{**} shape with a variation of $+1\sigma$ (red) and -1σ.

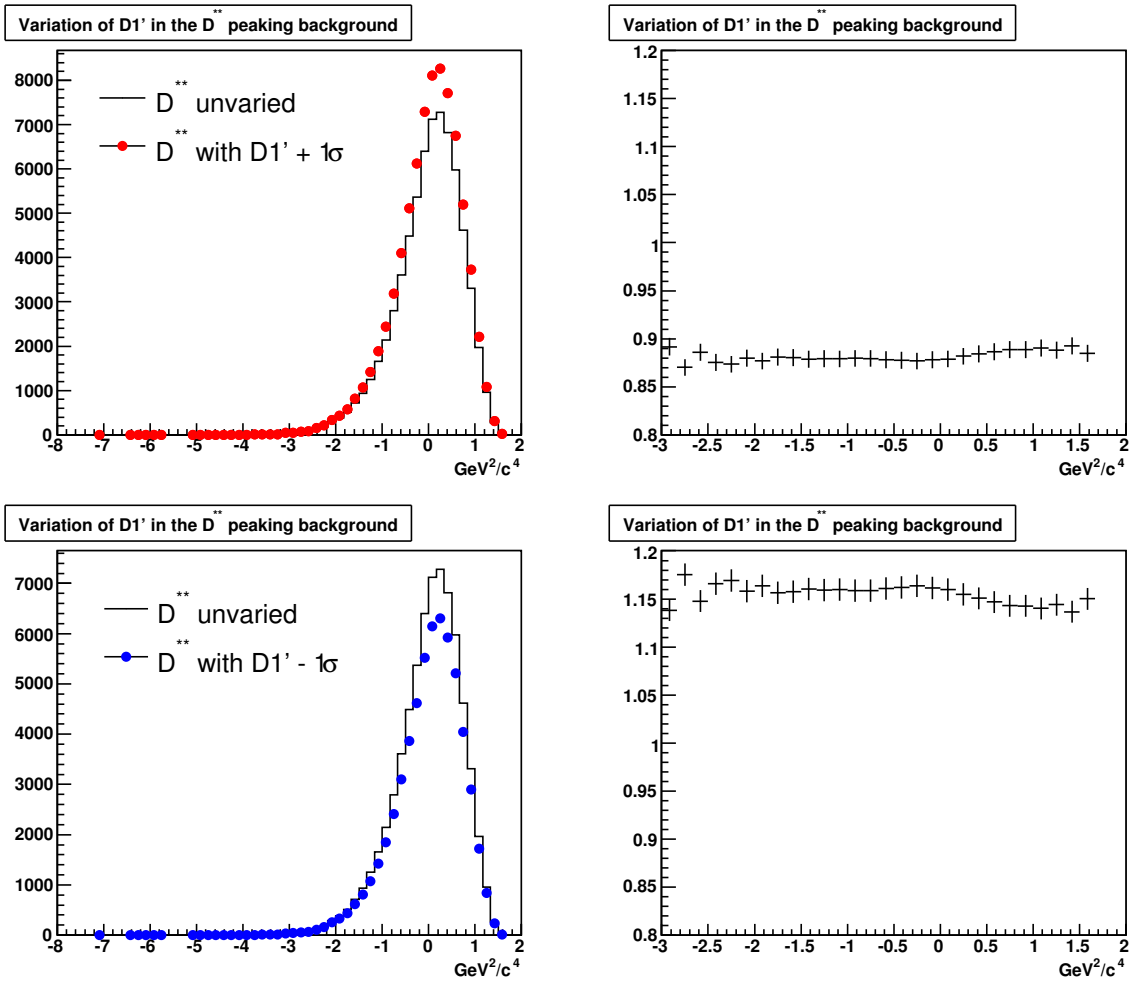

Figure 70: Variation of the $D1'$ contribution to the D^{**} peaking background. Shown are the unvaried shape (black) and the total D^{**} shape with a variation of $+1\sigma$ (red) and -1σ.

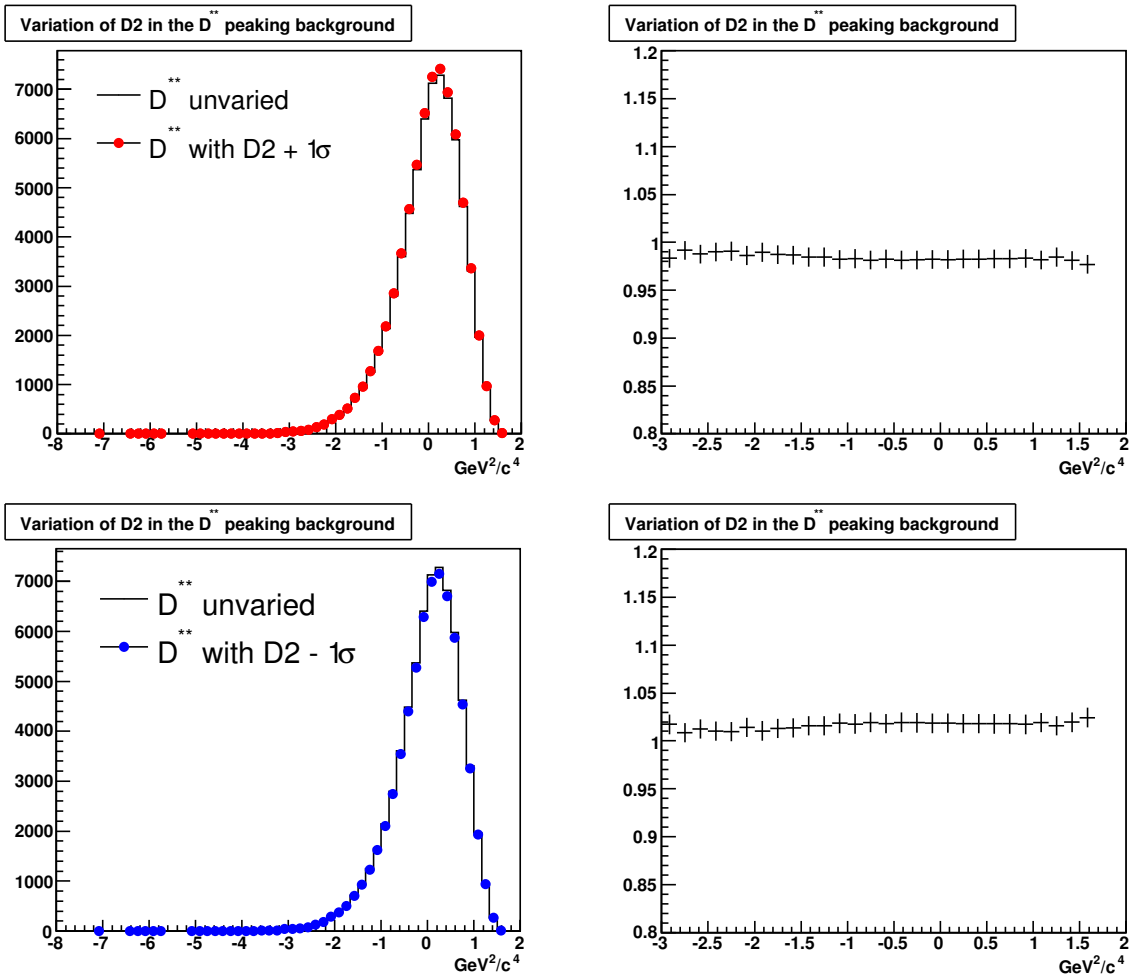

Figure 71: Variation of the $D2$ contribution to the D^{**} peaking background. Shown are the unvaried shape (black) and the total D^{**} shape with a variation of $+1\sigma$ (red) and -1σ.

7.5.3 Combinatoric Background

Throughout the analysis the $\mathcal{B}(\bar{B}^0 \to D^{*+}\ell^-\bar{\nu}_\ell)$ branching fraction was determined using the three different types of RS MC, WS MC and WS data combinatoric background. The differences in the resulting branching fractions are used to assess a systematic error on the analysis for each individual method due to this background. The systematic error is assessed by averaging the deviation of the individual measurements shown in Table 42 weighted by their confidence levels and luminosities. The systematic error is therefore:

$$\Delta BF_{avg} = \frac{1}{\mathcal{L}_{tot}} \cdot \sum_i \mathcal{L}_i \cdot \left(\frac{\sum_j |\Delta BF_{ij}| \cdot CL_{ij}}{\sum_j CL_{ij}} \right) \tag{88}$$

where $\mathcal{L}_i$ is the luminosity of the i^{th} run, CL_{ij} is the confidence level of the j^{th} branching fraction measurement of the i^{th} run and ΔBF_{ij} is the j^{th} branching fraction difference to the overall average of the i^{th} run. j represents the RC MC, WS MC or WS data combinatoric background measurement. This yields an overall systematic error 1.52% for method 2 (1D) and of 0.72% for method 3 (2D) due to this background shape.

7.6 Fit Error

The uncertainties due to the signal extraction fits are considered a systematic error σ_{syst} in the analysis. The error is taken as the residual uncertainty of the fitting procedure σ_{fit} and removing its statistical error σ_{stat} from the relation $\sigma_{fit}^2 = \sigma_{stat}^2 + \sigma_{syst}^2$. The statistical error σ_{stat} was previously determined by equation (79) in section 5.3. σ_{fit} is taken from the yield extraction tables of the fit methods as the reported fitting error on the signal. This results in a systematic error σ_{syst} due to fitting of 0.30% for method 2 (1D) and 0.20% for method 3 (2D).

7.7 Form Factor dependence

Since some of the essential assumptions of this analysis, such as the expected signal shape, are purely dependent on Monte Carlo production, the knowledge of the form factor of the signal decay plays an essential role in the determination of the branching fraction. As shown before in section 6.2.1, *BABAR* software provides reweighting packages to reshape Monte Carlo data according to new form factor values. Since Monte Carlo production for this analysis is based on SP8, the Monte Carlo signal shape is first reweighted to match the most recent form factor values reported by *BABAR* in [23]. The current values of $R_1(1)$, $R_2(2)$ and ρ^2 during this analysis including their errors are shown in Table 27.

To estimate the systematic error introduced by the uncertainties in the form factor the parameters $\rho^2, R_1(1)$ and $R_2(1)$ are each varied by the total of their quoted errors and the Monte Carlo data is reweighted. The analysis is repeated using signal extraction method 2, which is believed to be most dependent on these variations. Since Monte Carlo data is also used to find the detector efficiency, it is necessary to reevaluate the proper efficiency values each time. The analysis is only done on the combined data for Run 1 and 2 and for both combined samples of electrons and muons, since the separation of these samples has already been used for cross check. Each variation in the branching fraction is recorded and considered to be the systematic error due to the specific form factor parameter. The overall error is obtained by adding the mean error of each parameter in quadrature as a conservative estimate of the systematic error in the branching fraction due to this dependence. The results are summarized in Tables 39 through 41 below.

7.7.1 Reweighting Effects

As shown in equation (39) in section 1.7.2, the form factor is described in the variable w which is related to the square of the momentum transfer of the B meson to the W boson. A high value of w corresponds to a low lepton momentum and vice versa. In a proper signal decay, the remaining momentum is distributed between the neutrino and the D^* meson. Since the slow pion momentum is directly proportional to the D^* momentum,

a high momentum lepton favors a low momentum slow signal pion. The form factor $\mathcal{F}(w)$ directly shapes the differential decay rate (38) and therefore the lepton and pion momentum spectra. Figures 72, 73 and 74 show the effect of each variation of the form factor parameters. The top left plot shows the variation of the actual form factor in w space. The top right shows the true Monte Carlo signal for the form factor variations. The bottom left shows the distribution of pion momenta for RS Monte Carlo events and the bottom right shows the distribution of lepton momenta for RS Monte Carlo events for the signal decay. All graphs are color coded as follows: Unvaried (black), $+1\sigma$ (red), -1σ (blue). Changes in shapes due to form factor errors are small in all variations and histograms. The discussed dependence on the momentum spectra can be best seen in Figure 72 where the the steeper (more shallow) descending form factor causes a decrease (increase) of soft pion momentum in the higher momentum region around 200 MeV/c. This effect is not as evident on the lepton momentum spectrum which is much stronger shaped by the χ vertex probability cut than the pion momentum spectrum. While variations on the Monte Carlo signal shape, which is needed for the extraction of the detector efficiency, are minor, a general trend can be seen in Figures 72 and 74. A steeper form factor slope causes a slight shift in the signal peak towards higher values in the M_ν^2 plot. Since the separation between the signal peak and the peak of peaking background is used to extract this background, this small shift shows the largest effect off the systematic error of the form factor on the signal extraction.

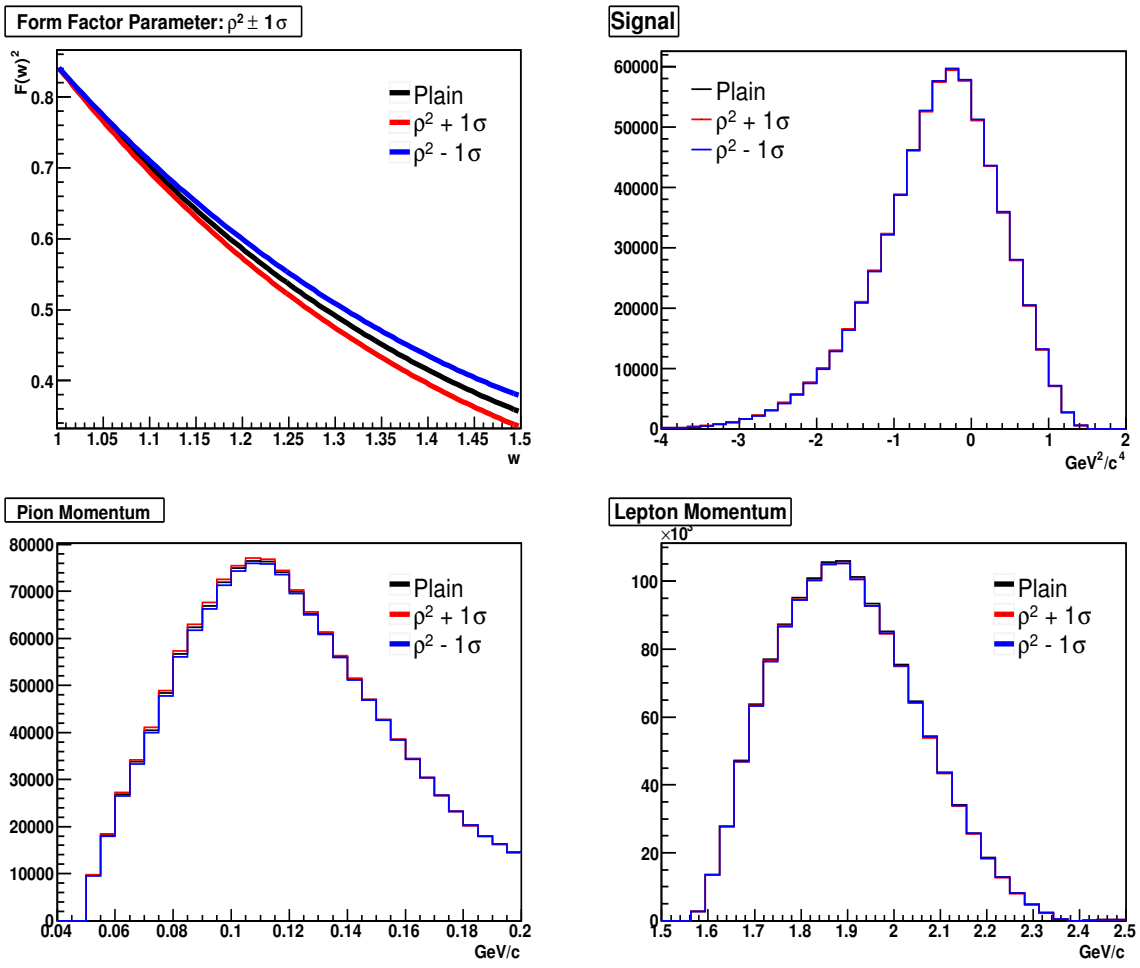

Figure 72: Form factor reweighting effects for the variation of ρ^2 by 1σ. All graphs are color codes as follows: Unvaried (black), $\rho^2 + 1\sigma$ (red), $\rho^2 - 1\sigma$ (blue): Top: (left) Effects of parameter variations on the $\mathcal{F}(w)^2$ versus w distribution. (right) Monte Carlo true signal for the form factor variations. Bottom: (left) Slow Pion momentum distribution for RS Monte Carlo form neutral B decays. (right) Lepton momentum distribution for RS Monte Carlo from neutral B decays.

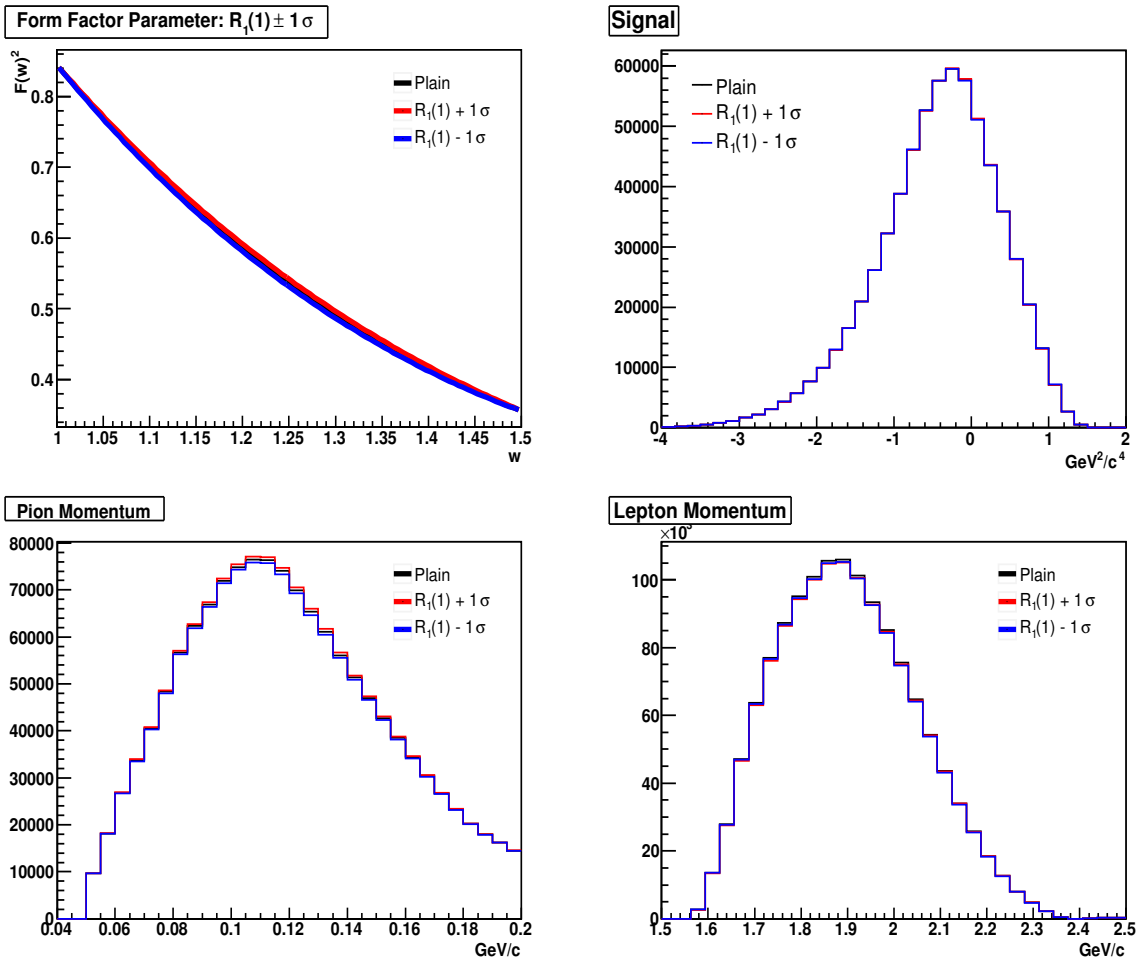

Figure 73: Form factor reweighting effects for the variation of $R_1(1)$ by 1σ. All graphs are color codes as follows: Unvaried (black), $R_1(1) + 1\sigma$ (red), $R_1(1) - 1\sigma$ (blue): Top: (left) Effects of parameter variations on the $\mathcal{F}(w)^2$ versus w distribution. (right) Monte Carlo true signal for the form factor variations. Bottom: (left) Slow Pion momentum distribution for RS Monte Carlo form neutral B decays. (right) Lepton momentum distribution for RS Monte Carlo from neutral B decays.

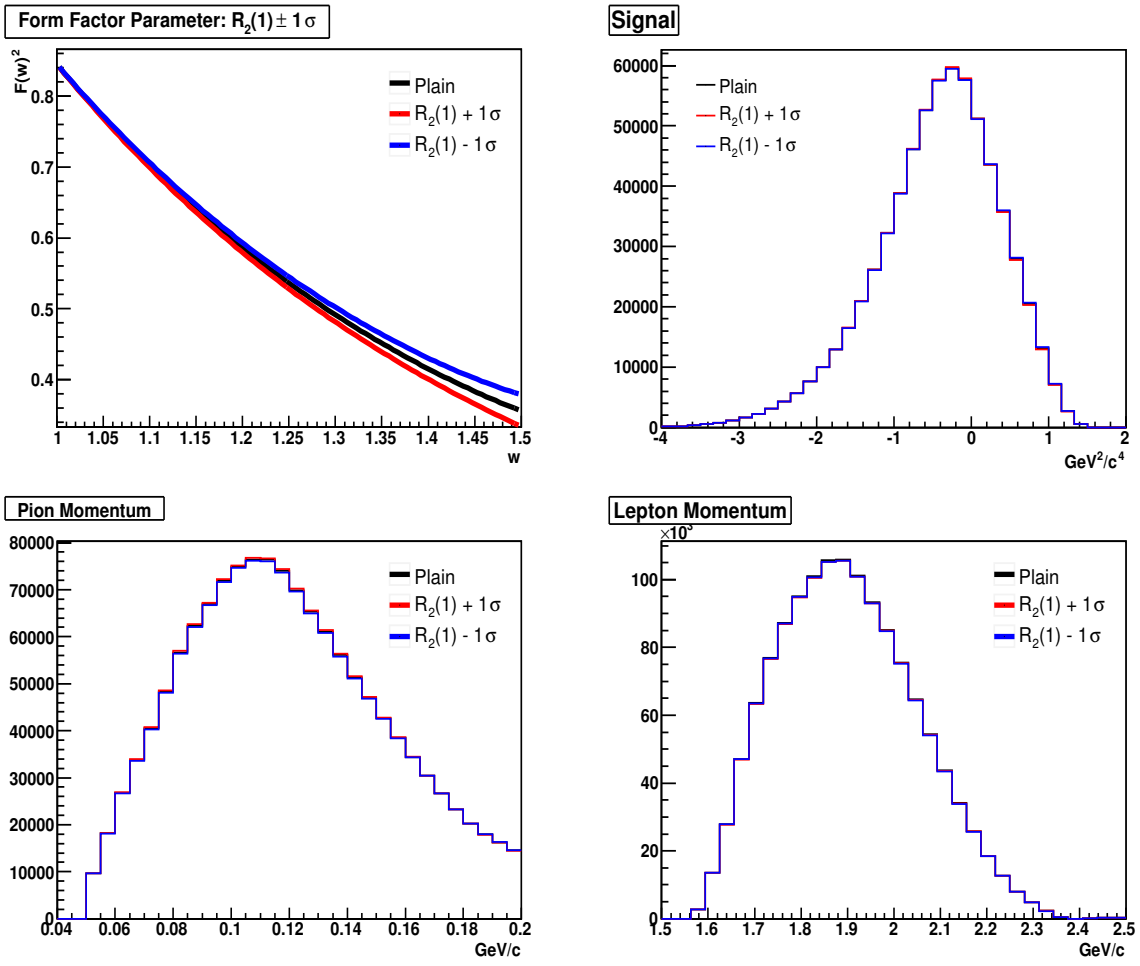

Figure 74: Form factor reweighting effects for the variation of $R_2(1)$ by 1σ. All graphs are color codes as follows: Unvaried (black), $R_2(1) + 1\sigma$ (red), $R_2(1) - 1\sigma$ (blue): Top: (left) Effects of parameter variations on the $\mathcal{F}(w)^2$ versus w distribution. (right) Monte Carlo true signal for the form factor variations. Bottom: (left) Slow Pion momentum distribution for RS Monte Carlo form neutral B decays. (right) Lepton momentum distribution for RS Monte Carlo from neutral B decays.

7.7.2 Signal Extraction

Analysis method 2 was repeated for each variation in the form factor and the branching fraction was recalculated. All reweighted data was processed through the same Monte Carlo tuning techniques after reweighting as before. The yields of combinatoric and peaking background as well as the signal yield are summarized in Table 39 for the signal region and in Table 40 for the sideband region. Table 39 shows that the variation of the combinatoric background yield in the signal region is minor with a RMS value of about 0.02%. Due to the change in signal shape from the variations we expect most of the variance to occur between the signal and peaking background extraction in the signal region due to their similar shape. Table 39 shows a RMS value of about 4.7% for the peaking background and 0.6% for the signal. Since the ratio of signal to peaking BG is about 10 to 1, both contribute to the systematic error with similar weights. Variations in the sideband region are minor. The RMS value of the combinatoric background, as shown in Table 40, is only 0.02%, showing that most of the form factor variation manifests itself in the signal region. This behavior is expected since the sideband consists of unrelated or different decay products not affected by the form factor.

The systematic error due to form factors in this analysis is assessed by recalculating the branching fraction with the reweighted Monte Carlo data. Since the reweighting technique causes a small shift in the Monte Carlo signal, as shown in Figures 72, 73 and 74, the detector efficiency has to be recalculated for each variation. Due to the hard cuts in the definition of the signal region this shape change causes some signal to leak out of the signal region, changing the overall efficiency. The reconstruction efficiency is reevaluated for each variation. The branching fraction is then recalculated using the signal yields and new efficiencies. The change in the branching fraction is recorded individually for each variation. Table 41 shows a summary of the efficiencies, branching fractions and errors due to variations. The analysis shows a higher dependence on ρ^2, where as $R_1(1)$ and $R_2(1)$ seem to be equally weighted. The uncertainties can be approximately regarded as symmetric. To assess a total systematic error, the mean variation in the branching

fraction is taken as the systematic error and added in quadrature. This results in a total systematic error of 1.02% for this analysis.

Table 39: Signal yields of form factor variation in signal region

Variation	Combinatoric BG	Peaking BG	Signal
unvaried	361367 ± 601	83603 ± 1778	661330 ± 2180
$rho^2 + 1\sigma$	361293 ± 601	88886 ± 1771	656145 ± 2169
$rho^2 - 1\sigma$	361443 ± 601	78440 ± 1786	666391 ± 2190
$R_1(1) + 1\sigma$	361263 ± 601	80932 ± 1777	664149 ± 2181
$R_1(1) - 1\sigma$	361475 ± 601	86349 ± 1780	658430 ± 2179
$R_2(1) + 1\sigma$	361372 ± 601	86981 ± 1765	657912 ± 2165
$R_2(1) - 1\sigma$	361364 ± 601	80183 ± 1792	664786 ± 2195

Table 40: Signal yields of form factor variation in sideband region

Variation	Combinatoric BG	Peaking BG	Signal
unvaried	498676 ± 706	754 ± 27	295 ± 17
$rho^2 + 1\sigma$	498576 ± 706	754 ± 27	298 ± 17
$rho^2 - 1\sigma$	498778 ± 706	755 ± 27	293 ± 17
$R_1(1) + 1\sigma$	498533 ± 706	755 ± 27	298 ± 17
$R_1(1) - 1\sigma$	498824 ± 706	754 ± 27	293 ± 17
$R_2(1) + 1\sigma$	498684 ± 706	755 ± 27	296 ± 17
$R_2(1) - 1\sigma$	498670 ± 706	754 ± 27	294 ± 17

Table 41: Efficiencies and branching fractions after form factor variation

Variation	Efficiency (%)	Branching Fraction (%)	Error (%)	Symmetric Error (%)
unvaried	22.96	4.90		
$rho^2 + 1\sigma$	22.95	4.86	0.76	0.75
$rho^2 - 1\sigma$	22.96	4.93	0.75	
$R_1(1) + 1\sigma$	22.95	4.92	0.46	0.46
$R_1(1) - 1\sigma$	22.97	4.87	0.47	
$R_2(1) + 1\sigma$	22.96	4.87	0.50	0.50
$R_2(1) - 1\sigma$	22.96	4.92	0.51	

8 Results

8.1 Branching Fraction Results

The $\mathcal{B}(\bar{B}^0 \to D^{*+}\ell^-\bar{\nu}_\ell)$ branching fraction in this analysis was determined through a one dimensional fitting technique to the M_ν^2 neutrino missing mass squared as well as from a two dimensional fitting technique to the M_ν^2 versus p_ℓ distribution. Each technique produced a result for the RS MC, WS MC and WS data combinatoric background. The one dimensional fitting technique seemed to produce slightly better fits while the two dimensional technique was able to produce slightly smaller fit errors. Table 42 shows a summary of the determined branching fractions together with their confidence levels for the individual backgrounds, methods and runs. To assess an averaged result of each of the two fit methods and all backgrounds the individual results are averaged according to their confidence levels as determined by the extraction fits and luminosity weights. This weighted average favors extractions with good fit values while only moderately taking weaker fits into account. The final result is therefore averaged according to:

$$BF_{avg} = \frac{1}{\mathcal{L}_{tot}} \cdot \sum_i \mathcal{L}_i \cdot \left(\frac{\sum_j BF_{ij} \cdot CL_{ij}}{\sum_j CL_{ij}} \right) \tag{89}$$

where $\mathcal{L}_i$ is the luminosity of the i^{th} run, CL_{ij} is the confidence level of the j^{th} branching fraction measurement of the i^{th} run and BF_{ij} is the j^{th} branching fraction of the i^{th} run. j represents the RC MC, WS MC or WS data combinatoric background measurement. This yields an average branching fraction for the individual methods of:

$$\begin{aligned} &\text{Method2(1D)}: && \mathcal{B}(\bar{B}^0 \to D^{*+}\ell^-\bar{\nu}_\ell) = (4.95 \pm 0.02 \pm 0.16)\% \\ &\text{Method3(2D)}: && \mathcal{B}(\bar{B}^0 \to D^{*+}\ell^-\bar{\nu}_\ell) = (4.91 \pm 0.01 \pm 0.15)\% \end{aligned} \tag{90}$$

Here the quoted errors are statistical and systematic respectively. Differences due to the different combinatoric background shapes have been accounted for in the systematic error.

The systematic error is dominated by the combinatoric background shape differences (for method 2 only) and PID uncertainties, followed by the error on the f_{00} branching fraction, B counting, and the form factor dependence in descending order. Both methods produce very consistent measurements. For the final result, the two dimensional fitting method was selected due to its smaller errors. The larger separation of the peaking background to the signal in this method lowers fit errors and softens the dependence of the extraction fit to shape changes from different combinatoric background sources, hence lowering the systematic error. This leads to the final result for the $\mathcal{B}(\bar{B}^0 \to D^{*+}\ell^-\bar{\nu}_\ell)$ branching fraction for this analysis of:

$$\mathcal{B}(\bar{B}^0 \to D^{*+}\ell^-\bar{\nu}_\ell) = (4.91 \pm 0.01 \pm 0.15)\% \tag{91}$$

The result is compared to the published measurements of this branching fraction currently used in [4]. Table 43 shows a listing of these measurements, their statistical and systematic errors, the current average [4], as well as this measurement for comparison. All quoted measurements were conducted using a full reconstruction technique. It can be seen that this analysis, due to the partial reconstruction technique, is the most precise measurement, both statistical and systematic, of this branching fraction to date. Adding the quoted errors in quadrature and comparing this result with the measurements in Table 43 it can be seen that this analysis agrees with four of the eight measurements within 1σ, as well as the PDG value within 1.4σ of the errors.

Table 42: Branching fractions for both methods, both leptons and combined over both runs ($NDF = 58$)

Run #	Method	BG Type	$\mathcal{B}(\bar{B}^0 \to D^{*+}\ell^-\bar{\nu}_\ell)$	CL (%)	χ^2/NDF
1	1D	RS MC	$(4.81 \pm 0.03)\%$	83	0.82
1	1D	WS MC	$(4.84 \pm 0.03)\%$	54	0.97
1	1D	WS data	$(4.88 \pm 0.03)\%$	52	0.98
1	2D	RS MC	$(4.82 \pm 0.02)\%$	76	0.86
1	2D	WS MC	$(4.86 \pm 0.02)\%$	43	1.02
1	2D	WS data	$(4.92 \pm 0.02)\%$	3	1.41
2	1D	RS MC	$(4.92 \pm 0.02)\%$	53	0.97
2	1D	WS MC	$(4.95 \pm 0.02)\%$	11	1.23
2	1D	WS data	$(5.05 \pm 0.02)\%$	63	0.93
2	2D	RS MC	$(4.92 \pm 0.01)\%$	47	1.00
2	2D	WS MC	$(4.95 \pm 0.01)\%$	8	1.29
2	2D	WS data	$(5.05 \pm 0.01)\%$	5	1.34

Table 43: $\mathcal{B}(\bar{B}^0 \to D^{*+}\ell^-\bar{\nu}_\ell)$ comparison with published results

$\mathcal{B}(B^0 \to D^{*+}\ell^-\bar{\nu}_\ell)$	Reference
$5.49 \pm 0.16 \pm 0.25$	*BABAR* [15]
$4.69 \pm 0.04 \pm 0.34$	*BABAR* [14]
$5.90 \pm 0.22 \pm 0.50$	*DELPHI* [70]
$6.09 \pm 0.19 \pm 0.40$	*CLEO2* [71]
$4.59 \pm 0.23 \pm 0.40$	*BELLE* [72]
$4.70 \pm 0.13 \pm 0.34$	*DELPHI* [73]
$5.26 \pm 0.20 \pm 0.46$	*OPAL* [74]
$5.53 \pm 0.26 \pm 0.52$	*ALEPH* [75]
5.16 ± 0.11	*PDG* [4]
$4.91 \pm 0.01 \pm 0.15$	***This Result***

8.2 Consideration of $|V_{cb}|$

The weak mixing matrix element $|V_{cb}|$ is directly connected to the $\bar{B}^0 \to D^{*+}\ell^-\bar{\nu}_\ell$ branching fraction through its partial decay width (38). The branching fraction result of this dissertation, together with the integrated decay width and the B^0 lifetime τ_{B^0} can be used to obtain a value of $|V_{cb}|$ directly. In order to keep the result independent of the form factor value at zero recoil F(1) at the time of determination, which is the common representation in literature, $F(1)|V_{cb}|$ will be calculated. In this dissertation $h_{A_1}(1)$ and F(1) are identical and represent different naming conventions only. Solving equation (47) for $F(1)|V_{cb}|$ the relation becomes:

$$I = \frac{1}{(F(1)|V_{cb}|)^2} \int_{w_{min}}^{w_{max}} \frac{d\Gamma(\bar{B}^0 \to D^{*+}\ell^-\bar{\nu}_\ell)}{dw} dw$$

$$F(1)|V_{cb}| = \sqrt{\frac{\mathcal{B}(\bar{B}^0 \to D^{*+}\ell^-\bar{\nu}_\ell)}{\tau_{B^0} \cdot I}} \tag{92}$$

We perform the integration using the following form factor parameters and B^0 lifetime. Statistical and systematic errors have been combined in the values below, which only show one error:

$$\begin{aligned} R_1(1) &= 1.429 \pm 0.075 \\ R_2(1) &= 0.827 \pm 0.044 \\ \rho^2 &= 1.191 \pm 0.056 \\ \tau_{B^0} &= (1.525 \pm 0.009) \times 10^{-12} \text{ s [4]} \\ \mathcal{B}(\bar{B}^0 \to D^{*+}\ell^-\bar{\nu}_\ell) &= (4.91 \pm 0.01 \pm 0.14)\% \end{aligned} \tag{93}$$

All errors are considered in the calculation. The integration is repeated with the individual form factor parameters varied up and down by 1σ. The differences are added in quadrature and considered the systematic error due to the form factor shape. The sys-

tematic error on the branching fraction has been reduced by the form factor contribution to avoid overcounting of this dependence. The error on τ_{B^0} is taken from [4]. All errors are combined in quadrature for the final systematic error. This results in a value for $F(1)|V_{cb}|$ of:

$$F(1)|V_{cb}| = (35.4 \pm 0.1 \pm 1.2) \times 10^{-3} \tag{94}$$

This result agrees with five of the eight measurements included in the world average, as well as with the world average [4] within 1σ of the errors. Table 44 shows a summary of the V_{cb} measurements included in the world average, as well as the world average for comparison. The proper determination of $|V_{cb}|$ is beyond the scope of this dissertation. The above calculation is rather intended to emphasize the importance of the precise knowledge of the $\mathcal{B}(\bar{B}^0 \to D^{*+}\ell^-\bar{\nu}_\ell)$ branching fraction.

Table 44: $F(1)|V_{cb}|$ comparison with published results

$F(1)\|V_{cb}\|$	Reference
$(35.9 \pm 0.2 \pm 1.2) \times 10^{-3}$	*BABAR* [76]
$(35.9 \pm 0.6 \pm 1.4) \times 10^{-3}$	*BABAR* [77]
$(39.2 \pm 1.8 \pm 2.3) \times 10^{-3}$	DELPHI [78]
$(43.1 \pm 1.3 \pm 1.8) \times 10^{-3}$	CLEO2 [79]
$(35.4 \pm 1.9 \pm 1.8) \times 10^{-3}$	BELLE [80]
$(35.5 \pm 1.4 \pm 2.3) \times 10^{-3}$	DELPHI [81]
$(37.1 \pm 1.0 \pm 2.0) \times 10^{-3}$	OPAL [82]
$(31.9 \pm 1.8 \pm 1.9) \times 10^{-3}$	ALEPH [83]
$(36.6 \pm 1.0) \times 10^{-3}$	*PDG* Avg. [4]
$(35.5 \pm 0.5) \times 10^{-3}$	*PDG* Eval. [4]
$(35.4 \pm 0.1 \pm 1.2) \times 10^{-3}$	***This Result***

REFERENCES

References

[1] J. H. Christenson *et al.*, Phys. Rev. Lett. **13**, 138 (1964)

[2] The *BABAR* Physics Book, P. F. Harrison, H. R. Quinn, SLAC-R-504 (1998)

[3] The *BABAR* Collaboration, B. Aubert *et al.*, Phys. Rev. D **66**, 032003 (2002)

[4] C. Amsler *et al.* (Particle Data Group), Phys. Lett. **B667**, 1 (2008)

[5] C. Itzykson, J. Zuber, Quantum Field Theory, Dover (2005)

[6] J. D. Richman, Lecture at the *BABAR* physics school (2008)

[7] N. Cabibbo, Phys. Rev. Lett. **10**, 531 (1963)
M. Kobayashi and T. Maskawa, Prog. Theor. Phys. **49**, 652 (1973)

[8] Particle Physics, A Comprehensive Introduction, A. Seiden, Addison Wesley (2004)

[9] L. Wolfenstein, Phys. Rev. Lett. **51**, 1945 (1983)

[10] J. C. Anjos *et al.*, Phys. Rev. Lett. **65**, 2630 (1990)
E. M. Aitala *et al.*, Eur. Phys. J. direct **C1**, 4 (1999)

[11] F. Abe *et al.*, Phys. Rev. Lett. **74**, 2626 (1994)
S. Abachi *et al.*, Phys. Rev. Lett. **74**, 2632 (1995)
V. M. Abazov *et al.*, Phys. Rev. Lett. **98**, 181802 (2007)

[12] H. Albrecht *et al.*, Phys. Lett. B **197**, 452 (1987)

[13] H. Albrecht *et al.*, Phys. Lett. B **324**, 249 (1994)

[14] B. Aubert *et al.*, Phys. Rev. D. **77**, 032002 (2008)

[15] B. Aubert *et al.*, Phys. Rev. Lett. **100**, 151802 (2008)

[16] Heavy Quark Symmetry, M. Neubert, Phys. Rept. **245**, 259 (1994)

[17] N. Isgur, M. Wise, Phys. Lett. B **232**, 113 (1989)

[18] N. Isgur, M. Wise, Phys. Lett. B **237**, 527 (1990)

[19] D. Cote *et al.*, arXiv:hep-ex/0409046v1 (2004)

[20] J. Schubert, BAD 1350, Version 5 (2007)

[21] D. Cote, BAD 809, Version 3 (2004)

[22] I. Caprini *et al.*, Nucl. Phys. B **530**, 153 (1998)

[23] The *BABAR* Collaboration, B. Aubert *et al.*, Phys. Rev. D **77**, 032002 (2008)

[24] S. Hashimoto *et al.*, Phys. Rev. D **66**, 014503 (2002)

[25] M. Bomben *et al.*, BAD 532, Version 13 (2004)

[26] I. Caprini *et al.*, Phys. Lett. B **380**, 376 (1996)

[27] M. S. Zisman, Ann. Rev. Nucl. Part. Sci. 47, 315 (1997)

[28] CLEO Collaboration, M. Artuso *et al.*, Phys. Rev. Lett. **62**, 2233 (1989)
ARGUS Collaboration, H. Albrecht *et al.*, Phys. **B192**, 245 (1987)
UA1 Collaboration, C. Albajar *et al.*, Phys. Lett. **B186**, 247 (1987)

[29] P. Oddone, Detector Considerations, UCLA Workshop, pp. 423 (Jan 1987)

[30] The *BABAR* Collaboration, B. Aubert *et al.*, Phys. Rev. D. **72**, 032005, (2005)

[31] Lecture on event reconstruction, J. Coleman, *BABAR* Physics School (2008)

[32] B. Aubert *et al.*, The *BABAR* Collaboration, Nucl. Instrum. Meth. A**479**, 1 (2002)

[33] The *BABAR* Workbook, http://www.slac.stanford.edu/BFROOT/www/doc/workbook/detector/detector.html

[34] P. R. Burchat *et al.*, Nucl. Instrum. Meth. **A316**, 217 (1992)

[35] The *BABAR* DCH web page, http://www.slac.stanford.edu/BFROOT/www/Detector/CentralTracker/index.html

[36] The DIRC Particle Identification System for the *BABAR* Experiment, L. Adam *et al.*, Nucl. Instrum. Meth. **A538**, 281 (2005)

[37] T. Sumiyoshi *et al.*, Nucl. Instrum. Meth. A **433**, 385 (1999)
L. Cremaldi *et al.*, IEEE Trans. Nucl. Sci. 56, 1475 (2009)

[38] D. Barlett *et al.*, Nucl. Instrum. Meth. A **260**, 55 (1987)

[39] The *BABAR* Collaboration, Technical Design Report, SLAC-R-457 (1995)

[40] R. Bartoldus *et al.*, BAD 194, Version 1 (2002)

[41] S. B. Bracker *et al*, IEEE Trans. Nucl. Sci. **43**, 2457 (1996), SLAC-BaBar-Note-128
N. Geddes, Comp. Phys. Commun. **110**, 38 (1998)

[42] H. Albrecht *et al.*, Phys. Lett. B **324**, 249 (1994)

[43] S. B. Athar *et al.*, Phys. Rev. D **66**, 052003 (2002)

[44] P. Abreu *et al*, Z. Phys. C **74**, 19 (1997)

[45] B. Aubert *et al.*, Phys. Rev. Lett. **95**, 042001 (2005)
B. Aubert *et al.*, Phys. Rev. Lett. **100**, 051802 (2008)

[46] G. C. Fox and S. Wolfram, Nucl. Phys. B **149**, 413 (1979)

[47] M. Rotondo, F. Simonetto, BAD 1377, Version 4 (2006)

[48] A. Mohapatra *et al.*, BAD 474, Version 3 (2004)

[49] T. Brandt, BAD 396, Version 1 (2002)

[50] R. Godang *et al.*, BAD 731, Version 24 (2005)

[51] D. Lopes Pegna *et al.*, BAD 2005, Version 14 (2005)

[52] The *BABAR* Collaboration, B. Aubert *et al.*, Phys. Rev. D **79**, 012002 (2009)

[53] J. Dingfelder, Overview of changes between simulation productions SP4 to SP8, AWG Note (2006) http://www.slac.stanford.edu/BFROOT/www/Physics/Analysis/AWG/Semileptonic/SPChanges_Overview.txt

[54] J. C. Anjos *et al.*, Phys. Rev. Let. **62**, 1717 (1989)

[55] E. Barberio *et al.*, Comput. Phys. Commun. **66** 115 (1991)

[56] Z. Was, Acta Phys. Polon. B **18**, 1099 (1985)

[57] F.A. Brends *et. al*, Comput. Phys. Commun. **29**, 185 (1983)

[58] F. Simonetto *et al.*, BAD 182, Version 11 (2001)

[59] W. Verkerke, D. Kirkby, CHEP-2003-MOLT007, physics/0306116

[60] R. Brun *et al.*, Nucl. Instrum. Meth. A **389**, 81 (1997)

[61] D. Lopes Pegna, V. Luth, $B \to Xcl\nu$ Reweighting 2007, AWG note, http://www.slac.stanford.edu/BFROOT/www/Physics/Analysis/AWG/Semileptonic/Reweighting2007.html

[62] D. Lopes Pegna, Princeton University, Dept. of Physics, private communication

[63] *BABAR* PID notes, http://www.slac.stanford.edu/BFROOT/www/Physics/Tools/Pid/PidOnMc/pidonmc.html

[64] *BABAR* tracking notes, http://www.slac.stanford.edu/BFROOT/www/Physics/TrackEfficTaskForce/TrackingTaskForce-2007-R22.html

[65] A. Telnov, *BABAR* PID HyperNews communication # 1794

[66] M. Purohit . *et al.*, BAD 1465, Version 3 (2007)

[67] O. Long, BAD 54, Version 7 (2001)

[68] Slow Pion Efficiency in R22 and R24, Maurizio Martinelli, *BABAR* Collaboration Meeting, SLAC, October 28 (2008)

[69] B. Aubert *et al.* Phys. Rev. D **71**, 051502 (2005)

[70] J. Abdallah *et al.*, Eur. Phys. J. C **33**, 213 (2004)

[71] N. E. Adam *et al.*, Phys. Rev. D **67**, 032001 (2003)

[72] K. Abe *et al.*, Phys. Lett. B **526**, 247 (2002)

[73] P. Abreu *et al.*, Phys. Lett. B **510**, 55 (2001)

[74] G. Abbiendi *et al.*, Phys. Lett. B **482**, 15 (2000)

[75] D. Buskulic *et al.*, Phys. Lett. B **395**, 373 (1997)

[76] B. Aubert *et al.*, Phys. Rev. D **79**, 012002 (2009)

[77] B. Aubert *et al.*, Phys. Rev. Lett. **100**, 231803 (2008)

[78] J. Abdallah *et al.*, Eur. Phys. J. C **33**, 213 (2004)

[79] N. E. Adam *et al.*, Phys. Rev. D **67**, 032001 (2003)

[80] K. Abe *et al.*, Phys. Lett. B **526**, 247 (2002)

[81] P. Abreu *et al.*, Phys. Lett. B **510**, 55 (2001)

[82] G. Abbiendi *et al.*, Phys. Lett. B **482**, 15 (2000)

[83] D. Buskulic *et al.*, Phys. Lett. B **395**, 128 (1997)

VITA

Peter Sonnek was born in 1981 in Kempten, Germany as the son of architect Gerd Helmut Sonnek and homemaker Erna Sonnek. He resided in his home town until spending an academic year at Tishomingo County High School in Iuka, Mississippi, USA, as a part of a foreign exchange program. During his stay in Mississippi, he participated in the International Science and Engineering Fair in Fort Worth, Texas, in 1998 receiving an honorable mention award by the National Aeronautics and Space Administration for his work on the "Calculation and Rotation of 3D Objects". After returning to Germany he graduated high school form the Allgäu Gymnasium in Kempten with an emphasis on Mathematics and Physics. He pursued his undergraduate studies in Physics at the University of Augsburg in Germany successfully completing the "Vordiplom" examinations at the end of his studies in 2004. In 2005 he joined the graduate program of Physics at the University of Mississippi receiving a Master of Arts degree in Physics in 2006 and a Graduate Student Achievement Award in Physics in 2007. During his graduate studies he taught physics laboratory classes for premedical students and later became a research assistant for his adviser Prof. Dr. Lucien Cremaldi. He is currently pursuing the degree of Doctor of Philosophy at the University of Mississippi.